USC
UNIVERSIDADE
DE SANTIAGO
DE COMPOSTELA

INTERNATIONAL DOCTORAL
SCHOOL OF THE USC

Xoán
Mayo López

PhD Thesis

Jet imaging of evolving anisotropic QCD matter

Santiago de Compostela, 2025

Doctoral Programme In Nuclear and Particle Physics

ESCOLA DE DOUTORAMENTO
INTERNACIONAL DA USC

TESE DOUTORAL

JET IMAGING OF EVOLVING ANISOTROPIC QCD MATTER

Xoán Mayo López

Director: Prof. Carlos Salgado
Dr. Andrey V. Sadofyev

Tutor/a: Prof. Carlos Salgado

PHD PROGRAM IN NUCLEAR AND PARTICLE PHYSICS

SANTIAGO DE COMPOSTELA

“A vida non vai por quen toca,
vai por quen baila."

Avoa Filucha

Aos meus.

Agradecementos

Atrás quedan xa vinte e cinco anos de formación académica, unha década vivindo en Santiago e catro anos de doutoramento que pechan un capítulo incriblemente fermoso na miña vida. Se estou escribindo estes agradecementos, é porque unha boa chea de xente tivo a *culpa* de que chegase até aquí. O primeiro Carlos, quen me abriu as portas á física teórica acolléndome como estudante de master, e me ofreceu a oportunidade de quedar cando rematei. De Carlos como titor podería destacar unha infinidade de cousas, pero quizais as que máis me impresionaron son a súa grandísima intuición física e, por riba de todo, a súa proximidade e serenidade para ensinar e aconsellar. Non podería ter escollido un mellor guía para esta aventura tan emocionante. Grazas.

From a young age, I have deeply admired science and scientists. However, it was not until recently, thanks to Andrey, that I truly understood what science and being a scientist really means. I am constantly impressed by his immense patience, kindness and willingness to teach me, and, of course, his exceptional talent for theoretical physics. He is the epitome of inspiration, a lighthouse in the often foggy journey of a Ph.D., the scientist I admire most. I will always cherish those long discussions over (literally) countless cups of coffee, where I learned not only about phsysics, but also, and more importantly, about life. I may hold a Ph.D., but it is Andrey who made me a scientist. Thank you. Last, but not least, completing my trio of mentors, I have been incredibly fortunate to have João's invaluable support. A brilliant scientist and a worderful person, he has been a great source of strenght throughout this journey. Thank you.

Two research stays significantly enriched both my Ph.D. training and my life experience. Back in 2023, thanks to Dr. Urs Wiedemann, I had the opportunity to visit CERN, located on the shores of Lake Geneva. CERN is renowned for housing some of the most impresive machines ever built, but I can assure you that it is also home to an equally impresive group of people. I would like to express my gratitude to the entire heavy-ion group at CERN, and especially to Alba, Bruno and Rachel, whose companionship made my stay in Switzerland truly excepcional. E por suposto, non me podo lembrar de Xenebra sen que me veñan á cabeza as ceas e cervexas con Eloi e Erlantz, vaia figuras. Last year I had the opportunity to visit Prof. Zhongbo Kang's group at UCLA. Having the opportunity to be part of his group and learn physics from him for a few months felt like an absolute priviledge. Beyond the science, everybody knows that Los Angeles, the City of Stars, is full of wonders, but my best discovery there was the UCLA surfing team: Jani, Diego, Chuanqi, Luke, Meisen and Noah.

A tarefa de rematar un doutoramento en física, e chegar ata el, non é do máis sinxelo. Porén, se gardo tan bo recordo do camiño é, sen lugar a dúbida, pola xente que me acompañou nel. As fermosas rúas (e bares) de Compostela convertéronse nun fogar para min durante esta última década. Botar a vista atrás é sinónimo dun sorriso cheo de morriña e recordos marabillosos, protagonizados por Martina, Lucas, Cae, Iago, Catuxa, Mateo, Michu, Alicia, Carlos, Miguel, Clara... que comezaron sendo compañeiros, e remataron sendo os meus amigos. Quen me coñeza de veras pronto se decataría de que falta un nome nesa lista, Martín. Martín é o mellor que me deron Compostela e a física. Un amigo sincero, un apoio incondicional, unha tranquilidade pasmosa, e moita moita moita festa. A definición perfecta do meu compañeiro de batallas. Ademais, quero darlle as grazas a todos os estudantes do IGFAE cos que tantos *recreos* e charlas compartín, e aos que non vou poder mencionar para non facer que esta tese chegue ás trescentas páxinas. Porén, debo destacar á resistencia da cobacha, specially my beloved cellmates, Luigi and Praveen, e a Sergio, o meu socio en case todas as viaxes. Para poñerlle a guinda ao pastel, durante estes anos en Compostela tiven o pracer de compartir piso con Pablo, Jorge, David, Martín e David, aos que lle debo un sen fin de anécdotas que nos unirán para sempre.

Poucas cousas me gustan tanto como volver a Noia e todo o que iso conleva. Poñer un pé na praza do Tapal e sentar a falar da vida con Abel, Martino, Castro, Blanca, Manu, Jorge, Gloria, María, Pablo, Javi, Julia, David, Cris, Pete, Irene, Diego, Mace, Andrea, Marina, Ruben, Martiña... é a forma máis sinxela de volver a ser un cativo. A Noia débolle tamén ter coñecido a Jorge, a Alba e a Mariña, tres persoas completamente indispensables. Non podo imaxinar como sería a miña vida sen o seu cariño, apoio, confianza, risas e pizzas, pero é probable que eu non tivese chegado ata aquí, e é seguro que non sería así de feliz. Crecer xuntos nos (xa non poucos) últimos anos só me fai desexar descubrir o que nos espera nos moitos que están por vir.

Canto máis vello me fago, máis claro teño que a miña familia é un tesouro, un conxunto de persoas marabillosas e excepcionais que enchen o meu corazón. O amor das miñas avoas, dos meus tíos e dos meus primos é do máis prezado que teño na miña vida. Cómo pode ser que haxa quen viva sen un tío Basi?

Papá, Mamá, e Uxi son o meu pasado, o meu presente e o meu futuro. Con eles son un cativo inquieto, un mozo entusiasta e un home feliz. Eles fan que calquera reto semelle posible. Xamais lles poderei devolver todo o que lles debo. Se algo teño aprendido nestes anos é que eu sen a miña familia son un ninguén que vai para ningures.

E para rematar, esta tese e eu mesmo non poderíamos ser sen Paula, o amor da miña vida. Tan boa, tan intelixente, tan pura, tan sinxela. Cantas aventuras nos quedan por vivir, empezando por Boston, que xa está agardando por nós!

Abstract

The exploration of Quantum Chromodynamics under extreme conditions provides a window into a wide range of fascinating phenomena: from the fundamental properties of the strong interaction, a fundamental force governing the subatomic world, to the conditions present in the primordial Universe, immediately after the Big Bang. This is achieved through the study of relativistic heavy-ion collisions at RHIC and LHC, where a novel phase of complex nuclear matter is created. This thesis presents a novel formalism for describing jet propagation within this complex matter, designed to use jets as differential probes of its spatio-temporal structure. The three scientific papers comprising this thesis [1, 2, 3] detail this novel formalism, deriving the two dominant perturbative processes of jet modifications, transverse momentum broadening and medium-induced gluon radiation, in the presence of an evolving medium with non-trivial structure.

Keywords: Jet quenching, Heavy-ion collisions, High Energy QCD, pQCD.

Resumo

A exploración da Cromodinámica Cuántica en condicións extremas ofrécenos unha fiestra a fenómenos fascinantes que abarcan dende as propiedades fundamentais da interacción forte, unha das forzas fundamentais que gobernan o mundo subatómico, até as condicións presentes no Universo primordial, instantes despois do Big Bang. O seu estudo lévase a cabo mediante colisións de ións pesados relativistas en instalacións como RHIC e LHC, onde se produce unha nova fase da materia nuclear complexa. Nesta tese preséntase un novo formalismo para describir a propagación de jets dentro desta materia complexa, cuxo obxectivo é utilizar os jets como sondas da súa estrutura espazo-temporal. Os tres artigos científicos que a compoñen [1, 2, 3] detallan este formalismo, e neles derívanse os dous procesos perturbativos dominantes que modifican os jets, o ensanchamento do momento transverso e a radiación de gluóns inducida polo medio, considerando a evolución do medio e a súa estrutura non trivial.

Palabras clave: Jet quenching, Colisión de ións pesados, QCD a altas enerxías, pQCD.

Resumen

La exploración de la Cromodinámica Cuántica en condiciones extremas nos abre una ventana a fenómenos fascinantes que abarcan desde las propiedades fundamentales de la interacción fuerte, una de las fuerzas fundamentales que gobiernan el mundo subatómico, hasta las condiciones presentes en el Universo primordial, instantes después del Big Bang. Su estudio se lleva a cabo mediante colisiones de iones pesados relativistas en instalaciones como RHIC y LHC, donde se produce una nueva fase de la materia nuclear compleja. En esta tesis se presenta un nuevo formalismo para describir la propagación de jets dentro de esta materia compleja, cuyo objetivo es utilizar los jets como sondas de su estructura espacio-temporal. Los tres artículos científicos que la componen [1, 2, 3] detallan este formalismo y en ellos se derivan los dos procesos perturbativos dominantes que modifican los jets, el ensanchamiento del momento transverso y la radiación de gluones inducida por el medio, considerando la evolución del medio y su estructura no trivial.

Palabras clave: Jet quenching, Colisiones de iones pesados, QCD a altas energías, pQCD.

Conventions and notations

The conventions used throughout this thesis, which are standard in the field, are detailed in this section. In all calculations, the reference frame is defined relative to the jets, with the z-axis aligned along the direction of propagation of the leading parton. The 4-vectors are in general noted $v_\mu = (v_0, \boldsymbol{v}, v_z)$, where bold quantities $\boldsymbol{v}$ are 2-dimensional vectors in the transverse plane. The Greek letters $\mu, \nu, \ldots$ are reserved as indices of the $3+1$-dimensional space. The Latin letters $a, b, c, \ldots$ are reserved for the $N_c^2 - 1$ adjoint indices of the $SU(N_c)$ group, while the fundamental indices are omitted to alleviate the notation, since they can be easily restored by following the color flow in each diagram. Whenever the components of a vector in the transverse plane must be specified, we use the index α, where $\alpha = 1, 2$ represents the two transverse directions. The Einstein summation convention is assumed for all index types within this work. The usual signature for the metric in particle physics is used,

$$g^{\mu\nu} = \begin{pmatrix} 1 & 0 & 0 & 0 \\ 0 & -1 & 0 & 0 \\ 0 & 0 & -1 & 0 \\ 0 & 0 & 0 & -1 \end{pmatrix} , \tag{1}$$

such that the square of a 4-vector reads $v^2 = v_0^2 - \boldsymbol{v}^2 - v_z^2$. Throughout the thesis, the large energy limit for the jet partons is assumed, expanding every quantity in a series of inverse powers of the parton energy. With this, the on-shell condition on the 4-momentum of a parton is

$$p_\mu = \left(E, \boldsymbol{p}, E - \frac{\boldsymbol{p}^2}{2E} + \mathcal{O}\left(\frac{\perp^4}{E^3}\right)\right) , \tag{2}$$

where $\perp$ represents the characteristic transverse scale of the momenta. Several shorthand notations have been introduced regarding the integrals. Integrals over space, the transverse plane, and the longitudinal direction are denoted, respectively, as

$$\int_x \equiv \int d^2\boldsymbol{x}\, dz \,, \qquad \int_{\boldsymbol{x}} \equiv \int d^2\boldsymbol{x} \,, \qquad \int_z \equiv \int dz \,. \tag{3}$$

On the other hand, integrals over the 3-momentum, the transverse momentum, and the longitudinal momentum are denoted, respectively, as

$$\int_p \equiv \int \frac{d^2\boldsymbol{p}\, dp_z}{(2\pi)^3}\,, \qquad \int_{\boldsymbol{p}} \equiv \frac{d^2\boldsymbol{p}}{(2\pi)^2}\,, \qquad \int_{p_z} \equiv \int \frac{dp_z}{2\pi}\,. \tag{4}$$

In Sections 2.2.3 and 2.3.3, where we deal with the chromoelectric fields present in the glasma phase, the 'absolute' value of the $SU(N_c)$ field in color space is defined as $E \equiv \sqrt{\sum_a (E^a)^2}$, and the integrals are denoted

$$\int_E \equiv \int_{-\infty}^{+\infty} \frac{d^{N_c^2-1}E^a}{(\sqrt{\pi}E_0)^{N_c^2-1}}\,, \qquad \int_E \equiv \int_{-\infty}^{+\infty} \frac{dE}{(\sqrt{\pi}E_0)}\,, \tag{5}$$

for $SU(N_c)$ and $U(1)$ fields respectively.

Contents

Abstract i

Resumo iii

Resumen v

Conventions and notations vii

1 Introduction and objectives 1

- 1.1 The basic principles of QCD . . . 1
  - 1.1.1 The QCD Lagrangian . . . 2
  - 1.1.2 Asymptotic freedom, factorization and IRC divergencies . . . 4
- 1.2 Jet physics in collider experiments . . . 6
- 1.3 QCD under extreme conditions . . . 8
- 1.4 Hard probes in HICs . . . 12
- 1.5 Objectives and methodology . . . 15
  - 1.5.1 Objectives . . . 15
  - 1.5.2 Methodology . . . 16

2 The novel formalism: a discussion of the results 17

- 2.1 The background field and the field correlators . . . 19
- 2.2 The transverse momentum broadening . . . 22
  - 2.2.1 Broadening in anisotropic, flowing matter in the dilute limit . . . 23
  - 2.2.2 Broadening in anisotropic, static matter in the dense limit . . . 30
  - 2.2.3 Broadening in the glasma phase . . . 36
- 2.3 The medium-induced radiation . . . 40
  - 2.3.1 Medium-induced radiation in anisotropic, flowing matter in the dilute limit . . . 42
  - 2.3.2 Medium-induced radiation in anisotropic, static matter in the dense limit . . . 48
  - 2.3.3 Medium-induced radiation in the glasma . . . 52

3 Conclusions 61

4 Published Results 65
Article I 66
Article II 89
Article III 105

Resumo estendido 123

Bibliography 132

1

Introduction and objectives

This chapter provides a brief overview of the key topics relevant for this thesis. We begin by exploring the fundamental principles of Quantum Chromodynamics (QCD), the theory of strong interactions. Then, we introduce the concept of a jet and its definition in the context of collider experiments. Subsequently, we examine the behavior of QCD under extreme conditions, focusing on the formation of extreme states of nuclear matter. Finally, we review the role of jets as probes of the hot/dense nuclear matter created in heavy ion collisions, introducing the main topic of this thesis.

1.1 The basic principles of QCD

During the 1950s, great advancements in experimental techniques, such as the invention of the vacuum chamber, triggered the discovery of a vast number of new subatomic particles. These subatomic particles, heavier than the pion, were named **hadrons** after the Ancient Greek word “hadrós”, meaning strong or bulky, which was chosen to contrast with lepton, derived from the Greek “leptos”, meaning small or light. The observed proliferation of hadrons led physicists to conclude that these particles were not fundamental, but rather composite structures. In the 1960s, Gell-Mann and Ne’eman proposed the *eightfold way* [4, 5], an organizational scheme for particles with similar properties and masses, based on the irreducible representations of the $SU(3)$ flavour symmetry group. The emergence of this symmetry could be explained by the existence of three flavours of fundamental spin-1/2 particles –later called quarks– which combine to form the different hadrons [6, 7]. However, the quark model alone was not able to solve the apparent violation of the spin-statistics theorem for certain particles with spin-3/2, such as the Δ^{++} and Ω^{-}, which are composed of three identical quarks, suggesting a symmetric wavefunction and, hence, contradicting the expected antisymmetrmy for fermionic states. To resolve this, a new $SU(3)$

gauge degree of freedom, later known as the color charge, was proposed for the quarks [8]. In addition, the impossibility of observing free quarks experimentally hinted at the existence of a strong attracting force that keeps quarks bounded together inside hadrons, later proposed by Greengberg, Han and Nambu [8, 9]. Notably, Han and Nambu correctly anticipated that the force carriers mediating this interaction would be eight vector gauge bosons: the QCD gluons. In 1968, deep inelastic scattering experiments at SLAC revealed three point-like scattering centers inside the proton, providing the first direct experimental evidence for the validity of the quark model [10, 11]. Building upon these ideas, the 1970s witnessed the development of QCD, a quantum field theory (QFT) that incorporates color charge as the source of the strong interaction. Today, QCD is widely regarded as one of the most successful physical theories, providing an extremely precise description of strong interactions across diverse scenarios and explaining a remarkable range of phenomena [12]. Despite its success, QCD still presents fundamental challenges, such as fully understanding confinement or chiral symmetry breaking, which are being actively investigated through a combination of theoretical approaches, like lattice QCD calculations, and experimental programs at colliders [13].

1.1.1 The QCD Lagrangian

Within the context of QFT, QCD is a Yang-Mills theory of the $SU(3)$ group, consisting of massless gauge spin-1 vector particles, gauge bosons called gluons; and massive spin-1/2 particles, fermions called quarks. To this day, there have been six different quarks discovered –u, d, c, s, t, b– usually grouped into three different generations of increasing mass, with electric charges $+2/3e$ or -1/3e. The coupling of a Yang-Mills theory to fermionic matter, a challenging problem due to the complex structure of $SU(N_c)$ gauge fields, was first derived in Ref. [14]. The conserved charge associated to the corresponding symmetry, equivalent to the electric charge for quantum electrodynamics (QED), is known as color. For generality, we consider a $SU(N_c)$ Yang-Mills theory, where N_c represents the number of colors. While QCD corresponds to $N_c = 3$, keeping N_c generic allows us to identify color structures and simplify calculations, particularly in the large-N_c limit ($N_c \to \infty$), where certain diagrams at each perturbative order can be neglected.

Since $SU(N_c)$ is a Lie group, it has two main representations: the fundamental representation and the adjoint one. The former is the smallest non-trivial irreducible representation of the group, and consist of $N_c^2 - 1$ different generators, noted t^a in what follows, which can be written in terms of $N_c \times N_c$ traceless Hermitian matrices. The fundamental generators satisfy the following algebra

$$\left[t^a, t^b\right] = i f_{abc} t^c \,, \tag{1.1}$$

with $a, b, c \in \{1, 2, ..., N_c\}$, and f_{abc} the so-called group structure constants. On the other hand, the adjoint representation consists of $N_c^2 - 1$ different generators, noted T^a in what follows, which can be written in terms of $(N_c^2 - 1) \times (N_c^2 - 1)$ antisymmetric matrices. The adjoint generators are fully determined by the structure constants, with their matrix elements being

$$(T^a)_{bc} = -i f_{abc} \,. \tag{1.2}$$

For the case of QCD, it is common to define the $N_c^2 - 1 = 8$ fundamental generators in terms of the eight Gell-Mann matrices λ^a as $t^a_{ij} = \frac{1}{2}\lambda^a_{ij}$, with $i, j \in \{1, 2, 3\}$. In general, $SU(N_c)$ Yang-Mills theories are usually referred to as non-Abelian because the $SU(N_c)$ groups themselves are non-Abelian, as demonstrated by the non-commutativity of their fundamental generators (1.1).

Let us deduce the QCD Lagrangian by enforcing the Lagrangian of free fermions to be symmetric with respect to local rotations of the $SU(3)$ group, see e.g. [15, 16, 17, 18]. We shall start by writing the Lagrangian density of free quarks as

$$\mathcal{L}_0 = \bar{\psi}^j_q \left[i\gamma^\mu \partial_\mu - m_q \right] \psi^j_q \tag{1.3}$$

where ψ^j_q $\left(\bar{\psi}^j_q\right)$ is the quark (antiquark) fermionic field, with color $j \in \{1, 2, ..., N_C\}$ in the fundamental representation of $SU(N_c)$, flavor $q \in$ {u,d,s,c,b,t}, and mass m_q. In order to make (1.3) invariant under $SU(N_c)$ transformations of the fermionic fields $\psi \to \psi' = e^{it^a\alpha^a(x)}\psi$, where $\alpha^a(x)$ are N_c local arbitrary functions, one must replace the normal derivative by the covariant derivative, defined as

$$D_\mu = \partial_\mu + igt^a A^a_\mu \,, \tag{1.4}$$

where color indices are omitted, and N_c gauge fields A^a_μ have been introduced. One might initially consider the transformation of these gauge fields to be $A^a_\mu \to A^{a\prime}_\mu = A^a_\mu - \frac{1}{g}\partial_\mu \alpha^a$. With this, the Lagrangian density becomes

$$\mathcal{L}_{\text{Dirac}} = \bar{\psi}_q \left[i\gamma^\mu D_\mu - m_q \right] \psi_q \,. \tag{1.5}$$

However, (1.5) is not enough to produce a gauge invariant Lagrangian. This can be solved by rewriting the actual gauge field transformation as $A^a_\mu \to A^{a\prime}_\mu = A^a_\mu - \frac{1}{g}\partial_\mu \alpha^a - f_{abc}\alpha^b A^c_\mu$. Furthermore, a gauge invariant kinetic term for the gauge fields

$$\mathcal{L}_{\text{gauge}} = -\frac{1}{4} F^a_{\mu\nu} F^{a\mu\nu} \,, \tag{1.6}$$

with the gauge field tensor being

$$F^a_{\mu\nu} = \partial_\mu A^a_\nu - \partial_\nu A^a_\mu + g f^{abc} A^b_\mu A^c_\nu \,, \tag{1.7}$$

may be added to the Lagrangian. Thus, the QCD Lagrangian density can be finally written as

$$\mathcal{L}_{\text{QCD}} = \mathcal{L}_{\text{Dirac}} + \mathcal{L}_{\text{gauge}} = \bar{\psi}_q \left[i\gamma^\mu D_\mu - m_q \right] \psi_q - \frac{1}{4} F^a_{\mu\nu} F^{a\mu\nu} \,, \tag{1.8}$$

which is explicitly invariant under $SU(N_c)$ transformations by construction.

Some key aspects of strong interactions can be directly inferred from the Lagrangian of interacting quarks and gluons shown in (1.8). For instance, local gauge invariance requires the gauge bosons to be massless, since a mass term for A^a_μ would break its symmetry. This is analogous to the case of QED, where the photon is massless as a consequence of local $U(1)$ gauge invariance. On the other hand, the pure gauge term in the Lagrangian (1.6) shows a crucial distinction between non-Abelian gauge theories like QCD and Abelian ones like QED. This term includes self-interactions among the gauge bosons, leading to three- and four-point vertices. These self interactions imply that gluons carry the color charge conserved by the $SU(N_c)$ symmetry, unlike photons in QED. For a thorough discussion on the QCD Lagrangian and its properties, see e.g. [15, 16, 17, 18].

1.1.2 Asymptotic freedom, factorization and IRC divergencies

One of the most extraordinary features of QCD is that the strength of the strong interaction decreases as the energy scale of the studied process, Q, increases. This property is reflected in the theory by the running of the coupling constant: the renormalization of the ultraviolet (UV) divergences forces the coupling constant $\alpha_s = \frac{g_s^2}{4\pi}$ to be a function of Q, following the so-called renormalization group equation (RGE). At first order, i.e. including correction up to one loop, the coupling evolves as [19, 20]

$$\alpha_s(Q^2) = \frac{1}{\beta \log \frac{Q^2}{\Lambda^2_{\rm QCD}}}\,, \tag{1.9}$$

where $\beta = (11N_c - 2n_f)/(12\pi)$ with n_f the number of active light flavors at the scale Q, and $\Lambda_{\rm QCD}$ is the so-called Landau pole of QCD. The coupling constant (1.9) has two limiting behaviours depending on the value of the energy scale of the process. First, when $Q \gg \Lambda_{\rm QCD}$, the effective coupling becomes small, $\alpha_s(Q) \to 0$, and quarks and gluons (partons) become the physically relevant degrees of freedom of the theory. A perturbative description of weakly interacting partons is valid in this regime, enabling the use of perturbation theory. This phenomenon is known in the literature as **asymptotic freedom**, and was predicted theoretically by Gross, Wilczek and Politzer in 1973 [19, 20]. On the other hand, when $Q \sim \Lambda_{\rm QCD}$ (but larger), the effective coupling diverges, $\alpha_s(Q^2) \to \infty$, and the perturbative picture breaks, with partons being strongly bounded inside hadrons. In fact, there is extensive experimental evidence supporting the fact that color charged particles, such as quarks and gluons, cannot be observed directly, but are always confined within hadrons. This phenomenon, known in the literature as **color confinement**, has not been proven analytically yet, but has been extensively observed in numerical simulations [21, 22]. Notice that the running of the coupling given by (1.9) has been computed at first order, and, therefore, cannot be used to study the limit of small Q, which would require a resummation of higher order corrections. The scale that separates the weakly and

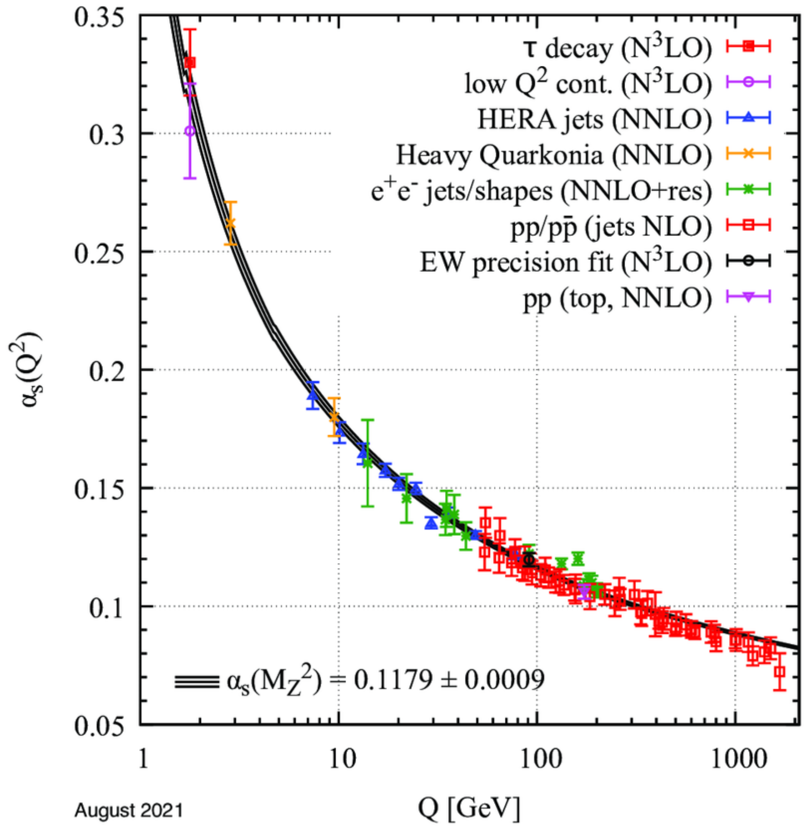

August 2021

Figure 1.1: Summary of measurements of α_s as a function of the energy scale Q obtained for several different physical processes compared to the theoretical prediction using the RGE evolution. This figure has been extracted from [23] under a Creative Commons license.

strongly coupled regimes in QCD is not predicted by the theory itself but determined from experiment to be approximately the inverse typical size of a hadron: $\Lambda_{\text{QCD}} \approx 200\,\text{MeV}$. The running of the QCD coupling constant has been experimentally verified in several different physical processes, see Figure 1.1, demonstrating excellent agreement with the high-precision theory predictions.

The running of the coupling constant with the energy scale is crucial to understand high energy scattering processes involving hadrons. In these processes, the coupling constant becomes small for the hard scatterings, i.e. the part of the collision involving high energies $Q \gg \Lambda_{\text{QCD}}$ (or short distances $\sim 1/Q \ll 1/\Lambda_{\text{QCD}}$). This allows us to treat the physical degrees of freedom –weakly coupled partons– using perturbative methods. In contrast, the distribution of partons within hadrons, governed by low energy $Q \sim \Lambda_{\text{QCD}}$ (or large distance) physics, is inherently non-perturbative. However, one would expect the internal structure of hadrons to be universal, i.e. independent of the specific collision process. Therefore, the hard scattering dynamics and the soft universal features of the internal structure of hadrons seem to be separable. This property is known in the literature as **factorization**, and it is a crucial feature of QCD. As an illustration, let us examine the cross-section for the collision of two hadrons, A and B, producing a hadronic final state C and an additional state X. Assuming factorization, it can be written schematically as

$$\sigma^{A+B\to C+X} = f_{a/A}(x_a, Q^2) \otimes f_{b/B}(x_b, Q^2) \otimes \hat{\sigma}^{a+b\to c}(x_a, x_b, Q^2, \alpha_s(Q^2)) \otimes D_{c/C}(x_c, Q^2)\,, \tag{1.10}$$

where $f_{a/A}(x_a, Q^2)$ is a parton distribution function (PDF) giving the probability of finding parton a with energy fraction x_a inside the hadron A, $D_{c/C}(x_c, Q^2)$ is the fragmentation function (FF) corresponding to the hadronization of the parton c into the hadron C, and $\hat{\sigma}$ is the partonic cross-section of the hard scattering. While the PDFs and FFs are universal non-perturbative objects that must be extracted from experimental data, the partonic cross-section can be computed to the desired order in perturbation theory. A rigorous proof of factorization of the cross-section, as formulated in (1.10), has been developed only for a limited class of processes, see [24, 25]. However, phenomenologically motivated factorization schemes have been highly successful in describing a wide range of experimental data for various observables.

QCD calculations are populated by three types of divergences: UV, infrared (IR), and collinear. UV divergences arise from the short-distance behaviour of the theory and are handled through renormalization, reabsorbing infinities into redefinitions of the parameters of the theory, as in the case of the coupling constant. On the other hand, both IR and collinear divergences arise from the long-distance behaviour of the theory and are associated with the (near) massless light quarks and massless gluons. The IR divergences appear when the momentum of a gluon or a light quark approaches zero, while the collinear divergences occur when two partons become collinear, i.e. with their momenta nearly aligned. Notice that collinear divergences could be understood as a type of IR divergences, however they are singled out here for convenience. For suitably defined inclusive observables, the IR and collinear divergences are expected to cancel order by order in perturbation theory, leaving the computed values finite.

1.2 Jet physics in collider experiments

High energy collisions involving leptons, hadrons, or nuclei can result in the production of highly energetic partons through short-distance interactions (hard scatterings), which can be described perturbatively thanks to factorization. As this parton propagates away from the collision point, it undergoes parton showering, emitting gluons that subsequently split into more gluons and quark-antiquark pairs. As the system expands to length scales of order $\sim 1/\Lambda_{\text{QCD}}$, quarks and gluons undergo hadronization, forming color neutral hadrons that can be measured in the final state of the process. Thus, studying the collimated spray of hadrons produced by this fragmentation process, known in the literature as **jets**, allows us to access the properties of the parton shower of the initial highly energetic parton. Jets have proven to be a very successful tool in particle physics, and particularly in QCD. For instance, early jet studies allowed for the discovery of the gluon in electron-positron annihilation experiments in 1979 [26, 27, 28, 29]. For more recent reviews on jet physics for hadronic colliders, see e.g. [30, 31].

Jets, which are not fundamental objects in QFT but rather composite objects emerging from its complex dynamics, need to be phenomenologically defined through jet reconstruction algorithms: a set of rules to cluster particles into individual jets. Ideally, these algorithms should be applicable to various input types, including partons, hadrons, and even experimental measurements like calorimeter towers, with minimal impact on the resulting set of observed jets. A condition usually required for these algorithms is the infrared and collinear (IRC) safety. IRC safety guarantees that the set of jets produced by the algorithm for a given event remains unmodified when an additional soft or collinear splitting of one of the inputs is included. This property is essential for making reliable prediction for jet cross-section using perturbative QCD. As an illustration, let us briefly discuss the clustering procedure of the generalised-k_t algorithm, one of the most used jet definitions at the Large Hadron Collider (LHC) [31]. First, one must compute the inter-particle distance between all possible pairs of particles as

$$d_{ij} = \min\left(p_{T,i}^{2p}, p_{T,j}^{2p}\right) \frac{\Delta R_{ij}^2}{R^2}\,, \tag{1.11}$$

and the beam distance of each particle as

$$d_{iB} = p_{T,i}^{2p}\,, \tag{1.12}$$

where $p_{T,i}(p_{T,j})$ is the transverse momentum (with respect to the beam axis) of the particle $i(j)$, R is a free parameter of the algorithm known as the jet radius, and $\Delta R_{ij} = \sqrt{(y_i - y_j)^2 + (\phi_i - \phi_j)^2}$ is the distance between particles i and j in the plane defined by the rapidity and the azimuthal angle (y, ϕ). The extra parameter p can be fixed to $p = 1, 0, -1$ to specifically select the k_t, Cambridge/Aachen or anti-k_t algorithms respectively [32, 33, 34]. Afterwards, the list of particles should be clustered into jets as follows:

1. Find the smallest d_{ij} and d_{iB}.
    - If the smallest distance is d_{ij}, i and j should be replaced by a new particle of momentum p_T obtained by applying a given recombination scheme to $p_{T,i}$ and $p_{T,j}$.
    - If the smallest is d_{iB}, declare i a jet and remove it from the list of particles.
2. If the list of particles is non-empty, return to step 1 and continue iterating until the list is fully processed.

In order to follow the latter algorithm, one must also choose a recombination scheme, i.e. a prescription on how the momenta of the particles are combined into the jet momentum. There are several different recombination schemes, and the choice depends on which properties of the initial parton one desires to preserve into the resulting jet for subsequent analysis.

In recent decades, the combination of experimental and theoretical techniques for analyzing the internal structure of jets, known as **jet substructure**, has become a cornerstone of modern particle physics, enabling the extraction of finer details from complex high-energy collider environments, for example identifying heavy particle decays. While jets themselves provide valuable insight into fundamental interactions, analyzing their internal structure provides a unique laboratory to study QCD. The structure of jets is tightly connected to the radiation cascade suffered by the initial energetic parton, allowing us to access the intricate details of how the latter evolves into the final spray of hadrons. Substructure techniques have achieved significant success recently, for instance, enabling the identification and study of boosted objects such as top quarks and Higgs bosons, which improves significantly the sensitivity of searches for physics beyond the Standard Model. For recent reviews of both theoretical and experimental advancements in jet substructure, see e.g. [30, 31, 35].

1.3 QCD under extreme conditions

QCD exhibits a rich and complex phase diagram as a function of temperature and baryon density, indicating multiple possible exotic states of hadronic matter. The QCD phase diagram – see a commonly conjectured form in Figure 1.2– provides insight into fundamental aspects of the strong force, the conditions of the early universe, and the composition of neutron stars, among other related phenomena. However, despite the intense research activity within the particle physics community for the last few decades, it remains largely unexplored both experimentally and theoretically. One of its most interesting exotic phases is the **quark-gluon plasma** (QGP). The QGP is the universal state of matter at high temperatures, where quarks and gluons are deconfined from the hadrons. This phase can be inferred from the property of asymptotic freedom: at high energy densities, corresponding to high temperatures and/or baryon densities, the QCD coupling constant weakens significantly, as discussed in Section 1.1.2, and partons deconfine from hadrons. The possibility of such a state of matter was first proposed by Collins and Perry [36], and Cabibbo and Parisi [37] in the early days of QCD. Notice that, although quarks and gluons are deconfined from hadrons in this phase, experiments indicate strong parton interactions, resulting in a (nearly) perfect fluid QGP [38].

Studying the QGP provides crucial insights into fundamental interactions, including

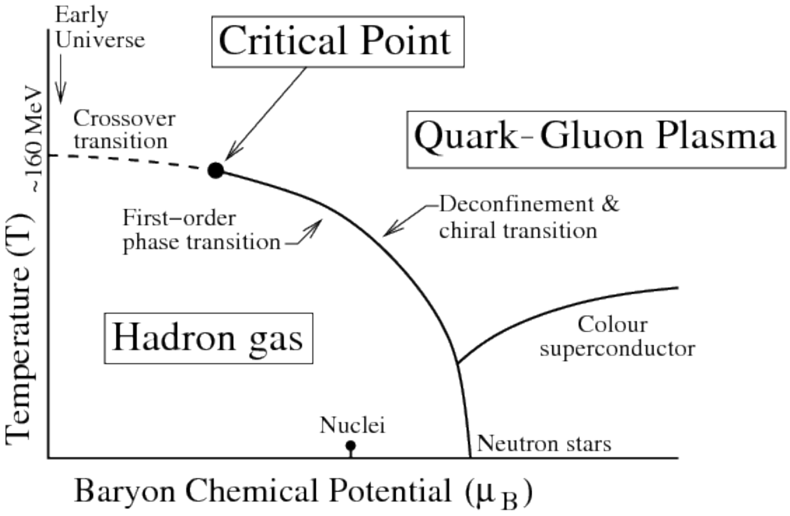

Figure 1.2: Conjectured phase diagram of QCD as a function of the temperature and baryon chemical potential. This figure has been extracted from [39] under a Creative Commons license.

the phase transition between confined and deconfined nuclear matter, the properties of the early universe, and the overall behaviour of the QCD equation of state. The QGP at high temperature can be experimentally produced in ultra relativistic heavy ion collision (HIC) at colliders such as the Relativistic Heavy Ion Collider (RHIC) at the Brookhaven National Laboratory (BNL) and the LHC at the European Organization for Nuclear Research (CERN), enabling a systematic investigation of this novel phase of nuclear matter. To understand the dynamics of HICs, let us qualitatively investigate the collision process as a function of increasing energy. At very low collision energies, nuclei interact as a whole, exhibiting phenomena such as giant dipole resonances and nucleus excitations. As the energy increases, individual nucleon-nucleon interactions dominate, and particle production is observed. These low-to-medium energy collisions can be well described within the framework of nuclear reactions. However, as the collision energy further increases, partonic interactions become more and more significant and the nuclear reaction picture breaks down. At relativistic energies, HICs undergo different stages that can be roughly classified as follows – see Figure 1.3 for a schematic representation:

1. Pre-equilibrium stage. Immediately after the collision of two Lorentz-contracted nuclei, intense non-Abelian QCD color fields, generated by partons within the color-glass condensate (CGC) framework, interact to produce a state of highly overoccupied gluonic matter. This phase, commonly known as the glasma in the literature, is short-lived, with a duration of less than 1 fm/c, and exhibits large anisotropies. The system subsequently undergoes rapid expansion, evolving towards a state of local thermal equilibrium. This equilibration process is commonly considered within the QCD effective kinetic theory (EKT), although it might be non-perturbative.

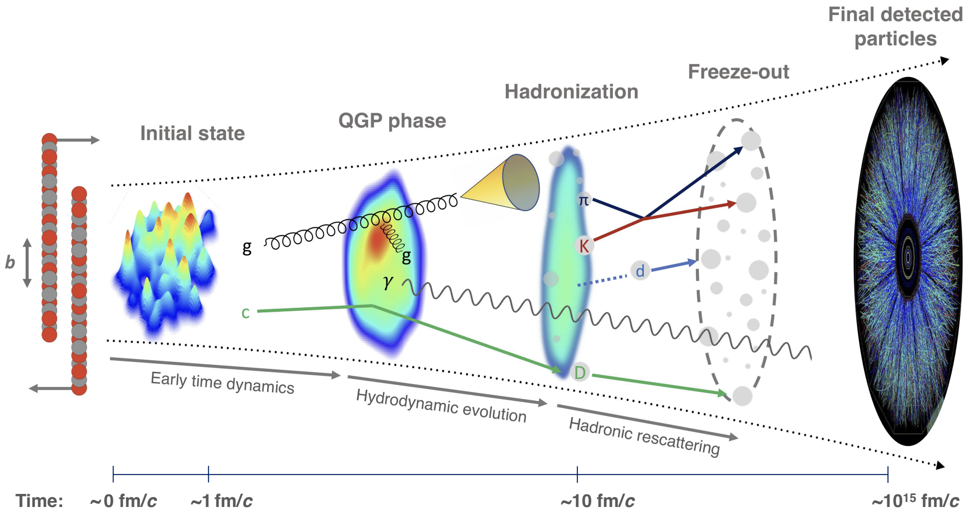

Figure 1.3: Schematic illustration of the different stages of the evolution of the fireball created in high energy HICs. This figure has been adapted from [40] under a Creative Commons license.

2. Thermal stage. Once the system reaches (quasi) local equilibrium, the evolution of the fireball, comprised of deconfined quarks and gluons, can be accurately described by viscous hydrodynamics. This phase marks the formation of the QGP. The internal pressure of the system exerted against the surrounding vacuum results in the hydrodynamic expansion of the QGP, leading to a decrease in energy density and consequent cooling. Below a critical temperature, $T \sim \Lambda_{\mathrm{QCD}}$, partons become confined within hadrons in a process known as hadronization. During this transition, the fireball continues to expand rapidly while maintaining an approximately constant temperature.

3. Freez-out stage. Following hadronization, hadrons undergo collisions, maintaining local thermal equilibrium as the system expands and cools. When the expansion reduces the frequency of inelastic collisions sufficiently, hadrons cannot change their indentity, and, therefore, their abundance remains constant. This phase is referred to as chemical freeze-out. Then, as the average distance between hadrons exceeds the strong interaction range, the remaining elastic interactions become insufficient to maintain thermal equilibrium, leading to the (near) complete decoupling of hadrons. This phase is known as kinetic freeze-out.

The complex nuclear matter produced in HICs is a short-lived transient state. Its initial degrees of freedom, whether the strong fields in the early stages or the quarks and gluons in the QGP phase, cannot be directly observed experimentally. Therefore, all information regarding the produced matter must be obtained from low-p_T particles, originated from the hadronizaton of the produced matter, or self-generated probes that are sensitive to the underlying medium and can be extracted from the hadrons, leptons or photons measured experimentally. For instance, two key signatures confirming QGP formation at RHIC were the suppression of high-energy jets relative to a proton-proton (pp) baseline when normalized by the number of nucleon-nucleon collisions, and the presence of anisotropic collective flow driven by the elliptical geometry of the collision, see [41, 42, 43, 44]. In general, the most common probes used to characterize the properties of the produced matter can be roughly divided into:

Correlations of low-p_T particles. In HICs, low-p_T hadrons, which are a significant fraction of all the produced particles, exhibit strong correlations in the momentum distribution, indicating the presence of collective flow. The initial spatial anisotropy of the colliding nuclei leads to a pressure gradient within the expanding fireball, resulting in a collective motion of the produced particles. The different patterns of anisotropic flow can be characterized by a Fourier expansion of the differential distribution of momenta as:

$$\frac{dN}{d^2\boldsymbol{p}dy} = \frac{1}{2\pi p_T}\frac{dN}{dp_T dy}\left(1 + 2\sum_{n=1}^{\infty} v_n \cos\left[n\left(\phi - \psi\right)\right]\right) , \tag{1.13}$$

where ϕ is the azimuthal angle, p_T is the transverse momentum, y is the rapidity, and ψ is the angle of the reaction plane, defined by the impact parameter of the collision and the beam direction, with a reference axis in the detector frame. The Fourier coefficients, v_n, are generally functions of p_T and y, and provide different insights about the initial geometry of the collision. Measurements of large values of the second flow coefficient v_2, known in the literature as elliptic flow, have been observed in both RHIC and LHC experiments, suggesting that the QGP behaves as a nearly perfect fluid with very low viscosity, see e.g. [42, 45]. For a review on correlations of low-p_T particles, see e.g. [46].

Electromagnetic probes. Unlike hadrons, which are emitted primarily from the hadronization hypersurface and undergo significant final-state interactions, photons and dileptons (electromagnetic (EM) probes) are emitted throughout all the stages and from the entire volume of the system. Since they do not carry color charge and the EM interaction is much weaker, the mean free path of EM probes within the medium is very large. This allows them to escape the matter practically undisturbed, providing unique insight into the evolution of the system from the early stages. Particularly, the ability to constrain the QGP temperature through measurements of thermal photon and dilepton production is a significant achievement of EM probes, see e.g. [47, 48]. For a recent review on both theory and experiment of EM probes, see [49].

Heavy quarks. Quarkonium, the bound state of a heavy quark –such as charm or bottom– and its antiquark, serves as a valuable probe of the QGP. Due to their large masses (m) compared to both the QGP temperature (T_{QGP}) and the QCD characteristic scale (Λ_{QCD}), i.e. $m \gg T_{\text{QGP}}$ and $m \gg \Lambda_{\text{QCD}}$, heavy quark production is largely unaffected by the medium and can be described by perturbative QCD. However, the properties of the quarkonium system, such as its diffusion and the probability of quarkonium formation, are significantly modified by the presence of QCD matter, encoding information about its properties. For instance, focusing on its formation probability, there are several mechanisms that contribute to modify the yield of quarkonia. On the one hand, the chromoelectric fields get screened at large distances due to the presence of QCD matter, weakening the binding attractive force between the pair, and leading to higher probability of dissociation. On the other hand, inelastic scattering of heavy quarks with the constituents of the medium can induce transitions of quarkonium from a color singlet to a color octet state, resulting in a finite thermal decay width. Conversely, unbound heavy quarks can recombine to form a bound state inside the medium. In general, the overall impact of these processes on quarkonium yields allows probing various properties of the QGP, such as the temperature and density. Quarkonium suppression, particularly the suppression of different quarkonium states with increasing binding energy, is considered a key signature of QGP formation, see [50, 51]. For a recent review on heavy quarks as probes of the QGP, see [52].

Jet quenching. In the presence of QCD matter, hard partons, highly energetic particles produced in hard scatterings in the initial collision, propagate through the medium interacting with its constituents and undergoing a parton cascade. Thus, the resulting jet gets modified by these interactions, encoding information about the properties of the matter. One of the main modifications to jets (and hard hadrons in general) is the energy loss due to scatterings with the medium constituents, which results in the suppression of the jet spectrum in HICs relative to pp collisions, see [53, 54]. The jet spectrum suppression –along with the correlations of low-p_T particles– is considered a key signature of QGP formation, and can be understood as a part of a larger group of effects collectively known as jet quenching. Since jet quenching is the main topic of this thesis, we introduce it in the next section in detail.

1.4 Hard probes in HICs

As it has been discussed in the previous section, the complex nuclear matter produced in HICs is a short-lived transient state that cannot be studied using external probes. Therefore, all information regarding the QCD medium must be obtained from self-generated probes that are sensitive to the underlying matter. **Hard probes** –strongly interacting particles produced at very high energy or mass scales–, such as jets and heavy quarks, are among the most interesting probes of nuclear matter. Due to their large energy (or mass), hard probes are produced shortly after the initial collision and traverse all stages of the evolution of the matter, providing sensitivity to the glasma phase, thermalization,

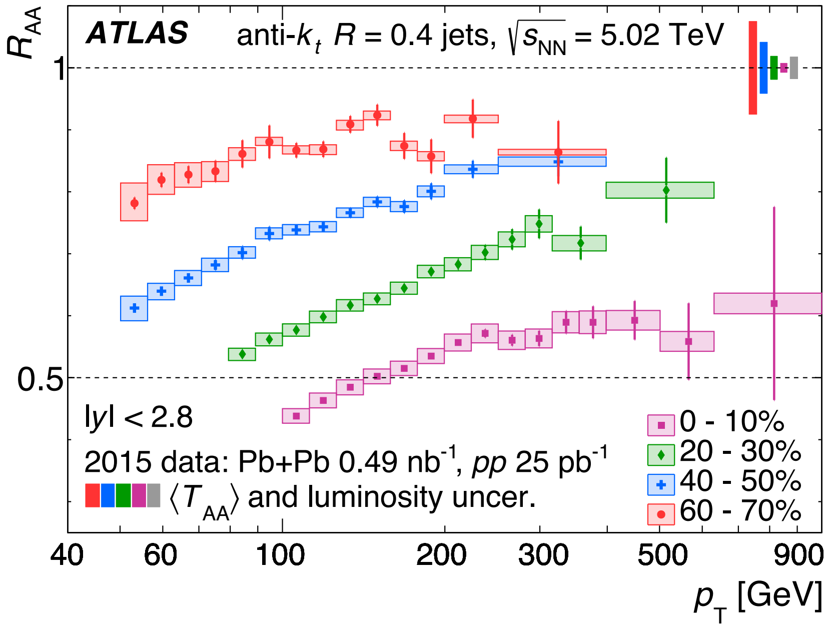

Figure 1.4: R_{AA} as a function of jet p_T for four different centrality intervals. This figure has been extracted from [54] under a Creative Commons license.

and the QGP. Hence, the study of their modifications due to the interaction with the QCD medium provides resolution of the temporal and spatial structure of the medium evolution. In the following discussion, we will focus on jets as probes of HICs, which, for convenience, will be referred to as hard probes indiscriminately.

One of the most significant modifications to jets in HICs is the energy loss, where the high-energy parton produced in the hard scattering loses energy as it transverses the medium. This effect is typically quantified experimentally by the nuclear modification factor, R_{AA}, which measures the modification in HICs of the yield of hadrons or jets at a given transverse momenta compared to that in pp collisions. The observable is usually defined as

$$R_{AA} = \frac{dN^{AA}/dp_T dy}{\langle N_{\text{coll}} \rangle \, dN^{pp}/dp_T dy}\,, \tag{1.14}$$

where $N^{AA}(N^{pp})$ is the yield of jets in nucleus-nucleus (pp) collisions, and $\langle N_{\text{coll}} \rangle$ is the average number of binary collisions of nucleons happening in the corresponding AA collision. Experimental measurements of R_{AA} consistently show values below unity ($R_{AA} < 1$), indicating a suppression of the jet spectrum relative to the pp baseline [54]. Futhermore, R_{AA} exhibits a significant centrality dependence, with values approaching 1 for more peripheral collisions, see Figure 1.4. This observation is interpreted as a clear signature of energy loss by partons traversing the medium, supported by the fact that more central collisions, with larger volumes of matter created, show increased suppression.

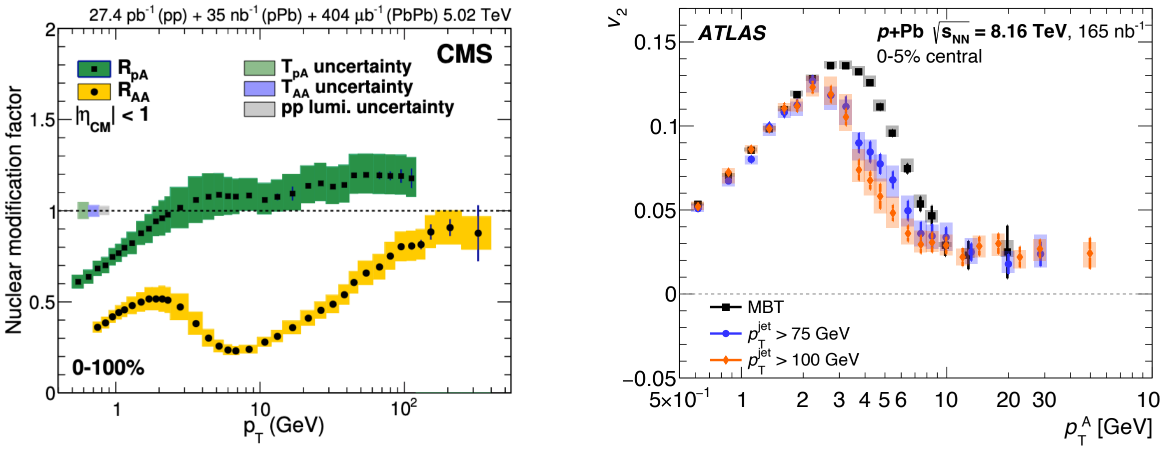

Figure 1.5: Left panel shows the minimum bias nuclear modification factor for charged hadrons in p-Pb collisions (R_{pPb}) at 5.02 TeV, compared to the minimum bias R_{AA} in Pb-Pb collisions at the same energy. This figure has been extracted from [56], under a Creative Commons license. The right panel shows the elliptic flow coefficient v_2 of high-p_T hadrons in 0-5% most central collisions at 8.16 Tev, suggesting a remnant anisotropy even for $p_T > 50$ GeV. This figure has been extracted from [57] under a Creative Commons license.

Beyond energy loss, in-medium jets show a large variety of distortions, including modifications to the parton branching process and to the fragmentation pattern of partons into hadrons. These modifications, which are collectively referred to as **jet quenching**, can be experimentally accessible using jet substructure observables. As proposed by Bjorken in 1982 [55], the main goal of the jet quenching program is to use these modifications to extract information about the properties of the QCD matter produced in HICs. However, a key challenge in achieving this goal lies in developing a robust theoretical understanding of how the matter affects the propagation of jets. This thesis aims to address this challenge by developing a novel theoretical framework that incorporates a more realistic description of the medium. This framework, which is thoroughly discussed in the next section, explicitly considers previously neglected effects, such as the medium structure and its evolution.

The observation of correlations of low-p_T particles, i.e. non-zero v_n, in small systems like proton-nucleus (pA) collisions raises a significant puzzle. While similar patterns in HICs are interpreted as a signature of collective flow and QGP formation, another key QGP signature –the suppression of high-energy jets and hadrons– is not observed in pA collisions, see Figure 1.5. Given the expected strong deviations from equilibrium and large gradients in pA collisions, the theoretical framework developed in this thesis offers a promissing approach to understanding the jet quenching in small systems, which may be crucial to resolve this discrepancy.

1.5 Objectives and methodology

This section presents the main objectives of this thesis and outlines the methodological approach employed in this research.

1.5.1 Objectives

The primary goal of this thesis is to investigate the properties of the state of matter formed in the initial moments of HICs using jets as probes. To this end, we have developed novel analytical tools, expanding the current jet quenching formalism to introduce the effect of matter evolution and structure during different stages of HICs. The three specific objectives addressed in this thesis are:

1. **Broadening and medium-induced radiation in flowing anisotropic matter**: Computing the leading corrections to the jet broadening and the spectrum of medium-induced radiated gluons due to the interplay between the flow and hydrodynamic gradients in the presence of a dilute QCD medium. This objective is fully achieved on [1].
2. **Medium induced radiation in dense inhomogeneous matter**: Computing the spectrum of gluons sourced by the branching of an energetic quark in the presence of a dense QCD medium with anisotropies. This objective is fully achieved in [2].
3. **Medium induced radiation in the HICs initial stages**: Computing the medium-induced radiation and energy loss rate of jets in the presence of the glasma formed in HIC initial stages. This objective is fully achieved in [3].

During the development of the Ph.D. that has led to this thesis, different research lines have been explored, resulting in three additional scientific papers that have not been published by the submission of this document, and therefore cannot be included. First, in [58], we compute the double differential medium-induced gluon spectrum within flowing matter, keeping the subeikonal corrections and considering real spin-1 emitted gluons. In [59], we revisit the caluclation of the soft gluon emission probability off a colour singlet $q\bar{q}$ system that evolves in the QGP, extending the previous studies by considering the effect of the interactions with the medium during the formation of the antenna and not only its propagations. Finally, in [60], we study the collinear limit of the Energy-Energy Correlator (EEC) in single inclusive jet production in pp and pA collisions, introducing a non-perturbative model that allows to describe the small angle region of the observable's distribution and the modifications from the interaction with the nuclear medium in small systems.

1.5.2 Methodology

This thesis focuses on deriving analytic tools to study processes involving strongly interacting particles inside QCD matter. To this end, the presented works employ standard perturbative QCD techniques within the framework of QFT to compute the relevant Feynman diagrams for the processes under investigation. In the next section, we will review in detail the formalism developed for hard probes propagating through evolving and anisotropic matter, as presented in the published papers comprising this thesis. We will discuss the color background field employed to model the effects of the QCD medium, which follows from matter considerations based on hydrodynamics and QCD kinetic theory, and its correlators. Furthermore, we will discuss the extension of the two primary approaches for in-medium jet calculations, the BDMPS-Z formalism for dense media and the simplifying limit of the truncated opacity expansion for dilute media, to account for the novel features of the matter.

2

The novel formalism: a discussion of the results

This chapter revisits the derivation of the novel theoretical framework developed in this thesis, reviews the fundamentals of jet quenching theory, and discusses the key results presented in Chapter 4. Here, we will emphasize the novel aspects and the underlying physics, rather than delving into technical details of well established calculations that can be easily found in the literature. For a thorough review of the jet quenching theory, see e.g. [61].

As explained in Chapter 1, jets are formed by the branching and subsequent hadronization of a highly energetic parton. In the following, a 'highly energetic' parton is defined as one that satisfies

$$E \gg |\boldsymbol{k}|, T, \Lambda_{\mathrm{QCD}} \, , \tag{2.1}$$

where E is the energy of the parton, $|\boldsymbol{k}|$ is its transverse momentum, and T represents the temperature of the thermalized stage of the medium. This condition implies that the energy of the parton is much larger than its transverse momentum and any characteristic scale of the medium, e.g. the temperature in the QGP phase. Under these assumptions, the interaction between the partons and the matter is assumed to be perturbative, and thus perturbative QCD is applicable. For recent developments on the treatment of probes in strongly coupled matter, see e.g. [62, 63, 64, 65, 66, 67, 68, 69].

The two leading perturbative processes governing the evolution of a high-energy parton traversing a QCD medium are the transverse momentum broadening and the medium-induced radiation. Transverse momentum broadening arises from elastic scatterings of the parton with the medium, leading to a modification of its transverse momentum. Medium-induced radiation describes the additional radiation emitted by a parton due to these scatterings with the matter. Actually, medium-induced radiation is the main mechanism of energy loss for energetic partons [70, 71, 72, 73, 74], in contrast to the low-energy regime where collisional energy loss dominates [55, 75, 76]. This thesis develops a new formalism to describe hard probes in matter, incorporating the effect of medium evolution and anisotropies. Our focus is on the two leading perturbative processes, momentum broadening and medium-induced radiation, which are examined within two phases of QCD matter, the QGP and the glasma. In both stages, the probe-matter interactions can be modelled as energetic partons interacting with a color background field. The derivation and specific characteristic of this field will be investigated in detail throughout Section 2.1.

The effective number of interactions between partons and the background field is determined by the characteristics of the matter. In the dense matter limit, partons undergo multiple interactions with the background field. These interactions can be resummed, resulting in effective propagators in the transverse plane, i.e. in 2+1 dimensions, that incorporate the effect of the medium on the partons appearing in a given process. This resummation building in-medium parton propagators at the level of the amplitude is known in the literature as the Baier, Dokshitzer, Mueller, Peigné, Schiff - Zakharov (BDMPS-Z) formalism [77, 78, 79, 80, 81, 82, 83], with its phenomenological implementation developed by Armesto, Salgado, Wiedemann (ASW) [84, 85]. In the dilute matter limit, one expects the effective number of scatterings with the medium, which is controlled by a combination of matter properties and the probe-matter effective coupling called opacity χ, to be close to unity. Consequently, an expansion in this parameter –the so-called opacity expansion– can be performed, simplifying calculations significantly. This approach is known as the Gyulasy, Levai, Vitev - Wiedemann (GLV-W) formalism [86, 87, 88, 89, 90, 91]. These two approaches are indeed equivalent, as demonstrated in [89, 90], where it was shown that a resummation of the opacity expansion in the limit of soft momentum exchanges precisely reproduces the BDMPS-Z result. This thesis extends both the BDMPS-Z and the GLV-W formalisms to incorporate the novel features arising by considering evolving anisotropic matter.

Similar to pp collisions, in-medium processes are also usually assumed to be factorizable [92, 93]. The factorization implies that the production of the hard parton can be treated independently of its subsequent evolution within the matter. The specific details of the production can be schematically described by (1.10) after replacing PDFs by nuclear PDFs (nPDFs), which encapsulate the non-perturbative structure of the colliding nucleus. Even thought the factorization may break for evolving and anisotropic matter in some scenarios, in what follows, we will focus solely on the evolution of the hard parton within the matter, while encapsulating the details of its production within a source function.

2.1 The background field and the field correlators

The study of how energetic partons behave while traversing dense nuclear matter is highly inspired in the seminal works of Landau, Pomeranchuk and Migdal (LPM) in QED. In the mid 20*th* century, LPM demonstrated that a highly energetic charged particle undergoing multiple soft scatterings with a dense medium will experience interference effects between adjacent scatterings, resulting in an overall suppression of the bremsstrahlung radiation [94, 95] known as the LPM effect. In the 90s, particularly driven by the upcoming RHIC experiment, a considerable effort was devoted to extend these studies to non-Abelian backgrounds, investigating the influence of dense color media on the propagation of strongly interacting particles [78, 79, 96, 97]. These works use a semiclassical approach, neglecting the changes in the medium configuration due to the passage of the particle (backreaction), see [98] for a review on attempts of relaxing this approximation. In this approach, the matter is treated as a classical background field produced by a stochastic ensemble of charged particles with correlations determined by the properties of the matter. This remains the most widely used formalism for treating jet quenching processes to date, see e.g. [61] for a review.

In line with these historical approaches, the effect of QCD matter on hard probes is modelled here by the field produced by an ensemble of $SU(N_c)$ charged quasiparticles, given by

$$gA^{a\mu}(q) = \int_{\boldsymbol{x},z} e^{-i(\boldsymbol{q}\cdot\boldsymbol{x}+q_z z)}\, u^\mu(\boldsymbol{x},z)\,\hat{\rho}^a(\boldsymbol{x},z)\,v(q;\boldsymbol{x},z)\,(2\pi)\delta(q\cdot u)\,, \tag{2.2}$$

where $u_\mu = (1,\boldsymbol{u},u_z)$ is the non-relativistic velocity (obtained by removing the relativistic γ-factor from the four-velocity) of the in-medium sources, $\hat{\rho}^a$ is the source color density, and $v(q;\boldsymbol{x},z)$ is a single source potential. The dependence on the coordinates of the latter arises from the local properties of the medium, which can exhibit non-trivial spatial structure. In the following, the reference frame will be chosen relative to the jet propagation, with the z-axis aligned with the direction of the leading parton. The field produced by a discrete collection of sources located at positions $(\boldsymbol{x}_i, z_i)$, as it is usually considered in the GLV formalism, can be directly obtained by substituting $\hat{\rho}^a(\boldsymbol{x},z) = \sum_i t_i^a\,\delta^{(2)}(\boldsymbol{x}-\boldsymbol{x}_i)\,\delta(z-z_i)$ in (2.2), where t_i^a represents the projection of the color of the i-th source onto the $SU(N_c)$ generators.

The field profile given in (2.2) can be simplified under various assumptions. For instance, in the case of homogeneous matter, where the local properties of the medium are constant in space, the spatial dependence of the velocity, color density and scattering potential vanishes. In the case of static matter, the non-relativistic velocity simplifies to $u_\mu = (1,\boldsymbol{0},0)$, and the field has only one non-zero component. To simplify the derivations, most jet quenching calculations employ the **brick approximation**, where the matter is assumed to be static and homogeneous in the transverse directions. However, these approximations decouple the jet quenching description from the evolution and structure of the medium, limiting theoretical control over the impact of matter on jet properties. Several attempts have been made to incorporate medium evolution effect into jet quenching theory with minimal modifications, such as incorporating medium dilution [99, 100, 101], using kinematic arguments [67, 102, 103], or treating the flow within phenomenologically motivated models [104, 105]. In recent years, there has been a growing effort to extend the theory of jet-matter interactions to the case of anisotropic evolving matter, relaxing the simplifying approximations gradually [1, 2, 3, 58, 106, 107, 108, 109, 110, 111, 112, 113, 114, 115, 116, 117]. This is essential for effectively utilizing the new jet substructure techniques, as accurate theoretical predictions require a more realistic picture of the medium, including anisotropies and flow effects, as it will be discussed later in this Chapter and in Chapter 3.

The single source scattering potential, $v(q;\boldsymbol{x},z)$, governs the details of the probe-matter interactions, and it is therefore expected to be different at different stages of HIC matter evolution. In the QGP phase, the potential is expected to be screened, with the screening scale usually referred to as the Debye mass. While a variety of choices exist in the literature, see e.g. the discussion in [118], the Gyulassy-Wang (GW) model [96] will be used to illustrate the results explicitly throughout this thesis. The corresponding potential is given by

$$v(q;\boldsymbol{x},z) = \frac{g^2}{q^2 - \mu^2(\boldsymbol{x},z)}\,, \tag{2.3}$$

where g is the effective strong coupling inside the medium, and $\mu(\boldsymbol{x},z)$ is the Debye mass, which can exhibit spatial dependence depending on the matter properties. Notice, however, that the generalization of the presented results to other choices of the in-medium potential is conceptually straightforward.

Since the field (2.2) is generated by a stochastic ensemble of in-medium sources, characterizing its statistical properties, which are encoded in its correlators, is essential. In the context of the QGP phase, a common assumption is that these correlators exhibit Gaussian white noise statistics. This implies that the colour charge sources fluctuate randomly around their average values with a Gaussian distribution and are uncorrelated at different spacetime points. Therefore, the two-point function –known as the medium average– is the only non-trivial field correlator and can be expressed in terms of the color source densities as

$$\left\langle \hat{\rho}^a(\boldsymbol{x},z_x)\hat{\rho}^b(\boldsymbol{y},z_y)\right\rangle = \frac{\delta^{ab}}{2C_{\bar{R}}}\,\delta^{(2)}(\boldsymbol{x}-\boldsymbol{y})\,\delta(z_x-z_y)\,\rho(\boldsymbol{x},z_x)\,, \tag{2.4}$$

where $C_{\bar{R}}$ is defined as $C_{\bar{R}} = N_c$ for fundamental sourcers and $C_{\bar{R}} = C_F$ for adjoint ones, and the number density of scattering centers $\rho(\boldsymbol{x},z)$ has been introduced. For the specific case of a field generated by a discrete collection of sources, the medium average (2.4) can be equivalently expressed as $\left\langle t_i^a t_j^b \right\rangle = \frac{1}{2C_{\bar{R}}}\delta_{ij}\delta^{ab}$.

Despite its short-lived nature (lasting less than $1\,\mathrm{fm}/c$), the glasma phase exhibits very high energy density, suggesting a significant potential to modify both the energy and the substructure of jets. While it is interesting to study jet quenching processes within this phase, the specific details of both the field and its correlator discussed above for the QGP are not well-suited for describing this stage of matter evolution. During the glasma phase, the matter can be characterized by strong color fields aligned along the beam axis, exhibiting a huge anisotropy between the longitudinal and transverse directions, see [119, 120, 121, 122, 123]. In addition, the matter has an intrinsic energy scale Q_s, known as saturation scale, which determines the characteristic correlation length of the color fields to be $1/Q_s$. Thus, the glasma stage can be modelled as a collection of independent color domains with size of approximately $1/Q_s$. With this picture in mind, one may envision a jet propagating at mid-rapid along the z-axis, orthogonally to the beam direction, as traversing a stack of transversely infinite slabs of thickness $\ell \sim 1/Q_s$, which will be referred to as color domains indistinctly in the following. This idealization allows for writing the background field during the glasma stage as, see [3] in Chapter 4 for further details on the model

$$gA^{a\mu}(\boldsymbol{x}, z) = \delta^{\mu 0}\, \boldsymbol{x} \cdot \boldsymbol{E}^a(z) = \begin{cases} \delta^{\mu 0}\boldsymbol{x} \cdot \boldsymbol{E}_1^a, & 0 \leq z < \ell \\ \delta^{\mu 0}\boldsymbol{x} \cdot \boldsymbol{E}_2^a, & \ell \leq z < 2\ell \\ \delta^{\mu 0}\boldsymbol{x} \cdot \boldsymbol{E}_3^a, & 2\ell \leq z < 3\ell \\ \vdots \end{cases}, \tag{2.5}$$

where both the beam axis and $\boldsymbol{x}$ are in the transverse direction to the momentum of the leading parton. Due to the non-vanishing correlation of the color fields within each domain, the white noise approximation is not applicable for the glasma. Conversely, assuming that the fluctuations of the field in each domain follow a Gaussian distribution with a characteristic width E_0, and choosing a reference frame in the transverse plane such that the chromoelectric field has only one component, the medium average can be written as

$$\langle f(E_1^a, E_2^a, E_3^a, \cdots)\rangle = \int_{E_1} e^{-E_1^2/E_0^2} \int_{E_2} e^{-E_2^2/E_0^2} \cdots f(E_1^a, E_2^a, E_3^a, \cdots)\,, \tag{2.6}$$

where $E_n^2 = \sum_a (E_n^a)^2$, and we have introduced the shorthand notation $\int_E = \int \frac{d^{N_c^2-1}E^a}{\left(\sqrt{\pi}E_0\right)^{N_c^2-1}}$. For further details regarding this model of field correlators in the glasma phase, including a discussion about alternative statistics omitted here, see [3].

With the background field and its statistical properties determined for both stages of HIC matter under investigation, we can subsequently proceed with the jet quenching calculations.

2.2 The transverse momentum broadening

This section demonstrates how the jet quenching formalism can be extended to account for the novel features of the matter described in Section 2.1, focusing on the derivation of transverse momentum broadening –the simplest relevant perturbative process. Hence, we will examine this process in the QGP phase, explaining the impact of matter anisotropies and flow, and in the glasma phase, analyzing it under anisotropic, correlated strong fields. To obtain the final transverse momentum distribution at any stage of the matter evolution, the amplitude of a parton propagating through the specific background field must be computed. However, in contrast to the classical picture, in QFT a particle interacting with a background field experiences a superposition of all possible number of interactions, not a fixed number of them. Therefore, the complete amplitude of the process can be written as the following series

$$M = \sum_{N=0}^{\infty} M_N = M_0 + M_1 + M_2 + \dots\,, \tag{2.7}$$

where M_N is the amplitude with N scatterings –see the Feynman diagram corresponding to M_4 in Figure 2.1– and M_0 corresponds to vacuum. To obtain the matrix element, i.e. the squared amplitude averaged over quantum numbers and medium configurations, needed to compute observable quantities from (2.7), two distinct approaches can be taken.On the one hand, within the BDMPS-Z formalism, the series (2.7) is resummed, resulting in an effective parton propagator. Then, the resummed amplitude is squared, and the medium averages are performed to obtain the corresponding matrix element. On the other hand, within the GLV formalism, the full amplitude M is squared before resumming the series, and the medium averages are performed on each term separately, i.e.

$$\left\langle |M|^2 \right\rangle = \underbrace{\left\langle |M_0|^2 \right\rangle}_{N_\chi=0} + \underbrace{\left\langle |M_1|^2 \right\rangle + \langle M_2 M_0^* \rangle + \langle M_0 M_2^* \rangle}_{N_\chi=1} + \dots\,. \tag{2.8}$$

This way, the calculation of each order in the opacity expansion, enumerated by N_χ in (2.8) and with the opacity (usually) defined as $\chi = \frac{\mathcal{C} g^4 \rho}{2N_c 4\pi\mu^2} L$ with L the length of the medium, can be performed separately.

To illustrate how each formalism is extended to incorporate the novelties of the medium model, we review three calculations of transverse momentum broadening. First, we revisit the calculation in a flowing, anisotropic QGP within the dilute matter limit, using the GLV formalism at first order in opacity $N_\chi = 1$, as presented in [1]. Second, we consider the broadening in a static, anisotropic QGP within the dense matter limit, using the BDMPS-Z formalism, as originally derived in [111]. Finally, we revisit the derivation of broadening in the glasma, using the BDMPS-Z formalism, as presented in [3]. Notice that both Refs. [1] and [3] form part of this thesis, see Chapter 4.

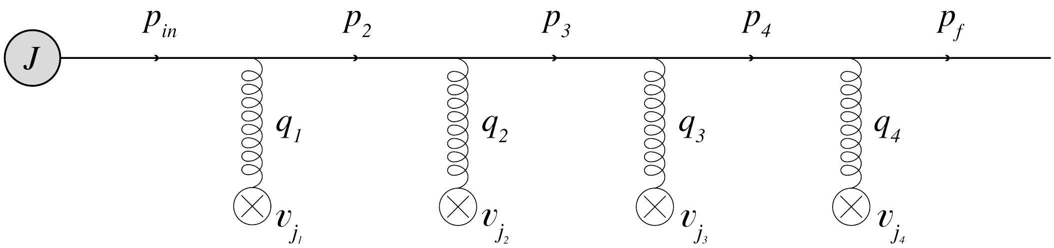

Figure 2.1: Feynman diagram of the contribution with $n = 4$ scatterings with the background filed to the full amplitude. This figure has been extracted from [111] under a Creative Commons license.

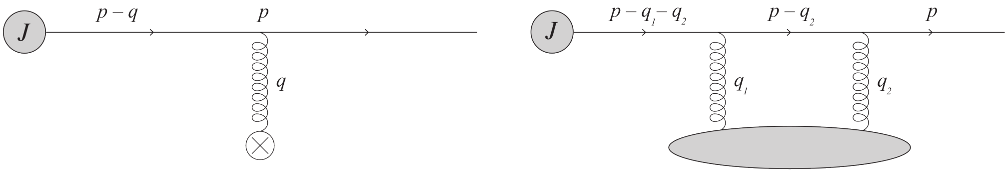

Figure 2.2: Feynman diagrams of the single-Born M_1 (left) and the double-Born M_2 (right) amplitudes of a parton traversing QCD matter. This figure has been extracted from [1].

2.2.1 Broadening in anisotropic, flowing matter in the dilute limit[1]

In this section, we revisit the derivation of the gradient correction to the momentum broadening distribution within flowing, anisotropic QCD matter to first order in opacity. We focus particularly on the interplay between velocity corrections and spatial gradients due to matter anisotropies. The following derivation will be performed at first subleading order in the expansion of inverse powers of the energy of the parton –the so-called eikonal expansion–, neglecting anything suppressed by two or more powers of the energy, and first order in the gradient expansion of the hydrodynamic variables, going beyond the usual GLV construction. At this level of accuracy, we can ignore the suppressed spin effects and consider scalar particles in the fundamental representation. At first order in opacity $N_\chi = 1$, there are two types of contributions to take into account: the single-Born (SB) contribution M_1 and the double-Born (DB) contribution M_2, see Figure 2.2. Then, the amplitude at $N_\chi = 1$ is given by the first four terms of the series shown in Eq. (2.8). In the following calculation, the reference frame is chosen relative to the jet, with the z-axis aligned with the leading parton's direction of propagation.

---

[1] This section presents an adapted summary and partial reproduction of content from [1], which forms part of this thesis and is detailed further in Chapter 4.

Single-Born contribution

We start by considering the SB contribution to the broadening of an energetic (scalar) quark. The corresponding $N_\chi = 1$ amplitude reads

$$\begin{aligned} iM_1 &= \int \frac{d^4q}{(2\pi)^4} \left[i t^a_{proj} (2p-q)_\mu A^{a\mu}_{\text{ext}}(q) \right] \left[\frac{i}{(p-q)^2 + i\epsilon} \right] J(p-q) \\ &= -\int_{x,q} t^a_{proj}\, \hat{\rho}^a(\boldsymbol{x}, z) \left(1 - \frac{\boldsymbol{u}\cdot\boldsymbol{p}}{(1-u_z)E} \right) e^{-i(\boldsymbol{q}\cdot\boldsymbol{x} + q_z z)}\, v(q)\, \frac{2(1-u_z)E}{(p-q)^2 + i\epsilon}\, J(p-q)\,, \end{aligned} \tag{2.9}$$

we have used the delta function in (2.2), and the dependence of the velocity components and the potential on the coordinates has been omitted to alleviate the notation. In the above equation, $J(p-q)$ is the source of the initial energetic quark controlling the initial distribution of partons — assumed to be centered at $\boldsymbol{x}_0 = 0$ and $z_0 = 0$ —, and t^a_{proj} is the leading parton ("projectile") color generator.

Integrating over q_z by residues, we assume that J is slowly varying, hence there are only four poles in (2.9) to account for in the evaluation of the integral. The two poles, coming from the scattering potential $v(q)$, have a finite imaginary part. For a sufficiently dilute and longitudinally-extended medium $\mu z \gg 1$, therefore the corresponding contributions are exponentially suppressed and can be neglected. The other two poles come from the quark propagator

$$Q^+_{p-q} \simeq \frac{2E}{1+u_z} \left(1 - \frac{\boldsymbol{q}\cdot\boldsymbol{u}}{2E} \right), \tag{2.10a}$$

$$Q^-_{p-q} \simeq \frac{\boldsymbol{q}\cdot\boldsymbol{u}}{1-u_z} + \frac{(\boldsymbol{p}-\boldsymbol{q})^2 - \boldsymbol{p}^2}{2(1-u_z)E}, \tag{2.10b}$$

where we have accounted for the first terms in the eikonal expansion. Given that Q^+_{p-q} is $\mathcal{O}(E)$ and $V(\boldsymbol{q}, Q^+_{p-q}) \sim \frac{1}{E^2}$, its residue is highly suppressed by the energy, and the only non-vanishing contribution to the integral comes from the residue corresponding to the pole at Q^-_{p-q}. Thus, the integration contour has to be closed below the real axis enforcing $z > 0$. After performing the q_z-integration, the SB contribution to the amplitude reduces to

$$iM_1 = i \int_{x,\boldsymbol{q}} t^a_{proj}\, \hat{\rho}^a(\boldsymbol{x}, z)\, \theta(z)\, e^{-i\boldsymbol{q}\cdot\boldsymbol{x}}\, e^{-iQ^-_{p-q}z} \left(1 - \frac{\boldsymbol{u}\cdot(\boldsymbol{p}-\boldsymbol{q})}{(1-u_z)E} \right) v(\tilde{q})\; J(p-\tilde{q})\,, \tag{2.11}$$

where the tilde indicates that q_0 and q_z have been fixed, and $\tilde{q}_\mu = \left(\boldsymbol{q}\cdot\boldsymbol{u} + Q^-_{p-q}u_z,\, \boldsymbol{q},\, Q^-_{p-q}\right)_\mu$.

We can now square the amplitude, average over initial and sum over final quantum numbers, as well as average over the field configurations. Doing so yields

$$\begin{aligned}\langle |M_1|^2\rangle = \mathcal{C}\int_{x,\boldsymbol{q},\boldsymbol{q}'} & \theta(z)\,\rho(\boldsymbol{x},z)\,e^{-i(\boldsymbol{q}-\boldsymbol{q}')\cdot\boldsymbol{x}}\,e^{-i\left(Q^-_{p-q}-Q^-_{p-q'}\right)z} \\ & \times\left(1-\frac{\boldsymbol{u}\cdot(\boldsymbol{p}-\boldsymbol{q})}{(1-u_z)E}-\frac{\boldsymbol{u}\cdot(\boldsymbol{p}-\boldsymbol{q}')}{(1-u_z)E}\right)v(\tilde{q})\,v^*(\tilde{q}')\,J(p-\tilde{q})\,J^*(p-\tilde{q}')\,, \qquad (2.12)\end{aligned}$$

where $\mathcal{C}=\frac{C_F}{2N_c}$. Note that we only explicitly show the arguments of $\rho(\boldsymbol{x},z)$ for illustrative purposes, keeping the arguments of the other hydrodynamic variables implicit. As can be seen in the latter equation, the q_z integration results in a shift in the argument of the potential and initial source. Expanding these functions, one readily finds

$$v(\tilde{q})\simeq v(\boldsymbol{q}^2)\left(1+\frac{\boldsymbol{q}\cdot\boldsymbol{u}}{(1-u_z)E}\frac{(\boldsymbol{p}-\boldsymbol{q})^2-\boldsymbol{p}^2}{v(\boldsymbol{q}^2)}\frac{\partial v}{\partial\boldsymbol{q}^2}\right), \qquad (2.13a)$$

$$J(p-\tilde{q})\simeq J\left(E,\boldsymbol{p}-\boldsymbol{q}\right)\left(1-\frac{\boldsymbol{q}\cdot\boldsymbol{u}}{(1-u_z)}\frac{1}{J}\frac{\partial J}{\partial E}\right), \qquad (2.13b)$$

where $v(\boldsymbol{q}^2)=-\frac{g^2}{\boldsymbol{q}^2+\mu^2}$. Thus, all the velocity corrections appearing in the squared amplitude are proportional to the transverse velocity $\boldsymbol{u}$, and it is convenient to define a new vector in the transverse plane

$$\begin{aligned}\boldsymbol{\Gamma}(\boldsymbol{q},\boldsymbol{q}')\equiv & -\frac{\boldsymbol{p}-\boldsymbol{q}}{(1-u_z)E}-\frac{\boldsymbol{p}-\boldsymbol{q}'}{(1-u_z)E}+\frac{\boldsymbol{q}}{(1-u_z)E}\frac{(\boldsymbol{p}-\boldsymbol{q})^2-\boldsymbol{p}^2}{v(\boldsymbol{q}^2)}\frac{\partial v}{\partial\boldsymbol{q}^2} \\ & +\frac{\boldsymbol{q}'}{(1-u_z)E}\frac{(\boldsymbol{p}-\boldsymbol{q}')^2-\boldsymbol{p}^2}{v^*(\boldsymbol{q}'^2)}\frac{\partial v^*}{\partial\boldsymbol{q}'^2}-\frac{\boldsymbol{q}}{(1-u_z)}\frac{1}{J}\frac{\partial J}{\partial E}-\frac{\boldsymbol{q}'}{(1-u_z)}\frac{1}{J}\frac{\partial J}{\partial E}, \qquad (2.14)\end{aligned}$$

which enables us to write the averaged squared-amplitude in a compact form

$$\begin{aligned}\langle |M_1|^2\rangle = \mathcal{C}\int_{x,\boldsymbol{q},\boldsymbol{q}'} & \theta(z)\,\rho(\boldsymbol{x},z)\,v(\boldsymbol{q}^2)\,v^*(\boldsymbol{q}'^2)\,J\left(E,\boldsymbol{p}-\boldsymbol{q}\right)J^*\left(E,\boldsymbol{p}-\boldsymbol{q}'\right) \\ & \times e^{-i(\boldsymbol{q}-\boldsymbol{q}')\cdot\boldsymbol{x}}\,e^{-i\left(Q^-_{p-q}-Q^-_{p-q'}\right)z}\left[1+\boldsymbol{u}\cdot\boldsymbol{\Gamma}(\boldsymbol{q},\boldsymbol{q}')\right]. \qquad (2.15)\end{aligned}$$

All the dependence on the matter's spatial structure in (2.15) comes from the hydrodynamic parameters of the matter model: the source spatial density $\rho(\boldsymbol{x},z)$, the Debye mass $\mu^2(\boldsymbol{x},z)$, and the three components of the velocity $\boldsymbol{u}(\boldsymbol{x},z)$ and $u_z(\boldsymbol{x},z)$. The matter properties are expected to change sufficiently slowly in the hydrodynamic phase, and thus these parameters can be expanded in hydrodynamic gradients transverse to the large parton momentum p_z. At the zeroth order, matter is uniform in the transverse plane, and thus the $\boldsymbol{x}$-integral trivially results in a delta function while the longitudinal z-integral is yet to be performed. Then the corresponding contribution to the squared amplitude reads

$$\langle |M_1|^2 \rangle = \mathcal{C} \int_0^L dz \int_{\boldsymbol{q}} \rho(z) \, |v(\boldsymbol{q}^2)|^2 \, |J\left(E, \boldsymbol{p}-\boldsymbol{q}\right)|^2 \, [1 + \boldsymbol{u} \cdot \boldsymbol{\Gamma}(\boldsymbol{q})] + \mathcal{O}\left(\boldsymbol{\nabla}\right) , \tag{2.16}$$

where $\boldsymbol{\Gamma}(\boldsymbol{q}) \equiv \boldsymbol{\Gamma}(\boldsymbol{q}, \boldsymbol{q})$ and we assume that the matter has a finite longitudinal size L. Given the weak dependence on the transverse coordinates, any hydrodynamic variable $G(\boldsymbol{x}, z)$ can be expanded about $\boldsymbol{x} = 0$, resulting in $G(\boldsymbol{x}, z) \simeq G(z) + \boldsymbol{x} \cdot \boldsymbol{\nabla} G(z) + \mathcal{O}\left(\boldsymbol{\nabla}^2\right)$. With this, the transverse integral in (2.15) can be performed explicitly by rewriting the $\boldsymbol{x}$ dependence as a momentum derivative of the Fourier factor. With this replacement, we integrate by parts. Assuming that J and v have at most constant imaginary phases and acting with the derivative on the remaining terms, we can express the linear gradient correction to (2.16) in a compact form

$$\begin{aligned}\delta \left\langle |M_1|^2 \right\rangle = \mathcal{C} \int_0^L dz \int_{\boldsymbol{q}} \hat{\boldsymbol{g}}_\alpha \, \rho(z) \, & \left[\left(-\frac{\boldsymbol{u}^\alpha}{1-u_z} + \frac{(\boldsymbol{p}-\boldsymbol{q})^\alpha}{(1-u_z)E} \right) z \right] \\ & \times [v(\boldsymbol{q}^2)]^2 \, |J(E, \boldsymbol{p}-\boldsymbol{q})|^2 \Bigg[1 + \boldsymbol{u} \cdot \boldsymbol{\Gamma}(\boldsymbol{q}) \Bigg] .\end{aligned} \tag{2.17}$$

where α runs over the 2D transverse space, and we have introduced a shorthand notation, the two-dimensional operator $\hat{\boldsymbol{g}}_\alpha \equiv \sum_G \left(\boldsymbol{\nabla} G \cdot \frac{\delta}{\delta G}\right)_\alpha$, which directly generates all gradient corrections and should be understood as summed over the hydrodynamic variables, i.e. the density, the Debye mass and the three components of the flow in this case.

Double Born contribution

Next we turn to the DB diagram, see Figure 2.2, which gives the second contribution to the transverse momentum broadening and corresponds to the double-scattering amplitude:

$$\begin{aligned} iM_2 = \int \frac{d^4 q_1}{(2\pi)^4} \frac{d^4 q_1}{(2\pi)^4} & \left[i g t^b_{proj} (2p - q_2)_\nu A^{b\nu}_{\text{ext}}(q_2) \right] \left[\frac{i}{(p-q_2)^2 + i\epsilon} \right] \\ \times & \left[i g t^a_{proj} (2(p-q_2) - q_1)_\mu A^{a\mu}_{\text{ext}}(q_1) \right] \left[\frac{i}{(p - q_1 - q_2)^2 + i\epsilon} \right] J(p - q_1 - q_2) . \end{aligned} \tag{2.18}$$

To first order in opacity, the DB diagram, which contains both field insertions, combines with the vacuum amplitude $iM_0 = J(p)$. Averaging over the stochastic fields and summing the quantum numbers, we find that

$$\begin{aligned} \langle M_2 M_0^* \rangle = \mathcal{C} \int_{x, q_1, q_2} & \left(1 - 2 \frac{\boldsymbol{u} \cdot \boldsymbol{p}}{E(1-u_z)} \right) \rho(\boldsymbol{x}, z) \, e^{-i(\boldsymbol{q}_1 + \boldsymbol{q}_2)\cdot \boldsymbol{x} - i(q_{1z} + q_{2z}) z} \, v(q_1) \, v(q_2) \\ & \times \frac{2E(1-u_z)}{(p-q_2)^2 + i\epsilon} \, \frac{2E(1-u_z)}{(p - q_2 - q_1)^2 + i\epsilon} \, J(p - q_2 - q_1) \, J^*(p) , \end{aligned} \tag{2.19}$$

where the delta function from the background field has been used. We further note that, as in the SB case, the dominant contribution to the q_{1z} integral corresponds to the pole at $q_{1z} = -q_{2z} + Q^-_{p-q_1-q_2} - i\epsilon$. Thus,

$$
\begin{aligned}
\langle M_2 M_0^* \rangle = i\,\mathcal{C} \int_{x,\boldsymbol{q}_1,q_2} & \theta(z)\, e^{-i(\boldsymbol{q}_1+\boldsymbol{q}_2)\cdot\boldsymbol{x}}\, e^{-iQ^-_{p-q_1-q_2} z}\, J(E,\boldsymbol{p}-\boldsymbol{q}_1-\boldsymbol{q}_2)\, J^*(p) \\
& \times \left(1 - \frac{\boldsymbol{u}\cdot(2\boldsymbol{p}-\boldsymbol{q}_1-\boldsymbol{q}_2)}{(1-u_z)E} - \frac{\boldsymbol{u}\cdot(\boldsymbol{q}_1+\boldsymbol{q}_2)}{1-u_z}\frac{1}{J}\frac{\partial J}{\partial E}\right) \\
& \times \frac{2E}{1+u_z}\, \frac{v(\tilde{q}_1)\, v(q_2)}{(q_{2z}-Q^+_{p-q_2}-i\epsilon)(q_{2z}-Q^-_{p-q_2}+i\epsilon)}\,,
\end{aligned}
\tag{2.20}
$$

where the tilde serves to remind one that q_{1z} and q_{10} are fixed, which introduces a non-trivial q_{2z}-dependence into $v(\tilde{q}_1)$.

Turning to the q_{2z} integration, one must also note that the Fourier factor is independent of q_{2z}, and the residues of the scattering potential poles are no longer suppressed. Therefore, the residues of the six poles may contribute. The two poles of the second scalar propagator are given by $Q^{\pm}_{p-q_2}$, while the four poles coming from the scattering potentials read

$$
v(\tilde{q}_1): \qquad \mathcal{P}_1^{\pm} \equiv Q^-_{p-q_1-q_2} - \frac{u_z}{1-u_z^2}(\boldsymbol{u}\cdot\boldsymbol{q}_1) \pm \frac{i}{1-u_z^2} R_1\,, \tag{2.21a}
$$

$$
v(q_2): \qquad \mathcal{P}_2^{\pm} \equiv \frac{u_z}{1-u_z^2}(\boldsymbol{u}\cdot\boldsymbol{q}_2) \pm \frac{i}{1-u_z^2} R_2\,, \tag{2.21b}
$$

where, keeping the expressions compact, we have introduced a shorthand notation $R^2 \equiv (1-u_z^2)(\boldsymbol{q}^2+\mu^2) - (\boldsymbol{u}\cdot\boldsymbol{q})^2 \geq 0$. Then, we can write the full DB contribution as

$$
\begin{aligned}
\langle M_2 M_0^* \rangle + \text{c.c.} = i\,\mathcal{C} \int_{x,\boldsymbol{q}_1,\boldsymbol{q}_2} & \theta(z)\, \rho(\boldsymbol{x},z)\, J(E,\boldsymbol{p}-\boldsymbol{q}_1-\boldsymbol{q}_2)\, J^*(p) \\
& \times \left(1 - \frac{\boldsymbol{u}\cdot(2\boldsymbol{p}-\boldsymbol{q}_1-\boldsymbol{q}_2)}{(1-u_z)E} - \frac{\boldsymbol{u}\cdot(\boldsymbol{q}_1+\boldsymbol{q}_2)}{1-u_z}\frac{1}{J}\frac{\partial J}{\partial E}\right) \\
& \times \left[e^{-i(\boldsymbol{q}_1+\boldsymbol{q}_2)\cdot\boldsymbol{x}}\, e^{-iQ^-_{p-q_1-q_2} z}\, \mathcal{J}_{DB} - e^{i(\boldsymbol{q}_1+\boldsymbol{q}_2)\cdot\boldsymbol{x}}\, e^{iQ^-_{p-q_1-q_2} z}\, \mathcal{J}^*_{DB}\right],
\end{aligned}
\tag{2.22}
$$

with

$$
\mathcal{J}_{DB} \equiv \int \frac{dq_{2\,z}}{2\pi}\, \frac{2E}{1+u_z}\, \frac{v(\tilde{q}_1)\, v(q_2)}{(q_{2z}-Q^+_{p-q_2}-i\epsilon)(q_{2z}-Q^-_{p-q_2}+i\epsilon)}\,. \tag{2.23}
$$

At zeroth order in gradients, the hydrodynamic parameters are constant in the transverse plane, and integrating over $\boldsymbol{x}$ sets $\boldsymbol{q}_1 = -\boldsymbol{q}_2 \equiv \boldsymbol{q}$. Therefore, the DB contribution then simplifies to

$$\begin{aligned} \langle M_2 M_0^* \rangle + \text{c.c.} = -\,\mathcal{C} \int_0^L dz \int_{\boldsymbol{q}} \rho(z) \, [v(\boldsymbol{q}^2)]^2 \, |J(E, \boldsymbol{p})|^2 & \\ \times \left[1 - \frac{2\,\boldsymbol{u} \cdot \boldsymbol{p}}{(1-u_z)E} - \frac{\boldsymbol{u} \cdot \boldsymbol{p}}{(1-u_z)E} \, \frac{\boldsymbol{q}^2}{v^2} \frac{\partial v^2}{\partial \boldsymbol{q}^2} \right] + \mathcal{O}\left(\boldsymbol{\nabla} \right) \, . & \end{aligned} \tag{2.24}$$

It is convenient to introduce a new transverse vector

$$\boldsymbol{\Gamma}_{DB}(\boldsymbol{q}) \equiv -2 \frac{\boldsymbol{p}}{(1-u_z)E} - \frac{\boldsymbol{p}}{(1-u_z)E} \frac{\boldsymbol{q}^2}{[v(\boldsymbol{q}^2)]^2} \frac{\partial v^2}{\partial \boldsymbol{q}^2} \, , \tag{2.25}$$

which allows to re-express (2.24) in a compact form analogous to (2.16)

$$\langle M_2 M_0^* \rangle + \text{c.c.} = -\,\mathcal{C} \int_0^L dz \int_{\boldsymbol{q}} \rho(z) \, [v(\boldsymbol{q}^2)]^2 \, |J(E, \boldsymbol{p})|^2 \, \left[1 + \boldsymbol{u} \cdot \boldsymbol{\Gamma}_{DB}(\boldsymbol{q}) \right] + \mathcal{O}\left(\boldsymbol{\nabla} \right) \, . \tag{2.26}$$

The leading gradient correction to the latter squared amplitude can be obtained by following the same logic as before. Therefore, expanding the hydrodynamic variables in (2.22), replacing the linear dependence in $\boldsymbol{x}$ by a derivative of a delta function $\delta^{(2)}(\boldsymbol{q}_1 + \boldsymbol{q}_2)$, integrating it by parts, and taking the corresponding derivatives, we find

$$\begin{aligned} \delta \langle M_2 M_0^* \rangle + \text{c.c.} = \mathcal{C} \int_0^L dz \int_{\boldsymbol{q}} \hat{\boldsymbol{g}}_\alpha \, \rho(z) \, \left[z \left(\frac{\boldsymbol{u}_\alpha}{1-u_z} - \frac{\boldsymbol{p}_\alpha}{(1-u_z)E} \right) \right] & \\ \times [v(\boldsymbol{q}^2)]^2 \, |J(E, \boldsymbol{p})|^2 \left[1 + \boldsymbol{u} \cdot \boldsymbol{\Gamma}_{DB}(\boldsymbol{q}) \right] , & \end{aligned} \tag{2.27}$$

where we have neglected subeikonal terms that are suppressed by the smallness of gradients but not length-enhanced, and, thus, are subleading to the ones kept explicitly.

Final parton distribution and jet quenching parameter

The impact of the flow and the anisotropies of the matter in the broadening can be gauged from the modification of the final state parton distribution, which can be related to the squared amplitude of the process and is defined by

$$E \frac{d\mathcal{N}}{d^2p \, dE} \equiv \frac{1}{2(2\pi)^3} \, \langle |M|^2 \rangle \, , \tag{2.28}$$

where we have chosen the energy of the parton, E, and the two transverse components of its momenta as the independent variables. Introducing the initial parton distribution

$E\frac{d\mathcal{N}^{(0)}}{d^2p\,dE} \equiv \frac{1}{2(2\pi)^3}\,|J(E,\boldsymbol{p})|^2$ and taking the combined effects of flow and gradient corrections together, we find

$$\begin{aligned}
E\frac{d\mathcal{N}}{d^2p\,dE} &= E\frac{d\mathcal{N}^{(0)}}{d^2p\,dE} \\
&+ \mathcal{C}\int_0^L dz \int_{\boldsymbol{q}} \left\{ \left[1 - \hat{\boldsymbol{g}}_\alpha\,\frac{(\boldsymbol{u}E - \boldsymbol{p} + \boldsymbol{q})_\alpha\, z}{(1-u_z)E}\right] \left[1 + \boldsymbol{u}\cdot\boldsymbol{\Gamma}(\boldsymbol{q})\right] E\frac{d\mathcal{N}^{(0)}}{d^2(p-q)\,dE} \right. \\
&\left. - \left[1 - \hat{\boldsymbol{g}}_\alpha\,\frac{(\boldsymbol{u}E - \boldsymbol{p})_\alpha\, z}{(1-u_z)E}\right] \left[1 + \boldsymbol{u}\cdot\boldsymbol{\Gamma}_{DB}(\boldsymbol{q})\right] E\frac{d\mathcal{N}^{(0)}}{d^2p\,dE} \right\} \rho(z)\,[v(\boldsymbol{q}^2)]^2\,, \qquad (2.29)
\end{aligned}$$

where the terms appearing at the second subeikonal order should be neglected.

It is instructive to consider how a particular ensemble of partons is modified by a flowing anisotropic distribution of matter. To do so, we focus on a narrow initial distribution parametrized as

$$E\frac{d\mathcal{N}^{(0)}}{d^2p\,dE} = \frac{f(E)}{2\pi w^2}e^{-\frac{\boldsymbol{p}^2}{2w^2}}\,. \qquad (2.30)$$

Starting with the corresponding family of partons in the initial state, one may understand how their distribution changes by focusing on the leading moments of the final state distribution, defined as

$$\langle \boldsymbol{p}_{\alpha_1}...\boldsymbol{p}_{\alpha_n}\rangle \equiv \frac{\int_{\boldsymbol{p}} (\boldsymbol{p}_{\alpha_1}...\boldsymbol{p}_{\alpha_n})\, E\frac{d\mathcal{N}}{d^2p\,dE}}{\int_{\boldsymbol{p}} E\frac{d\mathcal{N}^{(0)}}{d^2p\,dE}} = (2\pi)^2 \int_{\boldsymbol{p}} \frac{(\boldsymbol{p}_{\alpha_1}...\boldsymbol{p}_{\alpha_n})}{f(E)}\, E\frac{d\mathcal{N}}{d^2p\,dE}\,. \qquad (2.31)$$

The process of jet transverse momentum broadening is often quantified with the so-called jet quenching parameter. This parameter, which incorporates the information about the medium properties through the number density of scattering centers and the screening of the potential, is argued to govern the main features of both broadening and in-medium energy loss. In fact, many phenomenological models use the jet quenching parameter as the main input of the matter properties, for a review see e.g. [52, 61]. Thus, we start by computing the quadratic moment given by

$$\langle \boldsymbol{p}^2\rangle = 2w^2 + \mathcal{C}\int_0^L dz \left[1 - z\,\hat{\boldsymbol{g}}\cdot\frac{\boldsymbol{u}}{1-u_z}\right]\rho(z)\int_{\boldsymbol{q}} \boldsymbol{q}^2\,[v(\boldsymbol{q}^2)]^2\,, \qquad (2.32)$$

where the first term corresponds to the vacuum part of (2.29) and is fixed by the width of the initial distribution. Varying this moment with the medium length L — understood as the path length travelled by the parton — we find

$$\hat{q}(L) = \left[1 - L\,\hat{\boldsymbol{g}}\cdot\frac{\boldsymbol{u}}{1-u_z}\right]\hat{q}_0(L)\,, \qquad (2.33)$$

where $\hat{q}_0(L) = \mathcal{C}\rho(L) \int_{\boldsymbol{q}} \boldsymbol{q}^2 \, [v(\boldsymbol{q}^2)]^2$ corresponds to the limit of static transversely homogeneous matter, and all hydrodynamic variables and their gradients should be understood as functions of L. Thus, we can see that the interplay between the transverse medium structure and flow modifies the even moments of the final state distribution, including the fundamental jet quenching parameter, at the leading eikonal order. Moreover, this modification is length-enhanced, and consequently, expected to be the dominant effect of the medium's evolution.

It is also interesting to consider the first odd moments of the final distribution, which vanish in the case of static and isotropic matter for an isotropic initial distribution, but can be generated by flow and gradients effects. Hence, the first moment reads

$$\begin{aligned} \langle \boldsymbol{p}_\alpha \rangle = -\frac{1}{2}\mathcal{C} \int_0^L dz \, \left[1 - z \, \hat{\boldsymbol{g}} \cdot \frac{\boldsymbol{u}}{1-u_z} \right] \rho(z) \\ \times \frac{\boldsymbol{u}_\alpha}{(1-u_z)E} \int_{\boldsymbol{q}} \boldsymbol{q}^2 \left[E \frac{f'(E)}{f(E)} + \boldsymbol{q}^2 \frac{\partial}{\partial \boldsymbol{q}^2} \right] [v(\boldsymbol{q}^2)]^2 \, , \end{aligned} \tag{2.34}$$

while the cubic moment reads

$$\begin{aligned} \langle \boldsymbol{p}_\alpha \, \boldsymbol{p}^2 \rangle = \mathcal{C} \int_0^L dz \int_{\boldsymbol{q}} \Bigg\{ 2w^2 \, z \hat{\boldsymbol{g}}_\alpha \, \frac{\boldsymbol{q}^2}{(1-u_z)E} - \frac{1}{2} \left[1 - z \, \hat{\boldsymbol{g}} \cdot \frac{\boldsymbol{u}}{1-u_z} \right] \frac{\boldsymbol{u}_\alpha}{(1-u_z)E} \\ \times \boldsymbol{q}^2 \left[8w^2 + (10w^2 + \boldsymbol{q}^2) \, \boldsymbol{q}^2 \frac{\partial}{\partial \boldsymbol{q}^2} + \left(4w^2 + \boldsymbol{q}^2\right) \, E \frac{f'(E)}{f(E)} \right] \Bigg\} \, \rho(z) \, [v(\boldsymbol{q}^2)]^2 \, . \end{aligned} \tag{2.35}$$

One can see that the same re-scaling factor appearing in the quadratic moment also modifies (2.34) and (2.35). Furthermore, it is immediate that the moments of the distribution obtained here agree with the results of [107, 111] in the limit of static matter.

2.2.2 Broadening in anisotropic, static matter in the dense limit[2]

In this section, we revisit the derivation of the leading effect of spatial gradients due to matter anisotropies on the jet momentum broadening in the dense limit within the BDMPS-Z formalism. The calculation is performed at first subleading order in the eikonal expansion, only keeping length-enhanced terms suppressed by one power of the energy of the parton while neglecting anything beyond, and at first order in the gradient expansion of hydrodynamic variables. At this level of accuracy, the energy suppressed spin effects can be neglected, allowing us to consider scalar quarks, as in the calculation previously discussed in Section 2.2.1.

---

[2] This section follows the derivation and partially reproduces the results from [111].

The amplitude of an energetic (scalar) quark scattering N times off a background field, see Figure 2.1, reads

$$
\begin{aligned}
iM_N(\boldsymbol{p}_f) &= \prod_{r=1}^{N}\left[\int \frac{d^4p_r}{(2\pi)^4}\, it^{a_r}\, gA^{a_r\mu_r}(p_{r+1}-p_r)\,(p_{r+1}+p_r)_{\mu_r}\,\frac{i}{p_r^2+i\epsilon}\right] J(p_1)\\
&= \prod_{r=1}^{N}\left[(-1)\int_{p_r,x_r} e^{-i(\boldsymbol{p}_{r+1}-\boldsymbol{p}_r)\cdot\boldsymbol{x}_r}\, e^{-i(p_{r+1z}-p_{rz})z_r}\,\frac{2E}{p_r^2+i\epsilon}\, t^{a_r}\,\hat{\rho}^{a_r}(\boldsymbol{x}_r,z_r)\, v(p_{r+1}-p_r)\right] J(p_1)\,,
\end{aligned}
\tag{2.36}
$$

where we have used the delta function from (2.2) in the second line, and we keep the dependence of the scattering potential on the coordinates omitted. In the latter expression, $J(p_1)$ is the source of the initial energetic quark controlling the initial distribution of partons, which is assumed to be centered at $\boldsymbol{x}_0 = 0$ and $z_0 = 0$, and t^a is the leading parton color generator. Notice that, for notational convenience, the final momentum of the parton is denoted as $p_f \equiv p_{N+1}$.

To evaluate the integrals over p_{rz} using the residue theorem, we assume that J is slowly varying, i.e. does not introduce any poles, and that the characteristic distance between the color sources Δz, controlled by ρ^a, satisfies $\mu\Delta z \gg 1$. The latter condition ensures that the contribution from the poles of the scattering potential $v(q)$ are exponentially suppressed due to their finite imaginary part. Hence, the only two poles for each term in (2.36) come from the quark propagator

$$
Q_r^{\pm} \simeq \pm\left(E - \frac{\boldsymbol{p}_r^2}{2E} + i\epsilon\right)\,, \tag{2.37}
$$

where we have accounted only for the first terms in the eikonal expansion. Therefore, rearranging the exponentials using that $z_0 = 0$, and closing the integration contours above the real axis, and thus enclosing the Q_n^+ poles, the amplitude can be written as

$$
\begin{aligned}
iM_N(\boldsymbol{p}_f) = &\prod_{r=1}^{N}\left[i\int_{\boldsymbol{p}_r,\boldsymbol{x}_r} e^{-i(\boldsymbol{p}_{r+1}-\boldsymbol{p}_r)\cdot\boldsymbol{x}_r}\, e^{-i\frac{\boldsymbol{p}_r^2}{2E}(z_r-z_{r-1})}\,\theta_{r,r-1}\, t^{a_r}\,\hat{\rho}^{a_r}(\boldsymbol{x}_r,z_r)\, v(\boldsymbol{p}_{r+1}-\boldsymbol{p}_r)\right]\\
&\times e^{i\frac{\boldsymbol{p}_f^2}{2E}z_N} J(E,\boldsymbol{p}_1)
\end{aligned}
\tag{2.38}
$$

where the shorthand notation $\theta_{r,r-1} \equiv \theta(z_r - z_{r-1})$ has been introduced, and we have used that the final momentum of the parton is on shell $p_{f\mu} \simeq \left(E, \boldsymbol{p}_f, E - \frac{\boldsymbol{p}_f^2}{2E}\right)$. The amplitude (2.38) can be expressed as a convolution of the effective single particle propagator of the energetic parton and its initial source as follows:

$$
iM_N(\boldsymbol{p}_f) = \int_{\boldsymbol{p}_1} e^{i\frac{\boldsymbol{p}_f^2}{2E}L}\, \mathcal{G}_N(\boldsymbol{p}_f, L; \boldsymbol{p}_1, 0)\, J(E,\boldsymbol{p}_1)\,, \tag{2.39}
$$

where $\mathcal{G}_N(\boldsymbol{p}_f, L; \boldsymbol{p}_1, 0)$ is the contribution of N scatterings to the in-medium effective propagator of a parton with initial transverse momentum $\boldsymbol{p}_1$ and final transverse momentum $\boldsymbol{p}_f$ after travelling a distance L through the medium.

The full effective parton propagator can be obtained by resumming $\mathcal{G}_N$ over the number of scattering with the medium as

$$\mathcal{G}(\boldsymbol{p}_f, L; \boldsymbol{p}_1, 0) = \sum_{N=0}^{\infty} \mathcal{G}_N(\boldsymbol{p}_f, L; \boldsymbol{p}_1, 0)\,, \tag{2.40}$$

where $\mathcal{G}_0(\boldsymbol{p}_f, L; \boldsymbol{p}_1, 0)$ corresponds to the contribution without any scatterings, i.e. in vacuum, which would reduce the amplitude to the source function, being

$$\mathcal{G}_0(\boldsymbol{p}_f, L; \boldsymbol{p}_1, 0) = (2\pi)^2\,\delta^{(2)}(\boldsymbol{p}_f - \boldsymbol{p}_1)\, e^{-i\frac{\boldsymbol{p}_f^2}{2E}L}\,. \tag{2.41}$$

An integral equation for the full propagator can be derived by expressing $\mathcal{G}_n$ in terms of the propagator with $N-1$ scatterings and then resumming the series, obtaining

$$\begin{aligned}\mathcal{G}(\boldsymbol{p}_f, L; \boldsymbol{p}_1, 0) =& \mathcal{G}_0(\boldsymbol{p}_f, L; \boldsymbol{p}_1, 0) \\ &+ \int_0^L dz \int_{\boldsymbol{x},\boldsymbol{l}} e^{-i\boldsymbol{x}\cdot(\boldsymbol{p}_f - \boldsymbol{l})}\, e^{-i\frac{\boldsymbol{p}_f^2}{2E}(L-z)}\, it^a \hat{\rho}^a(\boldsymbol{x}, z)\, v(\boldsymbol{p}_f - \boldsymbol{l})\, \mathcal{G}(\boldsymbol{l}, z; \boldsymbol{p}_1, 0)\,.\end{aligned} \tag{2.42}$$

Differentiating the latter equation with respect to L yields the following differential evolution equation for the full propagator

$$\frac{\partial}{\partial L}\mathcal{G}(\boldsymbol{p}_f, L; \boldsymbol{p}_1, 0) = -i\frac{\boldsymbol{p}_f^2}{2E}\mathcal{G}(\boldsymbol{p}_f, L; \boldsymbol{p}_1, 0) + \int_{\boldsymbol{l},\boldsymbol{x}} e^{-i(\boldsymbol{p}_f - \boldsymbol{l})\cdot\boldsymbol{x}}\, i\, t^a\, \hat{\rho}^a(\boldsymbol{x}, L) v(\boldsymbol{p}_f - \boldsymbol{l})\, \mathcal{G}(\boldsymbol{l}, L; \boldsymbol{p}_1, 0)\,, \tag{2.43}$$

which takes the form of a two-dimensional Schrödinger equation with a matrix-valued potential. The initial condition for (2.43) is $\mathcal{G}(\boldsymbol{p}_f, 0; \boldsymbol{p}_1, 0) = (2\pi)^2\delta^{(2)}(\boldsymbol{p}_f - \boldsymbol{p}_1)$, ensuring that at $L = 0$, i.e. without any propagation of the parton inside a medium, the amplitude matches the initial parton production amplitude encoded in J. The solution to the evolution equation (2.43) is well known in the literature, and can be expressed as a path integral in position space as

$$\mathcal{G}(\boldsymbol{x}_f, L; \boldsymbol{x}_0, 0) = \int_{\boldsymbol{x}_0}^{\boldsymbol{x}_f} \mathcal{D}\mathbf{r}\, \exp\left(i\frac{E}{2}\int_0^L d\tau\, \dot{\mathbf{r}}^2\right) \mathcal{P}\exp\left(i\int_0^L d\tau t^a v^a(\mathbf{r}(\tau), \tau)\right)\,, \tag{2.44}$$

where $\mathcal{P}$ denotes path ordering, $\boldsymbol{x}_f$ and $\boldsymbol{x}_0$ are the final and initial positions of the trajectory respectively, and the shorthand notation $v^a(\boldsymbol{x}, z) = \int_{\boldsymbol{y}} \hat{\rho}^a(\boldsymbol{y}, z) v(\boldsymbol{x} - \boldsymbol{y})$, with $v(\boldsymbol{x})$ defined through the Fourier transform of the potential in momentum space, has been introduced. The path ordered exponentials of the in-medium potential appearing in the propagators are usually referred to as Wilson lines in the literature. With the full propagator in hand, the resummation of the number of scatterings at the level of the amplitude simply reduces to

$$iM(\boldsymbol{p}_f) = \sum_{N=0}^{\infty} iM_N(\boldsymbol{p}_f) = \int_{\boldsymbol{p}_1} e^{i\frac{\boldsymbol{p}_f^2}{2E}L}\, \mathcal{G}(\boldsymbol{p}_f, L; \boldsymbol{p}_1, 0)\, J(E, \boldsymbol{p}_1)\,, \tag{2.45}$$

which allows the squared and averaged matrix element of the process to be expressed as the correlator of two in-medium parton propagators as

$$\left\langle |M(\boldsymbol{p}_f)|^2 \right\rangle = \int_{\boldsymbol{p}_1, \bar{\boldsymbol{p}}_1} \left\langle \mathcal{G}(\boldsymbol{p}_f, L; \boldsymbol{p}_1, 0)\mathcal{G}^{\dagger}(\boldsymbol{p}_f, L; \bar{\boldsymbol{p}}_1, 0) \right\rangle \, J(E, \boldsymbol{p}_1) J^{*}(E, \bar{\boldsymbol{p}}_1)\,. \tag{2.46}$$

Since the in-medium propagators are functionals of the stochastic colour source densities, it is necessary to determine the correlator of $v^a(\boldsymbol{x}, z)$ to compute the two-point function in (2.46). Using the definition of v^a in terms of the color densities and the medium averages given by (2.4), one finds

$$\begin{aligned} \left\langle t^a v^a(\mathbf{r}, \tau) t^b v^{\dagger b}(\bar{\mathbf{r}}, \bar{\tau}) \right\rangle \simeq & \left(1 + \frac{\mathbf{r}(\tau) + \bar{\mathbf{r}}(\tau)}{2} \cdot \hat{\boldsymbol{g}} \right) \\ & \times \mathcal{C}\, \delta(\tau - \bar{\tau})\, \rho(0, \tau) \int_{\boldsymbol{q}} e^{i\boldsymbol{q}\cdot(\mathbf{r} - \bar{\mathbf{r}})}\, v(\boldsymbol{q})^2\,, \end{aligned} \tag{2.47}$$

where $\mathcal{C} = \frac{c_F}{2N_c}$ for quarks interacting with in-medium sources in the fundamental representation, and $\hat{\boldsymbol{g}}_\alpha \equiv \sum_G \left(\boldsymbol{\nabla} G \cdot \frac{\delta}{\delta G} \right)_\alpha$ is a two-dimensional operator which generates all gradient corrections. The sum in $\hat{\boldsymbol{g}}$ is over the hydrodynamic variables, namely the number density of scattering centers and the Debye mass of the potential here. To obtain the zeroth- and the first-order gradient corrections in (2.47), one can follow the procedure described in Section 2.2.1. This involves expanding the hydrodynamic variable to first order and rewriting the linear $\boldsymbol{x}$ dependence of the correction as a derivative of the Fourier factor, followed by integration by parts. First-order gradient corrections introduce a dependence on the dipole's center of mass, $\frac{\mathbf{r} + \bar{\mathbf{r}}}{2}$, in addition to the usual dependence on the dipole size, $\mathbf{r} - \bar{\mathbf{r}}$, in the two-point correlator of in-medium color potentials. This new dependence reflects the breakdown of translation invariance, expected from the presence of anisotropies. Using the two point correlator of v^a, the medium average of two Wilson lines can be written as

$$\begin{aligned} & \left\langle \mathcal{P} \exp\left(i \int_0^L d\tau\, t^a\, v^a(\mathbf{r}(\tau), \tau) \right) \mathcal{P} \exp\left(-i \int_0^L d\tau\, t^b v^{\dagger b}(\bar{\mathbf{r}}(\tau), \tau) \right) \right\rangle \\ & \qquad \simeq \exp\left(- \int_0^L d\tau \left[1 + \frac{\mathbf{r}(\tau) + \bar{\mathbf{r}}(\tau)}{2} \cdot \hat{\boldsymbol{g}} \right] \mathcal{V}\left(\mathbf{r}(\tau) - \bar{\mathbf{r}}(\tau) \right) \right)\,, \end{aligned} \tag{2.48}$$

where the re-exponentiation of the medium averaged potential follows from the fact that the averaging statistics is still Gaussian, and the dipole potential $\mathcal{V}\left(\mathbf{r}(\tau)-\bar{\mathbf{r}}(\tau)\right)$ is the Fourier transform of the following combination of in-medium color potentials

$$\mathcal{V}(\boldsymbol{q},z) \equiv -\mathcal{C}\rho(z)\left[v(\boldsymbol{q})^2-\delta^{(2)}(\boldsymbol{q})\int d^2\boldsymbol{l}\,v(\boldsymbol{l})^2\right] . \tag{2.49}$$

The first term in (2.49) comes from the medium average of one potential coming from each exponential, analogous to the SB contribution in Section 2.2.1, while the second term, the so-called contact term, comes from the medium average of two potentials from the same exponential, analogous to the DB contribution in Section 2.2.1. Notice that the derivation discussed here is valid only to first order in gradients, and, therefore, the exponential containing $\hat{\boldsymbol{g}}$ in (2.48) should be understood as a series truncated at that order. Using the medium average of two Wilson lines, the correlator of two propagators in position space reduces to

$$\begin{aligned}\left\langle \mathcal{G}(\boldsymbol{x}_f,L;\boldsymbol{x}_0,0)\mathcal{G}^\dagger(\bar{\boldsymbol{x}}_f,L;\bar{\boldsymbol{x}}_0,0)\right\rangle = &\int_{\boldsymbol{x}_0}^{\boldsymbol{x}_f}\mathcal{D}\mathbf{r}\int_{\bar{\boldsymbol{x}}_0}^{\bar{\boldsymbol{x}}_f}\mathcal{D}\bar{\mathbf{r}}\,\exp\left(i\frac{E}{2}\int_0^L d\tau\,\left[\dot{\mathbf{r}}^2-\dot{\bar{\mathbf{r}}}^2\right]\right)\\ &\times\exp\left(-\int_0^L d\tau\left[1+\frac{\mathbf{r}(\tau)+\bar{\mathbf{r}}(\tau)}{2}\cdot\hat{\boldsymbol{g}}\right]\mathcal{V}\left(\mathbf{r}(\tau)-\bar{\mathbf{r}}(\tau)\right)\right) .\end{aligned} \tag{2.50}$$

Performing the change of variables $\boldsymbol{u}=\mathbf{r}-\bar{\mathbf{r}}$ and $\boldsymbol{w}=\frac{\mathbf{r}+\bar{\mathbf{r}}}{2}$, one can see that the path integral (2.50) can be solved analytically, since the dependence on $\boldsymbol{w}$ appears only through the small gradient terms. Standard methods show that (2.50) is fixed by the solution of the classical equation of motion, $E\ddot{\boldsymbol{u}}=i\hat{\boldsymbol{g}}\,\mathcal{V}(\boldsymbol{u}(\tau))$, which can be separated into the contribution at zeroth-order in gradients, reading

$$\boldsymbol{u}_c^{(0)}(\tau)=\frac{\boldsymbol{u}_f-\boldsymbol{u}_0}{L}\tau+\boldsymbol{u}_0\,, \tag{2.51}$$

with $\boldsymbol{u}_f=\boldsymbol{x}_f-\bar{\boldsymbol{x}}_f$ and $\boldsymbol{u}_0=\boldsymbol{x}_0-\bar{\boldsymbol{x}}_0$, and the contribution containing the linear gradient corrections reading

$$\boldsymbol{u}_c^{(1)}(\tau)=\frac{i}{E}\hat{\boldsymbol{g}}\left[\int_0^\tau d\zeta\int_0^\zeta d\xi\,\mathcal{V}(\boldsymbol{u}_c^{(0)}(\xi))-\frac{\tau}{L}\int_0^L d\zeta\int_0^\zeta d\xi\,\mathcal{V}(\boldsymbol{u}_c^{(0)}(\xi))\right] , \tag{2.52}$$

which satisfies $\boldsymbol{u}_c^{(1)}(L)=\boldsymbol{u}_c^{(1)}(0)=\mathbf{0}$. After performing the algebra, omitted here for the sake of brevity but detailed in [111], the squared and averaged matrix element is found to be

$$\begin{aligned}\left\langle|M(\boldsymbol{p}_f)|^2\right\rangle \simeq &\frac{1}{L^2}\int_{\mathbf{P}_1,\boldsymbol{u}_0,\boldsymbol{u}_f} e^{-i\boldsymbol{p}_f\cdot\boldsymbol{u}_f}\,e^{i\mathbf{P}_1\cdot\boldsymbol{u}_0}\\ &\times\frac{\delta^{(2)}(\dot{\boldsymbol{u}}_c(L))\,\exp\left(-\int_0^L d\tau\,\mathcal{V}(\boldsymbol{u}_c(\tau))\right)}{1+\frac{i}{EL}\hat{\boldsymbol{g}}\cdot\int_0^L d\zeta\int_0^\zeta d\xi\,\xi\,\boldsymbol{\nabla}\mathcal{V}\left(\boldsymbol{u}_c(\xi)\right)}\;\left|J(E,\mathbf{P}_1)\right|^2 ,\end{aligned} \tag{2.53}$$

where $\mathbf{P}_1 = \frac{\boldsymbol{p}_1+\bar{\boldsymbol{p}}_1}{2}$, and J has been assumed to have at most a constant imaginary phase, as it is for a tree-level 2 → 2 process, neglecting further corrections coming from the coupling of gradients and the phases of the initial source functions. Notice that the expression (2.53) is only valid to first order in gradients and must be understood as a series truncated at the linear order. Also, it should be stressed that the corresponding path integral has a non-trivial measure, which enters in the denominator of Eq. 2.53.

Final parton distribution and its moments

The effect of the matter anisotropies on the single particle momentum broadening can be gauged through the gradient corrections to the final state parton distribution. This distribution can be defined in configuration space as

$$E\frac{d\mathcal{N}}{d^2x\,dE} = \frac{1}{2(2\pi)^3}\int_{\boldsymbol{p}} e^{i\boldsymbol{p}\cdot\boldsymbol{x}}\,\left\langle |M(\boldsymbol{p})|^2\right\rangle\,, \tag{2.54}$$

where we have chosen the energy of the parton, E, and its position in the transverse plane, $\boldsymbol{x}$, as the independent variables. Thus, substituting (2.53) in the latter definition, introducing the initial parton distribution $E\frac{d\mathcal{N}^{(0)}}{d^2x\,dE} = \frac{1}{2(2\pi)^3}\int_{\boldsymbol{p}} e^{i\boldsymbol{p}\cdot\boldsymbol{x}}\,|J(E,\boldsymbol{p})|^2$, taking the corresponding integrals and expanding to first order in gradients, the final parton distribution can be written as

$$\begin{aligned}\frac{d\mathcal{N}}{d^2x\,dE} &= \exp\left(-\int_0^L d\tau\,\mathcal{V}(\boldsymbol{x},\tau)\right)\\ &\times\left\{\left[1-\frac{i}{E}\int_0^L d\tau\,\boldsymbol{\nabla}\mathcal{V}(\boldsymbol{x},\tau)\cdot\left(\int_L^\tau d\zeta\int_0^\zeta d\xi+(L-\tau)\int_0^L d\xi\right)\hat{\boldsymbol{g}}\,\mathcal{V}(\boldsymbol{x},\xi)\right]\right.\\ &\qquad\left.+\frac{i}{E}\int_0^L d\zeta\int_0^\zeta d\xi\,\hat{\boldsymbol{g}}\,\mathcal{V}(\boldsymbol{x},\xi)\cdot\boldsymbol{\nabla}\right\}\frac{d\mathcal{N}^{(0)}}{d^2x\,dE}\,.\end{aligned} \tag{2.55}$$

The leading effect of matter gradients is the introduction of anisotropy in the momentum broadening, leading to a direction-dependent final jet momentum distribution. Probes traversing inhomogeneous matter acquire an additional contribution to the transverse momenta, which, due to the non-trivial matter structure, possesses a non-zero average. Formally, this can be illustrated by computing the odd moments of the final state distribution, which would be zero in the case of homogeneous matter for an isotropic initial distribution of partons. For instance, defining the moments of the distribution as (2.31) and focusing on a narrow initial distribution parametrized as (2.30), the cubic moment, which is the first non-zero momentum of the distribution , reads

$$\left\langle \boldsymbol{p}^\alpha\boldsymbol{p}^2\right\rangle = -\frac{w^2L^2}{E}\,\hat{\boldsymbol{g}}^\alpha\int_{\boldsymbol{q}}\boldsymbol{q}^2\,\mathcal{V}(\boldsymbol{q}) + \frac{L^3}{6E}\int_{\boldsymbol{q}_1}\boldsymbol{q}_1^2\,\mathcal{V}(\boldsymbol{q}_1)\,\hat{\boldsymbol{g}}^\alpha\int_{\boldsymbol{q}_2}\boldsymbol{q}_2^2\,\mathcal{V}(\boldsymbol{q}_2)\,, \tag{2.56}$$

where the properties of the matter have been assumed constant along the longitudinal direction. In contrast, to the case of anisotropic and flowing matter considered in Section 2.2.1, the effect of gradient correction to first order in static matter cannot modify the even moments of the distribution, since the directionality vanishes after the angular integration on the transverse plane. Consequently, the jet quenching parameter $\hat{q}$ does not get modified in this setup. One can easily see that the first term in the latter expression, which corresponds to the contribution of the first order in opacity, coincides with the static limit of Eq. 2.35.

2.2.3 Broadening in the glasma phase[3]

This section revisits the derivation of single-particle momentum broadening within the highly anisotropic Glasma phase, focusing on the impact of the chromoelectric fields, aligned with the beam direction, present in the early stages of HICs. Assuming the jet is at midrapidity, we define a coordinate system such that the jet propagates along the z-axis, with the direction of the beam lying in the transverse direction. The matter is modelled by the stochastic background field given in (2.5), assumed to follow a Gaussian distribution with correlators defined by (2.6). The calculation presented below is performed at leading order in the eikonal expansion, neglecting all energy suppressed contributions. As in Sections 2.2.1 and 2.2.2, we can neglect energy-suppressed spin effects at the working accuracy, focusing on scalar quarks.

In momentum space, the background field can be written as

$$gA^{a\mu}(q) = \delta^{\mu 0}\,(2\pi)\,\delta(q_0)\int_x e^{-i\boldsymbol{q}\cdot\boldsymbol{x}\;-iq_z z}\,\overbrace{\boldsymbol{x}\cdot\boldsymbol{E}^a(z)}^{\mathcal{A}^a(\boldsymbol{x},z)}\,, \tag{2.57}$$

so that the amplitude of an energetic (scalar) quark scattering N times off this field, see Figure 2.1, is given by

$$\begin{aligned} iM_N(\boldsymbol{p}_f) &= \prod_{r=1}^{N}\left[\int\frac{d^4p_r}{(2\pi)^4}\,it^{a_r}\,gA^{a_r\mu}(p_{r+1}-p_r)\,(p_{r+1}+p_r)_\mu\,\frac{i}{p_r^2+i\epsilon}\right]J(p_1)\\ &= \prod_{r=1}^{N}\left[(-1)\int_{p_r,x_r} e^{-i(\boldsymbol{p}_{r+1}-\boldsymbol{p}_r)\cdot\boldsymbol{x}_r}\,e^{-i(p_{r+1z}-p_{rz})z_r}\,\frac{2E}{p_r^2+i\epsilon}\,t^{a_r}\,\mathcal{A}^{a_r}(\boldsymbol{x}_r,z_r)\right]J(p_1)\,, \end{aligned} \tag{2.58}$$

where the second line is obtained by using the delta function from (2.57). In the latter expression, $J(p_1)$ is the source of the initial energetic quark controlling the initial distribution of partons, which is assumed to be centered at $\boldsymbol{x}_0 = 0$ and $z_0 = 0$, and t^a is the

---

[3] This section presents an adapted summary and partial reproduction of content from [3], which forms part of this thesis and is detailed further in Chapter 4.

color generator of the leading parton. Notice that the final momentum of the parton is denoted as $p_f \equiv p_{N+1}$.

As it is done in Section 2.2.1 and 2.2.2, we assume that J is slowly varying, i.e. does not introduce any new pole, in order to evaluate the integrals over p_{rz} using the residue theorem. Hence, the only two poles for each term of the amplitude come from the quark propagator, and are given by (2.37). Therefore, two contributions to each of these integrals are possible depending on the orderings of z_r. However, the longitudinal momentum of the final parton is positive, and the energy is extremely large ($E \to \infty$ formally). Thus, the contribution associated with large negative longitudinal momentum in the propagators, i.e. the Q_r^- contribution, is suppressed by a strongly oscillatory complex exponential. Consequently, the integration contour should be closed above the real axis, and the amplitude is given by

$$iM_N(\boldsymbol{p}_f) = \prod_{r=1}^{N} \left[i \int_{\boldsymbol{p}_r, \boldsymbol{x}_r} e^{-i(\boldsymbol{p}_{r+1}-\boldsymbol{p}_r)\cdot \boldsymbol{x}_r}\, \theta_{r,r-1}\, t^{a_r}\, \mathcal{A}^{a_r}(\boldsymbol{x}_r, z_r) \right] J(E, \boldsymbol{p}_1)\,, \tag{2.59}$$

where we have introduced the shorthand notation $\theta_{r,r-1} \equiv \theta(z_r - z_{r-1})$. The amplitude above is analogous to (2.38), differing in the specific form of the field and the absence of LPM phases, which are approximately zero at the strict eikonal limit. Eq. 2.59 can be expressed as a convolution of the effective single particle propagator of the energetic parton and its initial source as

$$iM_N(\boldsymbol{p}_f) = \int_{\boldsymbol{p}_1} \mathcal{G}_N^{\mathrm{eik}}(\boldsymbol{p}_f, L; \boldsymbol{p}_1, 0)\, J(E, \boldsymbol{p}_1) \tag{2.60}$$

where $\mathcal{G}_N^{\mathrm{eik}}(\boldsymbol{p}_f, L; \boldsymbol{p}_1, 0)$ is the contribution of n scatterings to the eikonal propagator of a parton with initial transverse momentum $\boldsymbol{p}_1$ and final transverse momentum $\boldsymbol{p}_f$ after travelling a distance L through the glasma.

The full eikonal propagator can be obtained by resumming $\mathcal{G}_N^{\mathrm{eik}}$ as in (2.40), with the vacuum contribution given by

$$\mathcal{G}_0^{eik}(\boldsymbol{p}_f, L; \boldsymbol{p}_1, 0) = (2\pi)^2\, \delta^{(2)}(\boldsymbol{p}_f - \boldsymbol{p}_1)\,, \tag{2.61}$$

which ensures that the amplitude with $N = 0$ medium scatterings reduces to the source function. Following the procedure discussed in Section 2.2.2, the evolution equation for the resummed eikonal propagator can be derived, and it reads

$$\frac{\partial}{\partial L} \mathcal{G}^{\mathrm{eik}}(\boldsymbol{p}_f, L; \boldsymbol{p}_1, 0) = \int_{\boldsymbol{l}, \boldsymbol{x}} e^{-i(\boldsymbol{p}_f - \boldsymbol{l})\cdot \boldsymbol{x}}\, i\, t^a\, \mathcal{A}^a(\boldsymbol{x}, L)\, \mathcal{G}^{eik}(\boldsymbol{l}, L; \boldsymbol{p}_1, 0)\,. \tag{2.62}$$

Working at the leading order in the eikonal expansion results in a significant simplification of the evolution equation of the propagator, (2.62), compared to (2.43). At this order, the kinetic term of the Schrödinger-like equation vanishes, and the resulting equation can be easily solved in configuration space, resulting in

$$\mathcal{G}^{\text{eik}}(\boldsymbol{x}_f, L; \boldsymbol{x}_0, 0) = \delta^{(2)}(\boldsymbol{x}_f - \boldsymbol{x}_0)\, \mathcal{P} \exp\left(i \int_0^L d\tau\, t^a\, \mathcal{A}^a(\boldsymbol{x}_f, \tau) \right) , \tag{2.63}$$

where we have used that the initial condition for (2.62) is $\mathcal{G}^{\text{eik}}(\boldsymbol{p}_f, 0; \boldsymbol{p}_i, 0) = (2\pi)^2\, \delta^{(2)}(\boldsymbol{p}_f - \boldsymbol{p}_1)$, ensuring that, at $L = 0$, the amplitude matches the initial parton production amplitude encoded in J. The solution (2.63) could have been directly obtained by taking the limit of infinite energy for the path integral of the full propagator (2.44), which would force the position on the transverse plane to be fixed and only the Wilson line, given by

$$\mathcal{W}(\boldsymbol{x}; L, 0) \equiv \mathcal{P} \exp\left(i \int_0^L d\tau\, t^a\, \boldsymbol{x} \cdot \boldsymbol{E}^a(\tau) \right) , \tag{2.64}$$

would survive. With the full propagator in hand, the resummation of the number of scatterings with the glasma fields at the level of the amplitude reduces to

$$iM(\boldsymbol{p}_f) = \sum_{N=0}^{\infty} iM_N(\boldsymbol{p}_f) = \int_{\boldsymbol{x}, \boldsymbol{p}_1} e^{-i(\boldsymbol{p}_f - \boldsymbol{p}_1)\cdot \boldsymbol{x}}\, \mathcal{W}(\boldsymbol{x}; L, 0)\, J(E, \boldsymbol{p}_1) \,, \tag{2.65}$$

which allows the squared amplitude of the process, to be expressed as two in-medium eikonal parton propagators–Wilson lines–convoluted with the initial sources,

$$|M(\boldsymbol{p}_f)|^2 = \int_{\boldsymbol{x}, \bar{\boldsymbol{x}}} e^{-i\boldsymbol{p}_f \cdot (\boldsymbol{x} - \bar{\boldsymbol{x}})}\, J^*(E, \bar{\boldsymbol{x}})\, \mathcal{W}^\dagger(\bar{\boldsymbol{x}}; L, 0)\, \mathcal{W}(\boldsymbol{x}; L, 0)\, J(E, \boldsymbol{x}) \,, \tag{2.66}$$

where $J(E, \boldsymbol{x})$ should be understood as the Fourier transform of the initial source of the energetic parton.

Final parton distribution and its moments

The single particle momentum broadening during the initial stages of HICs, produced by the glasma fields, can be studied by focusing on the properties of the final state parton distribution. This distribution can be related to the squared and averaged matrix element of the process and is defined by (2.28). Since the averaging procedure for the glasma field is much more involved than the one in the QGP phase, we are not going to compute the full distribution, but just one of its moments. In particular, we are going to focus on the jet quenching parameter, argued to govern the main features of both broadening and in-medium energy loss, that is obtained from the quadratic moment of the distribution as $\hat{q} = \frac{\partial}{\partial L} \langle \boldsymbol{p}^2 \rangle$, where $\langle \boldsymbol{p}^2 \rangle$ is defined in (2.31). To simplify the calculations, we choose a reference frame for the transverse plane such that the beam direction, and therefore the chromoelectric fields, lies along the x-axis.

It is illustrative to begin by considering the jet quenching before the averaging over the events is performed, $\hat{q}_{\rm na}$, which corresponds to the broadening in an ensemble of partons penetrating the same field configuration

$$\begin{aligned}\hat{q}_{\rm na} &= -\frac{1}{\mathcal{N}}\frac{1}{2(2\pi)^3}\frac{\partial}{\partial L}\int_{\boldsymbol{p}_f}\boldsymbol{p}_f^2\int_{\boldsymbol{x},\bar{\boldsymbol{x}}} e^{-i\boldsymbol{p}_f\cdot(\boldsymbol{x}-\bar{\boldsymbol{x}})}\, J^*(E,\bar{\boldsymbol{x}})\,\mathcal{W}^\dagger(\bar{\boldsymbol{x}})\,\mathcal{W}(\boldsymbol{x})\,J(E,\boldsymbol{x})\\ &= -\frac{1}{\mathcal{N}}\frac{1}{2(2\pi)^3}\frac{\partial}{\partial L}\int_{\boldsymbol{x}}\boldsymbol{\nabla}^2_{\boldsymbol{x}-\bar{\boldsymbol{x}}}\,\big(J^*(E,\bar{\boldsymbol{x}})\,\mathcal{W}^\dagger(\bar{\boldsymbol{x}})\,\mathcal{W}(\boldsymbol{x})\,J(E,\boldsymbol{x})\big)_{\bar{\boldsymbol{x}}=\boldsymbol{x}}\,,\end{aligned}\tag{2.67}$$

where the $\boldsymbol{p}_f^2$ is rewritten as a derivative acting on the Fourier factor and integrated by parts, and we have introduced $\mathcal{W}(\boldsymbol{x}) \equiv \mathcal{W}(\boldsymbol{x};L,0)$ to alleviate the notation. The normalization factor in the definition of the moments of the distribution reads $\mathcal{N} = \frac{1}{2(2\pi)^3}\int_{\boldsymbol{p}}|J(\boldsymbol{p})|^2$. The evolution equation of the two point function of Wilson lines can be easily derived, and it reads

$$\frac{\partial}{\partial L}\,\mathcal{W}(\boldsymbol{x})\mathcal{W}^\dagger(\bar{\boldsymbol{x}}) = i\boldsymbol{E}^a(L)\cdot\big[\boldsymbol{x}t^a\mathcal{W}(\boldsymbol{x})\mathcal{W}^\dagger(\bar{\boldsymbol{x}}) - \bar{\boldsymbol{x}}\mathcal{W}(\boldsymbol{x})\mathcal{W}^\dagger(\bar{\boldsymbol{x}})t^a\big]\,. \tag{2.68}$$

Projecting (2.68) onto the subspaces of the color structures, one can build a closed set of differential equation for the derivatives of the two point function, which can be solved analytically –the details, omitted here for brevity, are provided in Ref. [3] in Chapter 4. Assuming that the initial ensemble of particles has no net color and follows a Gaussian distribution, being

$$\frac{1}{\mathcal{N}}\frac{1}{2(2\pi)^3}\,J(E,\boldsymbol{p})J^*(E,\bar{\boldsymbol{p}}) = \frac{1}{2\pi E}\,e^{-\frac{\boldsymbol{p}^2+\bar{\boldsymbol{p}}}{4w^2}}\,, \tag{2.69}$$

the non-averaged jet quenching parameter can be written as

$$\hat{q}_{\rm na}(z) = \frac{w^2}{2\pi^3}\int_{\boldsymbol{Y}}\int_0^z d\tau\,\tilde{\mathcal{W}}^{ab}(\boldsymbol{Y};z,\tau)\,E^a_x(z)\,E^b_x(\tau)\,e^{-2w^2\boldsymbol{Y}^2}\,, \tag{2.70}$$

where we have made explicit that the chromoelectric fields only have x-component. We have also introduced a Wilson line in the adjoint representation, $\tilde{\mathcal{W}}^{ab}(\boldsymbol{Y};z,\tau)$, which can be defined as $\tilde{\mathcal{W}}^{ab}(\boldsymbol{x};L,0) = \mathcal{P}\exp\Big(iT^c\int_0^L d\tau\boldsymbol{x}\cdot\boldsymbol{E}^c(\tau)\Big)$, with $(T^c)_{ab} = -if^{abc}$ the corresponding adjoint generator.

The expression for the jet quenching parameter should be averaged over multiple events, following (2.6). Path ordering allows the Wilson line $\tilde{\mathcal{W}}(\boldsymbol{Y};z,\tau)$ to be expressed as a product of Wilson lines for each color tube. This simplifies the averaging procedure, as the field in each tube is only correlated with itself, allowing for separate averaging. Let $z_j = j\ell$ and $z_{j-1} = (j-1)\ell$ define the boundaries of the jth color slab, and let us assume that the two field insertions in (2.70) are in different tubes, specifically $z_{n+1} > z \geq z_n > \tau$. Consequently, the integral arising from the averaging procedure over the field of the final tube is given by $\int_{E_n} e^{-E_n^2/E_0^2}\, \tilde{\mathcal{W}}^{a,a_n}(\boldsymbol{Y})\, E^a_{xn}$ which vanishes for both SU(2) and SU(3), see the proof provided in [3] in Chapter 4. Thus, the only non-zero contribution comes from the two field insertion being in the same tube, and the averaged $\hat{q}$ becomes

$$\hat{q} = \frac{w^2}{2\pi^3} \int_{\boldsymbol{Y},E} \int_{z_n}^{z} d\tau\, E^2\, e^{-2w^2\boldsymbol{Y}^2}\, e^{-\frac{E^2}{E_0^2}} = \frac{E_0^2}{\pi^2}(z - z_n)\,, \tag{2.71}$$

where we have considered $SU(3)$ fields. For $SU(2)$ case, the first equality still holds, but the integral over the field has a different measure, see the discussion below (2.6), resulting in $\hat{q}_{SU(2)} = \frac{3E_0^2}{8\pi^2}(z - z_n)$. Thus, we see that in our model, the jet quenching parameter is linearly increasing while the parton propagates along the given tube, and then falls to zero at the edge of the next tube, restarting the linear growth afterward. However, in any realistic setup, the initial position within the first flux tube, z_{in}, cannot be fixed, and one has to average over it. This is equivalent to averaging over the position within the last flux tube, $z - z_n$, and we readily find that

$$\hat{q}_{z_{in}} = \frac{E_0^2}{2\pi^2}\ell\,, \qquad \hat{q}_{\mathrm{SU}(2),\, z_{in}} = \frac{3E_0^2}{16\pi^2}\ell\,, \tag{2.72}$$

where the subscript z_{in} indicates that the object has been additionally averaged over the initial position.

2.3 The medium-induced radiation

This section summarizes the main results of this thesis on medium-induced jet radiation in both the QGP and glasma phases, which are detailed in the papers contained in Chapter 4. The study of medium-induced gluon emissions is crucial for understanding jets inside QCD matter. In particular, jet energy loss, a key signature of the QGP formation, see Section 1.4, is primarily driven by medium-induced gluon emissions [55, 75, 76]. Furthermore, the single gluon emission spectrum within the medium provides essential insight into medium modifications of parton cascades. Additionally, these emissions modify the jet substructure compared to vacuum jets, offering a theoretical tool to understand these modifications and extract information about the properties of the medium in further analysis.

As discussed for the broadening, particles interacting with a background field in QFT experience a superposition of all possible number of interactions. Thus, analogously to (2.7), the amplitude of the branching process can be written as a series

$$\mathcal{R} = \sum_{N=0}^{\infty} \mathcal{R}_N = \mathcal{R}_0 + \mathcal{R}_1 + \mathcal{R}_2 + \dots\,, \tag{2.73}$$

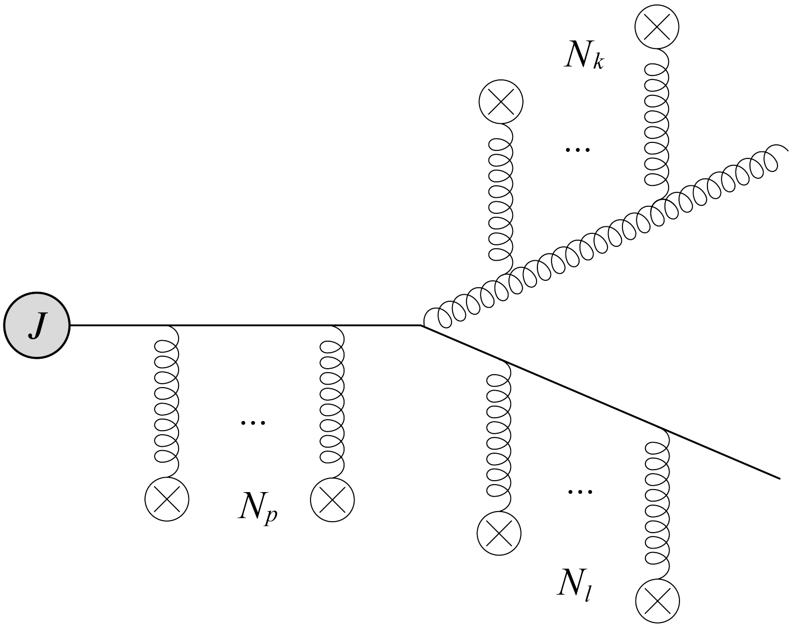

Figure 2.3: Feynman diagram of the in-medium parton branching with each particle interacting multiple times with the background field. This Figure has been extracted from [2].

where $\mathcal{R}_N$ is the amplitude with N scatterings and $\mathcal{R}_0$ corresponds to vacuum. In general, the amplitude of a parton branching with N scatterings with the background field, see Figure 2.1, is given by

$$
\begin{aligned}
i\mathcal{R}_{N_p,N_k,N_l} = & \prod_{n=1}^{N_p}\left[\int \frac{d^4p_n}{(2\pi)^4}\, igt^{a_n}(p_{n+1}+p_n)\cdot A^{a_n}(p_{n+1}-p_n)\,\frac{i}{p_n^2+i\epsilon}\right] \\
& \times \int \frac{d^4p_s}{(2\pi)^4}\, igt^{b_1}(p_s+l_1)_{\mu_1}\,\frac{i}{p_s^2+i\epsilon}\,(2\pi)^4\delta^{(4)}(p_s-l_1-k_1)\,J(p_1) \\
& \times \prod_{r=1}^{N_k}\left[\int \frac{d^4k_r}{(2\pi)^4}\,\frac{(-i)N^{\mu_r\nu_r}(k_r)}{k_r^2+i\epsilon}\,\Gamma^{b_r b_{r+1} c_r}_{\nu_r\mu_{r+1}\alpha_r}(k_r,-k_{r+1})\,A^{c_r\alpha_r}(k_{r+1}-k_r)\right]\,\epsilon^{*\mu_{N_k+1}}(k) \\
& \times \prod_{m=1}^{N_l}\left[\int \frac{d^4l_m}{(2\pi)^4}\, igt^{a_m}(l_{m+1}+l_m)\cdot A^{a_m}(l_{m+1}-l_m)\,\frac{i}{l_m^2+i\epsilon}\right], \qquad (2.74)
\end{aligned}
$$

where $\Gamma^{abc}_{\alpha\beta\gamma}$ is the three-gluon vertex, all the integrals should be understood as acting from the left on the whole expression, and we have introduced additional momentum labels $p_{N_p+1} = p_s$, $l_{N_l+1} = l$ and $k_{N_k+1} = k$. For convenience, we count the number of scattering of the quark before the branching N_p, after the branching N_l, and the scattering of the gluon N_k separately, such that $N = N_p + N_k + N_l$. Since all the medium-induced gluons emission calculations included in this thesis are computed, at most, to first subleading order in the eikonal expansion, the further energy-suppressed spin effects can be ignored, and the quark is considered a scalar particle in (2.74). Notice that, in all the considered cases below, the field is derived in the Lorenz gauge, and thus satisfies the gauge condition $k \cdot A(k) = 0$. Furthermore, the z-component of the background field vanishes $A_z = 0$, and it satisfies the axial gauge condition $n \cdot A = 0$, where $n_\mu = (0, \mathbf{0}, 1)$. This is the gauge used in (2.74), where the numerator of the gluon propagator is given by

$$N_{\mu\nu}(k) = g_{\mu\nu} + n^2 \frac{k_\mu k_\nu}{(k \cdot n)^2 - k^2 n^2} + k^2 \frac{n_\mu n_\nu}{(k \cdot n)^2 - k^2 n^2} - (k \cdot n) \frac{k_\mu n_\nu + k_\nu n_\mu}{(k \cdot n)^2 - k^2 n^2} , \quad (2.75)$$

and only the two physical gluon polarization must be considered.

Analogously to transverse momentum broadening calculations, there are two distinct approaches to obtain the matrix element from (2.74). Following the BDMPS-Z approach, the amplitude is resummed over the number of scatterings with the medium, obtaining a propagator for each partonic leg of the process. Then, the resummed amplitude is squared, and the medium averages are performed. This approach is used in [2] and [3], and their results are discussed in Section 2.3.2 and Section 2.3.3 respectively. On the other hand, following the GLV approach the full amplitude $\mathcal{R}$ is squared before resumming the series, and the medium averages are performed on each term separately, following the same structure as (2.8). This approach is used in [1], and its results are discussed in Section 2.3.1.

2.3.1 Medium-induced radiation in anisotropic, flowing matter in the dilute limit[4]

In this section, we review the main results obtained in [1], see Chapter 4. We derive the medium-induced radiation spectrum in an evolving inhomogeneous medium at the first order in opacity. Specifically, we focus on two particular types of the medium evolution effects. First, we study how the transverse gradients of the number density of scattering sources, ρ, and Debye mass, μ, modify the gluon spectrum in full kinematics but in the absence of any flow. Second, we search for the mixed flow-gradient effects analogous to the multiplicative modification of the jet quenching parameter in (2.33). For simplicity, we neglect gradients of u_z and choose a frame where $u_z = 0$, ensuring that $A_z = 0$ and the applicability of the axial gauge discussed in the previous section.

---

[4] This section presents an adapted summary and partial reproduction of content from [1], which forms part of this thesis and is detailed further in Chapter 4.

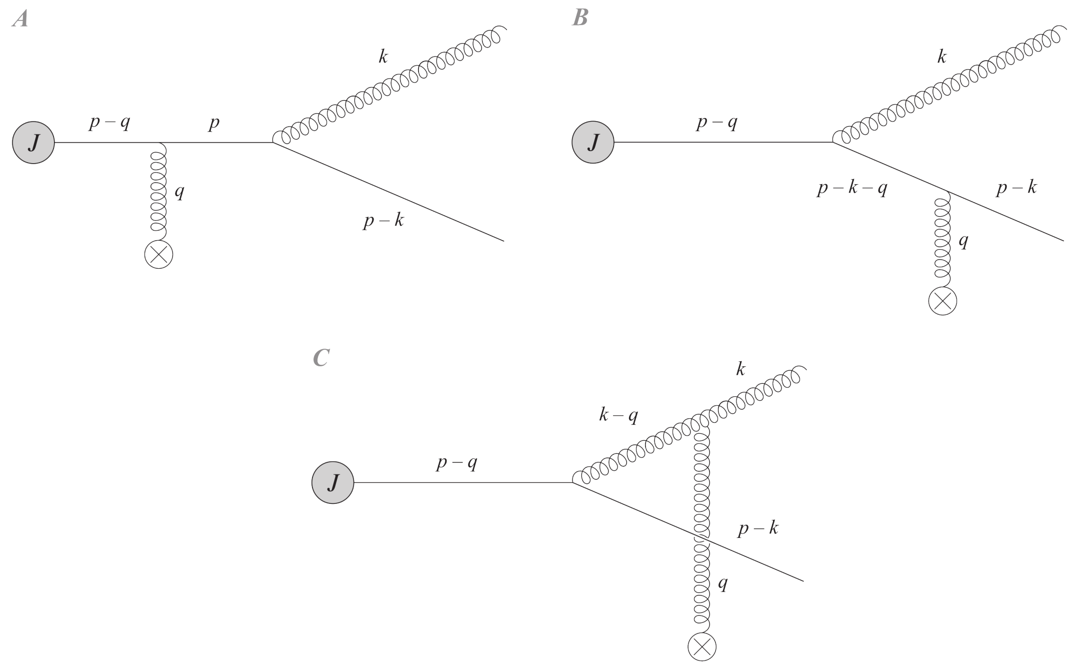

Figure 2.4: The three single-Born diagrams contributing to the medium-induced gluon emission at first order in opacity. This figure has been extracted from [1].

The amplitude of gluon emission at first order in opacity, $N_\chi = 1$, can be written as

$$\left\langle |\mathcal{R}_{N_\chi=1}|^2 \right\rangle = \left\langle |\mathcal{R}_0|^2 \right\rangle + \left\langle |\mathcal{R}_1|^2 \right\rangle + \langle \mathcal{R}_2 \mathcal{R}_0^* \rangle + \langle \mathcal{R}_0 \mathcal{R}_2^* \rangle \ , \tag{2.76}$$

where three different contributions can be identified. The first term, $\langle |\mathcal{R}_0|^2 \rangle$, corresponds to the process in vacuum, i.e. without any interaction with the background field. The second term, $\langle |\mathcal{R}_1|^2 \rangle$, is the single-Born contribution. This includes the squared amplitudes of the diagrams with one scattering with the field, and their interference terms. There are three different SB diagrams –see Figure 2.4– depending on which particle interacts with the medium, which give rise to six SB contributions. The third and the fourth terms, $\langle \mathcal{R}_2 \mathcal{R}_0^* \rangle + \langle \mathcal{R}_0 \mathcal{R}_2^* \rangle$, describe the interference between amplitudes involving two interactions with the background field and the vacuum amplitude. These are the six double-Born contributions, which correspond to the six diagrams with two scatterings, see Figure 2.5. The calculation of these amplitudes involves similar techniques to those presented for transverse momentum broadening in Section 2.2.1. Given that the techniques have been introduced before, and the high technical complexity of the derivation, we will focus solely on discussing the results. The interested reader is referred to the paper [1] in Chapter 4 for a detailed derivation and the corresponding discussion.

Given the squared and averaged matrix element of the emission, the final-state parton

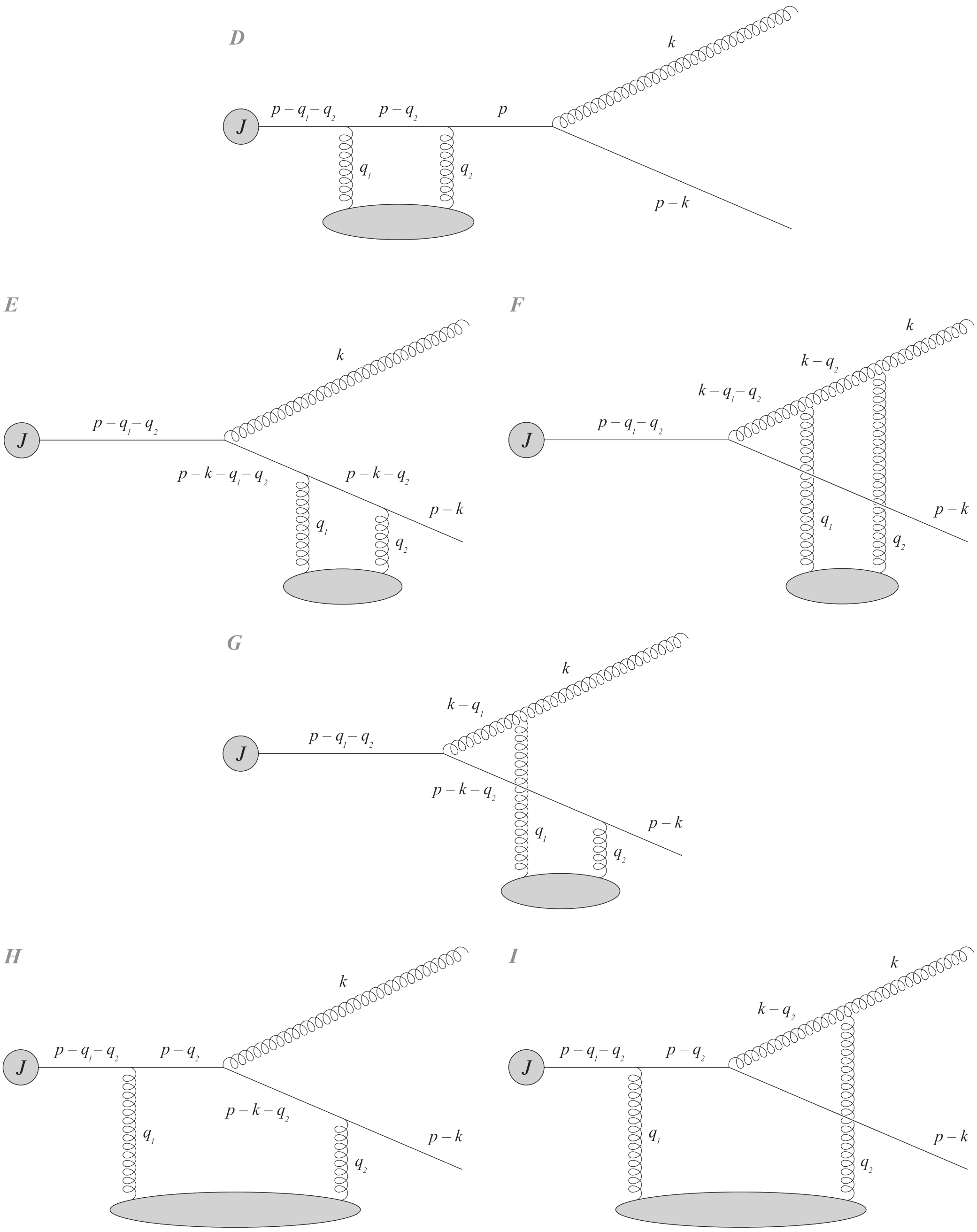

Figure 2.5: The six double-Born diagrams contributing to the medium-induced gluon emission at the first order in opacity. This figure has been extracted from [1].

distribution can be defined as

$$E\,\frac{d\mathcal{N}}{d^2k\,d\mathrm{x}\,d^2p\,dE} \equiv \frac{1}{\left[2(2\pi)^3\right]^2}\,\frac{1}{\mathrm{x}(1-\mathrm{x})}\,\langle|\mathcal{R}_{N_\chi=1}|^2\rangle\,, \tag{2.77}$$

where E is the total energy of the quark-gluon pair, $\boldsymbol{p}$ the total transverse momenta, x the energy fraction of the gluon, and $\boldsymbol{k}$ its final transverse momentum. For simplicity, we assume that the initial distribution $E\,\frac{d\mathcal{N}^{(0)}}{d^2p\,dE}$ is a slowly varying function of the transverse momentum, setting $E\,\frac{d\mathcal{N}^{(0)}}{d^2(p-q)\,dE} \simeq E\,\frac{d\mathcal{N}^{(0)}}{d^2p\,dE}$. Let us start focusing on the limit of static inhomogeneous matter. Considering the emission of spin-1 gluons, going beyond the scalar approximation used in [107], and full kinematics for the gluon, going beyond the soft gluon approximation used in [2] presented in Section 2.3.2, the final state parton distribution at first order in opacity reads

$$\begin{aligned}
E\,\frac{d\mathcal{N}^{(1)}}{d^2k\,d\mathrm{x}\,d^2p\,dE} =\ & \frac{(1-\mathrm{x})g^2}{(2\pi)^3\,\mathrm{x}}\,\frac{C_F^2}{N_c}\left(E\,\frac{d\mathcal{N}^{(0)}}{d^2p\,dE}\right)\int_0^L dz\,\int_{\boldsymbol{q}} \\
\times\Bigg\{ & \boldsymbol{\kappa}_0^2\,(1+\hat{\boldsymbol{g}}\cdot\boldsymbol{D}_A) + 2\boldsymbol{\kappa}^2\,(1-\cos\phi)\,(1+\hat{\boldsymbol{g}}\cdot\boldsymbol{D}_B) + 2\frac{N_c}{C_F}\bar{\boldsymbol{\kappa}}^2\,\left(1-\cos\bar{\phi}\right)(1+\hat{\boldsymbol{g}}\cdot\boldsymbol{D}_C) \\
& + \frac{\boldsymbol{\kappa}_0\cdot\boldsymbol{\kappa}}{2C_FN_c}\left[2\,(1-\cos\phi) + 2\,\hat{\boldsymbol{g}}\cdot(\boldsymbol{D}_A-\boldsymbol{D}_B\cos\phi) - \mathrm{x}\,\hat{\boldsymbol{g}}\cdot\left(2\boldsymbol{\kappa}-\boldsymbol{\kappa}^2\frac{\boldsymbol{\kappa}_0}{\boldsymbol{\kappa}_0\cdot\boldsymbol{\kappa}}\right)\sin\phi\right] \\
& - \frac{N_c}{2C_F}\boldsymbol{\kappa}_0\cdot\bar{\boldsymbol{\kappa}}\,\left[2\left(1-\cos\bar{\phi}\right) + 2\,\hat{\boldsymbol{g}}\cdot\left(\boldsymbol{D}_A-\boldsymbol{D}_C\cos\bar{\phi}\right) + (1-\mathrm{x})\,\hat{\boldsymbol{g}}\cdot\left(2\bar{\boldsymbol{\kappa}}-\bar{\boldsymbol{\kappa}}^2\frac{\boldsymbol{\kappa}_0}{\boldsymbol{\kappa}_0\cdot\bar{\boldsymbol{\kappa}}}\right)\sin\bar{\phi}\right] \\
& - \frac{N_c}{2C_F}\boldsymbol{\kappa}\cdot\bar{\boldsymbol{\kappa}}\Bigg[2\left(1+\cos\left(\phi-\bar{\phi}\right)-\cos\bar{\phi}-\cos\phi\right) \\
& \qquad + 2\,\hat{\boldsymbol{g}}\cdot\left(\boldsymbol{D}_A-\boldsymbol{D}_B\cos\phi-\boldsymbol{D}_C\cos\bar{\phi}+(\boldsymbol{D}_B+\boldsymbol{D}_C-\boldsymbol{D}_A)\cos\left(\phi-\bar{\phi}\right)\right) \\
& \qquad - \hat{\boldsymbol{g}}\cdot\left(2(1-\mathrm{x})\bar{\boldsymbol{\kappa}} - \frac{\boldsymbol{\kappa}_0}{\boldsymbol{\kappa}_0^2}\frac{\bar{\boldsymbol{\kappa}}^2\boldsymbol{\kappa}^2}{\boldsymbol{\kappa}\cdot\bar{\boldsymbol{\kappa}}} + 2\mathrm{x}\boldsymbol{\kappa}\right)\left(\sin\phi-\sin\bar{\phi}-\sin\left(\phi-\bar{\phi}\right)\right)\Bigg] \\
& - \boldsymbol{\kappa}_0^2\,\cos\phi_0\,(1+\hat{\boldsymbol{g}}\cdot\boldsymbol{D}_D) - \boldsymbol{\kappa}_0^2\,\left[(1-\cos\phi_0)+\hat{\boldsymbol{g}}\cdot(\boldsymbol{D}_E-\boldsymbol{D}_D\cos\phi_0)+\mathrm{x}\,\hat{\boldsymbol{g}}\cdot\boldsymbol{\kappa}_0\,\sin\phi_0\right] \\
& - \frac{N_c}{C_F}\boldsymbol{\kappa}_0^2\,\left[(1-\cos\phi_0)+\hat{\boldsymbol{g}}\cdot(\boldsymbol{D}_F-\boldsymbol{D}_D\cos\phi_0)-(1-\mathrm{x})\,\hat{\boldsymbol{g}}\cdot\boldsymbol{\kappa}_0\,\sin\phi_0\right] \\
& + \frac{N_c}{C_F}\boldsymbol{\kappa}_0\cdot\boldsymbol{\kappa}_G\Bigg[(\cos\phi_G-\cos\phi_0)+\hat{\boldsymbol{g}}\cdot(\boldsymbol{D}_G\cos\phi_G-\boldsymbol{D}_D\cos\phi_0) \\
& \qquad + \left(\mathrm{x}-\frac{1}{2}\right)\,\hat{\boldsymbol{g}}\cdot\left(2\,\boldsymbol{\kappa}_G-\boldsymbol{\kappa}_G^2\frac{\boldsymbol{\kappa}_0}{\boldsymbol{\kappa}_0\cdot\boldsymbol{\kappa}_G}\right)(\sin\phi_G+\sin\phi_0)\Bigg]\Bigg\}\,\rho(z)\,[v(\boldsymbol{q}^2)]^2\,,
\end{aligned} \tag{2.78}$$

where the operator producing all the gradient corrections is defined as $\hat{\boldsymbol{g}}_\alpha \equiv \sum_G\left(\boldsymbol{\nabla}G\cdot\frac{\delta}{\delta G}\right)_\alpha$, the following shorthand notation for LPM phases have been introduced

$$\phi = \frac{(\boldsymbol{k}-\mathrm{x}(\boldsymbol{p}-\boldsymbol{q}))^2}{2\mathrm{x}(1-\mathrm{x})E}\, z\,, \qquad \bar{\phi} = \frac{(\boldsymbol{k}-(1-\mathrm{x})\boldsymbol{q}-\mathrm{x}\boldsymbol{p})^2}{2\mathrm{x}(1-\mathrm{x})E}\, z\,,$$
$$\phi_0 = \frac{(\boldsymbol{k}-\mathrm{x}\boldsymbol{p})^2}{2\mathrm{x}(1-\mathrm{x})E}\, z\,, \qquad \phi_G = \frac{\boldsymbol{q}\cdot(2(\boldsymbol{k}-\mathrm{x}\boldsymbol{p})+\boldsymbol{q})}{2\mathrm{x}(1-\mathrm{x})E} z\,,$$

the light-front wave functions are expressed through their normalized arguments

$$\boldsymbol{\kappa} = \frac{\boldsymbol{k}-\mathrm{x}(\boldsymbol{p}-\boldsymbol{q})}{(\boldsymbol{k}-\mathrm{x}(\boldsymbol{p}-\boldsymbol{q}))^2}\,, \qquad \bar{\boldsymbol{\kappa}} = \frac{\boldsymbol{k}-(1-\mathrm{x})\boldsymbol{q}-\mathrm{x}\boldsymbol{p}}{(\boldsymbol{k}-(1-\mathrm{x})\boldsymbol{q}-x\boldsymbol{p})^2}\,,$$
$$\boldsymbol{\kappa}_0 = \frac{\boldsymbol{k}-\mathrm{x}\boldsymbol{p}}{(\boldsymbol{k}-\mathrm{x}\boldsymbol{p})^2}\,, \qquad \boldsymbol{\kappa}_G = \frac{\boldsymbol{k}+\boldsymbol{q}-\mathrm{x}\boldsymbol{p}}{(\boldsymbol{k}+\boldsymbol{q}-\mathrm{x}\boldsymbol{p})^2}\,,$$

and we have associated the particular momentum structures in the gradient corrections with the diagrams where they appear for the first time, following

$$\boldsymbol{D}_A = \frac{\boldsymbol{p}-\boldsymbol{q}}{E} z\,,\ \boldsymbol{D}_B = \frac{\boldsymbol{p}-\boldsymbol{q}}{2E} z + \frac{\boldsymbol{p}-\boldsymbol{k}-\boldsymbol{q}}{2(1-\mathrm{x})E} z\,,\ \boldsymbol{D}_C = \frac{\boldsymbol{p}-\boldsymbol{q}}{2E} z + \frac{\boldsymbol{k}-\boldsymbol{q}}{2\mathrm{x}E} z\,,$$
$$\boldsymbol{D}_D = \frac{\boldsymbol{p}}{E} z\,,\ \boldsymbol{D}_E = \frac{\boldsymbol{p}-\boldsymbol{k}}{(1-\mathrm{x})E} z\,,\ \boldsymbol{D}_F = \frac{\boldsymbol{k}}{\mathrm{x}E} z\,,\ \boldsymbol{D}_G = \frac{\boldsymbol{p}-\boldsymbol{k}-\boldsymbol{q}}{2(1-\mathrm{x})E} z + \frac{\boldsymbol{k}+\boldsymbol{q}}{2\mathrm{x}E} z\,.$$

Taking the limit of homogeneous matter with $\hat{\boldsymbol{g}}=0$, we can readily check that (2.78) agrees with the result for the $N_\chi = 1$ in-medium branching, see e.g. [124]. To make the features of the final-state parton distribution more apparent, it is instructive to consider the small-x limit of (2.78), where the distribution is known to take a particularly simple form in the case of homogeneous matter [88]. In this limit $\phi = \phi_0$, $\phi_G = \bar{\phi}|_{\boldsymbol{q}\to-\boldsymbol{q}} - \phi_0$, $\boldsymbol{\kappa} = \boldsymbol{\kappa}_0$, and $\boldsymbol{\kappa}_G = \bar{\boldsymbol{\kappa}}|_{\boldsymbol{q}\to-\boldsymbol{q}}$. Keeping only the subeikonal terms which scale as $\frac{1}{\mathrm{x}E}$, we set $\boldsymbol{D}_A = \boldsymbol{D}_B = \boldsymbol{D}_D = \boldsymbol{D}_E = 0$, then

$$\begin{aligned}
E\,\frac{d\mathcal{N}^{(1)}}{d^2k\,d\mathrm{x}\,d^2p\,dE} &= \frac{g^2\,C_F}{(2\pi)^3\,\mathrm{x}}\left(E\,\frac{d\mathcal{N}^{(0)}}{d^2p\,dE}\right)\int_0^L dz \int_{\boldsymbol{q}} \\
&\times \Bigg\{ \frac{2\,\boldsymbol{k}\cdot\boldsymbol{q}}{\boldsymbol{k}^2(\boldsymbol{k}-\boldsymbol{q})^2}\left(1-\cos\left(\frac{(\boldsymbol{k}-\boldsymbol{q})^2}{2\mathrm{x}E}z\right)\right)\left(1+\frac{\hat{\boldsymbol{g}}\cdot(\boldsymbol{k}-\boldsymbol{q})}{2\mathrm{x}E}z\right) - \frac{\hat{\boldsymbol{g}}\cdot\boldsymbol{k}}{\boldsymbol{k}^2}\left[\frac{z}{\mathrm{x}E}-\frac{1}{\boldsymbol{k}^2}\sin\left(\frac{\boldsymbol{k}^2}{2\mathrm{x}E}z\right)\right] \\
&+ \frac{\boldsymbol{k}\cdot(\boldsymbol{k}-\boldsymbol{q})}{\boldsymbol{k}^2(\boldsymbol{k}-\boldsymbol{q})^2}\left[\frac{\hat{\boldsymbol{g}}\cdot(\boldsymbol{k}-\boldsymbol{q})}{\mathrm{x}E}z - \hat{\boldsymbol{g}}\cdot\left(2\frac{\boldsymbol{k}-\boldsymbol{q}}{(\boldsymbol{k}-\boldsymbol{q})^2}-\frac{\boldsymbol{k}}{\boldsymbol{k}\cdot(\boldsymbol{k}-\boldsymbol{q})}\right)\sin\left(\frac{(\boldsymbol{k}-\boldsymbol{q})^2}{2\mathrm{x}E}z\right)\right]\Bigg\}\,\rho(z)\,[v(\boldsymbol{q}^2)]^2\,.
\end{aligned} \tag{2.79}$$

This expression can be compared with the results of [2], and, after some algebra, one can show that (2.79) precisely agrees with the $N_\chi = 1$ part of the small-x resummed parton distribution.

Turning to the mixed flow-gradient corrections, we only keep energy suppressed terms that are enhanced by the length of the medium, i.e. the LPM phases, obtaining

$$\begin{aligned}
E\,\frac{d\mathcal{N}^{(1)}}{d^2k\,d\mathrm{x}\,d^2p\,dE} &= \frac{(1-\mathrm{x})g^2}{(2\pi)^3\,\mathrm{x}}\frac{C_F^2}{N_c}\left(E\,\frac{d\mathcal{N}^{(0)}}{d^2p\,dE}\right)\int_0^L dz\int_{\boldsymbol{q}}(1-\hat{\boldsymbol{g}}\cdot\boldsymbol{u}\,z)\\
&\times\Bigg\{\boldsymbol{\kappa}_0^2+2\boldsymbol{\kappa}^2\,(1-\cos\phi)+2\frac{N_c}{C_F}\bar{\boldsymbol{\kappa}}^2\,\left(1-\cos\bar{\phi}\right)+\frac{\boldsymbol{\kappa}_0\cdot\boldsymbol{\kappa}}{C_FN_c}\,(1-\cos\phi)-\frac{N_c}{C_F}\boldsymbol{\kappa}_0\cdot\bar{\boldsymbol{\kappa}}\,\left(1-\cos\bar{\phi}\right)\\
&\quad-\frac{N_c}{C_F}\boldsymbol{\kappa}\cdot\bar{\boldsymbol{\kappa}}\,\left(1+\cos\left(\phi-\bar{\phi}\right)-\cos\bar{\phi}-\cos\phi\right)-\boldsymbol{\kappa}_0^2\,\cos\phi_0-\boldsymbol{\kappa}_0^2\,(1-\cos\phi_0)\\
&\quad-\frac{N_c}{C_F}\boldsymbol{\kappa}_0^2\,(1-\cos\phi_0)+\frac{N_c}{C_F}\boldsymbol{\kappa}_0\cdot\boldsymbol{\kappa}_G\,(\cos\phi_G-\cos\phi_0)\Bigg\}\,\rho(z)\,[v(\boldsymbol{q}^2)]^2.
\end{aligned} \tag{2.80}$$

One readily observes that this modification of the distribution results in a multiplicative modification of the radiation rate due to the jet-medium interactions, and, consequently, in a modification of the induced radiative energy loss, c.f. [88].

In order to estimate the effect of the mixed term in the spectrum, we focus on the small-x limit. Then, the final state distribution can be factorized into the initial quark distribution and an emission spectrum $d\mathcal{J}^{(1)}$, defined by

$$\mathrm{x}E\,\frac{d\mathcal{N}^{(1)}}{d^2k\,d\mathrm{x}\,d^2p\,dE}\equiv\mathrm{x}\,\frac{d\mathcal{J}^{(1)}}{d\mathrm{x}d^2k}\,E\,\frac{d\mathcal{N}^{(0)}}{d^2p\,dE}\,. \tag{2.81}$$

In order to treat the z-integral analytically, we choose a smooth longitudinal profile for the source density $\rho(\boldsymbol{x},z)=2\rho_0(\boldsymbol{x})e^{-\frac{2z}{L}}$ [1, 87, 88]. With this, the resulting medium-induced gluon spectrum reads

$$\begin{aligned}
\mathrm{x}\,\frac{d\mathcal{J}^{(1)}}{d\mathrm{x}d^2k} &= \frac{4\alpha_s\,\chi\,N_c}{\pi}\int_{\boldsymbol{q}}\frac{2\,\boldsymbol{k}\cdot\boldsymbol{q}}{\boldsymbol{k}^2(\boldsymbol{q}^2+\mu^2)^2}\,\frac{L^3(\boldsymbol{k}-\boldsymbol{q})^2}{L^2(\boldsymbol{k}-\boldsymbol{q})^4+16\mathrm{x}^2E^2}\\
&\times\left[1+\left(\frac{L^2(\boldsymbol{k}-\boldsymbol{q})^4}{L^2(\boldsymbol{k}-\boldsymbol{q})^4+16\mathrm{x}^2E^2}-\frac{3}{2}\right)L\,(\boldsymbol{g}\cdot\boldsymbol{u})\right]\,,
\end{aligned} \tag{2.82}$$

where we have introduced opacity $\chi=\frac{C_Fg^4\rho_0}{2N_c4\pi\mu^2}L$, and replaced $\hat{\boldsymbol{g}}$ by $\boldsymbol{g}=\frac{\boldsymbol{\nabla}T}{T}\left(3-\frac{4}{(\boldsymbol{q}^2+\mu^2)}\right)$, assuming that $\rho_0\sim T^3$ and $\mu\simeq gT$, neglecting the gradients of the transverse flow $\boldsymbol{u}$ present in (2.80) for simplicity. In Figure 2.6, we plot the spectrum (2.82) for two energies $E=50\,\mathrm{GeV}$ (left) and $E=100\,\mathrm{GeV}$ (right), while for each energy we also show two different medium lengths $L=5\,\mathrm{fm}$ and $L=2.5\,\mathrm{fm}$, keeping the mean free path $\lambda=\frac{L}{\chi}$ fixed. We set $\alpha_s=0.3$, $\mu=0.6\,\mathrm{GeV}$, $\mathrm{x}=0.1$, and assume that $\chi=3$ at $L=5\,\mathrm{fm}$. For

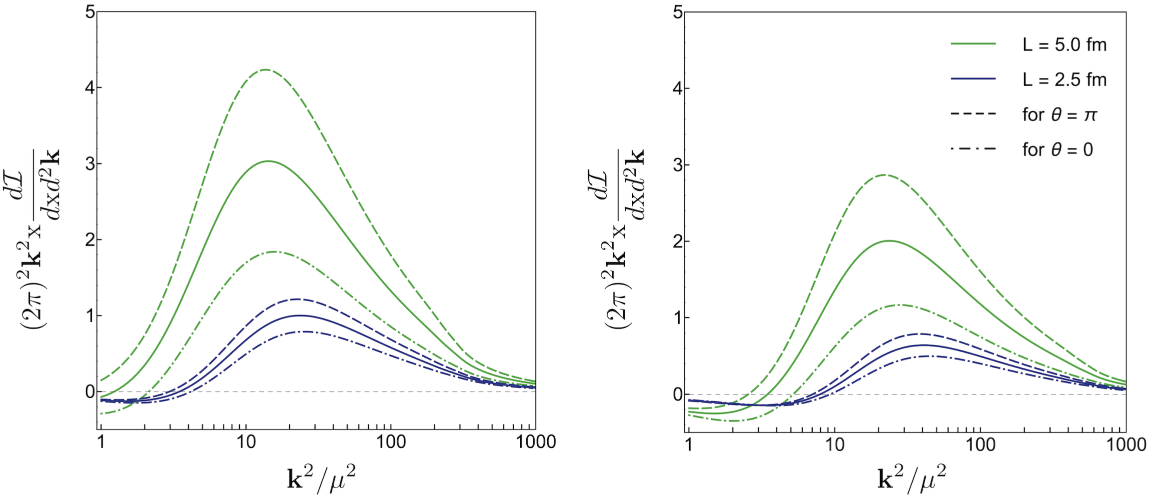

Figure 2.6: The (rescaled) medium-induced soft gluon spectrum plotted for two energies $E = 50\,\text{GeV}$ (left) and $E = 100\,\text{GeV}$ (right). The colors distinguish the medium length, while the mean free path is kept fixed ($\chi = 3$ at $L = 5\,\text{fm}$). The solid lines correspond to the homogeneous (or no transverse flow) limit, while the dashed lines correspond to $\boldsymbol{u}$ and $\boldsymbol{\nabla}T$ being parallel or antiparallel. This figure has been extracted from [1].

a qualitative estimate of the mixed flow-gradient term, we take $|\boldsymbol{u}| = 0.3$, $\frac{|\boldsymbol{\nabla}T|}{T^2} = 0.1$, and $T = 0.3\,\text{GeV}$. One may readily see that the modification of the spectrum could be substantial even for moderate flows and anisotropies, especially for longer trajectories.

2.3.2 Medium-induced radiation in anisotropic, static matter in the dense limit[5]

In this section, we review the main results obtained in [2], see Chapter 4. We derive the medium-induced radiation spectrum in an inhomogeneous medium. Particularly, we focus on the first order gradient corrections to the emission spectrum in the soft gluon approximation, i.e. with the gluon energy being much smaller than the quark energy, and to all orders in interactions. The calculation is performed at leading subeikonal order, keeping terms suppressed by one power of the gluon energy and enhanced by the medium length, while neglecting terms suppressed by powers of the quark energy. For simplicity, and as discussed previously, we treat the quark as a scalar particle at this accuracy. In addition, since the matter is static, we can work in the axial gauge, as discussed at the beginning of Section 2.3. The resummation procedure follows the same general strategy discussed in Sections 2.2.2 and 2.2.3. Thus, we only provide a brief outline of the derivation before discussing the results, referring the interested reader to the paper [2] in Chapter 4 for

---

[5] This section presents an adapted summary and partial reproduction of content from [2], which forms part of this thesis and is detailed further in Chapter 4.

further detail.

The amplitude of parton branching with $N = N_p + N_k + N_l$ scatterings with the QCD matter, see Figure 2.3, is given by (2.74). As explained in Section 2.2.2, the integrals over the z-component of the intermediate momenta can be evaluated using residues after substituting the background field from (2.2). After integration, we identify the contributions of N_p scatterings to the in-medium effective quark propagator before branching, N_l scatterings to the in-medium effective quark propagator after branching, and N_k scatterings to the in-medium effective gluon propagator. Since we neglect terms suppressed by the quark energy –including LPM phases–, the in-medium propagators for the quarks, both before and after branching, simplify to Wilson lines, as shown in Section 2.2.3. The effective gluon propagator, however, retains the relevant LPM phases, and therefore can be expressed as (2.44). Finally, after resumming the multiple scattering interactions using the obtained propagators for each parton, the resummed amplitude simplifies considerably, taking the form

$$\begin{aligned} i\mathcal{R} \simeq -\frac{g}{\omega} \lim_{z_f\to\infty} \int_0^\infty dz_s \int_{\boldsymbol{x}_{in}} e^{-i\boldsymbol{x}_{in}\cdot\boldsymbol{l}} J(E, \boldsymbol{x}_{in}) \\ \times \mathcal{W}(\boldsymbol{x}_{in}; \infty, z_s)\, t^a_{proj}\, \mathcal{W}(\boldsymbol{x}_{in}; z_s, 0)\, e^{i\frac{\boldsymbol{k}^2}{2\omega} z_f} \left[\boldsymbol{\epsilon}\cdot\boldsymbol{\nabla}_{\boldsymbol{x}_{in}} \mathcal{G}^{ba}\left(\boldsymbol{k}, z_f; \boldsymbol{x}_{in}, z_s\right)\right] , \end{aligned} \tag{2.83}$$

where $\boldsymbol{l}$ and $\boldsymbol{k}$ are the final transverse momenta of the quark and gluon respectively, E and ω are the energies of the quark and the gluon respectively, and $\boldsymbol{\epsilon}$ is the transverse polarization vector of the final state gluon. Due to the matter anisotropies, the in-medium scattering potential in the gluon propagator and the Wilson lines for the quarks depends on the transverse coordinates through the Debye mass,

$$\tilde{v}^a(\boldsymbol{x}, z) = \int_{q,\boldsymbol{y}} e^{i\boldsymbol{q}\cdot(\boldsymbol{x}-\boldsymbol{y})}\, \hat{\rho}^a(\boldsymbol{y}, z)\, v(\boldsymbol{q}; \boldsymbol{y}, z)\, , \tag{2.84}$$

where the tilde reminds the reader about this dependence. As seen in Section 2.2.2 for the broadening, the resummation of the radiation amplitude does not get modified due to the anisotropies of the matter, which enter the formalism when the medium averages are performed.

With the explicit form of the resummed amplitude describing the medium-induced branching, the final state gluon distribution can be defined as

$$2(2\pi)^3 \omega E \frac{d\mathcal{N}}{d\omega dE d^2k} \equiv \frac{1}{4\pi}\frac{1}{N_c} \sum \int \frac{d^2\boldsymbol{l}}{(2\pi)^2} \left\langle |\mathcal{R}|^2 \right\rangle . \tag{2.85}$$

Combining the fundamental Wilson lines for the quarks with the two $SU(N_c)$ generators to form an adjoint Wilson line, defined as

$$\mathcal{W}^{ab}(\boldsymbol{x}; z_f, z_i) \equiv \mathcal{P} \exp\left(i \int_{z_i}^{z_f} d\tau\, (T^c)^{ab}\, \tilde{v}^c(\boldsymbol{x}, \tau)\right) , \tag{2.86}$$

and using that the medium average of the in-medium color potentials at first order in gradients, given by (2.47), is local in the z-component and trivial in color, the final state gluon distribution can be written as

$$2(2\pi)^3\omega E\frac{d\mathcal{N}}{d\omega dEd^2k} = \lim_{z_f\to\infty}\frac{2\alpha_s C_F}{\omega^2}\Re\int_0^\infty d\bar{z}\int_0^{\bar{z}} dz\int_{\boldsymbol{x}_{in},\boldsymbol{y}} |J(E,\boldsymbol{x}_{in})|^2\Bigg[\boldsymbol{\nabla}_{\boldsymbol{x}}\cdot\boldsymbol{\nabla}_{\bar{\boldsymbol{x}}}$$

$$\times\, S_2\left(\boldsymbol{k},\boldsymbol{k},z_f;\boldsymbol{y},\bar{\boldsymbol{x}},\bar{z}\right)\mathcal{K}\left(\boldsymbol{y},\boldsymbol{x}_{in},\bar{z};\boldsymbol{x},\boldsymbol{x}_{in},z\right)\Bigg]\Bigg|_{\boldsymbol{x}=\bar{\boldsymbol{x}}=\boldsymbol{x}_{in}}\,, \tag{2.87}$$

where we have used that the final soft gluon distribution factorizes into two correlators, with the effect of the matter anisotropies entering each one of them independently. These two correlators are the emission kernel, $\mathcal{K}$, and a broadening kernel, S_2, which can be defined as

$$S_2\left(\boldsymbol{k},\boldsymbol{k},z_f;\boldsymbol{y},\bar{\boldsymbol{x}},\bar{z}\right) = \frac{1}{N_c^2-1}\left\langle\mathcal{G}^{bc}\left(\boldsymbol{k},z_f;\boldsymbol{y},\bar{z}\right)\mathcal{G}^{\dagger\,cb}\left(\boldsymbol{k},z_f;\bar{\boldsymbol{x}},\bar{z}\right)\right\rangle\,,$$

$$\mathcal{K}\left(\boldsymbol{y},\boldsymbol{x}_{in},\bar{z};\boldsymbol{x},\boldsymbol{x}_{in},z\right) = \frac{1}{N_c^2-1}\left\langle\mathcal{G}^{ba}\left(\boldsymbol{y},\bar{z};\boldsymbol{x},z\right)\mathcal{W}^{\dagger\,ab}(\boldsymbol{x}_{in};\bar{z},z)\right\rangle\,. \tag{2.88}$$

In order to obtain the final state gluon distribution, the latter correlators must be obtained. The broadening two-point function, S_2, has been previously derived in [111], computing the first order gradient corrections to the transverse momentum broadening, as reviewed in Section 2.2.2. On the other hand, the emission kernel can be expressed as the following path integral

$$\mathcal{K}\left(\boldsymbol{y},\boldsymbol{x}_{in},\bar{z};\boldsymbol{x},\boldsymbol{x}_{in},z\right) = \int_{\boldsymbol{x}}^{\boldsymbol{y}} D\mathbf{r}\, e^{i\frac{\omega}{2}\int d\tau\,\dot{\mathbf{r}}^2-\int_z^{\bar{z}} d\tau\,\left(1+\frac{\mathbf{r}(\tau)+\boldsymbol{x}_{in}}{2}\cdot\hat{\boldsymbol{g}}\right)\mathcal{V}(\mathbf{r}(\tau)-\boldsymbol{x}_{in})}\,, \tag{2.89}$$

where $\mathcal{V}(\boldsymbol{x})$ is given by the Fourier transform of (2.49). The radiative kernel, $\mathcal{K}$, has been previously computed in the homogenous case, see [61] for a review, and the first order gradient correction can be obtained by expanding the path integral around the homogeneous solution. Thus, with both correlators in hand –the interested reader is referred to [2] in Chapter 4 for the detailed calculation–, we take the broad source approximation setting $|J(E,\boldsymbol{x}_{in})|^2 = f(E)\delta^{(2)}(\boldsymbol{x}_{in})$, which simplifies $\mathcal{K}$ after integrating over $\boldsymbol{x}_{in}$, and allows us to relate the particle distribution to the medium-induced gluon spectrum following

$$(2\pi)^2\omega E\frac{dN}{d\omega dEd^2k} = (2\pi)^2\omega\frac{dI}{d\omega d^2\boldsymbol{k}}\,E\frac{dN_0}{dE}\,, \tag{2.90}$$

where $E\frac{dN_0}{dE} = \frac{1}{2(2\pi)}f(E)$.

To illustrate the results obtained in [2], let us assume that the effective scattering potential is quadratic, $\mathcal{V}(\boldsymbol{y}) = \frac{\hat{q}}{4}\boldsymbol{y}^2$, focusing on the so-called harmonic oscillator (HO)

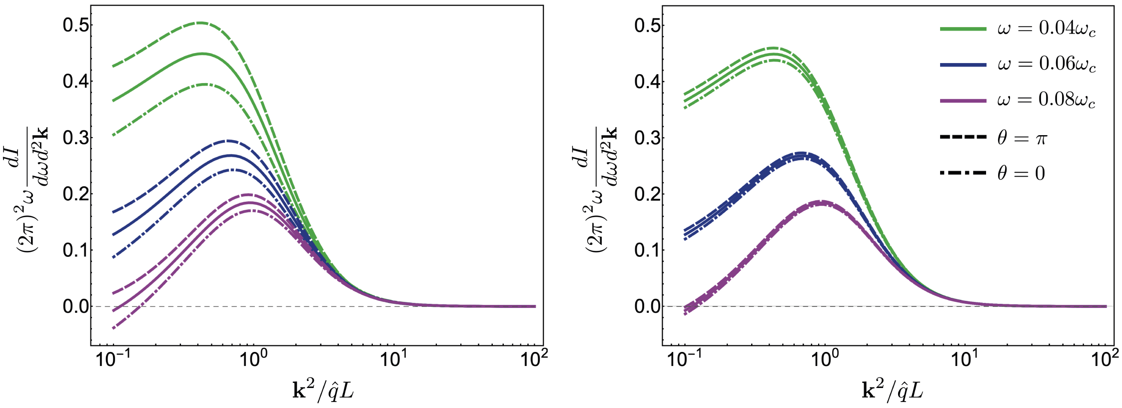

Figure 2.7: The medium-induced soft gluon spectrum is given for three gluon energies, $\omega = 0.04\,\omega_c$, $\omega = 0.06\,\omega_c$, and $\omega = 0.08\,\omega_c$. The solid lines denote the spectrum in the homogeneous limit. The dashed and dash-dotted lines correspond to the full spectrum with gradients along ($\theta = 0$) and opposite to ($\theta = \pi$) the direction of $\boldsymbol{k}$ respectively. The gradients are quantified with $\gamma_T = 0.05$ (left) and $\gamma_T = 0.01$ (right). This figure has been extracted from [2].

approximation, where the proportionality coefficient $\hat{q}$ is the jet quenching parameter, defined as $\hat{q} = \frac{\partial}{\partial L}\langle \boldsymbol{p}^2 \rangle$, and computed in Section 2.2 for various configurations of QCD matter. While this approximation simplifies the calculation, the analytic form of the medium-induced soft gluon spectrum remains quite involved. Consequently, we omit the analytic details here, referring the reader to [2] in Chapter 4, and we present a numerical analysis using phenomenologically relevant parameters to illustrate the key features of the spectrum. First, we define the medium to have $L = 5$ fm and $T = 0.3$ GeV, and assume that $\boldsymbol{\nabla} T \lesssim T^2$ for hydrodynamically evolving matter. The only parameter in the HO is $\hat{q}$, and its characteristic value can be chosen to be about $\hat{q} \simeq 1\,\mathrm{GeV}^2 \cdot \mathrm{fm}^{-1}$, see e.g. [125, 126, 127]. Assuming a naive scaling of $\hat{q}$, the gradient vector can be related to the gradient of temperature as $\boldsymbol{g} = 3\frac{\boldsymbol{\nabla} T}{T}$, that will be used for all our estimates. The angular dependence of the medium-induced soft gluon spectrum, controlled by $\boldsymbol{g} \cdot \boldsymbol{k}$, will be studied in the two limiting cases, when the angle between the two vectors, θ, is either 0 or π. The gluon frequencies will be measured with respect to the critical medium frequency $\omega_c \equiv \hat{q}L^2 \simeq 125$ GeV, which is the typical frequency for gluons with formation length of the order L in homogeneous matter. Finally, we will introduce the dimensionless gradient strength, defined as $\gamma_T = |\boldsymbol{\nabla} T/T^2|$.

In Figure 2.7, we show the full spectrum up to first order in gradient corrections for $\omega = 0.04\,\omega_c$, $\omega = 0.06\,\omega_c$, and $\omega = 0.08\,\omega_c$, differentiating for $\gamma_T = 0.05$ (left) and $\gamma_T = 0.01$ (right). For $\theta = 0$, the gradient effects suppress the gluon radiation at small values of $\boldsymbol{k}$, while when $\theta = \pi$, it is enhanced. One can notice that the gradient effects in Figure 2.7 become stronger for softer gluons, and may be substantial even for sufficiently small γ_T. This behavior is in line with the properties of the gradient effects in broadening [111], where the anisotropic contributions are suppressed by the energy of the leading parton. Since the energy of soft emitted gluons is smaller than the energy of the leading parton, the gradient effects become more important. However, one should notice, that very soft gluons lose their energy on shorter time scales, and the single gluon spectrum cannot describe the evolution of the system reliably in this case, since gluons that soft quickly thermalize inside the matter.

2.3.3 Medium-induced radiation in the glasma[6]

In this section, we review the main results obtained in [3], see Chapter 4. We derive the medium-induced radiation rate in the initial stages of HICs. Particularly, we focus on the effect of the highly anisotropic and correlated chromoelectric fields of the glasma stage on the radiation rate. This is done within the soft gluon approximation, i.e. with the gluon energy being much smaller than the quark energy, and with a full resummation of the number of scatterings with the matter. The calculation is performed at leading subeikonal order, keeping terms suppressed by one power of the gluon energy and enhanced by the medium length, while neglecting terms suppressed by powers of the quark energy. At this order of the eikonal expansion, the quark is treated as a scalar particle for simplicity, neglecting the energy-suppressed spin effects as discussed in the previous sections. Furthermore, since the matter is static, the calculation can be performed in the axial gauge, as discussed at the beginning of Section 2.3.

Applying the resummation strategy followed in Section 2.2.3 to the parton branching amplitude (2.74) –see [3] in Chapter 4 for further detail–, the resummed amplitude of parton branching inside the glasma reads, c.f. (2.83)

$$\begin{aligned} i\mathcal{R} \simeq -\frac{g}{\omega} \lim_{z_f\to\infty} \int_0^\infty dz_s \int_{\boldsymbol{x}_{in}} e^{-i\boldsymbol{x}_{in}\cdot\boldsymbol{l}} J(E,\boldsymbol{x}_{in}) \\ \times \mathcal{W}(\boldsymbol{x}_{in};\infty,z_s)\, t^a_{proj}\, \mathcal{W}(\boldsymbol{x}_{in};z_s,0)\; e^{i\frac{\boldsymbol{k}^2}{2\omega}z_f} \left[\boldsymbol{\epsilon}\cdot\boldsymbol{\nabla}_{\boldsymbol{x}_{in}} \mathcal{G}^{ba}\left(\boldsymbol{k},z_f;\boldsymbol{x}_{in},z_s\right)\right] , \end{aligned} \tag{2.91}$$

where $\boldsymbol{l}$ and $\boldsymbol{k}$ are the final transverse momenta of the quark and gluon respectively, E and ω are the energies of the quark and the gluon respectively, and $\boldsymbol{\epsilon}$ is the transverse polarization vector of the final state gluon. While the resummed amplitude expressed in terms of effective propagators has a form analogous to (2.83) from Section 2.3.2, the potential entering the propagators is different in each case. In the latter expression, the Wilson lines for the quark are given by (2.64), and the gluon propagator reads, c.f. (2.44)

$$\mathcal{G}(\boldsymbol{x}_f,L;\boldsymbol{x}_0,0) = \int_{\boldsymbol{x}_0}^{\boldsymbol{x}_f} \mathcal{D}\mathbf{r}\, \exp\left(i\frac{\omega}{2}\int_0^L d\tau\, \dot{\mathbf{r}}^2\right) \mathcal{P}\exp\left(i\int_0^L d\tau\, t^a\, \mathbf{r}(\tau)\cdot\boldsymbol{E}^a(\tau)\right) . \tag{2.92}$$

---

[6] This section presents an adapted summary and partial reproduction of content from [3], which forms part of this thesis and is detailed further in Chapter 4.

With the explicit form of the resummed amplitude of the medium-induced parton branching process, the final state gluon distribution is given by (2.85). Combining the Wilson lines in the fundamental representation with the two $SU(N_c)$ generators into an adjoint Wilson line, the final gluon state distribution can be written as

$$\begin{aligned} 2(2\pi)^3\omega E\frac{d\mathcal{N}}{d\omega dE d^2k} = \lim_{z_f\to\infty}\frac{\alpha_s}{N_c\omega^2}\Re\int_0^\infty d\bar{z}\int_0^{\bar{z}}dz\int_{\boldsymbol{x}_{in},\boldsymbol{y}}|J(E,\boldsymbol{x}_{in})|^2\Bigg[\boldsymbol{\nabla}_{\boldsymbol{x}}\cdot\boldsymbol{\nabla}_{\bar{\boldsymbol{x}}} \\ \times\left\langle\mathcal{G}^{\dagger,\bar{a}b}(\boldsymbol{k},L;\bar{\boldsymbol{x}},\bar{z})\mathcal{G}^{bc}(\boldsymbol{k},L;\boldsymbol{y},\bar{z})\,\mathcal{G}^{ca}(\boldsymbol{y},\bar{z};\boldsymbol{x},z)\mathcal{W}^{\dagger,a\bar{a}}(\boldsymbol{x}_{in};\bar{z},z)\right\rangle\Bigg]_{\boldsymbol{x}=\bar{\boldsymbol{x}}=\boldsymbol{x}_{in}}, \end{aligned} \tag{2.93}$$

where the spectrum cannot be split into two separate correlators as in (2.87) due to the finite correlation length of the medium averages in the glasma. Due to this, the calculation becomes more challenging than the one presented in Section 2.3.2, and, therefore, we focus solely on the radiation rate. To obtain the rate, we can integrate out the final transverse momentum of the gluon, which simplifies the calculation. Using the evolution equation of the gluon propagator, which can be obtained following the same strategy used in deriving (2.43), one can see that $\frac{\partial}{\partial L}\int_{\boldsymbol{k}}\mathcal{G}^{\dagger,\bar{a}b}(\boldsymbol{k},L;\bar{\boldsymbol{x}},\bar{z})\mathcal{G}^{bc}(\boldsymbol{k},L;\boldsymbol{y},\bar{z})=0$. Therefore, the contraction of the propagators integrated over the final transverse momenta reduces to

$$\int_{\boldsymbol{k}}\mathcal{G}^{\dagger,\bar{a}b}(\boldsymbol{k},L;\bar{\boldsymbol{x}},\bar{z})\mathcal{G}^{bc}(\boldsymbol{k},L;\boldsymbol{y},\bar{z}) = \delta^{(2)}(\bar{\boldsymbol{x}}-\boldsymbol{y})\,\delta^{\bar{a}c}\,, \tag{2.94}$$

which demonstrate that, after integrating over $\boldsymbol{k}$, the sensitivity to the gluon's broadening is lost. With this, the final state gluon distribution becomes

$$\begin{aligned} 2(2\pi)^3\omega E\frac{d\mathcal{N}}{d\omega dE} = \lim_{z_f\to\infty}\frac{\alpha_s}{N_c\omega^2}\Re\int_0^\infty d\bar{z}\int_0^{\bar{z}}dz\int_{\boldsymbol{x}_{in},\boldsymbol{y}}|J(E,\boldsymbol{x}_{in})|^2\Bigg[\boldsymbol{\nabla}_{\boldsymbol{x}}\cdot\boldsymbol{\nabla}_{\bar{\boldsymbol{x}}} \\ \times\left\langle\mathcal{G}^{\bar{a}a}(\boldsymbol{y},\bar{z};\boldsymbol{x},z)\mathcal{W}^{\dagger,a\bar{a}}(\boldsymbol{x}_{in};\bar{z},z)\right\rangle\Bigg]_{\boldsymbol{x}=\bar{\boldsymbol{x}}=\boldsymbol{x}_{in}}. \end{aligned} \tag{2.95}$$

Taking the broad source approximation setting $|J(E,\boldsymbol{x}_{in})|^2 = f(E)\delta^{(2)}(\boldsymbol{x}_{in})$, and introducing $E\frac{d\mathcal{N}^{(0)}}{dE} = \frac{1}{2(2\pi)}f(E)$, Eq. (2.95) can be factorized into the medium-induced radiation spectrum and the initial energy distribution of the leading quark following

$$\omega E\frac{d\mathcal{N}}{d\omega dE}\equiv\omega\frac{d\mathcal{I}}{d\omega}\,E\frac{d\mathcal{N}^{(0)}}{dE}\,.$$

Thus, defining the radiation rate as $\Gamma = \frac{d\mathcal{I}}{dt}$, with t being the distance travelled by the partons inside the medium, we get

$$\left\langle\frac{d\Gamma}{d\mathrm{x}}\right\rangle = \frac{2\alpha_s C_F}{\mathrm{x}\omega^2}\Re\int_0^t ds\,\boldsymbol{\nabla}_{\boldsymbol{x}}\cdot\boldsymbol{\nabla}_{\boldsymbol{y}}\,\langle\mathcal{K}(\boldsymbol{x},t;\boldsymbol{y},s)-\mathcal{K}_0(\boldsymbol{x},t;\boldsymbol{y},s)\rangle\Big|_{\boldsymbol{x}=\boldsymbol{y}=\boldsymbol{0}}\,, \tag{2.96}$$

where x $= \omega/E$ is the energy fraction of the emitted gluon with respect to the parent parton, and the angle brackets remind the reader that the averaging over different field configurations is being performed. We have also introduced the in-medium emission kernel, defined as, *c.f.* (2.88)

$$\mathcal{K}(\boldsymbol{x},t;\boldsymbol{y},s) \equiv \frac{1}{N_c^2-1}\,\mathcal{G}^{\bar{a}a}(\boldsymbol{x},t;\boldsymbol{y},s)\mathcal{W}^{\dagger,a\bar{a}}(\mathbf{0};t,s)\,, \tag{2.97}$$

and we have subtracted the emission kernel in the vacuum, $\mathcal{K}_0$, to get the radiation rate of the extra emissions induced by the medium. More explicitly, the radiation kernel can be expressed as a path integral, where the Wilson line accounts for the precession in the background field

$$\mathcal{K}(\boldsymbol{x},t;\boldsymbol{y},s) = \frac{1}{N_c^2-1}\int_{\boldsymbol{y}}^{\boldsymbol{x}}\mathcal{D}\mathbf{r}\,\exp\left(i\frac{\omega}{2}\int_s^t d\tau\,\dot{\mathbf{r}}^2\right)\,\mathrm{Tr}\,\mathcal{P}\exp\left(i\int_s^t d\tau\,T^c\,\mathbf{r}(\tau)\cdot\boldsymbol{E}^c(\tau)\right)\,, \tag{2.98}$$

with T^c being the $SU(N_c)$ generators in the adjoint representation.

The more complex averaging procedure in the glasma phase makes computing the averaged radiation rate considerably more challenging than in the QGP phase. Therefore, to illustrate the key features of medium-induced emissions during this stage, we begin with the simpler Abelian $U(1)$ case as a toy model before turning to the non-Abelian $SU(2)$ case.

Induced radiation for $U(1)$

Let us focus here on the $U(1)$ case. For Abelian fields, the color structure becomes trivial, with the radiation kernel being

$$\mathcal{K}_{\mathrm{U(1)}}(\boldsymbol{x},t;\boldsymbol{y},s) = \int\mathcal{D}\mathbf{r}\,\exp\left[i\int_s^t dt\,\left(\frac{\omega}{2}\dot{\boldsymbol{r}}^2+\boldsymbol{E}(\tau)\cdot\boldsymbol{r}(\tau)\right)\right]\,, \tag{2.99}$$

and the path integral can be straightforwardly evaluated, see e.g. [128],

$$\begin{aligned}\mathcal{K}_{\mathrm{U(1)}}(\boldsymbol{x},t;\boldsymbol{y},s) = \frac{\omega}{2\pi i(t-s)}\exp\Bigg\{ & i\frac{\omega}{2}\frac{(\boldsymbol{x}-\boldsymbol{y})^2}{t-s} \\ & + \frac{i}{(t-s)}\left(\boldsymbol{x}\cdot\int_s^t d\tau(\tau-s)\boldsymbol{E}(\tau)+\boldsymbol{y}\cdot\int_s^t d\tau(t-\tau)\boldsymbol{E}(\tau)\right) \\ & - \frac{i}{\omega(t-s)}\int_s^t d\tau\int_s^\tau d\bar{\tau}\,(t-\tau)(\bar{\tau}-s)\boldsymbol{E}(\bar{\tau})\cdot\boldsymbol{E}(\tau)\Bigg\}\,.\end{aligned} \tag{2.100}$$

This form of the kernel is valid for a general background field $\mathbf{E}(\tau)$, and we further focus on the piecewise case of our matter model.

The special case where emissions take place inside a single flux tube is particularly illustrative. For a single tube, the field $\mathbf{E}$ is constant, and the kernel is translationally invariant in the longitudinal direction, simplifying to

$$\mathcal{K}_{\mathrm{U}(1)}(\boldsymbol{x},t;\boldsymbol{y},0) = \frac{\omega}{2\pi i t}\exp\left\{ i\left(\frac{\omega}{2t}(\boldsymbol{x}-\boldsymbol{y})^2 + \frac{\boldsymbol{E}t}{2}\cdot(\boldsymbol{x}+\boldsymbol{y}) - \frac{\boldsymbol{E}^2}{24\omega}t^3 \right)\right\}. \tag{2.101}$$

Thus, one may readily write the medium-induced radiation rate for constant background field [129, 130, 131, 132] as

$$\frac{d\Gamma_{\mathrm{U}(1)}}{d\mathrm{x}} = \frac{2\alpha_s C_F}{\mathrm{x}\pi}\mathrm{Re}\int_0^t ds\,\frac{1}{s^2}\left(1-\left(1-i\frac{E^2 s^3}{8\omega}\right)e^{-i\frac{E^2 s^3}{24\omega}}\right). \tag{2.102}$$

This regime, corresponding to the field being constant during the emission process, is realized when the correlation length $l \sim 1/Q_s$ is longer than the formation time. Before averaging over the field configuration using Eq. (2.6), let us consider the rate in the given event for the case of a single flux tube. At earlier times, the rate in Eq. (2.102) grows as a power of the travelled distance: $\frac{d\Gamma_{\mathrm{U}(1)}}{d\mathrm{x}} \simeq \frac{7\alpha_s C_F}{24\mathrm{x}\pi}\frac{E^4}{\omega^2}\frac{t^5}{5!}$. At later times, it saturates, $\frac{d\Gamma_{\mathrm{U}(1)}}{d\mathrm{x}}\Big|_{t\to\infty} = 3^{1/6}\,\Gamma\left(\frac{2}{3}\right)\frac{\alpha_s C_F}{\mathrm{x}\pi}E^{2/3}\omega^{-1/3}$, after a characteristic time $t_{\mathrm{ch}} = (24\omega/E^2)^{1/3}$, which can be understood as the in-medium formation time.

We now examine the event-averaged results, considering the case of a single long tube. Averaging the emission kernel, Eq. (2.101), over multiple events, we get

$$\begin{aligned}&\left\langle \boldsymbol{\nabla}_{\boldsymbol{x}}\cdot\boldsymbol{\nabla}_{\boldsymbol{y}}\Big(\mathcal{K}_{\mathrm{U}(1)}(\boldsymbol{x},t;\boldsymbol{y},0)-\mathcal{K}_0(\boldsymbol{x},t;\boldsymbol{y},0)\Big)_{\boldsymbol{x}=\boldsymbol{y}=0}\right\rangle \\ &\qquad = \frac{\omega^2}{\pi t^2}\left[\frac{1}{\sqrt{i\frac{E_0^2 t^3}{24\omega}+1}}\left(-1+\frac{3}{2\left(1-i\frac{24\omega}{E_0^2 t^3}\right)}\right)+1\right],\end{aligned} \tag{2.103}$$

where the Gaussian integration in Eq. (2.6) has been performed explicitly. Then, the averaged rate of the medium-induced radiation is given by

$$\left\langle\frac{d\Gamma_{\mathrm{U}(1)}}{d\mathrm{x}}\right\rangle = \frac{2\alpha_s C_F}{\pi\mathrm{x}}\mathrm{Re}\int_0^t\frac{ds}{s^2}\left[\frac{1}{\sqrt{i\frac{E_0^2 s^3}{24\omega}+1}}\left(-1+\frac{3}{2\left(1-i\frac{24\omega}{E_0^2 s^3}\right)}\right)+1\right]. \tag{2.104}$$

Taking the same limits as before, one can see that at earlier times the averaged rate scales as $\left\langle\frac{d\Gamma_{\mathrm{U}(1)}}{d\mathrm{x}}\right\rangle \simeq \frac{7\alpha_s C_F}{32\mathrm{x}\pi}\frac{E_0^4}{\omega^2}\frac{t^5}{5!}$, while at later times it tends to

$$\left\langle\frac{d\Gamma_{\mathrm{U}(1)}}{d\mathrm{x}}\right\rangle\Big|_{t\to\infty} = 3^{1/6}\,\Gamma\left(\frac{2}{3}\right)\Gamma\left(\frac{5}{6}\right)\frac{\alpha_s C_F}{\mathrm{x}\pi^{3/2}}E_0^{2/3}\omega^{-1/3}.$$

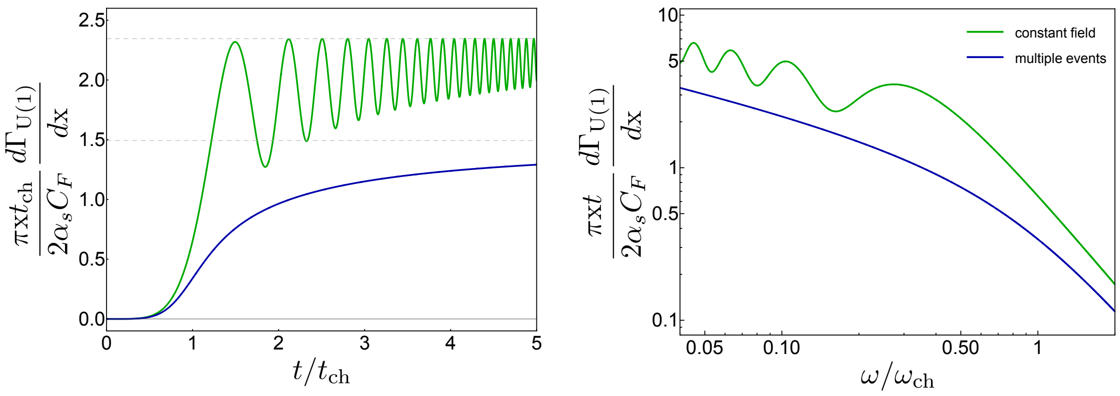

Figure 2.8: The rate of the medium-induced radiation for the background Abelian field is plotted for the constant field case (green) and Gaussian averaging over multiple events (blue), assuming a single long flux tube. Dashed lines indicate the corresponding asymptotic values. The characteristic time t_{ch} and the characteristic frequency ω_{ch} are defined with respect to E (green) and E_0 (blue). This figure has been extracted from [3].

All these characteristic features of the single flux tube case are summarized in Figure 2.8.

The structure of the rate is more involved for the more realistic case when the leading parton traverses multiple tubes. Redefining the characteristic time $t_{\mathrm{ch}} = (24\omega/E_0^2)^{1/3}$ with respect to E_0 of the averaging procedure in Eq. (2.6), one sees that the full multi-tube rate can be written simply as $t_{\mathrm{ch}}\frac{d\Gamma_{\mathrm{U}(1)}}{dx} = t_{\mathrm{ch}}\frac{d\Gamma_{\mathrm{U}(1)}}{dx}(t/t_{\mathrm{ch}}, \ell/t, \boldsymbol{E}_i/E_0)$. Averaging over the fields in each flux tube, the rate further simplifies, and its parametric dependence is captured by a single function $t_{\mathrm{ch}}\left\langle\frac{d\Gamma_{\mathrm{U}(1)}}{dx}\right\rangle = F(t/t_{\mathrm{ch}}, \ell/t)$, which depends solely on the ratios t/t_{ch} and ℓ/t. Finding analytic results for F quickly becomes unwieldy when ℓ/t is small, i.e. when the radiation occurs over multiple flux tubes, requiring multiple Gaussian integrals in the averaging procedure. However, with the explicit form of Eq. (2.100) in hand, one can readily evaluate any finite number of Gaussian integrations over the field in Eq. (2.6) numerically.

To illustrate the features of the spectrum, we present numerical results for $\left\langle\frac{d\Gamma_{\mathrm{U}(1)}}{dx}\right\rangle$ and $\left\langle\frac{d\Gamma_{\mathrm{U}(1)}}{dx}\right\rangle_{z_{in}}$ in Figure 2.9. We find that, while the leading parton is traversing the first tube, the rate follows the single-tube case. Upon crossing the border between two tubes, the rate experiences some destructive interference, falling after that point. However, propagating further within each given tube, the rate builds up resembling its behavior in the first tube. This series of oscillations of the rate continues, staying under the single-tube curve. The peaks of the rate occur at the edges of the tubes, as depicted in the left panel of Figure 2.9. If the starting position z_{in} within the first tube is varied, the rate curve gets

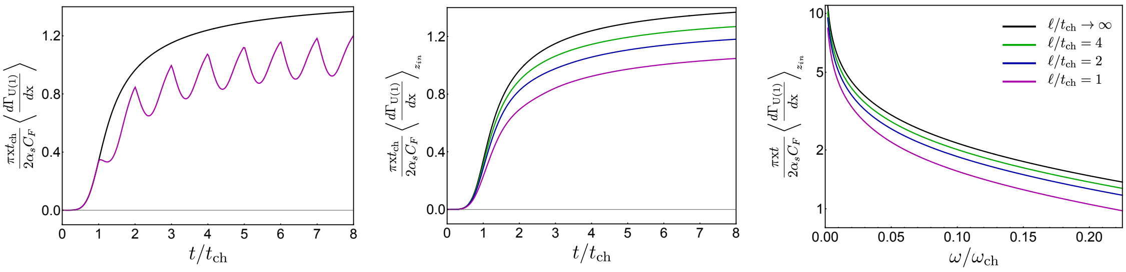

Figure 2.9: An illustration of the U(1) averaged rate. The left panel gives $\frac{\pi \mathrm{x}}{2\alpha_s C_f} t_{\mathrm{ch}} \left\langle \frac{d\Gamma_{\mathrm{U(1)}}}{dx} \right\rangle$ with the leading parton starting from the edge of the first tube $z_{in} = 0$. The middle and right panels depict $\frac{\pi \mathrm{x}}{2\alpha_s C_f} t_{\mathrm{ch}} \left\langle \frac{d\Gamma_{\mathrm{U(1)}}}{dx} \right\rangle_{z_{in}}$ and $\frac{\pi x}{2\alpha_s C_f} t \left\langle \frac{d\Gamma_{\mathrm{U(1)}}}{dx} \right\rangle_{z_{in}}$ averaged over the starting position within the first tube. The colors correspond to the rate evaluated for different tube sizes, including the long tube limit (black), which appears in all three panels and is given by Eq. (2.104). This figure has been extracted from [3].

modified, yet the overall pattern remains the same with the minima and peaks shifted. Averaging over the initial position of the leading parton in the first flux tube, we see that the series of minima and peaks is smeared, and the rate takes a shape similar to the constant field case. The greater the number of tubes traversed by the leading parton by the given t/t_{ch} the lower the averaged rate at that given point, and the curves for different ℓ/t_{ch} appear to be ordered, as depicted in the middle panel of Figure 2.9. Finally, we find it instructive to plot the rate $t \left\langle \frac{d\Gamma_{\mathrm{U(1)}}}{dx} \right\rangle_{z_{in}}$ as a function of frequency $\omega/\omega_{\mathrm{ch}}$, as shown in the right panel of Figure 2.9, where the curves are ordered in the same way. Notice that the averaged rate as a function of $\omega/\omega_{\mathrm{ch}}$ is independent of the particular position of measurement t when scaled with it.

The ordering of the rate curves can also be understood at the level of the broadening pattern. Indeed, in the case of shorter flux tubes, accumulating transverse momentum is harder, as the fields in different tubes can oppose each other. This results in a longer in-medium formation time for the emission process, leading to a lower rate. This effect becomes stronger the shorter the tubes are, reducing the rate further. It is moreover particularly important at larger measurement times t/t_{ch}, when the system has had sufficient time to propagate through multiple flux tubes, and at higher energies, where the formation time is longer and, thus, more flux tubes are traversed during the radiation process. One should keep in mind that t_{ch} is independent of the number of flux tubes, but the physical in-medium formation time does depend on ℓ. In the case of constant field, corresponding to large ℓ, the two times coincide, but in general it is not the case.

Induced radiation for $SU(2)$

In our model, characterized by a piecewise field, the path ordered exponential can be expressed as an ordered product of simple matrix exponentials. Each of these matrix exponentials can be expanded, and, using the Taylor series of sine and cosine along with the properties of the $SU(2)$ generators, one finds that the Wilson line within one tube is

$$\begin{aligned}\mathcal{W}^{ab}_{\mathrm{SU}(2)}(\mathbf{r}; z_i, z_{i-1}) &= \exp\left[\epsilon^{abc}\, E_i^c r\ell\right] \\ &= \delta^{ab}\cos\left(E_i r\ell\right) + 2\frac{E_i^a E_i^b}{E_i^2}\sin^2\left(\frac{1}{2}E_i r\ell\right) + \epsilon^{abc}\frac{E_i^c}{E_i}\sin\left(E_i r\ell\right), \qquad (2.105)\end{aligned}$$

where $E_i = \sqrt{E_i^a E_i^a}$, and $\mathbf{r}$ is the position of the Wilson line on the transverse plane. The structure constants of the $SU(2)$ group are given by the Levi-Civita tensor, ϵ^{abc}, and we have chosen a frame in the transverse plane such that the field only has one component, as described in Section 2.2.3. Averaging the rate over the orientation of the fields in the color space, one may notice that each such term can be treated independently. Indeed,

$$\left\langle \tilde{\mathcal{W}}^{ab}_{\mathrm{SU}(2)}(\mathbf{r}; z_i, z_{i-1})\right\rangle = \left\langle \frac{1}{3}\delta^{ab}\left\{2\cos\left(E_i\int_{z_{i-1}}^{z_i} r_x(\tau)d\tau\right)+1\right\}\right\rangle \qquad (2.106)$$

while for the first and last flux tubes, the limits should be adjusted accordingly. Consequently, all the color structures in the kernel become trivial, and we can express the $SU(2)$ kernel as a convolution of $U(1)$ kernels before averaging the full expression over E_i.

To illustrate the procedure, let us first focus on the case of a single flux tube. Then, we can express the full $SU(2)$ kernel as

$$\left\langle \mathcal{K}_{\mathrm{SU}(2)}(\boldsymbol{x},t;\boldsymbol{y},0)\right\rangle = \frac{1}{3}\left\langle \mathcal{K}_{+}(\boldsymbol{x},t;\boldsymbol{y},0) + \mathcal{K}_{-}(\boldsymbol{x},t;\boldsymbol{y},0) + \mathcal{K}_{0}(\boldsymbol{x},t;\boldsymbol{y},0)\right\rangle_{\mathrm{SU}(2)}, \qquad (2.107)$$

where $\mathcal{K}_+$, $\mathcal{K}_-$, and $\mathcal{K}_0$ are the $U(1)$ kernels for a single flux tube with electric field E, $-E$, and $E = 0$ respectively, with $E > 0$ since the absolute value has been taken in the color space. However, one should notice that the averaging in Eq. (2.107) is for the $SU(2)$ field strength E, and the residual radial integral $\int_0^\infty \frac{4\pi E^2 dE}{\pi^{3/2}E_0^3}$ incorporates a Jacobian from the full color averaging. Therefore, we keep the corresponding subscript on the averaging to indicate that point. Noticing that the expression in Eq. (2.107) is even under $E \to -E$, one may further write

$$\left\langle \mathcal{K}_{+}(\boldsymbol{x},t;\boldsymbol{y},0) + \mathcal{K}_{-}(\boldsymbol{x},t;\boldsymbol{y},0)\right\rangle_{SU(2)} = \frac{4}{E_0^2}\left\langle E^2\,\mathcal{K}_{+}(\boldsymbol{x},t;\boldsymbol{y},0)\right\rangle_{\mathrm{U}(1)}, \qquad (2.108)$$

where the E-integration in the r.h.s. runs from $-\infty$ to ∞. In what follows, we will omit the $U(1)$ subscript in the average of $\mathcal{K}_\pm$. Then, the averaged $SU(2)$ radiation rate for the case of a single flux tube can be explicitly written as

$$\left\langle \frac{d\Gamma_{\mathrm{SU(2)}}}{d\mathrm{x}} \right\rangle = \frac{4\alpha_s C_F}{3\mathrm{x}\omega^2}\mathrm{Re}\int_0^t ds\, \boldsymbol{\nabla}_{\boldsymbol{x}} \cdot \boldsymbol{\nabla}_{\boldsymbol{y}} \left(\frac{2}{E_0^2} \left\langle E^2 \mathcal{K}_+(\boldsymbol{x}, t; \boldsymbol{y}, s) \right\rangle - \mathcal{K}_0(\boldsymbol{x}, t; \boldsymbol{y}, s) \right)_{\boldsymbol{x}=\boldsymbol{y}=0}$$

$$= \frac{4\alpha_s C_F}{3\pi \mathrm{x}}\mathrm{Re}\int_0^t \frac{ds}{s^2} \left(\frac{1}{\left(i\frac{E_0^2 s^3}{24\omega} + 1 \right)^{\frac{3}{2}}} \left(-1 + \frac{9}{2\left(1 - i\frac{24\omega}{E_0^2 s^3} \right)} \right) + 1 \right) . \qquad (2.109)$$

Similarly to the $U(1)$ case, in the early time limit $\frac{d\Gamma_{\mathrm{SU(2)}}}{dx} \sim t^5$, while at later times it scales with the inverse of the characteristic time $\left\langle \frac{d\Gamma_{\mathrm{SU(2)}}}{dx} \right\rangle \big|_{t\to\infty} \sim 1/t_{\mathrm{ch}}$.

With this simplification of the color structure of the averaged kernel, the case of multiple flux tubes can be treated in the same way as in the $U(1)$ case. For instance, for $t < 2\ell$ we can readily write

$$\left\langle \frac{d\Gamma_{\mathrm{SU(2)}}}{dx} \right\rangle = \frac{2\alpha_s C_F}{\mathrm{x}\omega^2}\mathrm{Re}\int_0^t ds\, \boldsymbol{\nabla}_{\boldsymbol{x}} \cdot \boldsymbol{\nabla}_{\boldsymbol{y}} \Big[(\theta(\ell - t) + \theta(s - \ell)) \left\langle \mathcal{K}^{(1)}_{\mathrm{SU(2)}}(\boldsymbol{x}, t; \boldsymbol{y}, s) \right\rangle$$

$$+ \theta(t-\ell)\theta(\ell - s) \int_{\boldsymbol{w}} \left\langle \mathcal{K}^{(1)}_{\mathrm{SU(2)}}(\boldsymbol{x}, t; \boldsymbol{w}, \ell) \right\rangle \left\langle \mathcal{K}^{(1)}_{\mathrm{SU(2)}}(\boldsymbol{w}, \ell; \boldsymbol{y}, s) \right\rangle - \mathcal{K}_0(\boldsymbol{x}, t; \boldsymbol{y}, s) \Big]_{\boldsymbol{x}=\boldsymbol{y}=0} , \qquad (2.110)$$

where all the averagings run over $SU(2)$ fields, and the superscript indicates that the particular kernels are taken for the single tube case as given by Eq. (2.107). Thus, obtaining the $SU(2)$ kernel for a few tubes in a closed analytical form is sufficiently straightforward. However, the Gaussian integrals of the averaging procedure still need to be treated numerically. Additionally, the need for the integrations over the intermediate transverse positions at the edges of the tubes complicates the numerical calculations, and we focus on a smaller number of tubes. Following the logic of the previous subsection, we present the numerical results for $\left\langle \frac{d\Gamma_{\mathrm{SU(2)}}}{dx} \right\rangle$ and $\left\langle \frac{d\Gamma_{\mathrm{SU(2)}}}{dx} \right\rangle_{z_{in}}$ in Figure 2.10. As previously, the rate follows the constant field case within the first tube, experiencing some destructive interference at the edges and growing within the tubes. However, in contrast with the case of $U(1)$, the $SU(2)$ rate may grow somewhat faster and seems to approach the constant field curve from the above, see the left panel of Figure 2.10. This behaviour is featured by longer tubes, while for the shorter tubes, the rate tends to stay under the constant field curve (at least within the range of times accessible in our numerics). Varying the starting position z_{in} within the first tube at a fixed tube size and averaging the rate, we find that the suppression still dominates, see the middle and right panels of Figure 2.10, which show the dependence of the rate on t/t_{ch} and $\omega/\omega_{\mathrm{ch}}$ correspondingly. Thus, we find the physical picture to be sufficiently similar to the $U(1)$ case: as the size of the flux tubes l/t_{ch} decreases, there is more destructive interference, the in-medium formation time is longer, and the rate goes down.

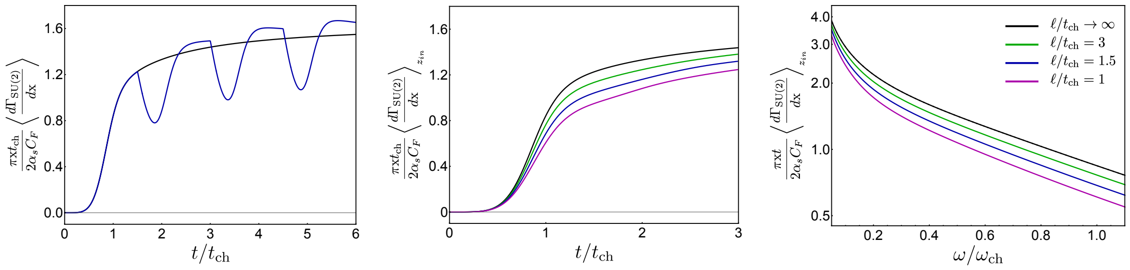

Figure 2.10: An illustration of the averaged $SU(2)$ rate. The left panel gives $\frac{\pi x}{2\alpha_s C_f} t_{\rm ch}\left\langle\frac{d\Gamma_{\rm SU(2)}}{dx}\right\rangle$ with the leading parton starting from the edge of the first tube $z_{in}=0$. The middle and right panels depict $\frac{\pi x}{2\alpha_s C_f} t_{\rm ch}\left\langle\frac{d\Gamma_{\rm SU(2)}}{dx}\right\rangle_{z_{in}}$ and $\frac{\pi x}{2\alpha_s C_f} t\left\langle\frac{d\Gamma_{\rm SU(2)}}{dx}\right\rangle_{z_{in}}$ averaged over the starting position within the first tube. The colors correspond to the rate evaluated for different tube sizes, including the long tube limit (black), which appears in all three panels and is given by Eq. (2.109). This figure has been extracted from [3].

3

Conclusions

"It is not knowledge, but the act of learning,
not possession but the act of getting there,
which grants the greatest enjoyment."

Carl Friedrich Gauss

This thesis has introduced a novel theoretical framework for understanding jet quenching, addressing the role of the matter evolution and its anisotropies. After reviewing the foundational concepts and placing it in context in Chapter 1, we revisit the derivation of the formalism in Chapter 2, examining the fundamentals of jet quenching theory, and discussing the key results presented in Chapter 4, also published in [1, 2, 3]. These three papers contribute to the development of this novel analytic tool by addressing three specific objectives. Paper [1] presents the calculation of the leading corrections to jet broadening and the spectrum of medium-induced radiated gluons, considering the interplay between flow and hydrodynamic gradients within a dilute QCD medium. In [2], we compute the spectrum of gluons sourced by the branching of an energetic quark in a dense, anisotropic QCD medium. Finally, paper [3] computes the broadening, medium-induced radiation and energy loss rate of jets traversing the glasma formed in the initial stages of HICs. Let us now present the main conclusions of each work.

Paper [1] studies the mutual effect of the transverse flow and matter gradients on jet momentum broadening and in-medium branching processes. We have derived the momentum broadening distribution up to first order in gradients, including the gradients of the longitudinal and transverse flow velocities, and keeping the leading subeikonal corrections for the first time. We have also evaluated the leading gradient corrections to the medium-induced gluon spectrum in the full kinematics. As we have shown, the interplay of the flow and gradient effects results in the leading modification of the final parton distributions and their moments. For instance, the jet quenching parameter $\hat{q}$ is rescaled by an overall factor (2.33), which may substantially modify its value in the homogeneous static limit. Indeed, let us focus on the contribution proportional to the gradient of the source density $\boldsymbol{\nabla}\rho$. Assuming that $\rho \sim T^3$, we set $\hat{\boldsymbol{g}} = 3\frac{\boldsymbol{\nabla}T}{T}$. In the hydrodynamic phase, one expects that $LT \gg 1$ with $\frac{\boldsymbol{\nabla}T}{T^2} \ll 1$, but the change in the matter properties over the matter size is not required to be small $\frac{L\boldsymbol{\nabla}T}{T} \sim 1$. Thus, for relativistic velocities $\frac{|\boldsymbol{u}|}{1-u_z} \sim 1$, our crude estimate indicates that the modification in $\hat{q}$ can be as large as the leading contribution. For instance, taking the same moderate estimates for the transverse flow and temperature gradients as for $L = 5\,\text{fm}$ curve in Figure 2.6, one readily finds that $\frac{\hat{q}}{\hat{q}_0} \simeq 0.775$. Regarding the medium-induced radiation, we compute the branching distribution at first order in gradients within static matter, keeping the leading subeikonal corrections, and in the full gluon kinematics. The obtained distribution, given by (2.78), can be compared with the results of [2] under the soft gluon approximation, and, after some algebra, one can show that (2.79) precisely agrees with the $N = 1$ part of the small-x resummed parton distribution. We also obtain the leading flow-gradient effects in the eikonal limit for the full gluon kinematics, which results in a multiplicative modification of the radiation rate and, consequently, in a modification of the induced radiative energy loss (2.80).

In [2], we have derived the double differential medium-induced soft gluon spectrum in a dense static transversely inhomogeneous medium with finite longitudinal extension. The spectrum is obtained within the hydrodynamic gradient expansion up to the leading first order. As explained for the broadening in Chapter 2, the gradient effects only enter the final distribution upon averaging over the stochastic background field configurations. In addition to deriving the general form of the spectrum, we have considered its behavior for quadratic $\mathcal{V}(\boldsymbol{y})$, in the so-called harmonic approximation, evaluating the path integrals explicitly. In this regime, the full spectrum can be written in a form suitable for numerical simulations, and its structure results in no additional computational complications, comparing to the homogeneous case. The soft gluon spectrum is evaluated and presented in Figure 2.7. The medium gradients distort the softer part of the jet substructure, while the harder radiation is less sensitive to the underlying medium structure. The spectrum is depleted for the transverse gradient vector $\boldsymbol{g}$ parallel with $\boldsymbol{k}$, and enhanced for the opposite situation, for most of the phase space. However, there are parametric regions, where the ordering is modified, and the spectrum is enhanced for $\boldsymbol{k}$ parallel with $\boldsymbol{g}$. Thus, we find that the medium-induced soft gluons are preferably emitted along the temperature gradient, but the particular direction depends on the region of the gluon phase space.

In [3], we develop a formalism to describe jet quenching during the early times of HICs, when the medium is dominated by strong color fields. Throughout our considerations, we have relied on a simplified matter model that captures the main features of this glasma phase. In particular, we have assumed that the matter is made up of color domains with chromoelectric fields confined in transversely infinite slabs aligned with the beam axis. The field is homogeneous and constant within any given slab, and varies independently in different domains on an event-by-event basis. Thus, we relax several assumptions that are ubiquitous in most of the jet quenching considerations. First, we go beyond the approximation of local field correlations widely used in the jet quenching claculations in the quark-gluon plasma context, and assume a finite correlation length. This is also in contrast with the constant (slowly-varying) field limit employed in considerations of the synchrotron-like radiation of energetic partons. Second, we consider the event-by-event fluctuations of the glasma background and its interplay with the jet physics, providing a starting point for jet tomography of the early stages of heavy-ion collisions. With this, we start by calculating the transverse momentum broadening of jet partons for both SU(2) and SU(3) backgrounds, investigating how the results depend on the size of the color domains ℓ. The jet quenching parameter for a jet parton traversing the given flux tube increases with time. Conversely, for a jet parton traversing many small flux tubes, the stochastic kicks it receives average out, leading to a constant rate of broadening. We further focus on the medium-induced radiation in the glasma background, restricting our consideration to the emission rate in the soft gluon limit. Most of our results are obtained for a SU(2) background, where the model can be treated semi-analytically, and compared with the toy consideration for the U(1) case. The behavior of the rate can be understood by comparing the relevant timescales of the problem. When a single flux tube is longer than the formation time for gluon emission, the resulting rate reproduces the well-known form for synchrotron radiation in a constant field. Considering the characteristic energy scales for the saturation and jet quenching processes in HICs, one may expect this regime to be relevant only for very soft emissions. At higher energies, the partons traverse multiple flux tubes during the emission process. This leads to an intricate interplay between different flux tubes, due to both momentum kicks in different directions and color decoherence between flux tubes. The net result is a reduction in the rate when the flux tubes are smaller, which is especially pronounced for higher gluon energies or at later times.

The work presented in this thesis makes only the first steps along the discussion of jet-medium interaction in evolving anisotropic matter, and the results could and should be extended in multiple ways. For instance, obtaining the leading flow-gradient effects in the dense matter limit, resumming multiple interactions with the medium, extending the calculations beyond the first order in the gradient expansion, and improving the matter models to make them more and more realistic. In addition, the presented work should be further included into phenomenological considerations of particular observables. For example, the possible substantial modification in $\hat{q}$ and the energy loss rate can considerably affect the existing simulations of jets interacting with evolving backgrounds, see e.g. [106, 133, 134, 135, 136, 137, 138, 139]. Moreover, the directional effects obtained in the QGP phase strongly distort the softer jet components, leaving harder radiation relatively less affected, and making the jet substructure a highly sensitive tomographic tool. Therefore, studying modifications to jet substructure observables, such as collinear energy-energy correlators or the v_n within jets, due to matter evolution and anisotropies is essential to unravel the properties of the jet-matter interactions. See Refs. [116, 140, 141] for recent attempts on studying these effects on jet substructure observables. Another promising direction would be to combine our approach for jet quenching in the early stages of HICs with realistic numerical simulations of the glasma. This would allow us to compute the medium-induced soft gluon rate, similarly to the previous studies on single particle momentum broadening [108, 142, 143]. In particular, such an exercise would help determine if the early time evolution of jets is indeed described by a multiple scattering picture, in the style of the BDMPS-Z formalism.

4

Published Results

Article I

Jet quenching in anisotropic flowing matter

Authors

Matvey V. Kuzmin[1,2], Xoán Mayo López[3],

Jared Reiten[4,5], Andrey V. Sadofyev[3,6]

(1) NRC Kurchatov Institute, Moscow 123182, Russia
(2) Faculty of Physics, Moscow State University, Moscow 119991, Russia
(3) Instituto Galego de Física de Altas Enerxías, Universidade de Santiago de Compostela, Santiago de Compostela 15782, Galicia, Spain
(4) Department of Physics and Astronomy, University of California, Los Angeles, California 90095, USA
(5) Mani L. Bhaumik Institute for Theoretical Physics, University of California, Los Angeles, California 90095, USA
(6) LIP, Avenida Professor Gama Pinto, 2, P-1649-003 Lisboa, Portugal

PhD Student Contribution

Independently derived the presented calculations and collaborated equally on the discussions and writing

Journal and Article Information

Journal name: Physical Review D
Publisher: American Physical Society
ISSN: 2470-0029
Year of publication: 2024
DOI: 10.1103/PhysRevD.109.014036
Impact factor in 2023: 4.6
CiteScore in 2023: 9.3
Quartile and decile in 2023: Q1 and D1

PHYSICAL REVIEW D **109,** 014036 (2024)

Jet quenching in anisotropic flowing matter

Matvey V. Kuzmin,[1,2,*] Xoán Mayo López,[3,†] Jared Reiten,[4,5,‡] and Andrey V. Sadofyev[3,6,§]
[1]*NRC Kurchatov Institute, Moscow 123182, Russia*
[2]*Faculty of Physics, Moscow State University, Moscow 119991, Russia*
[3]*Instituto Galego de Física de Altas Enerxías, Universidade de Santiago de Compostela,*
Santiago de Compostela 15782, Galicia, Spain
[4]*Department of Physics and Astronomy, University of California, Los Angeles, California 90095, USA*
[5]*Mani L. Bhaumik Institute for Theoretical Physics, University of California,*
Los Angeles, California 90095, USA
[6]*LIP, Avenida Professor Gama Pinto, 2, P-1649-003 Lisboa, Portugal*

(Received 15 September 2023; accepted 17 December 2023; published 29 January 2024)

We study the interplay between the flow and hydrodynamic gradients in jet quenching at first order in opacity. We find that the mixed flow-gradient contributions in jet quenching are enhanced by the medium length and survive in the eikonal limit, dominating over other medium evolution effects. The resulting modification to the jet quenching parameter and energy loss rate can be substantial, leading to ample phenomenological implications. We also compute the leading corrections to the jet broadening due to the flow velocity gradients and consider the leading gradient effects in the medium-induced branching for general kinematics, extending the recent considerations of jets in inhomogeneous media. These results can be straightforwardly coupled to matter simulations, providing new opportunities for jet tomography in heavy-ion collisions.

DOI: 10.1103/PhysRevD.109.014036

I. INTRODUCTION

In-medium energy loss and the related suppression of energetic partons provide primary evidence for the formation of collective matter in heavy-ion collisions (HICs); for a review see, e.g., [1–3]. Jets formed through the branching of such energetic partons interact with the resulting matter across multiple length scales and are sensitive to the details of the medium evolution. Thus, the medium-induced modification of jets can be used for imaging of the quark-gluon plasma (QGP) created in HICs, laying the foundation of so-called jet tomography; see, e.g., [4–12] and references therein.

Describing the interaction of energetic partons with the medium within the framework of perturbative QCD, one typically characterizes the matter with a collective background color field; see, e.g., [13–20]. Partons are then deflected by the matter field and lose energy in the process, mainly through gluon bremsstrahlung. The matter field is inherently stochastic, and hence all observables should be averaged over its possible configurations. The resulting formalisms are usually treated under multiple simplifying assumptions, such as the eikonal approximation (the limit of infinitely energetic leading parton) or the limit of static, transversely[1] homogeneous matter. Consequently, the description of jet quenching decouples from the evolution and structure of the matter (especially in the transverse directions); see the discussion in [21].

There have been multiple attempts to extend the theoretical approaches to jet quenching by including medium evolution effects with minimal modifications: from taking matter dilution into account [22–24] or using basic kinematic arguments [25–27], to treating the transverse flow within phenomenologically motivated models [28,29]. More recently, the theory of jet-matter interactions has been extended to the case of an evolving medium, including the effects of flow [21,30–32] and anisotropies [21,30,33–44]. In these works, flow- and anisotropy-induced effects are considered separately. However, such considerations already allow one to probe the coupling of jets with a variety of features of the medium evolution.

---

[*] kuzmin.mv19@physics.msu.ru
[†] xoan.mayo.lopez@usc.es
[‡] jdreiten@physics.ucla.edu
[§] andrey.sadofyev@usc.es

[1] The longitudinal/transverse directions are defined with respect to the momentum of the leading parton.

In this work, we focus on the interplay between the effects of flow and anisotropy in jet quenching calculations. Following [21], we work within the opacity expansion and consider jet momentum broadening and medium-induced gluon radiation in an anisotropic flowing matter. First, we extend the formalism developed in [21], where the structure of matter is treated within a gradient expansion.[2] In [21], the gradient effects are considered only for momentum broadening and in the absence of flow or flow velocity gradients. Here, we start by including the effects of all hydrodynamic gradients at first order in the gradient expansion into the jet momentum broadening consideration, going beyond the discussion in [21,37]. Next, we derive the leading gradient corrections to medium-induced gluon radiation for general kinematics, extending the results available in the literature, cf. [21,43]. Finally, we show that the mixed flow-gradient contributions modify the final-state parton distributions already in the eikonal limit, and, moreover, these terms are additionally enhanced by the medium length. Thus, they dominate over other medium evolution effects. As a simple illustration of the effect of these mixed terms, we show that the jet quenching parameter in flowing anisotropic matter reads

$$\hat{q}(z) = \left[1 - z\hat{\boldsymbol{g}}\cdot\frac{\boldsymbol{u}}{1-u_z}\right]\hat{q}_0(z),$$

where z is the path length of the energetic parton, the transverse gradients are compactly introduced with $\hat{\boldsymbol{g}}_\alpha \equiv \left(\boldsymbol{\nabla}_\alpha T\frac{\delta}{\delta T} + \boldsymbol{\nabla}_\alpha u_z\frac{\delta}{\delta u_z} + \boldsymbol{\nabla}_\alpha \boldsymbol{u}_\beta\frac{\delta}{\delta \boldsymbol{u}_\beta}\right)$, where T is the temperature, $\boldsymbol{u}$ and u_z are the transverse and longitudinal velocity components, $\hat{q}_0$ is the jet quenching parameter of a static homogeneous matter with the same local properties, and all these objects should be understood as functions of z. We argue that such modifications in jet quenching calculations can be substantial for characteristic evolution of the QGP in HICs.

II. MOMENTUM BROADENING

In this work, we study the broadening and medium-induced radiation pattern of a highly energetic parton interacting with nuclear matter within opacity expansion, closely following the formalism developed in [21,32,37,39,43]. Before turning to particular processes, let us first specify the details of the setup used in this work. Here, we will ignore the energy-suppressed spin effects and work with scalar particles in the fundamental representation. In contrast to [21], where the medium-induced emission in flowing matter is studied in the case of a scalar “gluon,” we focus on the emission of actual spin-1 gluons of the underlying gauge theory—see, e.g., [43] for a discussion.

The matter is modeled by a classical stochastic color field generated by moving massive quasiparticle sources, neglecting their recoil. This background field can be written as

$$gA^{a\mu}_{\mathrm{ext}}(q) = \sum_i u_i^\mu e^{-i(\boldsymbol{q}\cdot\boldsymbol{x}_i+q_z z_i)} t_i^a v_i(q)(2\pi) \times \delta(q_0 - \boldsymbol{q}\cdot\boldsymbol{u}_i - q_z u_{zi}), \tag{1}$$

where $u_\mu = (1, \boldsymbol{u}, u_z)$ is the nonrelativistic velocity (i.e., it is the four-velocity with the relativistic γ factor removed), $v_i(q)$ is the single-source potential, t_i^a controls the color of the given source, $(\boldsymbol{x}_i, z_i)$ are the spatial coordinates of the ith source, and the sum runs over all the sources in the medium, while the matter properties can change from point to point. We will use compact notation—suppressing the i subscript—where doing so leads to no confusion.

The particular scattering potential $v(q)$ is model dependent and there exist multiple choices in the literature; see, e.g., the discussion in [21,31] Throughout this paper, we will use the Gyulassy-Wang (GW) model to make results more explicit, although generalization is straightforward. The corresponding potential reads

$$v_i(q) = \frac{g^2}{q^2 - \mu_i^2}, \tag{2}$$

where g is the effective strong coupling inside the medium, and μ_i is the Debye mass at the position of the given source.

Finally, one must specify how the final distributions are averaged over configurations of the background field, fixing the structure of multipoint stochastic correlators. Following [21], we assume the color fields to have Gaussian statistics, taking only pairwise averages into account and enforcing color neutrality, as it is often used in perturbative QCD calculations. The averaging over color sources then results in

$$\langle t_i^a t_j^b\rangle = \frac{1}{2C_{\bar{R}}}\delta_{ij}\delta^{ab}, \tag{3}$$

where $C_{\bar{R}}$ is the quadratic Casimir in the representation opposite to the representation of the color sources. Here, we will assume that all the sources are in the same fundamental representation, setting $C_{\bar{R}} = N_c$.

In this section, we further derive the gradient correction to the momentum broadening distribution within flowing, anisotropic QCD matter to first order in opacity, going beyond the discussion in [21]. We focus particularly on the interplay between velocity corrections and spatial gradients in the matter variables at first subleading order, neglecting anything suppressed by two or more powers of the initial energy. At first order in opacity $N = 1$, up to two interactions in the amplitude squared, there are two types of contributions to take into account: the single Born (SB)

---

[2] See also [45–49] for other applications of the gradient expansion to probe-matter interactions.

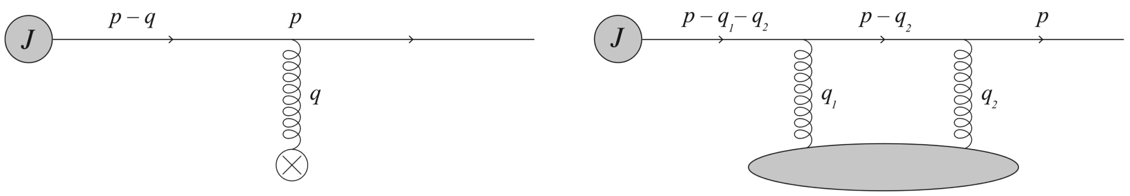

FIG. 1. The single Born amplitude M_1 (left) and the double Born amplitude M_2 (right) for transverse-momentum broadening.

contribution M_1 and the double Born (DB) contribution M_2, see Fig. 1. Using this decomposition of the amplitude and omitting the terms whose average vanishes, we can write its square as

$$\langle |M_{N=1}|^2\rangle = \langle |M_1|^2\rangle + \langle M_2 M_0^*\rangle + \langle M_2^* M_0\rangle, \tag{4}$$

where M_0 corresponds to vacuum propagation.

A. Single Born contribution

We start by considering the SB contribution to the broadening of an energetic (scalar) quark. The corresponding $N=1$ amplitude reads

$$\begin{aligned} iM_1 &= \int \frac{d^4q}{(2\pi)^4}[it^a_{\rm proj}(2p-q)_\mu A^{a\mu}_{\rm ext}(q)]\left[\frac{i}{(p-q)^2+i\epsilon}\right]J(p-q)\\ &= -\sum_i t^a_{\rm proj}t^a_i\left(1-\frac{\boldsymbol{u}\cdot\boldsymbol{p}}{(1-u_z)E}\right)\int_q e^{-i(\boldsymbol{q}\cdot\boldsymbol{x}_i+q_z z_i)}v(q)\frac{2(1-u_z)E}{(p-q)^2+i\epsilon}J(p-q), \end{aligned} \tag{5}$$

where we have used the δ function in (1). In the above equation, $J(p-q)$ is the source of the initial energetic quark controlling the initial distribution of energetic partons—assumed to be centered at $\boldsymbol{x}_0=0$ and $z_0=0$—and $t^a_{\rm proj}$ is the leading parton ("projectile") color generator. We have also introduced shorthand notation for integrals running over the full three-dimensional space as $\int_x \equiv d^3x$ (and $\int_k \equiv \frac{d^3k}{(2\pi)^3}$) and over the transverse space as $\int_{\boldsymbol{x}} \equiv \int d^2\boldsymbol{x}$ (and $\int_{\boldsymbol{k}} \equiv \int \frac{d^2\boldsymbol{k}}{(2\pi)^2}$).

Integrating over q_z by residues, we assume that J is slowly varying, hence there are only four poles in (5) to account for in the evaluation of the integral. The two poles, coming from the scattering potential $v(q)$, have a finite imaginary part. For a sufficiently dilute and longitudinally extended medium $\mu_i z_i \gg 1$, and so the corresponding contributions are exponentially suppressed and can be neglected. The other two poles come from the quark propagator

$$Q^+_{p-q} \simeq \frac{2E}{1+u_z}\left(1-\frac{\boldsymbol{q}\cdot\boldsymbol{u}}{2E}\right), \tag{6a}$$

$$Q^-_{p-q} \simeq \frac{\boldsymbol{q}\cdot\boldsymbol{u}}{1-u_z}+\frac{(\boldsymbol{p}-\boldsymbol{q})^2-\boldsymbol{p}^2}{2(1-u_z)E}, \tag{6b}$$

where we have accounted for the first terms in the eikonal expansion. The pole Q^+_{p-q} is $\mathcal{O}(E)$, so its residue will be highly suppressed by the leading parton energy and can be neglected. Therefore, the only nonvanishing contribution comes from the residue corresponding to the pole at Q^-_{p-q}. The integration contour has to be closed below the real axis enforcing $z_i>0$. After performing the q_z integration, the SB contribution to the amplitude reduces to

$$\begin{aligned} iM_1 &= -i\sum_i t^a_{\rm proj}t^a_i\left(1-\frac{\boldsymbol{u}\cdot\boldsymbol{p}}{(1-u_z)E}\right)\int_{\boldsymbol{q}}\theta(z_i)e^{-i\boldsymbol{q}\cdot\boldsymbol{x}_i}e^{-iQ^-_{p-q}z_i}v(\tilde{q})\frac{2E}{1+u_z}\frac{1}{Q^-_{p-q}-Q^+_{p-q}}J(p-\tilde{q})\\ &= i\sum_i t^a_{\rm proj}t^a_i\int_{\boldsymbol{q}}\theta(z_i)e^{-i\boldsymbol{q}\cdot\boldsymbol{x}_i}e^{-iQ^-_{p-q}z_i}\left(1-\frac{\boldsymbol{u}\cdot(\boldsymbol{p}-\boldsymbol{q})}{(1-u_z)E}\right)v(\tilde{q})J(p-\tilde{q}), \end{aligned} \tag{7}$$

where the tilde indicates that q_0 and q_z have been fixed, and $\tilde{q}_\mu = (\boldsymbol{q}\cdot\boldsymbol{u}+Q^-_{p-q}u_z, \boldsymbol{q}, Q^-_{p-q})_\mu$.

We can now square the amplitude and average over initial and sum over final quantum numbers, as well as average over the field configurations. We will also assume that the sources are smoothly distributed, replacing any sum over the scattering centers by a continuous integral

$$\sum_i f_i = \int_{\boldsymbol{x},z} \rho(\boldsymbol{x},z) f(\boldsymbol{x},z), \tag{8}$$

where $\rho(\boldsymbol{x},z)$ is the source number density. Doing so yields

$$\begin{aligned}\langle |M_1|^2\rangle = \mathcal{C}\int_{x,\boldsymbol{q},\boldsymbol{q}'} &\theta(z)\rho(\boldsymbol{x},z)e^{-i(\boldsymbol{q}-\boldsymbol{q}')\cdot\boldsymbol{x}}e^{-i(Q^-_{p-q}-Q^-_{p-q'})z}\\ &\times\left(1-\frac{\boldsymbol{u}\cdot(\boldsymbol{p}-\boldsymbol{q})}{(1-u_z)E}-\frac{\boldsymbol{u}\cdot(\boldsymbol{p}-\boldsymbol{q}')}{(1-u_z)E}\right)\\ &\times v(\tilde{q})v^*(\tilde{q}')J(p-\tilde{q})J^*(p-\tilde{q}'),\end{aligned} \tag{9}$$

where $\mathcal{C}=\frac{C_F}{2N_c}$. Note that we only explicitly show the arguments of $\rho(\boldsymbol{x},z)$ for illustrative purposes, keeping the arguments of the other hydrodynamic variables implicit.

Contrary to the case with vanishing medium velocity, the q_z integration results in a shift in the argument of the potential and initial source. Expanding these functions, one readily finds

$$v(\tilde{q})\simeq v(\boldsymbol{q}^2)\left(1+\frac{\boldsymbol{q}\cdot\boldsymbol{u}}{(1-u_z)E}\frac{(\boldsymbol{p}-\boldsymbol{q})^2-\boldsymbol{p}^2}{v(\boldsymbol{q}^2)}\frac{\partial v}{\partial\boldsymbol{q}^2}\right), \tag{10a}$$

$$J(p-\tilde{q})\simeq J(E,\boldsymbol{p}-\boldsymbol{q})\left(1-\frac{\boldsymbol{q}\cdot\boldsymbol{u}}{(1-u_z)}\frac{1}{J}\frac{\partial J}{\partial E}\right), \tag{10b}$$

where $v(\boldsymbol{q}^2)=-\frac{g^2}{\boldsymbol{q}^2+\mu^2}$.

Upon inspection of (9) and (10), one sees that all the velocity corrections appearing in the squared amplitude are proportional to the transverse velocity $\boldsymbol{u}$. Hence, it is useful to define a new vector in the transverse plane,

$$\begin{aligned}\boldsymbol{\Gamma}(\boldsymbol{q},\boldsymbol{q}')\equiv &-\frac{\boldsymbol{p}-\boldsymbol{q}}{(1-u_z)E}-\frac{\boldsymbol{p}-\boldsymbol{q}'}{(1-u_z)E}+\frac{\boldsymbol{q}}{(1-u_z)E}\frac{(\boldsymbol{p}-\boldsymbol{q})^2-\boldsymbol{p}^2}{v(\boldsymbol{q}^2)}\frac{\partial v}{\partial\boldsymbol{q}^2}\\ &+\frac{\boldsymbol{q}'}{(1-u_z)E}\frac{(\boldsymbol{p}-\boldsymbol{q}')^2-\boldsymbol{p}^2}{v^*(\boldsymbol{q}'^2)}\frac{\partial v^*}{\partial\boldsymbol{q}'^2}-\frac{\boldsymbol{q}}{(1-u_z)}\frac{1}{J}\frac{\partial J}{\partial E}-\frac{\boldsymbol{q}'}{(1-u_z)}\frac{1}{J}\frac{\partial J}{\partial E},\end{aligned} \tag{11}$$

which enables us to write the averaged squared amplitude in a compact form,

$$\langle|M_1|^2\rangle=\mathcal{C}\int_{x,\boldsymbol{q},\boldsymbol{q}'}\theta(z)\rho(\boldsymbol{x},z)v(\boldsymbol{q}^2)v^*(\boldsymbol{q}'^2)J(E,\boldsymbol{p}-\boldsymbol{q})J^*(E,\boldsymbol{p}-\boldsymbol{q}')e^{-i(\boldsymbol{q}-\boldsymbol{q}')\cdot\boldsymbol{x}}e^{-i(Q^-_{p-q}-Q^-_{p-q'})z}[1+\boldsymbol{u}\cdot\boldsymbol{\Gamma}(\boldsymbol{q},\boldsymbol{q}')]. \tag{12}$$

All the dependence on the matter's spatial structure in (12) comes from the hydrodynamic parameters of the matter model. In our case of the GW potential, these parameters are the source spatial density $\rho(\boldsymbol{x},z)$, the Debye mass $\mu^2(\boldsymbol{x},z)$, and the three components of the velocity $\boldsymbol{u}(\boldsymbol{x},z)$ and $u_z(\boldsymbol{x},z)$. For arbitrary $\boldsymbol{x}$ dependence in (12), the final distribution cannot be simplified further. We proceed by noting that the matter properties are expected to change sufficiently slowly in the hydrodynamic phase and thus expand in hydrodynamic gradients transverse to the large parton momentum p_z, see [21]. At the zeroth order, matter is uniform in the transverse plane, and thus the $\boldsymbol{x}$ integral trivially results in a δ function, while the longitudinal z integral is yet to be performed. Then the corresponding contribution to the squared amplitude reads

$$\begin{aligned}\langle|M_1|^2\rangle=\mathcal{C}\int_0^L dz\int_{\boldsymbol{q}}&\rho(z)|v(\boldsymbol{q}^2)|^2|J(E,\boldsymbol{p}-\boldsymbol{q})|^2\\ &\times[1+\boldsymbol{u}\cdot\boldsymbol{\Gamma}(\boldsymbol{q})]+\mathcal{O}(\boldsymbol{\nabla}),\end{aligned} \tag{13}$$

where $\boldsymbol{\Gamma}(\boldsymbol{q})\equiv\boldsymbol{\Gamma}(\boldsymbol{q},\boldsymbol{q})$ and we assume that the matter has a finite longitudinal size L.

Given weak dependence on the transverse coordinates, any hydrodynamic variable $G(\boldsymbol{x},z)$ can be expanded about $\boldsymbol{x}=0$, resulting in

$$G(\boldsymbol{x},z)\simeq G(z)+\boldsymbol{x}\cdot\boldsymbol{\nabla}G(z)+\mathcal{O}(\boldsymbol{\nabla}^2).$$

Then the transverse integral in (12) can be performed explicitly by noting that

$$\int_{\boldsymbol{x}}\boldsymbol{x}_\alpha e^{-i(\boldsymbol{q}-\boldsymbol{q}')\cdot\boldsymbol{x}}=i(2\pi)^2\frac{\partial}{\partial(\boldsymbol{q}-\boldsymbol{q}')_\alpha}\delta^{(2)}(\boldsymbol{q}-\boldsymbol{q}'), \tag{14}$$

where α runs over the 2D transverse space. With these replacements, we can express the linear gradient correction to (13) in a compact form,

$$\begin{aligned}\delta\langle|M_1|^2\rangle = -i\mathcal{C}\int_0^L dz \int_{\boldsymbol{Q},\boldsymbol{q}_{12}} \delta^{(2)}(\boldsymbol{q}_{12})\hat{\boldsymbol{g}}_\alpha\rho(z) \\ \times \frac{\partial}{\partial \boldsymbol{q}_{12,\alpha}}\left\{J\left(E,\boldsymbol{p}-\boldsymbol{Q}-\frac{1}{2}\boldsymbol{q}_{12}\right)J^*\left(E,\boldsymbol{p}-\boldsymbol{Q}+\frac{1}{2}\boldsymbol{q}_{12}\right)v\left(\left(\boldsymbol{Q}+\frac{1}{2}\boldsymbol{q}_{12}\right)^2\right)v^*\left(\left(\boldsymbol{Q}-\frac{1}{2}\boldsymbol{q}_{12}\right)^2\right)\right. \\ \left.\times \exp\left[-i\left(\frac{\boldsymbol{u}\cdot\boldsymbol{q}_{12}}{1-u_z}-\frac{\boldsymbol{q}_{12}\cdot(\boldsymbol{p}-\boldsymbol{Q})}{(1-u_z)E}\right)z\right]\left[1+\boldsymbol{u}\cdot\boldsymbol{\Gamma}\left(\boldsymbol{Q}+\frac{1}{2}\boldsymbol{q}_{12},\boldsymbol{Q}-\frac{1}{2}\boldsymbol{q}_{12}\right)\right]\right\}, \qquad (15)\end{aligned}$$

where $\boldsymbol{Q}\equiv\frac{1}{2}(\boldsymbol{q}+\boldsymbol{q}')$, $\boldsymbol{q}_{12}\equiv\boldsymbol{q}-\boldsymbol{q}'$, and we have integrated the derivative acting on the δ function by parts. All gradient corrections can be derived from the same expression upon variation over the corresponding hydrodynamic variable. We use a shorthand notation, the two-dimensional operator $\hat{\boldsymbol{g}}_\alpha\equiv\sum_G\left(\boldsymbol{\nabla}G\cdot\frac{\delta}{\delta G}\right)_\alpha$, which should be understood as summed over the hydrodynamic variables. Note that if a μ-dependent cutoff is introduced for the momentum integration, $\hat{\boldsymbol{g}}$ should, in principle, act on such a cutoff as well.

In order to simplify our considerations, we follow [21] and assume that the initial source J and v have, at most, constant imaginary phases.[3] Therefore, all the terms in the integrand of (15)—except for the Landau-Pomeranchuk-Migdal (LPM) phases [50,51]—are even and regular functions of $\boldsymbol{q}_{12}$ with zero derivative with respect to $\boldsymbol{q}_{12}$ at zero. This reduces the gradient correction to the amplitude to

$$\delta\langle|M_1|^2\rangle = \mathcal{C}\int_0^L dz\int_{\boldsymbol{q}}\hat{\boldsymbol{g}}_\alpha\rho(z)\left[\left(-\frac{\boldsymbol{u}^\alpha}{1-u_z}+\frac{(\boldsymbol{p}-\boldsymbol{q})^\alpha}{(1-u_z)E}\right)z\right][v(\boldsymbol{q}^2)]^2|J(E,\boldsymbol{p}-\boldsymbol{q})|^2\left[1+\boldsymbol{u}\cdot\boldsymbol{\Gamma}(\boldsymbol{q})\right]. \qquad (16)$$

B. Double Born contribution

Next we turn to the DB diagram, see Fig. 1, which gives the second contribution to the transverse-momentum broadening and corresponds to the double-scattering amplitude,

$$\begin{aligned}iM_2 = \int\frac{d^4q_1}{(2\pi)^4}\frac{d^4q_1}{(2\pi)^4}[igt^b_{\text{proj}}(2p-q_2)_\nu A^{b\nu}_{\text{ext}}(q_2)]\left[\frac{i}{(p-q_2)^2+i\epsilon}\right] \\ \times[igt^a_{\text{proj}}(2(p-q_2)-q_1)_\mu A^{a\mu}_{\text{ext}}(q_1)]\left[\frac{i}{(p-q_1-q_2)^2+i\epsilon}\right]J(p-q_1-q_2). \qquad (17)\end{aligned}$$

Unlike the case of the SB diagram, both field insertions in M_2 come at the amplitude level, and to the first order in opacity the DB diagram combines with the vacuum amplitude $iM_0=J(p)$. Averaging over the stochastic fields and summing the quantum numbers, we find that

$$\begin{aligned}\langle M_2M_0^*\rangle = \mathcal{C}\sum_i\left(1-2\frac{\boldsymbol{u}\cdot\boldsymbol{p}}{E(1-u_z)}\right)\int_{q_1,q_2}e^{-i(\boldsymbol{q}_1+\boldsymbol{q}_2)\cdot\boldsymbol{x}_i-i(q_{1z}+q_{2z})z_i}v(q_1)v(q_2) \\ \times\frac{2E(1-u_z)}{(p-q_2)^2+i\epsilon}\frac{2E(1-u_z)}{(p-q_2-q_1)^2+i\epsilon}J(p-q_2-q_1)J^*(p), \qquad (18)\end{aligned}$$

where we have used the constraints coming from the external field fixing the temporal components of the two momenta. We further note that, as in the SB case, the dominant contribution to the q_{1z} integral corresponds to the pole at $q_{1z}=-q_{2z}+Q^-_{p-q_1-q_2}-i\epsilon$. Thus,

---

[3] Indeed, for arbitrary complex functions J and v one would expect additional contributions proportional to, e.g., $J^*(\boldsymbol{p})\overleftrightarrow{\nabla}_p J(\boldsymbol{p})$. While nontrivial phases, controlling such structures, are not expected in the commonly used models for the source potential, the initial source is generally less constrained. Here, we will imply this assumption, leaving the case of more general initial distributions aside.

$$\langle M_2 M_0^* \rangle = i\mathcal{C}\sum_i \int_{\boldsymbol{q}_1,\boldsymbol{q}_2} \theta(z_i) e^{-i(\boldsymbol{q}_1+\boldsymbol{q}_2)\cdot\boldsymbol{x}_i} e^{-iQ^-_{p-q_1-q_2} z_i} J(E,\boldsymbol{p}-\boldsymbol{q}_1-\boldsymbol{q}_2) J^*(p)\left(1-\frac{\boldsymbol{u}\cdot(2\boldsymbol{p}-\boldsymbol{q}_1-\boldsymbol{q}_2)}{(1-u_z)E}-\frac{\boldsymbol{u}\cdot(\boldsymbol{q}_1+\boldsymbol{q}_2)}{1-u_z}\frac{1}{J}\frac{\partial J}{\partial E}\right)$$
$$\times\frac{2E}{1+u_z}\frac{v(\tilde{q}_1)v(q_2)}{(q_{2z}-Q^+_{p-q_2}-i\epsilon)(q_{2z}-Q^-_{p-q_2}+i\epsilon)}, \tag{19}$$

where the tilde serves to remind one that q_{1z} and q_{10} are fixed, which introduces a nontrivial q_{2z} dependence into $v(\tilde{q}_1)$.

Turning to the q_{2z} integration, one must also note that the Fourier factor is independent of q_{2z}, and the residues of the scattering potential poles are no longer suppressed. Therefore, the residues of the all six poles may contribute. The two poles of the second scalar propagator are given by $Q^{\pm}_{p-q_2}$, while the four poles coming from the scattering potentials read

$$v(\tilde{q}_1)\colon \mathcal{P}_1^{\pm} \equiv Q^-_{p-q_1-q_2} - \frac{u_z}{1-u_z^2}(\boldsymbol{u}\cdot\boldsymbol{q}_1) \pm \frac{i}{1-u_z^2}R_1, \tag{20a}$$

$$v(q_2)\colon \mathcal{P}_2^{\pm} \equiv \frac{u_z}{1-u_z^2}(\boldsymbol{u}\cdot\boldsymbol{q}_2) \pm \frac{i}{1-u_z^2}R_2, \tag{20b}$$

where, keeping the expressions compact, we have introduced the shorthand notation

$$R^2 \equiv (1-u_z^2)(\boldsymbol{q}^2+\mu^2) - (\boldsymbol{u}\cdot\boldsymbol{q})^2 \geq 0. \tag{21}$$

Then, introducing the source number density, we can write the full DB contribution as

$$\langle M_2 M_0^* \rangle + \text{c.c.} = i\mathcal{C}\int_{x,\boldsymbol{q}_1,\boldsymbol{q}_2} \theta(z)\rho(\boldsymbol{x},z) J(E,\boldsymbol{p}-\boldsymbol{q}_1-\boldsymbol{q}_2) J^*(p)\left(1-\frac{\boldsymbol{u}\cdot(2\boldsymbol{p}-\boldsymbol{q}_1-\boldsymbol{q}_2)}{(1-u_z)E}-\frac{\boldsymbol{u}\cdot(\boldsymbol{q}_1+\boldsymbol{q}_2)}{1-u_z}\frac{1}{J}\frac{\partial J}{\partial E}\right)$$
$$\times\left[e^{-i(\boldsymbol{q}_1+\boldsymbol{q}_2)\cdot\boldsymbol{x}} e^{-iQ^-_{p-q_1-q_2} z}\mathcal{I}_{DB} - e^{i(\boldsymbol{q}_1+\boldsymbol{q}_2)\cdot\boldsymbol{x}} e^{iQ^-_{p-q_1-q_2} z}\mathcal{I}^*_{DB}\right], \tag{22}$$

with

$$\mathcal{I}_{DB} \equiv \int \frac{dq_{2z}}{2\pi}\frac{2E}{1+u_z}\frac{v(\tilde{q}_1)v(q_2)}{(q_{2z}-Q^+_{p-q_2}-i\epsilon)(q_{2z}-Q^-_{p-q_2}+i\epsilon)}. \tag{23}$$

At zeroth order in gradients, the hydrodynamic parameters are considered to be constant in the transverse plane, and integrating over $\boldsymbol{x}$ sets $\boldsymbol{q}_1 = -\boldsymbol{q}_2 \equiv \boldsymbol{q}$. Therefore, only the imaginary part of the integral $\mathrm{Im}\,\mathcal{I}_{DB}(\boldsymbol{q},-\boldsymbol{q})$ contributes to (22). The DB contribution then simplifies to

$$\langle M_2 M_0^* \rangle + \text{c.c.} = -\mathcal{C}\int_0^L dz \int_{\boldsymbol{q}} \rho(z)[v(\boldsymbol{q}^2)]^2 |J(E,\boldsymbol{p})|^2$$
$$\times\left[1-\frac{2\boldsymbol{u}\cdot\boldsymbol{p}}{(1-u_z)E}-\frac{\boldsymbol{u}\cdot\boldsymbol{p}}{(1-u_z)E}\frac{\boldsymbol{q}^2}{v^2}\frac{\partial v^2}{\partial\boldsymbol{q}^2}\right]$$
$$+\mathcal{O}(\boldsymbol{\nabla}). \tag{24}$$

Introducing a new transverse vector

$$\boldsymbol{\Gamma}_{DB}(\boldsymbol{q}) \equiv -2\frac{\boldsymbol{p}}{(1-u_z)E} - \frac{\boldsymbol{p}}{(1-u_z)E}\frac{\boldsymbol{q}^2}{[v(\boldsymbol{q}^2)]^2}\frac{\partial v^2}{\partial\boldsymbol{q}^2}, \tag{25}$$

we can reexpress (24) in a compact form analogous to (13),

$$\langle M_2 M_0^* \rangle + \text{c.c.} = -\mathcal{C}\int_0^L dz \int_{\boldsymbol{q}} \rho(z)[v(\boldsymbol{q}^2)]^2 |J(E,\boldsymbol{p})|^2$$
$$\times[1+\boldsymbol{u}\cdot\boldsymbol{\Gamma}_{DB}(\boldsymbol{q})] + \mathcal{O}(\boldsymbol{\nabla}). \tag{26}$$

Following the same logic as before, we replace the linear dependence in $\boldsymbol{x}$ by a derivative of a δ function $\delta^{(2)}(\boldsymbol{q}_1+\boldsymbol{q}_2)$. Integrating by parts and using shorthand notation, we find the leading gradient corrections to (22), which read

$$\delta\langle M_2 M_0^* \rangle + \text{c.c.} = \mathcal{C}\int_0^L dz \int_{\boldsymbol{Q},\boldsymbol{q}_{12}} \frac{(2\pi)^2\delta^{(2)}(2\boldsymbol{Q})}{2}\hat{\boldsymbol{g}}_\alpha\frac{\partial}{\partial\boldsymbol{Q}_\alpha}\left\{\rho(z)J(E,\boldsymbol{p}-2\boldsymbol{Q})J^*(p)\left(1-2\frac{\boldsymbol{u}\cdot(\boldsymbol{p}-\boldsymbol{Q})}{(1-u_z)E}-2\frac{\boldsymbol{u}\cdot\boldsymbol{Q}}{1-u_z}\frac{1}{J}\frac{\partial J}{\partial E}\right)\right.$$
$$\left.\times\left[e^{-iQ^-_{p-q_1-q_2} z}\mathcal{I}_{DB} + e^{iQ^-_{p-q_1-q_2} z}\mathcal{I}^*_{DB}\right]\right\}, \tag{27}$$

where $\boldsymbol{Q} = \frac{1}{2}(\boldsymbol{q}_1 + \boldsymbol{q}_2)$ and $\boldsymbol{q}_{12} = \boldsymbol{q}_1 - \boldsymbol{q}_2$. The structure of this expression is more involved, and so it is instructive to consider each contribution separately. First, when the derivative acts on the terms in the first line of (27), the only $\boldsymbol{q}_{12}$ dependence enters through $\mathrm{Re}\,\mathcal{I}_{DB}(\boldsymbol{q}_{12}, 0)$. Its angular average scales as $\frac{1}{E}$ and can be explicitly derived. When the derivative hits the LPM phases, the integrand is proportional to $\mathrm{Im}\,\mathcal{I}_{DB}(\boldsymbol{q}_{12}, 0)$, and, after averaging over the angles, the corresponding contribution looks like a naive combination of gradient and flow corrections in [21]. Finally, when the derivative acts on the integral $\mathcal{I}_{DB}$, only its real part contributes. Its eikonal term $\mathrm{Re}\,\mathcal{I}^{(0)}_{DB}$ is a regular, even function of $\boldsymbol{Q}$, and its derivative at $\boldsymbol{Q} = 0$ is zero. In turn, the subeikonal part satisfies $\frac{\partial}{\partial Q_\alpha}\mathrm{Re}\,\mathcal{I}^{(1)}_{DB}(\boldsymbol{q}_{12}, 0) = -\frac{\partial}{\partial Q_\alpha}\mathrm{Re}\,\mathcal{I}^{(1)}_{DB}(-\boldsymbol{q}_{12}, 0)$. Since the rest of the integrand in (27) is $\boldsymbol{q}_{12}$ independent, the corresponding contribution to the integral vanishes after angular averaging. Combining these contributions, we find

$$\delta\langle M_2 M_0^*\rangle + \text{c.c.} = \mathcal{C}\int_0^L dz \int_{\boldsymbol{q}} \hat{\boldsymbol{g}}_\alpha \rho(z)[v(\boldsymbol{q}^2)]^2 |J(E,\boldsymbol{p})|^2 \Bigg\{ -\frac{1}{|J|^2}\frac{\partial |J(E,\boldsymbol{p})|^2}{\partial \boldsymbol{p}_\alpha} \frac{\pi g^4 \sqrt{1-\boldsymbol{u}^2-u_z^2}}{4\mu(1-u_z)E} \frac{\delta^{(2)}(\boldsymbol{q})}{[v(\boldsymbol{q}^2)]^2} + z\left(\frac{\boldsymbol{u}_\alpha}{1-u_z} - \frac{\boldsymbol{p}_\alpha}{(1-u_z)E}\right)[1 + \boldsymbol{u}\cdot\boldsymbol{\Gamma}_{DB}(\boldsymbol{q})]\Bigg\}. \tag{28}$$

Finally, one may notice that working with scalar quarks we have to treat the seagull vertex present in the theory and required by consistency. This contribution is commonly omitted in the jet quenching calculations based on scalar QCD, since it is expected to be subeikonal; see, e.g., the discussion in [21]. However, it may contribute to the leading subeikonal corrections and cannot be ignored here. It can be easily checked that the corresponding contribution appears only in the presence of transverse anisotropy and has the same structure as the term in the first line of (28). This subeikonal term is additionally suppressed by the smallness of the gradients with no length enhancement and thus appears to be subleading to the rest of the terms. In what follows, we will neglect such terms, keeping only the length-enhanced subeikonal gradient corrections and consequently neglecting all the diagrams involving the seagull vertex.

C. Final parton distribution and its moments

The final-state parton distribution can be related to the squared amplitude of the process and is defined by

$$E\frac{d\mathcal{N}}{d^2p\,dE} \equiv \frac{1}{2(2\pi)^3}\langle |M|^2\rangle, \tag{29}$$

where we have chosen E and the two transverse components of the momenta as the independent variables. Introducing the initial parton distribution $E\frac{d\mathcal{N}^{(0)}}{d^2p\,dE} \equiv \frac{1}{2(2\pi)^3}|J(E,\boldsymbol{p})|^2$ and taking the combined effects of flow and gradient corrections together, we find

$$E\frac{d\mathcal{N}}{d^2p\,dE} = E\frac{d\mathcal{N}^{(0)}}{d^2p\,dE} + \mathcal{C}\int_0^L dz \int_{\boldsymbol{q}} \Bigg\{ \left[1 - \hat{\boldsymbol{g}}_\alpha \frac{(\boldsymbol{u}E - \boldsymbol{p} + \boldsymbol{q})_\alpha z}{(1-u_z)E}\right][1 + \boldsymbol{u}\cdot\boldsymbol{\Gamma}(\boldsymbol{q})]E\frac{d\mathcal{N}^{(0)}}{d^2(p-q)dE} - \left[1 - \hat{\boldsymbol{g}}_\alpha \frac{(\boldsymbol{u}E - \boldsymbol{p})_\alpha z}{(1-u_z)E}\right][1 + \boldsymbol{u}\cdot\boldsymbol{\Gamma}_{DB}(\boldsymbol{q})]E\frac{d\mathcal{N}^{(0)}}{d^2p\,dE}\Bigg\}\rho(z)[v(\boldsymbol{q}^2)]^2, \tag{30}$$

where the terms appearing at the second subeikonal order should be neglected. Integrating the final-state distribution over the transverse momentum, one can show that the number of energetic partons is unchanged as long as the initial distribution falls fast enough at infinity, as required by unitarity.

It is instructive to consider how a particular ensemble of partons is modified by a flowing anisotropic distribution of matter. To do so, we focus on a narrow initial distribution parametrized as

$$E\frac{d\mathcal{N}^{(0)}}{d^2p\,dE} = \frac{f(E)}{2\pi w^2}e^{-\frac{p^2}{2w^2}}. \tag{31}$$

Starting with the corresponding family of partons in the initial state, one may understand how their distribution changes by focusing on the leading moments of the final-state distribution, defined as

$$\langle \boldsymbol{p}_{\alpha_1}\cdots\boldsymbol{p}_{\alpha_n}\rangle \equiv \frac{\int_{\boldsymbol{p}}(\boldsymbol{p}_{\alpha_1}\cdots\boldsymbol{p}_{\alpha_n})E\frac{d\mathcal{N}}{d^2pdE}}{\int_{\boldsymbol{p}}E\frac{d\mathcal{N}^{(0)}}{d^2pdE}} = (2\pi)^2\int_{\boldsymbol{p}}\frac{(\boldsymbol{p}_{\alpha_1}\cdots\boldsymbol{p}_{\alpha_n})}{f(E)}E\frac{d\mathcal{N}}{d^2pdE}. \qquad (32)$$

The process of jet-transverse-momentum broadening is often quantified with the so-called jet quenching parameter, which is argued to control many of the related processes. Thus, we start by computing the quadratic moment given by

$$\langle \boldsymbol{p}^2\rangle = 2w^2 + \mathcal{C}\int_0^L dz\left[1 - z\hat{\boldsymbol{g}}\cdot\frac{\boldsymbol{u}}{1-u_z}\right]\rho(z)\int_{\boldsymbol{q}}\boldsymbol{q}^2[v(\boldsymbol{q}^2)]^2, \qquad (33)$$

where the first term corresponds to the vacuum part of (30) and is fixed by the width of the initial distribution. Varying this moment with the medium length L—understood as the path length traveled by the parton—we find

$$\hat{q}(L) = \left[1 - L\hat{\boldsymbol{g}}\cdot\frac{\boldsymbol{u}}{1-u_z}\right]\hat{q}_0(L), \qquad (34)$$

where $\hat{q}_0(L) = \mathcal{C}\rho(L)\int_{\boldsymbol{q}}\boldsymbol{q}^2[v(\boldsymbol{q}^2)]^2$ corresponds to the limit of static transversely homogeneous matter, and all hydrodynamic variables and their gradients should be understood as functions of L. Thus, we can see that the interplay between the transverse medium structure and flow modifies the even moments of the final-state distribution, including the fundamental jet quenching parameter, at the leading eikonal order. Moreover, this modification is length enhanced and, consequently, expected to be the dominant effect of the medium's evolution. This is one of the main results of this work.

Following [21,32,37], we also consider the leading odd moments of the final distribution, which vanish in the case of static and isotropic matter (for isotropic initial distribution), but generated by flow and gradient effects. One readily finds that

$$\langle \boldsymbol{p}_\alpha\rangle = -\frac{1}{2}\mathcal{C}\int_0^L dz\left[1 - z\hat{\boldsymbol{g}}\cdot\frac{\boldsymbol{u}}{1-u_z}\right]\rho(z) \times\frac{\boldsymbol{u}_\alpha}{(1-u_z)E}\int_{\boldsymbol{q}}\boldsymbol{q}^2\left[E\frac{f'(E)}{f(E)} + \boldsymbol{q}^2\frac{\partial}{\partial\boldsymbol{q}^2}\right][v(\boldsymbol{q}^2)]^2, \qquad (35)$$

where we recognize the same rescaling factor as in the case of even moments combined with the averaged transverse momentum obtained in [21,32].

As shown in [21,37], the directional gradient effects appear only in higher odd moments of the final parton distribution. Focusing on the cubic moment, we find

$$\langle \boldsymbol{p}_\alpha\boldsymbol{p}^2\rangle = \mathcal{C}\int_0^L dz\int_{\boldsymbol{q}}\left\{2w^2 z\hat{\boldsymbol{g}}_\alpha\frac{\boldsymbol{q}^2}{(1-u_z)E} - \frac{1}{2}\left[1 - z\hat{\boldsymbol{g}}\cdot\frac{\boldsymbol{u}}{1-u_z}\right]\frac{\boldsymbol{u}_\alpha}{(1-u_z)E} \times\boldsymbol{q}^2\left[8w^2 + (10w^2+\boldsymbol{q}^2)\boldsymbol{q}^2\frac{\partial}{\partial\boldsymbol{q}^2} + (4w^2+\boldsymbol{q}^2)E\frac{f'(E)}{f(E)}\right]\right\}\rho(z)[v(\boldsymbol{q}^2)]^2, \qquad (36)$$

which agrees with the results of [21,37] in the limit of static matter at first order in opacity and can be compared to the results of [21] in the homogeneous limit at $w = 0$.

III. MEDIUM-INDUCED GLUON SPECTRUM

In this section, we will derive the medium-induced radiation spectrum in an evolving inhomogeneous nuclear matter at the first order in opacity and discuss the resulting modifications of the energy loss. This consideration is technically more involved, and here we will focus on two particular types of the medium evolution effects. First, we will study how the transverse gradients of μ and ρ modify the full gluon spectrum in the absence of any flow, at the first order in opacity, but in full kinematics, thereby extending the results of [21,43]. Second, we will search for the mixed flow-gradient effects analogous to the multiplicative modification in (34), keeping only the leading terms in the eikonal expansion. For notational compactness, we will put the two types of gradient corrections together in intermediate equations, although one should note that the subeikonal terms sourced by the transverse flow (and their combinations with the leading gradient corrections) are omitted.[4] In the absence of u_z gradients, the longitudinal flow effects can be obtained with the corresponding boost, and for simplicity, we will set $u_z = 0$.

Before turning to details, we should note that the external field (1) has been obtained from the classical field equation in the Lorenz gauge. However, it is convenient to impose a stronger gauge condition, additionally requiring $n \cdot A = 0$.

---

[4] It should be mentioned here that in this limit the class of diagrams involving the seagull or four-gluon vertices can be freely neglected. Indeed, they contribute as gradient corrections and appear only at the first subeikonal order, lacking any length enhancement in the absence of the transverse flow.

In this gauge, only the two physical gluon polarizations appear, and the consideration simplifies. This constraint is compatible with the form of (1), and one may choose n^μ to be any vector transverse to the velocity u^μ. Here, we will use $n_\mu = (0, \mathbf{0}, 1)$, since $A^z_{\text{ext}} = 0$ for $u_z = 0$. In this gauge, the propagator of a gluon is given by

$$G_{\mu\nu}(k) = \frac{-iN_{\mu\nu}(k)}{k^2 + i\epsilon}, \tag{37}$$

where the numerator is transverse to the gauge vector n and gluon momentum k,

$$N_{\mu\nu}(k) = g_{\mu\nu} + n^2 \frac{k_\mu k_\nu}{(k\cdot n)^2 - k^2 n^2} + k^2 \frac{n_\mu n_\nu}{(k\cdot n)^2 - k^2 n^2} - (k\cdot n)\frac{k_\mu n_\nu + k_\nu n_\mu}{(k\cdot n)^2 - k^2 n^2}. \tag{38}$$

The polarization vector now satisfies $k \cdot \epsilon(k) = n \cdot \epsilon(k) = 0$ and can be parametrized as

$$\epsilon^*_\mu(k) = \left(\frac{\boldsymbol{\epsilon}\cdot\boldsymbol{k}}{\omega}, \boldsymbol{\epsilon}, 0\right), \tag{39}$$

where $\boldsymbol{\epsilon}$ is the transverse polarization,[5] $k = (\omega, \boldsymbol{k}, k_z)$, and we keep the polarization index implicit.

Following the notation of [21,43], we consider the leading perturbative contribution to the medium-induced branching of the initial energetic quark to an on-shell quark of momentum $(p-k)_\mu$ and an on-shell gluon of momentum k_μ, working at the leading eikonal order but to all orders in LPM phases. We also rely on the broad source approximation, assuming that the dependence of the initial source on the transverse momenta is sufficiently weak. Under the aforementioned assumptions, the vacuum emission amplitude (see Fig. 2) corresponding to the zeroth order in opacity, reads

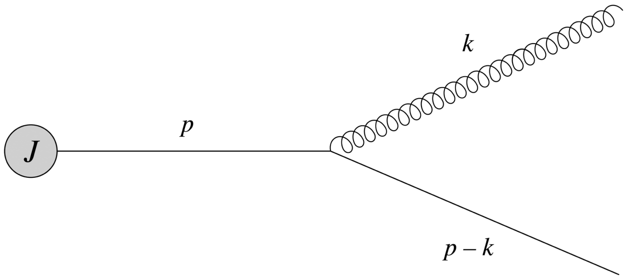

FIG. 2. The elementary vacuum splitting, corresponding to the zeroth order in opacity expansion.

$$i\mathcal{R}_0 = [igt^r_{\text{proj}}(2p-k)_\mu \epsilon^{*\mu}(k)]\frac{i}{p^2 + i\epsilon}J(p) \simeq -gt^r_{\text{proj}}\frac{2(1-\mathrm{x})\boldsymbol{\epsilon}\cdot(\boldsymbol{k}-\mathrm{x}\boldsymbol{p})}{(\boldsymbol{k}-\mathrm{x}\boldsymbol{p})^2}J(p), \tag{40}$$

where t^r_{proj} comes from the emission vertex, r is the color of the final gluon, $\mathrm{x} = \frac{\omega}{E}$ is its energy fraction, and one may recognize the (light-front) wave function of the splitting $\psi(\mathrm{x}, \boldsymbol{k} - \mathrm{x}\boldsymbol{p}) = \frac{2(1-\mathrm{x})\boldsymbol{\epsilon}\cdot(\mathrm{x}\boldsymbol{p}-\boldsymbol{k})}{(\boldsymbol{k}-\mathrm{x}\boldsymbol{p})2}$, which controls the branching probability; see, e.g., the discussion in [52]. In turn, at the first order in opacity $N = 1$, there are nine diagrams contributing to the amplitude of the medium-induced branching shown in Figs. 3 and 4, and we will consider them one by one in what follows.

A. Single Born contributions

1. The amplitude level

Let us start by computing the simplest contribution to the medium-induced branching, $\mathcal{R}_A$, which corresponds to the initial-state scattering. This amplitude reads

$$\begin{aligned} i\mathcal{R}_A &= \int \frac{d^4q}{(2\pi)^4}[igt^r_{\text{proj}}(2p-k)_\nu \epsilon^{*\nu}(k)]\frac{i}{p^2+i\epsilon}[it^a_{\text{proj}}(2p-q)_\mu g A^{a\mu}(q)]\frac{i}{(p-q)^2+i\epsilon}J(p-q) \\ &= \frac{2(1-\mathrm{x})\boldsymbol{\epsilon}\cdot(\boldsymbol{k}-\mathrm{x}\boldsymbol{p})}{(\boldsymbol{k}-\mathrm{x}\boldsymbol{p})^2}\sum_i t^r_{\text{proj}}t^a_{\text{proj}}t^a_i \int_q e^{-i(\boldsymbol{q}_i\cdot\boldsymbol{x}_i + q_z z_i)}\frac{(2gE)v(q)}{(p-q)^2+i\epsilon}J(p-q), \end{aligned} \tag{41}$$

where we have explicitly used the constraint on q_0. Turning to the q_z integration, we again assume that the residues of the scattering potential poles are exponentially suppressed.

In turn, the poles coming from the quark propagator are given by

$$\mathcal{Q}^+_{p-q} \simeq 2E\left(1 - \frac{\boldsymbol{q}\cdot\boldsymbol{u}}{2E}\right), \tag{42a}$$

$$\mathcal{Q}^-_{p-q} \simeq \boldsymbol{q}\cdot\boldsymbol{u} - \frac{(1-\mathrm{x})\boldsymbol{k}^2 + \mathrm{x}(\boldsymbol{p}-\boldsymbol{k})^2 - \mathrm{x}(1-\mathrm{x})(\boldsymbol{p}-\boldsymbol{q})^2}{2\mathrm{x}(1-\mathrm{x})E}, \tag{42b}$$

---

[5] The transverse polarization vectors are functions of k, since the sum over polarizations should be properly normalized. However, up to the higher subeikonal corrections, we find that $\sum_\lambda \boldsymbol{\epsilon}^\lambda_\alpha \boldsymbol{\epsilon}^\lambda_\beta = \delta_{\alpha\beta} + \mathcal{O}(\frac{1}{\omega^2})$, with α and β running in the 2D transverse space.

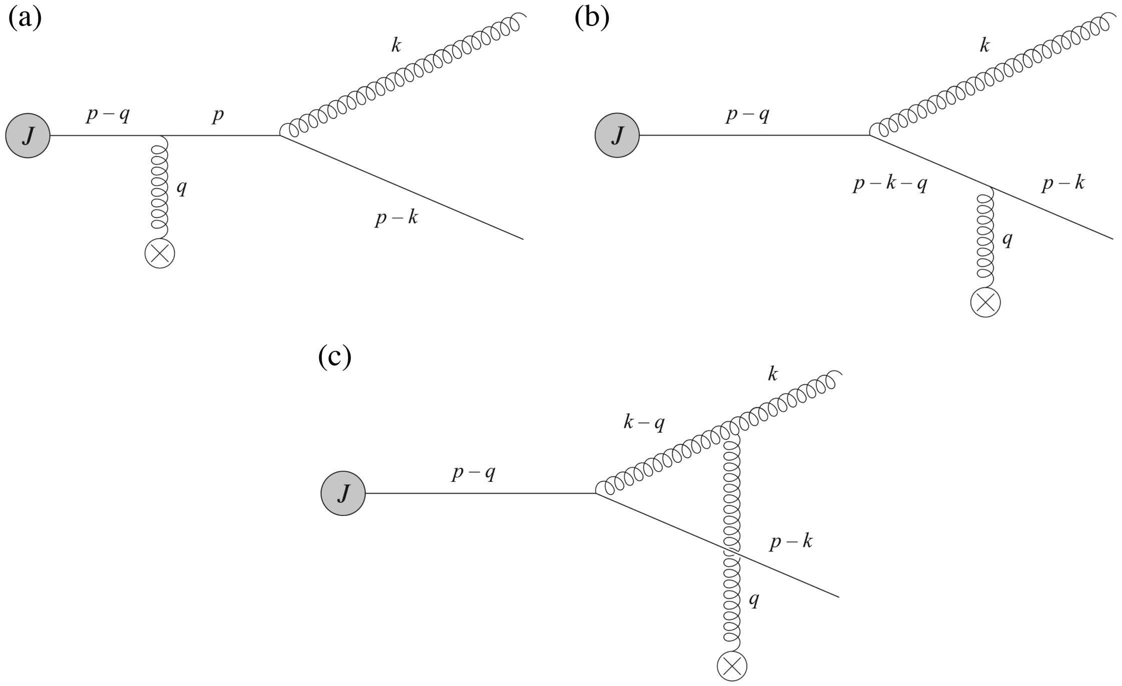

FIG. 3. The three single Born diagrams contributing to the medium-induced radiation at the first order in opacity.

while the initial source is assumed to result in no new poles. Thus, collecting all the relevant contributions, we can write the initial-state scattering amplitude as

$$i\mathcal{R}_A = -ig\frac{2(1-\mathrm{x})\boldsymbol{\epsilon}\cdot(\boldsymbol{k}-\mathrm{x}\boldsymbol{p})}{(\boldsymbol{k}-\mathrm{x}\boldsymbol{p})^2}\sum_i t^r_{\mathrm{proj}}t^a_{\mathrm{proj}}t^a_i\int_{\boldsymbol{q}}\theta(z_i)e^{-i\boldsymbol{q}\cdot\boldsymbol{x}_i}e^{-i\mathcal{Q}^-_{p-q}z_i}v(\boldsymbol{q}^2)J(E,\boldsymbol{p}-\boldsymbol{q}). \tag{43}$$

The next diagram corresponds to the final-state scattering process in the quark line, and its amplitude reads

$$\begin{aligned} i\mathcal{R}_B = \int\frac{d^4q}{(2\pi)^4}\,[it^a_{\mathrm{proj}}(2(p-k)-q)_\mu gA^{a\mu}_{\mathrm{ext}}]\frac{i}{(p-k-q)^2+i\epsilon} \\ \times[igt^r_{\mathrm{proj}}(2(p-q)-k)_\nu\epsilon^{*\nu}(k)]\frac{i}{(p-q)^2+i\epsilon}J(p-q), \end{aligned} \tag{44}$$

which, after both q_0 and q_z integrals are evaluated, can be rewritten as

$$i\mathcal{R}_B = ig\sum_i t^a_{\mathrm{proj}}t^a_i t^r_{\mathrm{proj}}\int_{\boldsymbol{q}}\theta(z_i)e^{-i\boldsymbol{q}\cdot\boldsymbol{x}_i}\frac{2(1-\mathrm{x})\boldsymbol{\epsilon}\cdot(\boldsymbol{k}-\mathrm{x}(\boldsymbol{p}-\boldsymbol{q}))}{(\boldsymbol{k}-\mathrm{x}(\boldsymbol{p}-\boldsymbol{q}))^2}\left[e^{-i\mathcal{Q}^-_{p-q}z_i}-e^{-i\mathcal{Q}^-_{p-k-q}z_i}\right]v(\boldsymbol{q}^2)J(E,\boldsymbol{p}-\boldsymbol{q}), \tag{45}$$

where we have used the explicit form of the poles of the second quark propagator

$$\mathcal{Q}^+_{p-k-q} \simeq 2(1-\mathrm{x})E\left(1-\frac{\boldsymbol{q}\cdot\boldsymbol{u}}{2(1-\mathrm{x})E}\right), \tag{46a}$$

$$\mathcal{Q}^-_{p-k-q} \simeq \boldsymbol{q}\cdot\boldsymbol{u}+\frac{(\boldsymbol{p}-\boldsymbol{k}-\boldsymbol{q})^2-(\boldsymbol{p}-\boldsymbol{k})^2}{2(1-\mathrm{x})E}. \tag{46b}$$

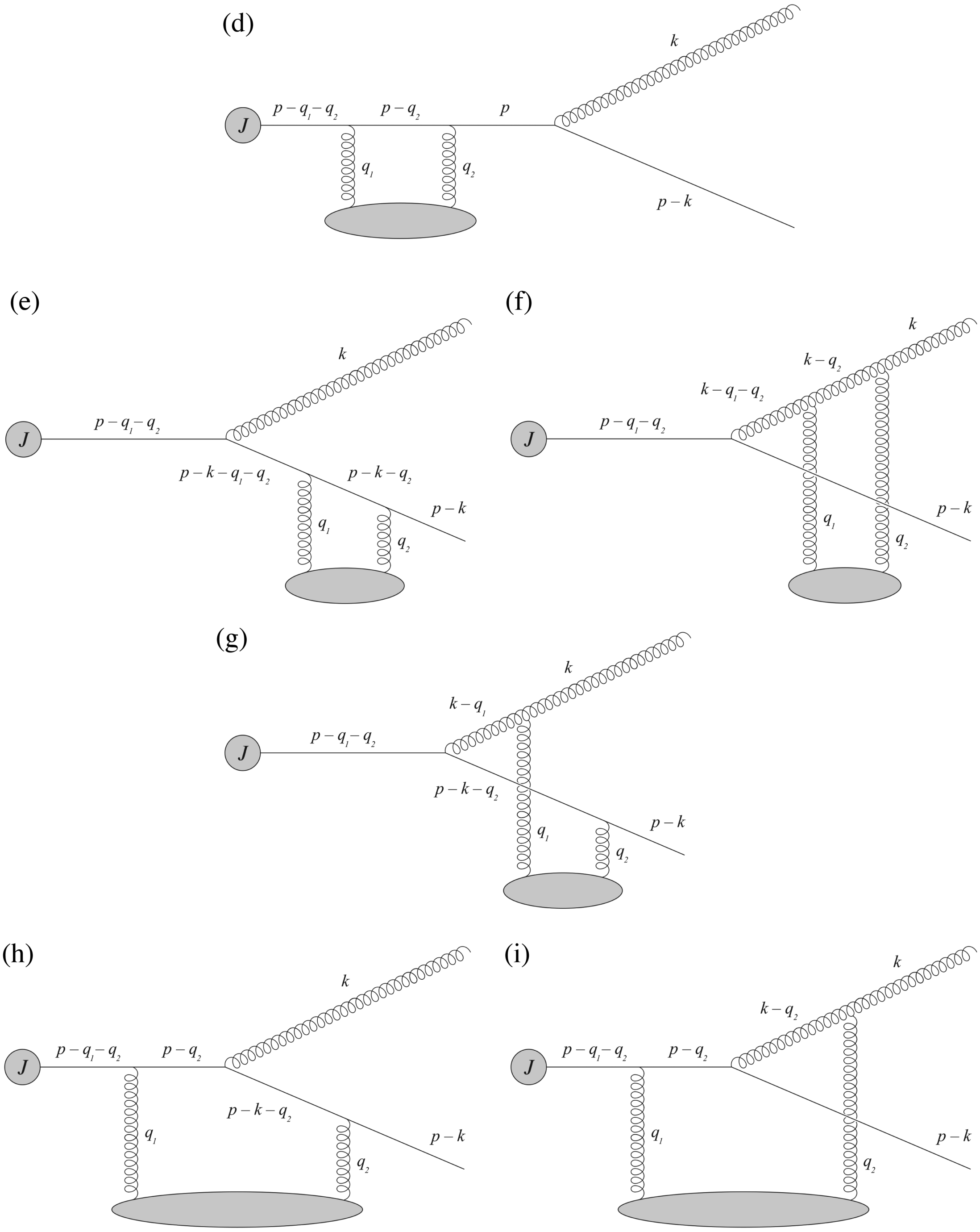

FIG. 4. The six double Born diagrams contributing to the medium-induced radiation at the first order in opacity.

Turning to the last SB contribution in the amplitude, corresponding to the final-state scattering in the emitted gluon line, we write

$$i\mathcal{R}_C = \int \frac{d^4q}{(2\pi)^4}\, i(2p-k-q)_\mu t^a_{\mathrm{proj}} \frac{-iN^{\mu\nu}(k-q)}{(k-q)^2+i\epsilon}\Gamma^{abc}_{\nu\alpha\rho}(k-q,q,-k)gA^{b\alpha}(q)\epsilon^{*\rho}(k)\frac{i}{(p-q)^2+i\epsilon}J(p-q), \qquad (47)$$

where $\Gamma^{abc}_{\nu\alpha\rho}(k-q,q,-k)$ is the three-gluon vertex defined as

$$\Gamma^{abc}_{\mu\nu\rho}(k,p,q) = gf^{abc}[g_{\mu\nu}(k-p)_\rho + g_{\nu\rho}(p-q)_\mu + g_{\rho\mu}(q-k)_\nu], \tag{48}$$

with all the momenta going toward the vertex. Since $N^{\mu\nu}$, ϵ^*_μ, and $A^{a\mu}_{\text{ext}}$ are all transverse to $n_\mu = (0,\mathbf{0},1)$ by construction, the product of these three objects and the three-gluon vertex is independent of the z components of momenta, resulting in no new poles. Performing both the q_0 and q_z integrals, we can write $\mathcal{R}_C$ as

$$i\mathcal{R}_C = g\sum_i f^{abc} t^a_{\text{proj}} t^b_i \int_{\boldsymbol{q}} \theta(z_i) e^{-i\boldsymbol{q}\cdot\boldsymbol{x}_i} \frac{2(1-\mathrm{x})\boldsymbol{\epsilon}\cdot(\boldsymbol{k}-(1-\mathrm{x})\boldsymbol{q}-\mathrm{x}\boldsymbol{p})}{(\boldsymbol{k}-(1-\mathrm{x})\boldsymbol{q}-\mathrm{x}\boldsymbol{p})^2} v(\boldsymbol{q}^2)\left[e^{-i\mathcal{Q}^-_{p-q}z_i} - e^{-i\mathcal{Q}^-_{k-q}z_i}\right] J(E,\boldsymbol{p}-\boldsymbol{q}), \tag{49}$$

where the poles of the gluon propagator have been used,

$$\mathcal{Q}^+_{k-q} \simeq 2\mathrm{x}E\left(1 - \frac{\boldsymbol{q}\cdot\boldsymbol{u}}{2\mathrm{x}E}\right), \tag{50a}$$

$$\mathcal{Q}^-_{k-q} \simeq \boldsymbol{q}\cdot\boldsymbol{u} + \frac{(\boldsymbol{k}-\boldsymbol{q})^2 - \boldsymbol{k}^2}{2\mathrm{x}E}. \tag{50b}$$

2. *SB contributions to the squared amplitude*

Now we are in position to obtain the full SB contribution to the amplitude squared. As done in the case of jet broadening, we have to average over initial and sum over final quantum numbers, as well as perform the medium averages.

Let us start by squaring $\mathcal{R}_A$, which after averaging but before integrating over the transverse coordinates results in

$$\begin{aligned}\langle|\mathcal{R}_A|^2\rangle = \frac{C_F^2}{2N_c} g^2 \frac{4(1-\mathrm{x})^2}{(\boldsymbol{k}-\mathrm{x}\boldsymbol{p})^2} \int_{x,\boldsymbol{q},\bar{\boldsymbol{q}}} \theta(z)\rho(\boldsymbol{x},z) e^{-i(\boldsymbol{q}-\bar{\boldsymbol{q}})\cdot\boldsymbol{x}} \\ \times e^{-i(\mathcal{Q}^-_{p-q}-\mathcal{Q}^-_{p-\bar{q}})z} v(\boldsymbol{q}^2) v(\bar{\boldsymbol{q}}^2) \\ \times J(E,\boldsymbol{p}-\boldsymbol{q}) J^*(E,\boldsymbol{p}-\bar{\boldsymbol{q}}),\end{aligned} \tag{51}$$

where the color factors combine into an overall multiple $\frac{C_F^2}{2N_c}$. In the case of a transversely homogeneous matter, corresponding to the zeroth order in the gradient expansion, we can readily evaluate the $\boldsymbol{x}$ integral. It results in a constraint $(2\pi)^2\delta^{(2)}(\boldsymbol{q}-\bar{\boldsymbol{q}})$, and integrating over one of the momenta, the standard form of the leading contribution is obtained. In turn, treating the gradient corrections as in the broadening case, one may note that only the LPM phases contribute to the momentum derivative at $\boldsymbol{q}-\bar{\boldsymbol{q}} = 0$. Thus, up to the first order in gradients and in the eikonal limit for the flow-induced terms, the corresponding contribution to the amplitude squared reads

$$\begin{aligned}\langle|\mathcal{R}_A^2|\rangle = \frac{C_F^2}{N_c} g^2 \int_0^L dz \int_{\boldsymbol{q}} \frac{2(1-\mathrm{x})^2}{(\boldsymbol{k}-\mathrm{x}\boldsymbol{p})^2}\left[1 - \hat{\boldsymbol{g}}\cdot\left(\boldsymbol{u} - \frac{\boldsymbol{p}-\boldsymbol{q}}{E}\right)z\right] \\ \times \rho(z)[v(\boldsymbol{q}^2)]^2 |J(E,\boldsymbol{p}-\boldsymbol{q})|^2.\end{aligned} \tag{52}$$

It should be stressed that if the subeikonal flow corrections, scaling as $\mathcal{O}(\frac{1}{E})$, were added here, they would mix with the eikonal gradient terms, scaling as $\mathcal{O}(|\boldsymbol{u}|z)$, giving contributions of order $\mathcal{O}(|\boldsymbol{u}|^2\frac{1}{E}z)$, which are formally of the same smallness as the subeikonal (but length-enhanced) gradient corrections, scaling as $\mathcal{O}(\frac{1}{E}z)$. These are the terms that we omit in our consideration, focusing on the two limits described above: (i) keeping the terms scaling as $\mathcal{O}(\frac{1}{E}z)$, but with no transverse flow, and (ii) keeping only the eikonal gradient corrections in the presence of a transverse flow.

Squaring $\mathcal{R}_B$ and averaging the result over the background field configurations, we find

$$\begin{aligned}\langle|\mathcal{R}_B|^2\rangle = \frac{C_F^2}{2N_c} g^2 \int_{x,\boldsymbol{q},\bar{\boldsymbol{q}}} \theta(z)\rho(\boldsymbol{x},z) e^{-i(\boldsymbol{q}-\bar{\boldsymbol{q}})\cdot\boldsymbol{x}} \times \frac{4(1-\mathrm{x})^2(\boldsymbol{k}-\mathrm{x}(\boldsymbol{p}-\boldsymbol{q}))\cdot(\boldsymbol{k}-\mathrm{x}(\boldsymbol{p}-\bar{\boldsymbol{q}}))}{(\boldsymbol{k}-\mathrm{x}(\boldsymbol{p}-\boldsymbol{q}))^2(\boldsymbol{k}-\mathrm{x}(\boldsymbol{p}-\bar{\boldsymbol{q}}))^2} v(\boldsymbol{q}) v(\bar{\boldsymbol{q}}) J(E,\boldsymbol{p}-\boldsymbol{q}) J^*(E,\boldsymbol{p}-\bar{\boldsymbol{q}}) \\ \times\left[e^{-i(\mathcal{Q}^-_{p-q}-\mathcal{Q}^-_{p-\bar{q}})z} + e^{-i(\mathcal{Q}^-_{p-k-q}-\mathcal{Q}^-_{p-k-\bar{q}})z} - e^{-i(\mathcal{Q}^-_{p-q}-\mathcal{Q}^-_{p-k-\bar{q}})z} - e^{i(\mathcal{Q}^-_{p-\bar{q}}-\mathcal{Q}^-_{p-k-q})z}\right].\end{aligned} \tag{53}$$

Accounting for the fact that this SB contribution involves two LPM phases, we find that up to the first order in gradients the corresponding contribution to the amplitude squared reads

$$\begin{aligned}\langle|\mathcal{R}_B|^2\rangle = \frac{C_F^2}{N_c} g^2 \int_0^L dz \int_{\boldsymbol{q}} \frac{4(1-\mathrm{x})^2}{(\boldsymbol{k}-\mathrm{x}(\boldsymbol{p}-\boldsymbol{q}))^2}&\left[1-\hat{\boldsymbol{g}}\cdot\left(\boldsymbol{u}-\frac{\boldsymbol{p}-\boldsymbol{q}}{2E}-\frac{\boldsymbol{p}-\boldsymbol{k}-\boldsymbol{q}}{2(1-\mathrm{x})E}\right)z\right]\\ &\times\left[1-\cos\left(\frac{(\boldsymbol{k}-\mathrm{x}(\boldsymbol{p}-\boldsymbol{q}))^2}{2\mathrm{x}(1-\mathrm{x})E}z\right)\right]\rho(z)[v(\boldsymbol{q}^2)]^2|J(E,\boldsymbol{p}-\boldsymbol{q})|^2.\end{aligned}\tag{54}$$

The last SB contribution $\mathcal{R}_C$, corresponding to the final-state scattering process in the emitted gluon line, also involves two LPM phases, and, after squaring and averaging, it reads

$$\begin{aligned}\langle|\mathcal{R}_C|^2\rangle = \frac{C_F C_A}{2N_c} g^2 &\int_{x,\boldsymbol{q},\bar{\boldsymbol{q}}} \theta(z)\rho(\boldsymbol{x},z)e^{-i(\boldsymbol{q}-\bar{\boldsymbol{q}})\cdot\boldsymbol{x}}\\ &\times\frac{4(1-\mathrm{x})^2(\boldsymbol{k}-(1-\mathrm{x})\boldsymbol{q}-\mathrm{x}\boldsymbol{p})\cdot(\boldsymbol{k}-(1-\mathrm{x})\bar{\boldsymbol{q}}-\mathrm{x}\boldsymbol{p})}{(\boldsymbol{k}-(1-\mathrm{x})\boldsymbol{q}-\mathrm{x}\boldsymbol{p})^2(\boldsymbol{k}-(1-\mathrm{x})\bar{\boldsymbol{q}}-\mathrm{x}\boldsymbol{p})^2}v(\boldsymbol{q})v(\bar{\boldsymbol{q}})J(E,\boldsymbol{p}-\boldsymbol{q})J^*(E,\boldsymbol{p}-\bar{\boldsymbol{q}})\\ &\times\left[e^{-i(\mathcal{Q}^-_{p-q}-\mathcal{Q}^-_{p-\bar{q}})z}+e^{-i(\mathcal{Q}^-_{k-q}-\mathcal{Q}^-_{k-\bar{q}})z}-e^{-i(\mathcal{Q}^-_{p-q}-\mathcal{Q}^-_{k-\bar{q}})z}-e^{i(\mathcal{Q}^-_{p-\bar{q}}-\mathcal{Q}^-_{k-q})z}\right].\end{aligned}\tag{55}$$

As in the cases of $\mathcal{R}_A$ and $\mathcal{R}_B$, the only nonvanishing contribution to the linear gradient correction comes from the derivative acting on the phases, and we find

$$\begin{aligned}\langle|\mathcal{R}_C|^2\rangle = C_F g^2 \int_0^L dz \int_{\boldsymbol{q}} \frac{4(1-\mathrm{x})^2}{(\boldsymbol{k}-(1-\mathrm{x})\boldsymbol{q}-\mathrm{x}\boldsymbol{p})^2}&\left[1-\hat{\boldsymbol{g}}\cdot\left(\boldsymbol{u}-\frac{\boldsymbol{p}-\boldsymbol{q}}{2E}-\frac{\boldsymbol{k}-\boldsymbol{q}}{2\mathrm{x}E}\right)z\right]\\ &\times\left[1-\cos\left(\frac{(\boldsymbol{k}-(1-\mathrm{x})\boldsymbol{q}-\mathrm{x}\boldsymbol{p})^2}{2\mathrm{x}(1-\mathrm{x})E}z\right)\right]\rho(z)[v(\boldsymbol{q}^2)]^2|J(E,\boldsymbol{p}-\boldsymbol{q})|^2.\end{aligned}\tag{56}$$

The three SB interference terms can be computed following the very same procedure—the $\boldsymbol{x}$ dependence of the matter parameters is expressed through the corresponding momentum derivatives. However, the light-front wave functions are structurally different in the direct and conjugated amplitudes, and that results in a new class of gradient corrections. For instance, the interference term $\langle\mathcal{R}_A\mathcal{R}_B^*\rangle$ can be written as

$$\begin{aligned}\langle\mathcal{R}_A\mathcal{R}_B^*\rangle+\text{c.c.}=\frac{C_F}{N_c^2}g^2\int_0^L dz\int_{\boldsymbol{q}}&\frac{2(1-\mathrm{x})^2(\boldsymbol{k}-\mathrm{x}\boldsymbol{p})\cdot(\boldsymbol{k}-\mathrm{x}(\boldsymbol{p}-\boldsymbol{q}))}{(\boldsymbol{k}-\mathrm{x}\boldsymbol{p})^2(\boldsymbol{k}-\mathrm{x}(\boldsymbol{p}-\boldsymbol{q}))^2}\left\{[1-\hat{\boldsymbol{g}}\cdot\boldsymbol{u}z]\left[1-\cos\left(\frac{(\boldsymbol{k}-\mathrm{x}(\boldsymbol{p}-\boldsymbol{q}))^2}{2\mathrm{x}(1-\mathrm{x})E}z\right)\right]\right.\\ &+\hat{\boldsymbol{g}}\cdot\left(\frac{\boldsymbol{p}-\boldsymbol{q}}{E}z-\left(\frac{\boldsymbol{p}-\boldsymbol{q}}{2E}z+\frac{\boldsymbol{p}-\boldsymbol{k}-\boldsymbol{q}}{2(1-\mathrm{x})E}z\right)\cos\left(\frac{(\boldsymbol{k}-\mathrm{x}(\boldsymbol{p}-\boldsymbol{q}))^2}{2\mathrm{x}(1-\mathrm{x})E}z\right)\right)\\ &\left.-\mathrm{x}\hat{\boldsymbol{g}}\cdot\left(\frac{\boldsymbol{k}-\mathrm{x}(\boldsymbol{p}-\boldsymbol{q})}{(\boldsymbol{k}-\mathrm{x}(\boldsymbol{p}-\boldsymbol{q}))^2}-\frac{\boldsymbol{k}-\mathrm{x}\boldsymbol{p}}{2(\boldsymbol{k}-\mathrm{x}\boldsymbol{p})\cdot(\boldsymbol{k}-\mathrm{x}(\boldsymbol{p}-\boldsymbol{q}))}\right)\sin\left(\frac{(\boldsymbol{k}-\mathrm{x}(\boldsymbol{p}-\boldsymbol{q}))^2}{2\mathrm{x}(1-\mathrm{x})E}z\right)\right\}\rho[v(\boldsymbol{q}^2)]^2|J(E,\boldsymbol{p}-\boldsymbol{q})|^2,\end{aligned}\tag{57}$$

where the sine phase structure has no explicit length enhancement since it involves no momentum derivatives of the LPM phases. In turn, the two other combinations read

$$\begin{aligned}\langle\mathcal{R}_A\mathcal{R}_C^*\rangle+\text{c.c.}=-C_F g^2\int_0^L dz\int_{\boldsymbol{q}}&\frac{2(1-\mathrm{x})^2(\boldsymbol{k}-\mathrm{x}\boldsymbol{p})\cdot(\boldsymbol{k}-(1-\mathrm{x})\boldsymbol{q}-\mathrm{x}\boldsymbol{p})}{(\boldsymbol{k}-\mathrm{x}\boldsymbol{p})^2(\boldsymbol{k}-(1-\mathrm{x})\boldsymbol{q}-\mathrm{x}\boldsymbol{p})^2}\left\{[1-\hat{\boldsymbol{g}}\cdot\boldsymbol{u}z]\left[1-\cos\left(\frac{(\boldsymbol{k}-(1-\mathrm{x})\boldsymbol{q}-\mathrm{x}\boldsymbol{p})^2}{2\mathrm{x}(1-\mathrm{x})E}z\right)\right]\right.\\ &+\hat{\boldsymbol{g}}\cdot\left[\frac{\boldsymbol{p}-\boldsymbol{q}}{E}z-\left(\frac{\boldsymbol{p}-\boldsymbol{q}}{2E}z+\frac{\boldsymbol{k}-\boldsymbol{q}}{2\mathrm{x}E}z\right)\cos\left(\frac{\boldsymbol{k}-(1-\mathrm{x})\boldsymbol{q}-\mathrm{x}\boldsymbol{p}^2}{2\mathrm{x}(1-\mathrm{x})E}z\right)\right]\\ &+(1-\mathrm{x})\hat{\boldsymbol{g}}\cdot\left(\frac{\boldsymbol{k}-(1-\mathrm{x})\boldsymbol{q}-\mathrm{x}\boldsymbol{p}}{(\boldsymbol{k}-(1-\mathrm{x})\boldsymbol{q}-\mathrm{x}\boldsymbol{p})^2}-\frac{\boldsymbol{k}-\mathrm{x}\boldsymbol{p}}{2(\boldsymbol{k}-\mathrm{x}\boldsymbol{p})\cdot(\boldsymbol{k}-(1-\mathrm{x})\boldsymbol{q}-\mathrm{x}\boldsymbol{p})}\right)\\ &\left.\times\sin\left(\frac{(\boldsymbol{k}-(1-\mathrm{x})\boldsymbol{q}-\mathrm{x}\boldsymbol{p})^2}{2\mathrm{x}(1-\mathrm{x})E}z\right)\right\}\rho[v(\boldsymbol{q}^2)]^2|J(E,\boldsymbol{p}-\boldsymbol{q})|^2,\end{aligned}\tag{58}$$

and

$$\begin{aligned}\langle\mathcal{R}_B\mathcal{R}_C^*\rangle+\text{c.c.}=&-C_Fg^2\int_0^L dz\int_{\boldsymbol{q}}\frac{2(1-\mathrm{x})^2(\boldsymbol{k}-\mathrm{x}(\boldsymbol{p}-\boldsymbol{q}))\cdot(\boldsymbol{k}-(1-\mathrm{x})\boldsymbol{q}-\mathrm{x}\boldsymbol{p})}{(\boldsymbol{k}-\mathrm{x}(\boldsymbol{p}-\boldsymbol{q}))^2(\boldsymbol{k}-(1-\mathrm{x})\boldsymbol{q}-\mathrm{x}\boldsymbol{p})^2}\\
&\times\left\{[1-\hat{\boldsymbol{g}}\cdot\boldsymbol{u}z]\left[1+\cos\left(\frac{\boldsymbol{q}\cdot(2\boldsymbol{k}-(1-2\mathrm{x})\boldsymbol{q}-2\mathrm{x}\boldsymbol{p})}{2\mathrm{x}(1-\mathrm{x})E}z\right)\right.\right.\\
&\left.-\cos\left(\frac{(\boldsymbol{k}-(1-\mathrm{x})\boldsymbol{q}-\mathrm{x}\boldsymbol{p})^2}{2\mathrm{x}(1-\mathrm{x})E}z\right)-\cos\left(\frac{(\boldsymbol{k}-\mathrm{x}(\boldsymbol{p}-\boldsymbol{q}))^2}{2\mathrm{x}(1-\mathrm{x})E}z\right)\right]\\
&+\hat{\boldsymbol{g}}\cdot\left[\frac{\boldsymbol{p}-\boldsymbol{q}}{E}z-\left(\frac{\boldsymbol{p}-\boldsymbol{q}}{2E}z+\frac{\boldsymbol{p}-\boldsymbol{k}-\boldsymbol{q}}{2(1-\mathrm{x})E}z\right)\cos\left(\frac{(\boldsymbol{k}-\mathrm{x}(\boldsymbol{p}-\boldsymbol{q}))^2}{2\mathrm{x}(1-\mathrm{x})E}z\right)\right.\\
&-\left(\frac{\boldsymbol{p}-\boldsymbol{q}}{2E}z+\frac{\boldsymbol{k}-\boldsymbol{q}}{2\mathrm{x}E}z\right)\cos\left(\frac{(\boldsymbol{k}-(1-\mathrm{x})\boldsymbol{q}-\mathrm{x}\boldsymbol{p})^2}{2\mathrm{x}(1-\mathrm{x})E}z\right)\\
&\left.+\left(\frac{\boldsymbol{p}-\boldsymbol{k}-\boldsymbol{q}}{2(1-\mathrm{x})E}z+\frac{\boldsymbol{k}-\boldsymbol{q}}{2\mathrm{x}E}z\right)\cos\left(\frac{\boldsymbol{q}\cdot(2\boldsymbol{k}-(1-2\mathrm{x})\boldsymbol{q}-2\mathrm{x}\boldsymbol{p})}{2\mathrm{x}(1-\mathrm{x})E}z\right)\right]\\
&-\hat{\boldsymbol{g}}\cdot\left((1-\mathrm{x})\frac{\boldsymbol{k}-(1-\mathrm{x})\boldsymbol{q}-\mathrm{x}\boldsymbol{p}}{(\boldsymbol{k}-(1-\mathrm{x})\boldsymbol{q}-\mathrm{x}\boldsymbol{p})^2}-\frac{\boldsymbol{k}-\mathrm{x}\boldsymbol{p}}{2(\boldsymbol{k}-\mathrm{x}(\boldsymbol{p}-\boldsymbol{q}))\cdot(\boldsymbol{k}-(1-\mathrm{x})\boldsymbol{q}-\mathrm{x}\boldsymbol{p})}\right.\\
&\left.+\mathrm{x}\frac{\boldsymbol{k}-\mathrm{x}(\boldsymbol{p}-\boldsymbol{q})}{(\boldsymbol{k}-\mathrm{x}(\boldsymbol{p}-\boldsymbol{q}))^2}\right)\left[\sin\left(\frac{(\boldsymbol{k}-\mathrm{x}(\boldsymbol{p}-\boldsymbol{q}))^2}{2\mathrm{x}(1-\mathrm{x})E}z\right)\right.\\
&\left.\left.-\sin\left(\frac{(\boldsymbol{k}-(1-\mathrm{x})\boldsymbol{q}-\mathrm{x}\boldsymbol{p})^2}{2\mathrm{x}(1-\mathrm{x})E}z\right)-\sin\left(\frac{\boldsymbol{q}\cdot(2\boldsymbol{k}-(1-2\mathrm{x})\boldsymbol{q}-2\mathrm{x}\boldsymbol{p})}{2\mathrm{x}(1-\mathrm{x})E}z\right)\right]\right\}\\
&\times\rho(z)[v(\boldsymbol{q}^2)]^2|J(E,\boldsymbol{p}-\boldsymbol{q})|^2,\end{aligned}\tag{59}$$

where the color factors can also be verified in the limit of homogeneous matter.

B. Double Born diagrams

Here, we consider the six DB contributions in the amplitude of the gluon radiation, see Fig. 4. Following [21], we note that, after averaging over medium configurations, the propagator poles, governing the q_{1z} integral, cancel q_{2z} in the exponential factors (except for a part of $\mathcal{R}_G$), and the contour can be closed in both directions. The scattering potentials are needed for convergence and should be taken into account explicitly.

Starting with $\mathcal{R}_D$, corresponding to the case of two initial-state scatterings, we find its contribution to the squared amplitude,

$$\begin{aligned}\langle\mathcal{R}_D\mathcal{R}_0^*\rangle+\text{c.c.}=&\,i\frac{C_F^2}{N_c}g^2\int_{x,\boldsymbol{q}_1,\boldsymbol{q}_2}\theta(z)\rho(\boldsymbol{x},z)\frac{4(1-\mathrm{x})^2}{(\boldsymbol{k}-\mathrm{x}\boldsymbol{p})^2}J^*(E,\boldsymbol{p}-\boldsymbol{q}_1-\boldsymbol{q}_2)J(E,\boldsymbol{p})\\
&\times\left[e^{-i(\boldsymbol{q}_1+\boldsymbol{q}_2)\cdot\boldsymbol{x}}e^{-i\mathcal{Q}^-_{p-q_1-q_2}z}\mathcal{I}_D-e^{i(\boldsymbol{q}_1+\boldsymbol{q}_2)\cdot\boldsymbol{x}}e^{i\mathcal{Q}^-_{p-q_1-q_2}z}\mathcal{I}_D^*\right],\end{aligned}\tag{60}$$

where the integral $\mathcal{I}_D$ is defined as

$$\mathcal{I}_D=\int\frac{dq_{2z}}{2\pi}\frac{Ev(q_2)v(\tilde{q}_1)}{(q_{2z}-\mathcal{Q}^+_{p-q_2}-i\epsilon)(q_{2z}-\mathcal{Q}^-_{p-q_2}+i\epsilon)},\tag{61}$$

with $\tilde{q}_{1\mu}=(\boldsymbol{u}\cdot\boldsymbol{q}_1,\boldsymbol{q}_1,-q_{2z}+\mathcal{Q}^-_{p-q_1-q_2})$. This integral can be explicitly evaluated, and since it involves no length-enhanced terms, we keep only its eikonal part. Then,

$$\begin{aligned}\mathrm{Im}\mathcal{I}_D(\boldsymbol{q},-\boldsymbol{q})&\simeq\frac{1}{4}[v(\boldsymbol{q}^2)]^2,\\
\mathrm{Re}\mathcal{I}_D(\boldsymbol{q},-\boldsymbol{q})&\simeq\frac{2(\boldsymbol{u}\cdot\boldsymbol{q})^3-3(\boldsymbol{u}\cdot\boldsymbol{q})(\mu^2+\boldsymbol{q}^2)}{8R_0^3}[v(\boldsymbol{q}^2)]^2,\end{aligned}\tag{62}$$

where R_0 is given by (21) at $u_z = 0$. One should also note that $\frac{\partial}{\partial(\boldsymbol{q}_1+\boldsymbol{q}_2)} \mathrm{Re}\mathcal{I}_D \Big|_{\boldsymbol{q}_1=-\boldsymbol{q}_2} = 0$, and it results in no eikonal gradient corrections. Thus, keeping only the terms with nonzero angular average, we find

$$\langle \mathcal{R}_D \mathcal{R}_0^* \rangle + \text{c.c.} = -\frac{C_F^2}{N_c} g^2 \int_0^L dz \int_{\boldsymbol{q}} \frac{2(1-\mathrm{x})^2}{(\boldsymbol{k}-\mathrm{x}\boldsymbol{p})^2} \left[1 - \hat{\boldsymbol{g}} \cdot \left(\boldsymbol{u} - \frac{\boldsymbol{p}}{E} \right) z \right] \cos\left(\frac{(\boldsymbol{k}-\mathrm{x}\boldsymbol{p})^2}{2\mathrm{x}(1-\mathrm{x})E} z \right) \rho(z) [v(\boldsymbol{q}^2)]^2 |J(E,\boldsymbol{p})|^2. \tag{63}$$

Similarly, for the contribution to the amplitude squared with two final-state scatterings in the quark line $\mathcal{R}_E$, we find[6]

$$\langle \mathcal{R}_E \mathcal{R}_0^* \rangle + \text{c.c.} = -i \frac{C_F^2}{N_c} g^2 \int_{x,\boldsymbol{q}_1,\boldsymbol{q}_2} \theta(z) \rho(\boldsymbol{x}, z) \frac{4(1-\mathrm{x})^2 (\boldsymbol{k}-\mathrm{x}\boldsymbol{p}) \cdot (\boldsymbol{k} - \mathrm{x}(\boldsymbol{p}-\boldsymbol{q}_1-\boldsymbol{q}_2))}{(\boldsymbol{k}-\mathrm{x}\boldsymbol{p})^2 (\boldsymbol{k}-\mathrm{x}(\boldsymbol{p}-\boldsymbol{q}_1-\boldsymbol{q}_2))^2} J(E,\boldsymbol{p}) J(E,\boldsymbol{p}-\boldsymbol{q}_1-\boldsymbol{q}_2)$$
$$\times \left[e^{-i(\boldsymbol{q}_1+\boldsymbol{q}_2)\cdot \boldsymbol{x}} \left(e^{-i\mathcal{Q}^-_{p-q_1-q_2} z} - e^{-i\mathcal{Q}^-_{p-k-q_1-q_2} z} \right) \mathcal{I}_E - e^{i(\boldsymbol{q}_1+\boldsymbol{q}_2)\cdot \boldsymbol{x}} \left(e^{i\mathcal{Q}^-_{p-q_1-q_2} z} - e^{i\mathcal{Q}^-_{p-k-q_1-q_2} z} \right) \mathcal{I}_E^* \right], \tag{64}$$

where

$$\mathcal{I}_E = \int \frac{dq_{2z}}{2\pi} \frac{(1-\mathrm{x}) E v(q_2) v(\tilde{q}_1)}{(q_{2z} - \mathcal{Q}^+_{p-k-q_2} - i\epsilon)(q_{2z} - \mathcal{Q}^-_{p-k-q_2} + i\epsilon)}, \tag{65}$$

with $\tilde{q}_{1\mu} = (\boldsymbol{u}\cdot \boldsymbol{q}_1, \boldsymbol{q}_1, -q_{2z} + \mathcal{Q}^-_{p-k-q_1-q_2})$. Evaluating this integral, one may note that at the leading order in the eikonal expansion $\mathcal{I}_E \simeq \mathcal{I}_D$, and we can again utilize (62). Thus, expanding in gradients, we find that

$$\langle \mathcal{R}_E \mathcal{R}_0^* \rangle + \text{c.c.} = -\frac{C_F^2}{N_c} g^2 \int_0^L dz \int_{\boldsymbol{q}} \frac{2(1-\mathrm{x})^2}{(\boldsymbol{k}-\mathrm{x}\boldsymbol{p})^2} \Bigg\{ [1 - \hat{\boldsymbol{g}} \cdot \boldsymbol{u} z]$$
$$\times \left[1 - \cos\left(\frac{(\boldsymbol{k}-\mathrm{x}\boldsymbol{p})^2}{2\mathrm{x}(1-\mathrm{x})E} z \right) \right] + \hat{\boldsymbol{g}} \cdot \left(\frac{\boldsymbol{p}-\boldsymbol{k}}{(1-\mathrm{x})E} z - \frac{\boldsymbol{p}}{E} z \cos\left(\frac{(\boldsymbol{k}-\mathrm{x}\boldsymbol{p})^2}{2\mathrm{x}(1-\mathrm{x})E} z \right) \right)$$
$$+ \mathrm{x} \hat{\boldsymbol{g}} \cdot \frac{\boldsymbol{k}-\mathrm{x}\boldsymbol{p}}{(\boldsymbol{k}-\mathrm{x}\boldsymbol{p})^2} \sin\left(\frac{(\boldsymbol{k}-\mathrm{x}\boldsymbol{p})^2}{2\mathrm{x}(1-\mathrm{x})E} z \right) \Bigg\} \rho(z) [v(\boldsymbol{q}^2)]^2 |J(E,\boldsymbol{p})|^2. \tag{66}$$

Turning to the contribution with two final-state scatterings in the gluon line, we have to deal with a product of two gluon propagators and two three-gluon vertices. As in the case of $\mathcal{R}_C$ above, this product does not depend on the z component of momenta since $N^{\mu\nu}$, u_μ, and ϵ^*_μ are transverse to n_μ, resulting in no new poles. Averaging the corresponding contribution to the amplitude squared, we write it as

$$\langle \mathcal{R}_F \mathcal{R}_0^* \rangle + \text{c.c.} = -i \frac{C_F}{2} g^2 \int_{x,\boldsymbol{q}_1,\boldsymbol{q}_2} \theta(z) \rho(\boldsymbol{x}, z) \frac{8(1-\mathrm{x})^2 (\boldsymbol{k}-\mathrm{x}\boldsymbol{p}) \cdot (\boldsymbol{k} - (1-\mathrm{x})(\boldsymbol{q}_1+\boldsymbol{q}_2) - \mathrm{x}\boldsymbol{p})}{(\boldsymbol{k}-\mathrm{x}\boldsymbol{p})^2 (\boldsymbol{k} - (1-\mathrm{x})(\boldsymbol{q}_1+\boldsymbol{q}_2) - \mathrm{x}\boldsymbol{p})^2} J(E,\boldsymbol{p}) J^*(E,\boldsymbol{p}-\boldsymbol{q}_1-\boldsymbol{q}_2)$$
$$\times \left[e^{-i(\boldsymbol{q}_1+\boldsymbol{q}_2)\cdot \boldsymbol{x}} \left(e^{-i\mathcal{Q}^-_{p-q_1-q_2} z} - e^{-i\mathcal{Q}^-_{k-q_1-q_2} z} \right) \mathcal{I}_F - e^{i(\boldsymbol{q}_1+\boldsymbol{q}_2)\cdot \boldsymbol{x}} \left(e^{i\mathcal{Q}^-_{p-q_1-q_2} z} - e^{i\mathcal{Q}^-_{k-q_1-q_2} z} \right) \mathcal{I}_F^* \right], \tag{67}$$

where

$$\mathcal{I}_F = \int \frac{dq_{2z}}{2\pi} \frac{\mathrm{x} E v(q_2) v(\tilde{q}_1)}{(q_{2z} - \mathcal{Q}^+_{k-q_2} - i\epsilon)(q_{2z} - \mathcal{Q}^-_{k-q_2} + i\epsilon)}, \tag{68}$$

with $\tilde{q}_{1\mu} = (\boldsymbol{u}\cdot \boldsymbol{q}_1, \boldsymbol{q}_1, -q_{2z} + \mathcal{Q}^-_{k-q_1-q_2})$. At the leading order in the eikonal expansion, one finds that $\mathcal{I}_F \simeq \mathcal{I}_D$, and we can again utilize (62). Expanding in gradients and treating $\boldsymbol{x}$ integral in the same fashion, one finds

---

[6] Taking the first q_{1z} integral, we pick up two residues, corresponding to the poles $\mathcal{Q}^-_{p-q_1-q_2}$ and $\mathcal{Q}^-_{p-k-q_1-q_2}$. At eikonal order, the scattering potentials look the same for both residues and the Fourier phases can be pulled out as a common factor for $\mathcal{I}_E$.

$$\langle\mathcal{R}_F\mathcal{R}_0^*\rangle+\text{c.c.}=-C_Fg^2\int_0^L dz\int_{\boldsymbol{q}}\frac{2(1-\mathrm{x})^2}{(\boldsymbol{k}-\mathrm{x}\boldsymbol{p})^2}\left\{[1-\hat{\boldsymbol{g}}\cdot\boldsymbol{u}z]\left[1-\cos\left(\frac{(\boldsymbol{k}-\mathrm{x}\boldsymbol{p})^2}{2\mathrm{x}(1-\mathrm{x})E}z\right)\right]+\hat{\boldsymbol{g}}\cdot\left(\frac{\boldsymbol{k}}{\mathrm{x}E}z-\frac{\boldsymbol{p}}{E}z\cos\left(\frac{(\boldsymbol{k}-\mathrm{x}\boldsymbol{p})^2}{2\mathrm{x}(1-\mathrm{x})E}z\right)\right)\right.$$
$$\left.-(1-\mathrm{x})\hat{\boldsymbol{g}}\cdot\frac{\boldsymbol{k}-\mathrm{x}\boldsymbol{p}}{(\boldsymbol{k}-\mathrm{x}\boldsymbol{p})^2}\sin\left(\frac{(\boldsymbol{k}-\mathrm{x}\boldsymbol{p})^2}{2\mathrm{x}(1-\mathrm{x})E}z\right)\right\}\rho(z)[v(\boldsymbol{q}^2)]^2|J(E,\boldsymbol{p})|^2. \tag{69}$$

Now we can turn to a more involved diagram, having two final-state scatterings in different lines. The corresponding contribution to the amplitude squared can be written as

$$\langle\mathcal{R}_G\mathcal{R}_0^*\rangle+\text{c.c.}=i\frac{C_F}{2}g^2\int_{x,\boldsymbol{q}_1,\boldsymbol{q}_2}\theta(z)\rho(\boldsymbol{x},z)\frac{4(1-\mathrm{x})(\boldsymbol{k}-\mathrm{x}\boldsymbol{p})\cdot(\boldsymbol{k}-\boldsymbol{q}_2-\mathrm{x}(\boldsymbol{p}-\boldsymbol{q}_1-\boldsymbol{q}_2))}{(\boldsymbol{k}-\mathrm{x}\boldsymbol{p})^2}$$
$$\times J(E,\boldsymbol{p})J^*(E,\boldsymbol{p}-\boldsymbol{q}_1-\boldsymbol{q}_2)\left[e^{-i(\boldsymbol{q}_1+\boldsymbol{q}_2)\cdot\boldsymbol{x}}\left(e^{-i(\mathcal{Q}^-_{k-q_2}+\mathcal{Q}^-_{p-k-q_1})z}-e^{-i\mathcal{Q}^-_{p-q_1-q_2}z}\right)\mathcal{I}_G\right.$$
$$\left.-e^{i(\boldsymbol{q}_1+\boldsymbol{q}_2)\cdot\boldsymbol{x}}\left(e^{i(\mathcal{Q}^-_{k-q_2}+\mathcal{Q}^-_{p-k-q_1})z}-e^{i\mathcal{Q}^-_{p-q_1-q_2}z}\right)\mathcal{I}_G^*\right], \tag{70}$$

where $\mathcal{I}_G\equiv\left(e^{-i(\mathcal{Q}^-_{k-q_2}+\mathcal{Q}^-_{p-k-q_1})z}-e^{-i\mathcal{Q}^-_{p-q_1-q_2}z}\right)^{-1}\bar{\mathcal{I}}_G$, and

$$\bar{\mathcal{I}}_G\equiv\int\frac{dq_{2z}}{2\pi}\frac{Ev(q_2)}{(q_{2z}-\mathcal{Q}^+_{k-q_2}-i\epsilon)(q_{2z}-\mathcal{Q}^-_{k-q_2}+i\epsilon)(q_{2z}-\mathcal{Q}^+_{p-q_1-q_2}+\mathcal{Q}^-_{p-k-q_1}-i\epsilon)}$$
$$\left[\frac{v(q_1')e^{-i(\mathcal{Q}^+_{p-k-q_1}+q_{2z})z}}{q_{2z}+\mathcal{Q}^-_{p-k-q_1}-\mathcal{Q}^+_{p-q_1-q_2}-i\epsilon}-\frac{(1-x)v(\tilde{q}_1)e^{-i\mathcal{Q}^+_{p-q_1-q_2}z}}{-q_{2z}+\mathcal{Q}^+_{p-q_1-q_2}-\mathcal{Q}^+_{p-k-q_1}-i\epsilon}\right], \tag{71}$$

with $q'_{1\mu}=(\boldsymbol{u}\cdot\boldsymbol{q}_1,\boldsymbol{q}_1,\mathcal{Q}^+_{p-k-q_1})$ and $\tilde{q}_{1\mu}=(\boldsymbol{u}\cdot\boldsymbol{q}_1,\boldsymbol{q}_1,-q_{2z}+\mathcal{Q}^+_{p-q_1-q_2})$. Evaluating this integral, we close the contour below the real axis so the explicit exponential factor can be utilized. In the eikonal limit, we further find that

$$\begin{aligned}&\mathrm{Im}\mathcal{I}_G(\boldsymbol{q}_1,\boldsymbol{q}_2)\simeq-\frac{1}{2}\frac{(1-\mathrm{x})}{(\boldsymbol{k}-\boldsymbol{q}_2-\mathrm{x}(\boldsymbol{p}-\boldsymbol{q}_1-\boldsymbol{q}_2))^2}v(\boldsymbol{q}_1^2)v(\boldsymbol{q}_2^2),\\&\mathrm{Re}\mathcal{I}_G(\boldsymbol{q}_1,\boldsymbol{q}_2)\simeq 0.\end{aligned} \tag{72}$$

Thus, the corresponding contribution to the amplitude squared reads

$$\langle\mathcal{R}_G\mathcal{R}_0^*\rangle+\text{c.c.}=C_Fg^2\int_0^L dz\int_{\boldsymbol{q}}\frac{2(1-\mathrm{x})^2(\boldsymbol{k}-\mathrm{x}\boldsymbol{p})\cdot(\boldsymbol{k}+\boldsymbol{q}-\mathrm{x}\boldsymbol{p})}{(\boldsymbol{k}-\mathrm{x}\boldsymbol{p})^2(\boldsymbol{k}+\boldsymbol{q}-\mathrm{x}\boldsymbol{p})^2}$$
$$\times\left\{[1-\hat{\boldsymbol{g}}\cdot\boldsymbol{u}z]\left[\cos\left(\frac{\boldsymbol{q}\cdot(2(\boldsymbol{k}-\mathrm{x}\boldsymbol{p})+\boldsymbol{q})}{2\mathrm{x}(1-\mathrm{x})E}z\right)-\cos\left(\frac{(\boldsymbol{k}-\mathrm{x}\boldsymbol{p})^2}{2\mathrm{x}(1-\mathrm{x})E}z\right)\right]\right.$$
$$+\hat{\boldsymbol{g}}\cdot\left(\frac{\boldsymbol{p}-\boldsymbol{k}-\boldsymbol{q}}{2(1-\mathrm{x})E}z+\frac{\boldsymbol{k}+\boldsymbol{q}}{2\mathrm{x}E}z\right)\cos\left(\frac{\boldsymbol{q}\cdot(2(\boldsymbol{k}-\mathrm{x}\boldsymbol{p})+\boldsymbol{q})}{2\mathrm{x}(1-\mathrm{x})E}z\right)-\hat{\boldsymbol{g}}\cdot\frac{\boldsymbol{p}}{E}z\cos\left(\frac{(\boldsymbol{k}-\mathrm{x}\boldsymbol{p})^2}{2\mathrm{x}(1-\mathrm{x})E}z\right)$$
$$+\left(\mathrm{x}-\frac{1}{2}\right)\hat{\boldsymbol{g}}\cdot\left(2\frac{\boldsymbol{k}+\boldsymbol{q}-\mathrm{x}\boldsymbol{p}}{(\boldsymbol{k}+\boldsymbol{q}-\mathrm{x}\boldsymbol{p})^2}-\frac{\boldsymbol{k}-\mathrm{x}\boldsymbol{p}}{(\boldsymbol{k}-\mathrm{x}\boldsymbol{p})\cdot(\boldsymbol{k}+\boldsymbol{q}-\mathrm{x}\boldsymbol{p})}\right)$$
$$\left.\times\left[\sin\left(\frac{\boldsymbol{q}\cdot(2(\boldsymbol{k}-\mathrm{x}\boldsymbol{p})+\boldsymbol{q})}{2\mathrm{x}(1-\mathrm{x})E}z\right)+\sin\left(\frac{(\boldsymbol{k}-\mathrm{x}\boldsymbol{p})^2}{2\mathrm{x}(1-\mathrm{x})E}z\right)\right]\right\}\rho(z)[v(\boldsymbol{q}^2)]^2|J(E,\boldsymbol{p})|^2, \tag{73}$$

where the gradient corrections have been treated in the same way as before.

The two remaining DB diagrams are not expected to contribute in the eikonal limit, since they have the gluon emission vertex in between the two interactions, attached to the same source. Starting with the case of initial- and final-state scatterings in the quark lines, we can write the corresponding contribution as

$$\langle \mathcal{R}_H \mathcal{R}_0^* \rangle + \text{c.c.} = i\frac{C_F}{N_c^2} g^2 \int_{x,\boldsymbol{q}_1,\boldsymbol{q}_2} \theta(z)\rho(\boldsymbol{x},z)\frac{4(1-\mathrm{x})^2(\boldsymbol{k}-\mathrm{x}\boldsymbol{p})\cdot(\boldsymbol{k}-\mathrm{x}(\boldsymbol{p}-\boldsymbol{q}_2))}{\mathrm{x}(\boldsymbol{k}-\mathrm{x}\boldsymbol{p})^2}$$
$$\times \left[e^{-i(\boldsymbol{q}_1+\boldsymbol{q}_2)\cdot\boldsymbol{x}} e^{-i\mathcal{Q}^-_{p-q_1-q_2}z}\mathcal{I}_H - e^{i(\boldsymbol{q}_1+\boldsymbol{q}_2)\cdot\boldsymbol{x}} e^{i\mathcal{Q}^-_{p-q_1-q_2}z}\mathcal{I}_H^*\right] J(E,\boldsymbol{p})J^*(E,\boldsymbol{p}-\boldsymbol{q}_1-\boldsymbol{q}_2), \tag{74}$$

where

$$\mathcal{I}_H = \int \frac{dq_{2z}}{2\pi}\frac{E v(\tilde{q}_1)v(q_2)}{(q_{2z}-\mathcal{Q}^+_{p-q_2}-i\epsilon)(q_{2z}-\mathcal{Q}^-_{p-q_2}+i\epsilon)(q_{2z}-\mathcal{Q}^+_{p-k-q_2}-i\epsilon)(q_{2z}-\mathcal{Q}^-_{p-k-q_2}+i\epsilon)}, \tag{75}$$

and $\tilde{q}_{1\mu} = (\boldsymbol{u}\cdot\boldsymbol{q}_1, \boldsymbol{q}_1, -q_{2z}+\mathcal{Q}^-_{p-q_1-q_2})$. Evaluating this integral, we indeed find that it is energy suppressed $\mathcal{I}_H = \mathcal{O}(\frac{1}{E})$, and $\mathcal{R}_H$ does not contribute in the considered limit.

Similarly, turning to the last contribution with initial-state scattering in the quark line and final-state scattering in the gluon line, we write it as

$$\langle \mathcal{R}_I \mathcal{R}_0^* \rangle + \text{c.c.} = -i\frac{C_F}{2} g^2 \int_{x,\boldsymbol{q}_1,\boldsymbol{q}_2} \theta(z)\rho(\boldsymbol{x},z)\frac{4(1-\mathrm{x})(\boldsymbol{k}-\mathrm{x}\boldsymbol{p})\cdot(\boldsymbol{k}-(1-\mathrm{x})\boldsymbol{q}_2-\mathrm{x}\boldsymbol{p})}{(\boldsymbol{k}-\mathrm{x}\boldsymbol{p})^2}$$
$$\times \left[e^{-i(\boldsymbol{q}_1+\boldsymbol{q}_2)\cdot\boldsymbol{x}} e^{-i\mathcal{Q}^-_{p-q_1-q_2}z}\mathcal{I}_I - e^{i(\boldsymbol{q}_1+\boldsymbol{q}_2)\cdot\boldsymbol{x}} e^{i\mathcal{Q}^-_{p-q_1-q_2}z}\mathcal{I}_I^*\right] J(E,\boldsymbol{p})J^*(E,\boldsymbol{p}-\boldsymbol{q}_1-\boldsymbol{q}_2), \tag{76}$$

where

$$\mathcal{I}_I = \int \frac{dq_{2z}}{2\pi}\frac{E v(\tilde{q}_1)v(q_2)}{(q_{2z}-\mathcal{Q}^+_{p-q_2}-i\epsilon)(q_{2z}-\mathcal{Q}^-_{p-q_2}+i\epsilon)(q_{2z}-\mathcal{Q}^+_{k-q_2}-i\epsilon)(q_{2z}-\mathcal{Q}^-_{k-q_2}+i\epsilon)}, \tag{77}$$

and $\tilde{q}_{1\mu} = (\boldsymbol{u}\cdot\boldsymbol{q}_1, \boldsymbol{q}_1, -q_{2z}+\mathcal{Q}^-_{p-q_1-q_2})$. One may readily show that this integral is also energy suppressed and cannot contribute to the squared amplitude in the considered limit.

C. Final distribution and its properties

The final-state parton distribution can now be expressed through the emission amplitude squared as

$$E\frac{d\mathcal{N}^{(1)}}{d^2k d\mathrm{x} d^2p dE} \equiv \frac{1}{[2(2\pi)^3]^2}\frac{1}{\mathrm{x}(1-\mathrm{x})}\langle|\mathcal{R}_{N=1}|^2\rangle, \tag{78}$$

where the superscript indicates that only $N = 1$ terms are included. It depends on the source of energetic quarks and allows for the study of how an ensemble of quarks radiates while propagating through the matter. In this work, we assume that the initial distribution $E\frac{d\mathcal{N}^{(0)}}{d^2pdE}$ is a slowly varying function of the transverse momentum, setting $E\frac{d\mathcal{N}^{(0)}}{d^2(p-q)dE} \simeq E\frac{d\mathcal{N}^{(0)}}{d^2pdE}$.

In what follows, we use a set of shorthand notation in order to make the final expressions more compact. First, we introduce the characteristic LPM phases, entering the final-state distribution,

$$\phi = \frac{(\boldsymbol{k}-\mathrm{x}(\boldsymbol{p}-\boldsymbol{q}))^2}{2\mathrm{x}(1-\mathrm{x})E}z, \qquad \bar{\phi} = \frac{(\boldsymbol{k}-(1-\mathrm{x})\boldsymbol{q}-\mathrm{x}\boldsymbol{p})^2}{2\mathrm{x}(1-\mathrm{x})E}z,$$
$$\phi_0 = \frac{(\boldsymbol{k}-\mathrm{x}\boldsymbol{p})^2}{2\mathrm{x}(1-\mathrm{x})E}z, \qquad \phi_G = \frac{\boldsymbol{q}\cdot(2(\boldsymbol{k}-\mathrm{x}\boldsymbol{p})+\boldsymbol{q})}{2\mathrm{x}(1-\mathrm{x})E}z.$$

It is also convenient to reexpress the light-front wave functions through their normalized arguments,

$$\boldsymbol{\kappa} = \frac{\boldsymbol{k}-\mathrm{x}(\boldsymbol{p}-\boldsymbol{q})}{(\boldsymbol{k}-\mathrm{x}(\boldsymbol{p}-\boldsymbol{q}))^2}, \qquad \bar{\boldsymbol{\kappa}} = \frac{\boldsymbol{k}-(1-\mathrm{x})\boldsymbol{q}-\mathrm{x}\boldsymbol{p}}{(\boldsymbol{k}-(1-\mathrm{x})\boldsymbol{q}-x\boldsymbol{p})^2},$$
$$\boldsymbol{\kappa}_0 = \frac{\boldsymbol{k}-\mathrm{x}\boldsymbol{p}}{(\boldsymbol{k}-\mathrm{x}\boldsymbol{p})^2}, \qquad \boldsymbol{\kappa}_G = \frac{\boldsymbol{k}+\boldsymbol{q}-\mathrm{x}\boldsymbol{p}}{(\boldsymbol{k}+\boldsymbol{q}-\mathrm{x}\boldsymbol{p})^2}.$$

Finally, we associate the particular momentum structures in the gradient corrections with the diagrams where they appear for the first time,

$$\boldsymbol{D}_A = \frac{\boldsymbol{p}-\boldsymbol{q}}{E}z, \qquad \boldsymbol{D}_B = \frac{\boldsymbol{p}-\boldsymbol{q}}{2E}z + \frac{\boldsymbol{p}-\boldsymbol{k}-\boldsymbol{q}}{2(1-\mathrm{x})E}z, \qquad \boldsymbol{D}_C = \frac{\boldsymbol{p}-\boldsymbol{q}}{2E}z + \frac{\boldsymbol{k}-\boldsymbol{q}}{2\mathrm{x}E}z,$$
$$\boldsymbol{D}_D = \frac{\boldsymbol{p}}{E}z, \qquad \boldsymbol{D}_E = \frac{\boldsymbol{p}-\boldsymbol{k}}{(1-\mathrm{x})E}z, \qquad \boldsymbol{D}_F = \frac{\boldsymbol{k}}{\mathrm{x}E}z, \qquad \boldsymbol{D}_G = \frac{\boldsymbol{p}-\boldsymbol{k}-\boldsymbol{q}}{2(1-\mathrm{x})E}z + \frac{\boldsymbol{k}+\boldsymbol{q}}{2\mathrm{x}E}z.$$

Let us now focus on the limit of static inhomogeneous matter, setting $\boldsymbol{u} = 0$ and keeping the leading subeikonal (but length-enhanced) terms. The resulting distribution extends the consideration in [21], where the gradient corrections to the jet broadening were studied within the opacity expansion, to the case of in-medium branching. It is obtained in the full kinematics, although only up to the first order in opacity, extending the recent results for the all-order soft gluon spectrum in inhomogeneous matter in [43]. Combining the contributions to the amplitude squared derived in Sec. III at $\boldsymbol{u} = 0$, we find

$$\begin{aligned}
E\frac{d\mathcal{N}^{(1)}}{d^2k\,d\mathrm{x}\,d^2p\,dE} = {} & \frac{(1-\mathrm{x})g^2}{(2\pi)^3\mathrm{x}}\frac{C_F^2}{N_c}\left(E\frac{d\mathcal{N}^{(0)}}{d^2p\,dE}\right)\int_0^L dz\int_{\boldsymbol{q}} \\
& \times\Bigg\{\boldsymbol{\kappa}_0^2(1+\hat{\boldsymbol{g}}\cdot\boldsymbol{D}_A) + 2\boldsymbol{\kappa}^2(1-\cos\phi)(1+\hat{\boldsymbol{g}}\cdot\boldsymbol{D}_B) + 2\frac{N_c}{C_F}\bar{\boldsymbol{\kappa}}^2(1-\cos\bar{\phi})(1+\hat{\boldsymbol{g}}\cdot\boldsymbol{D}_C) \\
& + \frac{\boldsymbol{\kappa}_0\cdot\boldsymbol{\kappa}}{2C_FN_c}\left[2(1-\cos\phi) + 2\hat{\boldsymbol{g}}\cdot(\boldsymbol{D}_A-\boldsymbol{D}_B\cos\phi) - \mathrm{x}\hat{\boldsymbol{g}}\cdot\left(2\boldsymbol{\kappa}-\boldsymbol{\kappa}^2\frac{\boldsymbol{\kappa}_0}{\boldsymbol{\kappa}_0\cdot\boldsymbol{\kappa}}\right)\sin\phi\right] \\
& - \frac{N_c}{2C_F}\boldsymbol{\kappa}_0\cdot\bar{\boldsymbol{\kappa}}\left[2(1-\cos\bar{\phi}) + 2\hat{\boldsymbol{g}}\cdot(\boldsymbol{D}_A-\boldsymbol{D}_C\cos\bar{\phi}) + (1-\mathrm{x})\hat{\boldsymbol{g}}\cdot\left(2\bar{\boldsymbol{\kappa}}-\bar{\boldsymbol{\kappa}}^2\frac{\boldsymbol{\kappa}_0}{\boldsymbol{\kappa}_0\cdot\bar{\boldsymbol{\kappa}}}\right)\sin\bar{\phi}\right] \\
& - \frac{N_c}{2C_F}\boldsymbol{\kappa}\cdot\bar{\boldsymbol{\kappa}}\Bigg[2(1+\cos(\phi-\bar{\phi})-\cos\bar{\phi}-\cos\phi) \\
& + 2\hat{\boldsymbol{g}}\cdot(\boldsymbol{D}_A-\boldsymbol{D}_B\cos\phi-\boldsymbol{D}_C\cos\bar{\phi}+(\boldsymbol{D}_B+\boldsymbol{D}_C-\boldsymbol{D}_A)\cos(\phi-\bar{\phi})) \\
& - \hat{\boldsymbol{g}}\cdot\left(2(1-\mathrm{x})\bar{\boldsymbol{\kappa}} - \frac{\boldsymbol{\kappa}_0}{\boldsymbol{\kappa}_0^2}\frac{\bar{\boldsymbol{\kappa}}^2\boldsymbol{\kappa}^2}{\boldsymbol{\kappa}\cdot\bar{\boldsymbol{\kappa}}} + 2\mathrm{x}\boldsymbol{\kappa}\right)(\sin\phi-\sin\bar{\phi}-\sin(\phi-\bar{\phi}))\Bigg] \\
& - \boldsymbol{\kappa}_0^2\cos\phi_0(1+\hat{\boldsymbol{g}}\cdot\boldsymbol{D}_D) - \boldsymbol{\kappa}_0^2[(1-\cos\phi_0)+\hat{\boldsymbol{g}}\cdot(\boldsymbol{D}_E-\boldsymbol{D}_D\cos\phi_0)+\mathrm{x}\hat{\boldsymbol{g}}\cdot\boldsymbol{\kappa}_0\sin\phi_0] \\
& - \frac{N_c}{C_F}\boldsymbol{\kappa}_0^2[(1-\cos\phi_0)+\hat{\boldsymbol{g}}\cdot(\boldsymbol{D}_F-\boldsymbol{D}_D\cos\phi_0)-(1-\mathrm{x})\hat{\boldsymbol{g}}\cdot\boldsymbol{\kappa}_0\sin\phi_0] \\
& + \frac{N_c}{C_F}\boldsymbol{\kappa}_0\cdot\boldsymbol{\kappa}_G\Bigg[(\cos\phi_G-\cos\phi_0)+\hat{\boldsymbol{g}}\cdot(\boldsymbol{D}_G\cos\phi_G-\boldsymbol{D}_D\cos\phi_0) \\
& + \left(\mathrm{x}-\frac{1}{2}\right)\hat{\boldsymbol{g}}\cdot\left(2\boldsymbol{\kappa}_G-\boldsymbol{\kappa}_G^2\frac{\boldsymbol{\kappa}_0}{\boldsymbol{\kappa}_0\cdot\boldsymbol{\kappa}_G}\right)(\sin\phi_G+\sin\phi_0)\Bigg]\Bigg\}\rho(z)[v(\boldsymbol{q}^2)]^2. \qquad (79)
\end{aligned}$$

Taking the limit of homogeneous matter with $\hat{\boldsymbol{g}} = 0$, we can readily check that this expression agrees with the result for the $N = 1$ in-medium branching; see, e.g., [52].

To make the features of the final-state parton distribution more apparent, it is instructive to consider the small-x limit of (79), where the distribution is known to take a particularly simple form in the case of homogeneous matter [18]. In this limit, $\phi = \phi_0$, $\phi_G = \bar{\phi}|_{\boldsymbol{q}\to-\boldsymbol{q}} - \phi_0$, $\boldsymbol{\kappa} = \boldsymbol{\kappa}_0$, and $\boldsymbol{\kappa}_G = \bar{\boldsymbol{\kappa}}|_{\boldsymbol{q}\to-\boldsymbol{q}}$. Keeping only the subeikonal terms that scale as $\frac{1}{\mathrm{x}E}$, we set $\boldsymbol{D}_A = \boldsymbol{D}_B = \boldsymbol{D}_D = \boldsymbol{D}_E = 0$, then

$$\begin{aligned}
E\frac{d\mathcal{N}^{(1)}}{d^2k\,d\mathrm{x}\,d^2p\,dE} = {} & \frac{g^2C_F}{(2\pi)^3\mathrm{x}}\left(E\frac{d\mathcal{N}^{(0)}}{d^2p\,dE}\right)\int_0^L dz\int_{\boldsymbol{q}} \\
& \times\Bigg\{\frac{2\boldsymbol{k}\cdot\boldsymbol{q}}{\boldsymbol{k}^2(\boldsymbol{k}-\boldsymbol{q})^2}\left(1-\cos\left(\frac{(\boldsymbol{k}-\boldsymbol{q})^2}{2\mathrm{x}E}z\right)\right)\left(1+\frac{\hat{\boldsymbol{g}}\cdot(\boldsymbol{k}-\boldsymbol{q})}{2\mathrm{x}E}z\right) - \frac{\hat{\boldsymbol{g}}\cdot\boldsymbol{k}}{\boldsymbol{k}^2}\left[\frac{z}{\mathrm{x}E}-\frac{1}{\boldsymbol{k}^2}\sin\left(\frac{\boldsymbol{k}^2}{2\mathrm{x}E}z\right)\right] \\
& + \frac{\boldsymbol{k}\cdot(\boldsymbol{k}-\boldsymbol{q})}{\boldsymbol{k}^2(\boldsymbol{k}-\boldsymbol{q})^2}\left[\frac{\hat{\boldsymbol{g}}\cdot(\boldsymbol{k}-\boldsymbol{q})}{\mathrm{x}E}z - \hat{\boldsymbol{g}}\cdot\left(2\frac{\boldsymbol{k}-\boldsymbol{q}}{(\boldsymbol{k}-\boldsymbol{q})^2}-\frac{\boldsymbol{k}}{\boldsymbol{k}\cdot(\boldsymbol{k}-\boldsymbol{q})}\right)\sin\left(\frac{(\boldsymbol{k}-\boldsymbol{q})^2}{2\mathrm{x}E}z\right)\right]\Bigg\}\rho(z)[v(\boldsymbol{q}^2)]^2. \qquad (80)
\end{aligned}$$

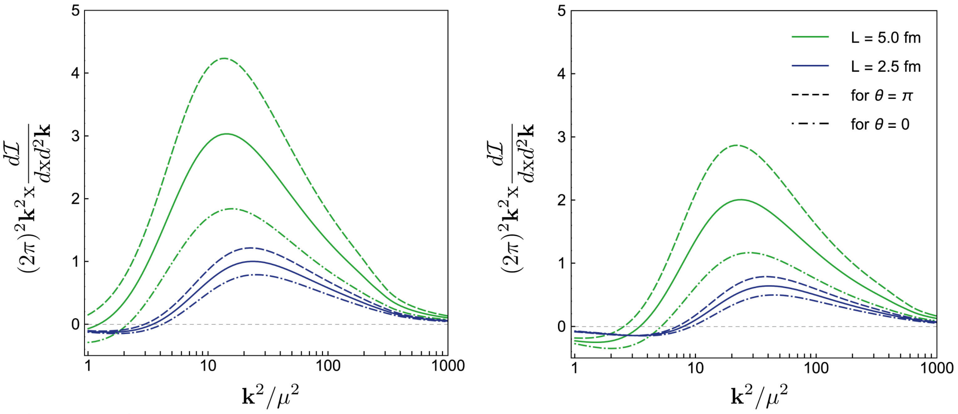

FIG. 5. The (rescaled) medium-induced soft gluon spectrum is plotted for two energies $E = 50$ GeV (left) and $E = 100$ GeV (right). The colors distinguish the medium length, while the mean free path is kept fixed ($\chi = 3$ at $L = 5$ fm). The solid lines correspond to the homogeneous (or no transverse flow) limit, while the dashed lines correspond to $\boldsymbol{u}$ and $\boldsymbol{\nabla}T$ being parallel or antiparallel.

This expression can be compared with the results of [43] and, after some algebra, one can show that (80) precisely agrees with the $N = 1$ part of the small-x resummed parton distribution.

Turning to the flow-gradient effects, we take the eikonal limit and note that only the same multiplicative factor in the integrand of the amplitude squared survives. Then, the final-state distribution reads

$$\begin{aligned}
E\frac{d\mathcal{N}^{(1)}}{d^2kd\mathrm{x}d^2pdE} = {}& \frac{(1-\mathrm{x})g^2}{(2\pi)^3\mathrm{x}}\frac{C_F^2}{N_c}\left(E\frac{d\mathcal{N}^{(0)}}{d^2pdE}\right)\int_0^L dz\int_{\boldsymbol{q}}(1-\hat{\boldsymbol{g}}\cdot\boldsymbol{u}z) \\
& \times\left\{\boldsymbol{\kappa}_0^2+2\boldsymbol{\kappa}^2(1-\cos\phi)+2\frac{N_c}{C_F}\bar{\boldsymbol{\kappa}}^2(1-\cos\bar{\phi})+\frac{\boldsymbol{\kappa}_0\cdot\boldsymbol{\kappa}}{C_FN_c}(1-\cos\phi)-\frac{N_c}{C_F}\boldsymbol{\kappa}_0\cdot\bar{\boldsymbol{\kappa}}(1-\cos\bar{\phi})\right. \\
& -\frac{N_c}{C_F}\boldsymbol{\kappa}\cdot\bar{\boldsymbol{\kappa}}(1+\cos(\phi-\bar{\phi})-\cos\bar{\phi}-\cos\phi)-\boldsymbol{\kappa}_0^2\cos\phi_0-\boldsymbol{\kappa}_0^2(1-\cos\phi_0) \\
& \left.-\frac{N_c}{C_F}\boldsymbol{\kappa}_0^2(1-\cos\phi_0)+\frac{N_c}{C_F}\boldsymbol{\kappa}_0\cdot\boldsymbol{\kappa}_G(\cos\phi_G-\cos\phi_0)\right\}\rho(z)[v(\boldsymbol{q}^2)]^2. \qquad (81)
\end{aligned}$$

One readily observes that this modification of the distribution results in a multiplicative modification of the radiation rate due to the jet-medium interactions and, consequently, in a modification of the induced radiative energy loss, cf. [18].

Estimating the effect of the mixed term in the spectrum, we focus on the small-x limit. Then, the final-state distribution can be factorized into the initial quark distribution and an emission spectrum $d\mathcal{I}^{(1)}$, defined by

$$\mathrm{x}E\frac{d\mathcal{N}^{(1)}}{d^2kd\mathrm{x}d^2pdE}\equiv\mathrm{x}\frac{d\mathcal{I}^{(1)}}{d\mathrm{x}d^2k}E\frac{d\mathcal{N}^{(0)}}{d^2pdE}. \qquad (82)$$

Following [18,53], we choose a smooth longitudinal profile for the source density $\rho(\boldsymbol{x},z) = 2\rho_0(\boldsymbol{x})e^{-\frac{2z}{L}}$, treating the z integral analytically. The resulting medium-induced gluon spectrum reads

$$\begin{aligned}
\mathrm{x}\frac{d\mathcal{I}^{(1)}}{d\mathrm{x}d^2k} = {}& \frac{4\alpha_s\chi N_c}{\pi}\int_{\boldsymbol{q}}\frac{2\boldsymbol{k}\cdot\boldsymbol{q}}{\boldsymbol{k}^2(\boldsymbol{q}^2+\mu^2)^2}\frac{L^3(\boldsymbol{k}-\boldsymbol{q})^2}{L^2(\boldsymbol{k}-\boldsymbol{q})^4+16\mathrm{x}^2E^2} \\
& \times\left[1+\left(\frac{L^2(\boldsymbol{k}-\boldsymbol{q})^4}{L^2(\boldsymbol{k}-\boldsymbol{q})^4+16\mathrm{x}^2E^2}-\frac{3}{2}\right)L(\boldsymbol{g}\cdot\boldsymbol{u})\right], \qquad (83)
\end{aligned}$$

where we have introduced opacity $\chi = \frac{C_Fg^4\rho_0}{2N_c4\pi\mu^2}L$ and replaced $\hat{\boldsymbol{g}}$ by $\boldsymbol{g} = \frac{\boldsymbol{\nabla}T}{T}\left(3-\frac{4}{(\boldsymbol{q}^2+\mu^2)}\right)$, assuming that $\rho_0\sim T^3$ and $\mu\simeq gT$, neglecting gradients of the transverse flow $\boldsymbol{u}$.

In Fig. 5, we plot the spectrum (83) for two energies $E = 50$ GeV (left) and $E = 100$ GeV (right), while for each energy we also show two different medium lengths $L = 5$ and $L = 2.5$ fm, keeping the mean free path $\lambda = \frac{L}{\chi}$ fixed. We set $\alpha_s = 0.3$, $\mu = 0.6$ GeV, and $\mathrm{x} = 0.1$ and assume that $\chi = 3$ at $L = 5$ fm. For a qualitative estimate of the mixed flow-gradient term, we take $|\boldsymbol{u}| = 0.3$, $\frac{|\boldsymbol{\nabla} T|}{T^2} = 0.1$, and $T = 0.3$ GeV. One may readily see that the modification of the spectrum could be substantial even for moderate flows and anisotropies, especially for larger systems.

IV. DISCUSSION AND CONCLUSIONS

In this work, we have studied the mutual effect of the transverse flow and matter gradients on jet momentum broadening and in-medium branching processes. We have derived the momentum broadening distribution up to first order in gradients, including the gradients of the longitudinal and transverse flow velocities and keeping the leading subeikonal corrections. We have also evaluated the leading gradient corrections to the medium-induced gluon spectrum in the full kinematics. These results are obtained within the opacity expansion framework, following the logic of the formalism developed in [21] and extending it.

As we have shown, the interplay of the flow and gradient effects results in the leading modification of the final parton distributions and their even moments. For instance, the jet quenching parameter $\hat{q}$ is rescaled by an overall factor (34), which may substantially modify its value in the homogeneous static limit. Indeed, let us focus on the contribution proportional to the gradient of the source density $\boldsymbol{\nabla}\rho$. Assuming that $\rho \sim T^3$, we set $\hat{\boldsymbol{g}} = 3\frac{\boldsymbol{\nabla} T}{T}$. In the hydrodynamic phase, one expects that $LT \gg 1$ with $\frac{\boldsymbol{\nabla} T}{T^2} \ll 1$, but the change in the matter properties over the matter size is not required to be small $\frac{L\boldsymbol{\nabla} T}{T} \sim 1$. Thus, for relativistic velocities $\frac{|\boldsymbol{u}|}{1-u_z} \sim 1$, our crude estimate indicates that the modification in $\hat{q}$ can be as large as the leading contribution. For instance, taking the same moderate estimates for the transverse flow and temperature gradients as for the $L = 5$ fm curve in Fig. 5, one readily finds that $\frac{\hat{q}}{\hat{q}_0} \simeq 0.775$.

The physical picture behind these larger modifications can be made more transparent if we attempt keeping the full $\boldsymbol{x}$ dependence in $\rho(\boldsymbol{x}, z)$, e.g., in (12). Assuming that only the Fourier factors are varying fast enough in $\boldsymbol{q} - \boldsymbol{q}'$, we find that the corresponding contribution to the amplitude squared is proportional to $\rho\left(-\frac{\boldsymbol{u}}{1-u_z} z + \frac{\boldsymbol{p}-\boldsymbol{q}}{E} z, z\right)$. This change in the local density along the leading parton trajectory agrees with (16) up to first order in gradients and can be identified with the shift of the matter in the transverse direction over the traveling time z; see the illustration in Fig. 6. One should note that the source number density is positive, and higher order gradient corrections ensure that (34) is positive. While the other hydrodynamic parameters enter the amplitude squared in a more involved way, the related gradient corrections as well as the full momentum dependence in the integrand are already taken into account in (30) [and in (81) for the medium-induced branching].

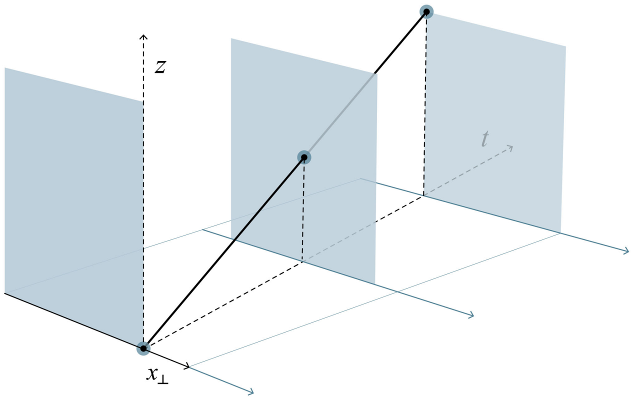

FIG. 6. The rectangles represent a medium element traveling along the transverse direction and pictured at three different moments. The leading parton traveling along the z direction at $\boldsymbol{x} = 0$ penetrates the matter element at different transverse positions at different times due to the medium transverse motion. Since the medium has transverse structure (introduced by the temperature gradient), the jet sees different local properties, while the matter is assumed to be longitudinally uniform in this illustration.

The presented results should be further included in phenomenological considerations of particular observables. The possible substantial modification in $\hat{q}$ and the energy loss rate can considerably affect the existing simulations of jets interacting with evolving backgrounds; see, e.g., [31,33,54–60]. It would also be interesting to see if the mixed flow-gradient effects leave clear signatures in more differential observables, discussed in the context of the evolving anisotropic matter; see, e.g., [44,61–64]. We leave all these considerations for future work.

ACKNOWLEDGMENTS

The authors are grateful to P. Arnold, J. Barata, T. Luo, D. Pablos, C. Salgado, and X. N. Wang for multiple discussions and comments on this work. The authors would like to particularly thank M. Sievert and P. Mitkin, who participated in the early discussions shaping this project. The work of X. M. L. and A. V. S. is supported by European Research Council project ERC-2018-ADG-835105 YoctoLHC, by Xunta de Galicia (Centro singular de investigación de Galicia accreditation 2019–2022), and by European Union ERDF. X. M. L. contribution to this work is supported under scholarship No. PRE2021-097748, funded by MCIN/AEI/10.13039/501100011033 and ESF+. The work of A. V. S. is also supported by the

Marie Sklodowska-Curie Individual Fellowship under JetT project (project reference 101032858) and by Fundao para a Cincia e a Tecnologia (FCT) under Contract No. 2022.06565.CEECIND. The IGFAE has the CIGUS recognition from the Xunta de Galicia, which accredits the quality and impact of its research. The work of M. V. K. is funded by the Russian Science Foundation Grant No. 22-22-00664. The work of J. R. is supported in part by the Mani L. Bhaumik Institute for Theoretical Physics.

---

[1] W. Busza, K. Rajagopal, and W. van der Schee, Heavy ion collisions: The big picture, and the big questions, Annu. Rev. Nucl. Part. Sci. **68**, 339 (2018).

[2] L. Cunqueiro and A. M. Sickles, Studying the QGP with jets at the LHC and RHIC, Prog. Part. Nucl. Phys. **124**, 103940 (2022).

[3] L. Apolinário, Y.-J. Lee, and M. Winn, Heavy quarks and jets as probes of the QGP, Prog. Part. Nucl. Phys. **127**, 103990 (2022).

[4] I. Vitev and M. Gyulassy, High p_T tomography of $d+$ Au and Au $+$ Au at SPS, RHIC, and LHC, Phys. Rev. Lett. **89**, 252301 (2002).

[5] E. Wang and X.-N. Wang, Jet tomography of dense and nuclear matter, Phys. Rev. Lett. **89**, 162301 (2002).

[6] K. M. Burke *et al.* (JET Collaboration), Extracting the jet transport coefficient from jet quenching in high-energy heavy-ion collisions, Phys. Rev. C **90**, 014909 (2014).

[7] B. Betz and M. Gyulassy, Constraints on the path-length dependence of jet quenching in nuclear collisions at RHIC and LHC, J. High Energy Phys. 08 (2014) 090; 10 (2014) 043(E).

[8] J. Xu, A. Buzzatti, and M. Gyulassy, Azimuthal jet flavor tomography with CUJET2.0 of nuclear collisions at RHIC and LHC, J. High Energy Phys. 08 (2014) 063.

[9] M. Djordjevic, B. Blagojevic, and L. Zivkovic, Mass tomography at different momentum ranges in quark-gluon plasma, Phys. Rev. C **94**, 044908 (2016).

[10] L. Apolinário, J. G. Milhano, G. P. Salam, and C. A. Salgado, Probing the time structure of the quark-gluon plasma with top quarks, Phys. Rev. Lett. **120**, 232301 (2018).

[11] L. Apolinário, A. Cordeiro, and K. Zapp, Time reclustering for jet quenching studies, Eur. Phys. J. C **81**, 561 (2021).

[12] Y.-L. Du, D. Pablos, and K. Tywoniuk, Jet tomography in heavy-ion collisions with deep learning, Phys. Rev. Lett. **128**, 012301 (2022).

[13] M. Gyulassy and X.-n. Wang, Multiple collisions and induced gluon bremsstrahlung in QCD, Nucl. Phys. **B420**, 583 (1994).

[14] B. G. Zakharov, Fully quantum treatment of the Landau-Pomeranchuk-Migdal effect in QED and QCD, JETP Lett. **63**, 952 (1996).

[15] R. Baier, Y. L. Dokshitzer, A. H. Mueller, S. Peigne, and D. Schiff, Radiative energy loss of high-energy quarks and gluons in a finite volume quark-gluon plasma, Nucl. Phys. **B483**, 291 (1997).

[16] U. A. Wiedemann, Transverse dynamics of hard partons in nuclear media and the QCD dipole, Nucl. Phys. **B582**, 409 (2000).

[17] U. A. Wiedemann, Gluon radiation off hard quarks in a nuclear environment: Opacity expansion, Nucl. Phys. **B588**, 303 (2000).

[18] M. Gyulassy, P. Levai, and I. Vitev, Reaction operator approach to non-Abelian energy loss, Nucl. Phys. **B594**, 371 (2001).

[19] M. Gyulassy, P. Levai, and I. Vitev, Reaction operator approach to multiple elastic scatterings, Phys. Rev. D **66**, 014005 (2002).

[20] P. B. Arnold, G. D. Moore, and L. G. Yaffe, Photon and gluon emission in relativistic plasmas, J. High Energy Phys. 06 (2002) 030.

[21] A. V. Sadofyev, M. D. Sievert, and I. Vitev, *Ab initio* coupling of jets to collective flow in the opacity expansion approach, Phys. Rev. D **104**, 094044 (2021).

[22] M. Gyulassy, I. Vitev, and X. Wang, High p_T azimuthal asymmetry in noncentral $A+A$ at RHIC, Phys. Rev. Lett. **86**, 2537 (2001).

[23] M. Gyulassy, I. Vitev, X.-N. Wang, and P. Huovinen, Transverse expansion and high p_T azimuthal asymmetry at RHIC, Phys. Lett. B **526**, 301 (2002).

[24] R. Baier, Y. L. Dokshitzer, A. H. Mueller, and D. Schiff, Radiative energy loss of high-energy partons traversing an expanding QCD plasma, Phys. Rev. C **58**, 1706 (1998).

[25] R. Baier, A. H. Mueller, and D. Schiff, How does transverse (hydrodynamic) flow affect jet-broadening and jet-quenching?, Phys. Lett. B **649**, 147 (2007).

[26] H. Liu, K. Rajagopal, and U. A. Wiedemann, Wilson loops in heavy ion collisions and their calculation in AdS/CFT, J. High Energy Phys. 03 (2007) 066.

[27] T. Renk, J. Ruppert, C. Nonaka, and S. A. Bass, Jet-quenching in a 3D hydrodynamic medium, Phys. Rev. C **75**, 031902 (2007).

[28] N. Armesto, C. A. Salgado, and U. A. Wiedemann, Measuring the collective flow with jets, Phys. Rev. Lett. **93**, 242301 (2004).

[29] N. Armesto, C. A. Salgado, and U. A. Wiedemann, Low-p_T collective flow induces high-p_T jet quenching, Phys. Rev. C **72**, 064910 (2005).

[30] A. V. Sadofyev, M. D. Sievert, and I. Vitev, Jets in evolving matter within the opacity expansion approach, SciPost Phys. Proc. **8**, 046 (2022).

[31] L. Antiporda, J. Bahder, H. Rahman, and M. D. Sievert, Jet drift and collective flow in heavy-ion collisions, Phys. Rev. D **105**, 054025 (2022).

[32] C. Andres, F. Dominguez, A. V. Sadofyev, and C. A. Salgado, Jet broadening in flowing matter: Resummation, Phys. Rev. D **106**, 074023 (2022).

[33] Y. He, L.-G. Pang, and X.-N. Wang, Gradient tomography of jet quenching in heavy-ion collisions, Phys. Rev. Lett. **125**, 122301 (2020).

[34] A. Ipp, D. I. Müller, and D. Schuh, Anisotropic momentum broadening in the $2+1$D glasma: Analytic weak field approximation and lattice simulations, Phys. Rev. D **102**, 074001 (2020).

[35] S. Hauksson, S. Jeon, and C. Gale, Momentum broadening of energetic partons in an anisotropic plasma, Phys. Rev. C **105**, 014914 (2022).

[36] M. E. Carrington, A. Czajka, and S. Mrowczynski, Jet quenching in glasma, Phys. Lett. B **834**, 137464 (2022).

[37] J. Barata, A. V. Sadofyev, and C. A. Salgado, Jet broadening in dense inhomogeneous matter, Phys. Rev. D **105**, 114010 (2022).

[38] Y. Fu, J. Casalderrey-Solana, and X.-N. Wang, Asymmetric transverse momentum broadening in an inhomogeneous medium, Phys. Rev. D **107**, 054038 (2023).

[39] J. Barata, A. V. Sadofyev, and X.-N. Wang, Quantum partonic transport in QCD matter, Phys. Rev. D **107**, L051503 (2023).

[40] M. E. Carrington, A. Czajka, and S. Mrowczynski, Transport of hard probes through glasma, Phys. Rev. C **105**, 064910 (2022).

[41] S. Hauksson and E. Iancu, Jet polarisation in an anisotropic medium, J. High Energy Phys. 08 (2023) 027.

[42] K. Boguslavski, A. Kurkela, T. Lappi, F. Lindenbauer, and J. Peuron, Jet momentum broadening during initial stages in heavy-ion collisions, arXiv:2303.12595.

[43] J. Barata, X. M. López, A. V. Sadofyev, and C. A. Salgado, Medium induced gluon spectrum in dense inhomogeneous matter, Phys. Rev. D **108**, 034018 (2023).

[44] J. Barata, J. G. Milhano, and A. V. Sadofyev, Picturing QCD jets in anisotropic matter: From jet shapes to energy energy correlators, arXiv:2308.01294.

[45] M. Lekaveckas and K. Rajagopal, Effects of fluid velocity gradients on heavy quark energy loss, J. High Energy Phys. 02 (2014) 068.

[46] K. Rajagopal and A. V. Sadofyev, Chiral drag force, J. High Energy Phys. 10 (2015) 018.

[47] A. V. Sadofyev and Y. Yin, The charmonium dissociation in an "anomalous wind", J. High Energy Phys. 01 (2016) 052.

[48] J. Reiten and A. V. Sadofyev, Drag force to all orders in gradients, J. High Energy Phys. 07 (2020) 146.

[49] I. Y. Aref'eva, A. A. Golubtsova, and E. Gourgoulhon, Holographic drag force in 5d Kerr-AdS black hole, J. High Energy Phys. 04 (2021) 169.

[50] L. D. Landau and I. Pomeranchuk, Limits of applicability of the theory of bremsstrahlung electrons and pair production at high-energies, Dokl. Akad. Nauk Ser. Fiz. **92**, 535 (1953), https://inspirehep.net/literature/9386.

[51] A. B. Migdal, Bremsstrahlung and pair production in condensed media at high energies, Phys. Rev. **103**, 1811 (1956).

[52] M. D. Sievert and I. Vitev, Quark branching in QCD matter to any order in opacity beyond the soft gluon emission limit, Phys. Rev. D **98**, 094010 (2018).

[53] M. Gyulassy, P. Levai, and I. Vitev, Non-Abelian energy loss at finite opacity, Phys. Rev. Lett. **85**, 5535 (2000).

[54] Y. He, T. Luo, X.-N. Wang, and Y. Zhu, Linear Boltzmann transport for jet propagation in the quark-gluon plasma: Elastic processes and medium recoil, Phys. Rev. C **91**, 054908 (2015); **97**, 019902(E) (2018).

[55] J. H. Putschke *et al.*, The JETSCAPE framework, arXiv: 1903.07706.

[56] D. Zigic, I. Salom, J. Auvinen, P. Huovinen, and M. Djordjevic, DREENA-A framework as a QGP tomography tool, Front. Phys. **10**, 957019 (2022).

[57] S. Stojku, J. Auvinen, L. Zivkovic, P. Huovinen, and M. Djordjevic, Jet-perceived anisotropy revealed through high-$p_\perp$ data, Phys. Lett. B **835**, 137501 (2022).

[58] L. Barreto, F. M. Canedo, M. G. Munhoz, J. Noronha, and J. Noronha-Hostler, Jet cone radius dependence of R_{AA} and v_2 at PbPb 5.02 TeV from JEWEL + T$_{\mathrm{R}}$ENTo + v-USPhydro, arXiv:2208.02061.

[59] D. Pablos, M. Singh, S. Jeon, and C. Gale, Minijet quenching in a concurrent jet + hydro evolution and the nonequilibrium quark-gluon plasma, Phys. Rev. C **106**, 034901 (2022).

[60] M. Singh, M. Kurian, S. Jeon, and C. Gale, Open charm phenomenology with a multistage approach to relativistic heavy-ion collisions, Phys. Rev. C **108**, 054901 (2023).

[61] C. Andres, F. Dominguez, R. Kunnawalkam Elayavalli, J. Holguin, C. Marquet, and I. Moult, Resolving the scales of the quark-gluon plasma with energy correlators, Phys. Rev. Lett. **130**, 262301 (2023).

[62] C. Andres, F. Dominguez, J. Holguin, C. Marquet, and I. Moult, A coherent view of the quark-gluon plasma from energy correlators, J. High Energy Phys. 09 (2023) 088.

[63] J. Barata and Y. Mehtar-Tani, Energy loss effects in EECs at LO, in *Proceedings of the 11th International Conference on Hard and Electromagnetic Probes of High-Energy Nuclear Collisions: Hard Probes 2023* (2024), https://inspirehep.net/literature/2678171.

[64] C. Andres, F. Dominguez, J. Holguin, C. Marquet, and I. Moult, Seeing beauty in the quark-gluon plasma with energy correlators, arXiv:2307.15110.

Article II

Medium induced gluon spectrum in dense inhomogeneous matter

Authors

João Barata[1], Xoán Mayo López[2],

Andrey V. Sadofyev[2], Carlos A. Salgado[2]

(1) Physics Department, Brookhaven National Laboratory, Upton, New York 11973, USA
(2) Instituto Galego de Física de Altas Enerxías, Universidade de Santiago de Compostela, Santiago de Compostela 15782, Galicia, Spain

PhD Student Contribution

Independently derived the presented calculations and collaborated equally on the discussions and writing

Journal and Article Information

Journal name: Physical Review D
Publisher: American Physical Society
ISSN: 2470-0029
Year of publication: 2023
DOI: 10.1103/PhysRevD.108.034018
Impact factor in 2023: 4.6
CiteScore in 2023: 9.3
Quartile and decile in 2023: Q1 and D1

PHYSICAL REVIEW D **108,** 034018 (2023)

Medium induced gluon spectrum in dense inhomogeneous matter

João Barata,[1,*] Xoán Mayo López,[2,†] Andrey V. Sadofyev,[2,‡] and Carlos A. Salgado[2,§]
[1]*Physics Department, Brookhaven National Laboratory, Upton, New York 11973, USA*
[2]*Instituto Galego de Física de Altas Enerxías, Universidade de Santiago de Compostela, Santiago de Compostela 15782, Galicia, Spain*

(Received 26 April 2023; accepted 19 July 2023; published 16 August 2023)

We calculate the spectrum of gluons sourced by the branching of an energetic quark in the presence of an inhomogeneous QCD medium, focusing on the soft radiation limit. We take into account multiple soft interactions between the partons and matter, treating the transverse variations of its parameters within a gradient expansion. Thus, we derive the general form of the medium induced spectrum up to the first order in gradients, and consider its simplifying limits. In particular, we show that to the leading order in matter gradients and using the harmonic approximation for the scattering potential, the full gluon spectrum can be written in a compact closed form suitable for numerical evaluation. The final gluon transverse momentum tends to align along the anisotropy direction, resulting in a nontrivial azimuthal pattern in the jet substructure.

DOI: 10.1103/PhysRevD.108.034018

I. INTRODUCTION

Over the past decades, the experiments on high-energy heavy-ion collisions (HIC) at RHIC and the LHC allowed to explore QCD at high energies and densities; for a review see, e.g., [1,2]. In these experiments, the nuclear matter is produced far from equilibrium, and undergoes a multiphase evolution. After the initial nonequilibrium dynamics, the matter thermalizes into a nearly ideal liquid, the quark-gluon plasma (QGP), which continues expanding and cooling. When the energy density is low enough, the matter turns into a hadron gas, which is eventually observed by the detectors. Following the initial observation of the QGP formation, the main community efforts have been concentrated on extracting the details of the matter evolution in HIC.

One of the evidences of the collective matter formation in HIC is the suppression of energetic partons due to the in-medium energy loss [3–5], known as jet quenching [6]; for recent reviews see [7–9]. Moreover, the cascades of secondary particles produced by the branching of such energetic partons, forming jets, are also modified by the matter, providing a differential tool to probe the medium at different length and energy scales. Using jets for such imaging of the nuclear matter and its evolution in HIC and other experiments is often referred to as jet tomography, see e.g. [10–27] and references therein.

Considering the jet-medium interactions in perturbative QCD, one usually has to describe the underlying hot matter in terms of a background stochastic color field, see e.g. [28–35]. Moreover, to make the calculations tractable, most works further rely on multiple simplifying assumptions. For instance, the medium is commonly considered to be transversely homogeneous with a finite longitudinal extension,[1] while the calculations are preformed in the large energy limit, known as the eikonal approximation. Under these assumptions, the problem allows for a semianalytic treatment, but the results cannot be applied to resolve the details of the medium evolution, and jets appear to be decoupled from the anisotropic matter expansion [18] and, moreover, from the large anisotropies of the initial out-of-equilibrium phase of the matter produced in HIC, see e.g. [18,20,36,37]. Only recently, the theory of jet-matter interactions has been extended to the case of inhomogeneous nuclear matter [18,24,38,39] with the transverse matter anisotropies treated within a gradient expansion.[2]

So far, the approach developed in [18,38] has been used to describe single parton evolution, the so-called jet

---

[*] jlourenco@bnl.gov
[†] xoan.mayo.lopez@usc.es
[‡] andrey.sadofyev@usc.es
[§] carlos.salgado@usc.es

[1] The longitudinal and transverse directions are defined with respect to the initial momentum of the leading parton momentum.

[2] See also [40–45] for applications of the same gradient expansion approach in holographic models of probe-matter interactions.

broadening, in dilute or dense media at the leading order in transverse gradients, but the case of in-medium branching in inhomogeneous matter has not been considered. In this paper, we continue developing the formalism by deriving the medium induced soft gluon spectrum up to the first order in transverse gradients but to all orders in opacity. Our main result is the double differential spectrum, which can be written as

$$\omega\frac{dI}{d\omega d^2\boldsymbol{k}} = \omega\frac{dI_0}{d\omega d^2\boldsymbol{k}} + (\hat{\boldsymbol{g}}\cdot\boldsymbol{k})\omega\frac{dI_1}{d\omega d^2\boldsymbol{k}} + \mathcal{O}(\hat{\boldsymbol{g}}^2), \quad (1)$$

where dI_0 denotes the gluon spectrum in homogeneous matter, dI_1 gives the functional dependence of the leading order gradient contribution on $\boldsymbol{k}^2$, resulting in a nontrivial azimuthal dependence of the overall spectrum, and ω and $\boldsymbol{k}$ are the energy and momentum of the emitted gluon. Notice that in this work we have derived (1) in the approximation of static matter (no flow), although the generalization for flowing medium is straightforward to obtain. As in [38], we use the Gyulassy-Wang (GW) model to make some of the expressions explicit, and the primary matter parameters are the number density of the scattering centers ρ and Debye mass μ. However, our results are general and can be directly extended to other models for the source potential. The corresponding transverse gradients are encapsulated in a two-dimensional vector operator $\hat{\boldsymbol{g}} \equiv (\boldsymbol{\nabla}\rho\frac{\delta}{\delta\rho} + \boldsymbol{\nabla}\mu^2\frac{\delta}{\delta\mu^2})$. Below, we will show that the gradient terms in the spectrum result in a deflection of the emitted gluons along $\hat{\boldsymbol{g}}$.

This paper is organized as follows: In Sec. II we derive the generic form of the medium induced gluon spectrum up to first order in transverse gradients for media with finite longitudinal extension. In Sec. III, we further simplify the generic form of the spectrum, utilizing the harmonic approximation limit for the in-medium scattering potential. In Sec. IV, we obtain the gradient corrections to the medium induced gluon spectrum in the considered limit. We discuss the properties of the spectrum in Sec. V, as well as provide some numerical results, illustrating its behavior. Finally, our findings are summarized in Sec. VI, where we also discuss potential extensions of the presented results.

II. MEDIUM INDUCED SPECTRUM IN THE SOFT GLUON LIMIT

A. Resummation at the amplitude level

It is instructive to briefly repeat the derivation of the amplitude describing the propagation of a quark with initial energy E and transverse momentum $\boldsymbol{p}_1$ in a medium, followed by an emission of a gluon, which is measured to have energy ω and transverse momentum $\boldsymbol{k}$ in the final state. Following [18], we will focus on the transverse gradients of the source density and Debye mass, assuming the matter to be static. We also assume the in-matter sources to be static by themselves, ignoring such effects as the medium response and collisional energy loss, which would significantly complicate our consideration, and require further generalization of the formalism developed in [18,38]. Thus, the medium induced color field can be chosen as

$$gA^{a\lambda}(q) = (2\pi)g^{\lambda 0}v^a(q)\delta(q^0), \quad (2)$$

and the jet-medium interactions are controlled by

$$v^a(q) = \int_x e^{-i(\boldsymbol{q}\cdot\boldsymbol{x}+q_z z)}\hat{\rho}^a(\boldsymbol{x},z)v(q,\boldsymbol{x},z), \quad (3)$$

where $\hat{\rho}^a$ is the source color density, and $v(q,\boldsymbol{x},z)$ is a single source potential, which depends on coordinates through the local medium properties. We have also introduced shorthand notations for integrals running over the full three-dimensional space as $\int_x \equiv d^3x$ and $\int_k \equiv \frac{d^3k}{(2\pi)^3}$, and over the transverse space as $\int_{\boldsymbol{x}} \equiv \int d^2\boldsymbol{x}$ and $\int_{\boldsymbol{k}} \equiv \int \frac{d^2\boldsymbol{k}}{(2\pi)^2}$.

The single source potential is expected to be exponentially screened in coordinate space, and we will generally refer to the screening scale as the Debye mass. While the medium induced soft gluon spectrum can be derived for the general potential, and we will do so here, it is instructive to consider an explicit form of $v(q,\boldsymbol{x},z)$ as well. For this purpose, we will follow [38], and refer to the GW model [28], corresponding to

$$v(q,\boldsymbol{x},z) = \frac{g^2}{q^2-\mu^2(\boldsymbol{x},z)+i\epsilon}. \quad (4)$$

Here, we assume that $\mu(\boldsymbol{x},z)$ varies slowly in the transverse direction over distances of order $\frac{1}{\mu(\boldsymbol{0},z)}$. Focusing on the limit, when the characteristic distance between the sources

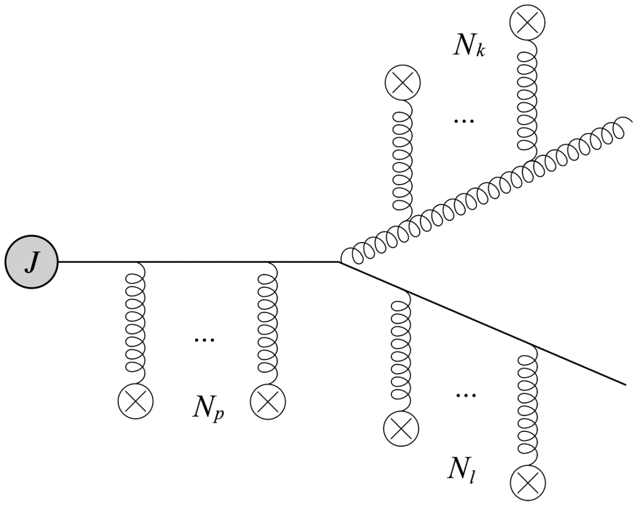

FIG. 1. Feynman diagram of the in-medium gluon emission from a quark with each particle interacting multiple times with the background field.

is larger than $\frac{1}{\mu(\mathbf{0},z)}$, we ignore the local modifications in general $v(q,\boldsymbol{x},z)$ for the given source, taking into account only the changes in the Debye mass between different sources.

Using this model for the medium, we can write the amplitude, $iR_{N_pN_lN_k}$, depicted in Fig. 1, with N_p insertions in the incoming quark line, N_l insertions in the outgoing quark line, and N_k insertions in the gluon line, as

$$\begin{aligned} i\mathcal{R}_{N_pN_lN_k} = &\prod_{n=1}^{N_p}\left[(-1)\int_{p_n} t^{a_n}_{proj}v^{a_n}(p_{n+1}-p_n)\frac{2E}{p_n^2+i\epsilon}\right] \\ &\times\int\frac{d^4p_s}{(2\pi)^4}(-1)gt^{b_1}_{proj}\frac{(p_s+l_1)_{\mu_1}}{p_s^2+i\epsilon}(2\pi)^4\delta^{(4)}(p_s-l_1-k_1)J(p_1) \\ &\times\prod_{r=1}^{N_k}\left[\left(-\frac{i}{g}\right)\int_{k_r}\frac{N^{\mu_r\nu_r}(k_r)}{k_r^2+i\epsilon}\Gamma^{b_rb_{r+1}c_r}_{\nu_r\mu_{r+1}0}(k_r,-k_{r+1})v^{c_r}(k_{r+1}-k_r)\right]\epsilon^{*\mu_{N_k+1}}(k) \\ &\times\prod_{m=1}^{N_l}\left[(-1)\int_{l_m} t^{d_m}_{proj}v^{d_m}(l_{m+1}-l_m)\frac{2(1-x)E}{l_m^2+i\epsilon}\right], \end{aligned} \tag{5}$$

where $\Gamma^{abc}_{\alpha\beta\gamma}$ is the three-gluon vertex, the zeroth components of the four-momenta have already been fixed with the delta functions coming from the background field insertions, and we have introduced additional momentum labels $p_{N_p+1}=p_s$, $l_{N_l+1}=l$, and $k_{N_k+1}=k$. Notice that the integrations in (5) should be understood as acting from the left on the whole expression, and are distributed now for structural simplicity.

This expression can be simplified if we use the particular kinematics of the process. Indeed, let us take a closer look at the first product in (5). Switching to the Fourier transformed in-medium potentials, and reordering the Fourier exponentials within the product, we can write it as

$$\begin{aligned} &\prod_{n=1}^{N_p}\Bigg[(-1)\int_{p_n,x_n} t^{a_n}_{\mathrm{proj}}\hat{\rho}^{a_n}(\boldsymbol{x}_n,z_n)v(p_{n+1}-p_n,\boldsymbol{x}_n,z_n) \\ &\quad\times\frac{2E}{p_n^2+i\epsilon}e^{-i\boldsymbol{x}_n\cdot(\boldsymbol{p}_{n+1}-\boldsymbol{p}_n)}e^{ip_{n,z}(z_n-z_{n-1})}\Bigg]e^{-ip_{s,z}z_{N_p}}J(p_1), \end{aligned} \tag{6}$$

where we have introduced $z_0=0$. One can further perform $p_{n,z}$ integrations by residues, collecting the corresponding poles. We also assume that $\mu\Delta z\gg 1$, where Δz is the characteristic distance between the color sources (described by ρ^a), and that the single source potential has no other poles apart from the screening ones. Thus, we neglect the poles of the in-medium potentials, which are exponentially suppressed in the considered limit. Assuming that the matter is extended in the positive z direction, we find that only the poles of the scalar propagators with $p_{n,z}>0$ contribute. Finally, we take the limit of small gluon energy fraction $x=\frac{\omega}{E}\ll 1$, and neglect all the subeikonal terms unless they are enhanced by the medium length and $\frac{1}{x}$ simultaneously. Under these approximations, we find

$$\begin{aligned} &\prod_{n=1}^{N_p}\left[i\int_{\mathbf{p}_n,x_n} t^{a_n}_{\mathrm{proj}}\tilde{v}^{a_n}(\boldsymbol{x}_n,z_n)\theta_{n,n-1}e^{-i\boldsymbol{x}_n\cdot(\boldsymbol{p}_{n+1}-\boldsymbol{p}_n)}\right] \\ &\quad\times e^{-i(p_{s,z}-E)z_{N_p}}J(p_1), \end{aligned} \tag{7}$$

where $\tilde{v}^a(\boldsymbol{x},z)=\int_{\boldsymbol{q},\boldsymbol{y}}e^{i\boldsymbol{q}\cdot(\boldsymbol{x}-\boldsymbol{y})}\hat{\rho}^a(\boldsymbol{y},z)v(q,\boldsymbol{y},z)|_{q_0=q_z=0}$. Fourier transforming the momentum conservation in the emission vertex and substituting (7), we can integrate over $p_{s,z}$ in (5). Thus, we set $p_{s,z}\simeq E$ and impose an upper limit on variations of z_{N_p}. Now one may sum (7) over all possible diagrams, treating the case of $N_p=0$ explicitly,

$$\begin{aligned} &J(p_s)+\sum_{N_p=1}^{\infty}\prod_{n=1}^{N_p}\left[i\int_{\mathbf{p}_n,x_n} t^{a_n}_{\mathrm{proj}}\tilde{v}^{a_n}(\boldsymbol{x}_n,z_n)\theta_{n,n-1}e^{-i\boldsymbol{x}_n\cdot(\boldsymbol{p}_{n+1}-\boldsymbol{p}_n)}\right]\theta_{sN_p}J(p_1) \\ &=\int_{\mathbf{p}_1,\boldsymbol{x}_1}e^{-i\boldsymbol{x}_1\cdot(\boldsymbol{p}_s-\boldsymbol{p}_1)}\mathcal{P}\exp\left\{i\int_0^{z_s}d\tau t^a_{\mathrm{proj}}\tilde{v}^a(\boldsymbol{x}_1,\tau)\right\}J(p_1), \end{aligned} \tag{8}$$

where the Wilson line of the scattering potential in the fundamental representation can be identified

$$\mathcal{W}(\boldsymbol{x}_1;z_s,0)=\mathcal{P}\exp\left\{i\int_0^{z_s}d\tau t^a_{\mathrm{proj}}\tilde{v}^a(\boldsymbol{x}_1,\tau)\right\}. \tag{9}$$

Similarly, looking at the other quark leg in the fourth line of (5), we readily find

$$
\begin{aligned}
&(p_s+l)_{\mu_1}+\sum_{N_l=1}^{\infty}\prod_{m=1}^{N_l}\left[(-1)\int_{l_m} t_{\mathrm{proj}}^{d_m} v^{d_m}(l_{m+1}-l_m)\frac{2(1-x)E}{l_m^2+i\epsilon}\right]e^{-i(l_{1,z}-(1-x)E)z_s}(p_s+l_1)_{\mu_1}\\
&\quad=\int_{\boldsymbol{l}_1,\boldsymbol{x}_1} e^{-i\boldsymbol{x}_1\cdot(\boldsymbol{l}-\boldsymbol{l}_1)}\mathcal{P}\exp\left\{i\int_{z_s}^{\infty}d\tau t_{\mathrm{proj}}^{d}\tilde{v}^d(\boldsymbol{x}_1,\tau)\right\}(p_s+l_1)_{\mu_1},
\end{aligned}
\tag{10}
$$

where[3] $z_0=z_s$, the exponential $e^{-il_{1,z}z_s}$ is coming from the emission vertex, and the final momentum of the quark $l_{N_l+1}=l$ is on shell.

Now, we have to consider the third type of insertions, attached to the emitted gluon line. Its structure is more involved, and it is instructive to make several simplifying observations upfront. First, one has to specify the gauge choice, fixing the form of $\epsilon^{*\mu}$ and $N^{\mu\nu}$. The background field (2) induced by the matter sources is derived in the Lorenz gauge. However, working in this gauge would considerably complicate the consideration, since the polarization vector would involve auxiliary components. To remove the residual gauge freedom, one should notice that the particular form of (2) is compatible with an additional gauge condition $A^z=0$. In this gauge, combining the two constraints together, we can write the polarization vector in terms of physical components,

$$
\epsilon_\mu^*(k)=\left\{\frac{\boldsymbol{\epsilon}\cdot\boldsymbol{k}}{\omega},\boldsymbol{\epsilon},0\right\},
\tag{11}
$$

while the numerator of the gluon propagator reads

$$
N^{\mu\nu}(k)=g^{\mu\nu}-\frac{k^\mu n^\nu+k^\nu n^\mu}{(k\cdot n)}-\frac{k^\mu k^\nu}{(k\cdot n)^2},
\tag{12}
$$

where we have introduced the four-vector $n_\mu=\{0,0,0,1\}$ entering through the gauge condition $n\cdot A=0$. Notice that we give the on-shell form of $N^{\mu\nu}$, since $k_{n,z}$ will be set on shell by the corresponding integrations.[4] Thus, one readily finds

$$
\begin{aligned}
&N^{\mu_r\nu_r}(k_r)\Gamma^{b_r b_{r+1} c_r}_{\nu_r\mu_{r+1}0}(k_r,-k_{r+1})\epsilon^{*\mu_{r+1}}(k_{r+1})\\
&\quad\simeq 2\omega g f^{b_r b_{r+1} c_r}\epsilon^{*\mu_r}(k_r),
\end{aligned}
\tag{13}
$$

where we have neglected the subeikonal terms.

Noticing that $(T^c)_{ab}=-if^{abc}$ and using (13), we can reexpress the second line in (5), adding the contribution $N_k=0$ explicitly, as

$$
\begin{aligned}
&e^{i\frac{\boldsymbol{k}^2}{2\omega}z_s}\delta^{b_{N_k+1}b_1}\epsilon^{*\mu_1}(k)+\sum_{N_k=1}^{\infty}\prod_{r=1}^{N_k}\left[i\int_{\boldsymbol{k}_r,x_r}(T^{c_r})_{b_{r+1}b_r}\tilde{v}^{c_r}(\boldsymbol{x}_r,z_r)\theta_{r,r-1}e^{-i\boldsymbol{x}_r\cdot(\boldsymbol{k}_{r+1}-\boldsymbol{k}_r)}e^{iQ_r(z_r-z_{r-1})}\right]e^{-ik_z z_{N_k}+i\omega z_s}\epsilon^{*\mu_1}(k_1)\\
&\quad=\lim_{z_f\to\infty}\int_{\boldsymbol{k}_1}e^{i\frac{\boldsymbol{k}^2}{2\omega}z_f}\mathcal{G}^{b_{N_k+1}b_1}(\boldsymbol{k},z_f;\boldsymbol{k}_1,z_s)\epsilon^{*\mu_1}(k_1),
\end{aligned}
\tag{14}
$$

where we keep the leading subeikonal contributions to the poles of the scalar propagators $Q_r=\omega-\frac{\boldsymbol{k}_r^2}{2\omega}$, resulting in the so-called Landau-Pomeranchuk-Migdal phases, which are enhanced in the soft gluon limit by $\frac{1}{x}$. Here, we have introduced a single-particle propagator, which has the following coordinate space representation:

$$
\mathcal{G}(\boldsymbol{x}_f,z_f;\boldsymbol{x}_{\mathrm{in}},z_{\mathrm{in}})=\int_{\boldsymbol{x}_{\mathrm{in}}}^{\boldsymbol{x}_f}\mathcal{D}\boldsymbol{r}\exp\left\{\frac{i\omega}{2}\int_{z_{\mathrm{in}}}^{z_f}d\tau\dot{\boldsymbol{r}}^2\right\}\mathcal{P}\exp\left\{i\int_{z_{\mathrm{in}}}^{z_f}d\tau T^c\tilde{v}^c(\boldsymbol{r}(\tau),\tau)\right\},
\tag{15}
$$

where z_f has been introduced in (14) to simplify the definition of $\mathcal{G}$.

Combining these three contributions and introducing $\boldsymbol{x}_{\mathrm{in}}\equiv\boldsymbol{x}_1$, we find that in the soft gluon limit, the resummed amplitude can be written as

$$
i\mathcal{R}\simeq-\frac{g}{\omega}\lim_{z_f\to\infty}\int_0^{\infty}dz_s\int_{\boldsymbol{x}_{\mathrm{in}}}e^{-i\boldsymbol{x}_{\mathrm{in}}\cdot\boldsymbol{l}}J(\boldsymbol{x}_{\mathrm{in}})\mathcal{W}(\boldsymbol{x}_{\mathrm{in}};\infty,z_s)t_{\mathrm{proj}}^a\mathcal{W}(\boldsymbol{x}_{\mathrm{in}};z_s,0)e^{i\frac{\boldsymbol{k}^2}{2\omega}z_f}[\boldsymbol{\epsilon}\cdot\boldsymbol{\nabla}_{\boldsymbol{x}_{\mathrm{in}}}\mathcal{G}^{ba}(\boldsymbol{k},z_f;\boldsymbol{x}_{\mathrm{in}},z_s)],
\tag{16}
$$

where the color indices have been renamed for simplicity.

---

[3] It should not be confused with z_0 in the initial quark line at $n=0$.

[4] The propagator numerators lead to no new poles, leaving the k_z integrations unaffected.

B. Medium average

With the explicit form of the resummed amplitude, we can now turn to the medium averaging, required to describe the medium induced branching. The final state gluon distribution $\mathcal{N}$ is defined as

$$2(2\pi)^3\omega E\frac{d\mathcal{N}}{d\omega dEd^2\boldsymbol{k}} \equiv \frac{1}{4\pi}\frac{1}{N_c}\sum\int\frac{d^2\boldsymbol{l}}{(2\pi)^2}\langle|\mathcal{R}|^2\rangle, \tag{17}$$

where we have averaged over the stochastic background field. Thus, upon squaring (16), summing over final state quantum numbers, and averaging over the initial ones, we find that

$$\begin{aligned}2(2\pi)^3\omega E\frac{d\mathcal{N}}{d\omega dEd^2\boldsymbol{k}} = \lim_{z_f\to\infty}\frac{\alpha_s}{N_c\omega^2}\int_0^\infty dz\int_0^\infty d\bar{z}\int_{\boldsymbol{x}_{\rm in}}|J(\boldsymbol{x}_{\rm in})|^2\langle\mathrm{Tr}[\mathcal{W}(\boldsymbol{x}_{\rm in};\infty,z)t^a_{\rm proj}\mathcal{W}(\boldsymbol{x}_{\rm in};z,0)[\nabla_{\alpha,\boldsymbol{x}_{\rm in}}\mathcal{G}^{ba}(\boldsymbol{k}_f,z_f;\boldsymbol{x}_{\rm in},z)]\\ \times(\mathcal{W}(\boldsymbol{x}_{\rm in};\infty,\bar{z})t^{\bar{a}}_{\rm proj}\mathcal{W}(\boldsymbol{x}_{\rm in};\bar{z},0)[\nabla_{\alpha,\boldsymbol{x}_{\rm in}}\mathcal{G}^{b\bar{a}}(\boldsymbol{k},z_f;\boldsymbol{x}_{\rm in},\bar{z})])^\dagger]\rangle,\end{aligned} \tag{18}$$

where the subscript α in the derivatives runs over the two components of the transverse vector $\boldsymbol{x}_{\rm in}$.

This expression can further be simplified if one notices that the fundamental Wilson lines can be combined to form the Wilson line in the adjoint representation, see e.g. [46–48]. Indeed, if $\bar{z} > z$, then

$$\begin{aligned}\mathrm{Tr}[\mathcal{W}(\boldsymbol{x}_{\rm in};\infty,z)t^a_{\rm proj}\mathcal{W}(\boldsymbol{x}_{\rm in};z,0)\mathcal{W}^\dagger(\boldsymbol{x}_{\rm in};\bar{z},0)t^{\bar{a}}_{\rm proj}\mathcal{W}^\dagger(\boldsymbol{x}_{\rm in};\infty,\bar{z})] &= \mathrm{Tr}[\mathcal{W}(\boldsymbol{x}_{\rm in};\bar{z},z)t^a_{\rm proj}\mathcal{W}^\dagger(\boldsymbol{x}_{\rm in};\bar{z},z)t^{\bar{a}}_{\rm proj}]\\ &= \frac{1}{2}\mathcal{W}_A^{\dagger a\bar{a}}(\boldsymbol{x}_{\rm in};\bar{z},z),\end{aligned} \tag{19}$$

which in terms of the adjoint generators reads

$$\mathcal{W}_A^{\dagger a\bar{a}}(\boldsymbol{x}_{\rm in};\bar{z},z) = \mathcal{P}\exp\left\{-i\int_z^{\bar{z}}d\tau(T^c)^{a\bar{a}}\tilde{v}^c(\boldsymbol{x}_{\rm in},\tau)\right\} \tag{20}$$

and we can rewrite (18) as

$$\begin{aligned}2(2\pi)^3\omega E\frac{d\mathcal{N}}{d\omega dEd^2\boldsymbol{k}} = \lim_{z_f\to\infty}\frac{\alpha_s}{N_c\omega^2}\mathrm{Re}\int_0^\infty d\bar{z}\int_0^{\bar{z}}dz\int_{\boldsymbol{x}_{\rm in}}|J(\boldsymbol{x}_{\rm in})|^2\langle[\nabla_{\alpha,\boldsymbol{x}_{\rm in}}\mathcal{G}^{ba}(\boldsymbol{k},z_f;\boldsymbol{x}_{\rm in},z)]\mathcal{W}_A^{\dagger a\bar{a}}(\boldsymbol{x}_{\rm in};\bar{z},z)\\ \times[\nabla_{\alpha,\boldsymbol{x}_{\rm in}}\mathcal{G}^{\dagger\bar{a}b}(\boldsymbol{k},z_f;\boldsymbol{x}_{\rm in},\bar{z})]\rangle,\end{aligned} \tag{21}$$

where the contributions from the two regions with $\bar{z} > z$ and $z > \bar{z}$ combine into the real part of the expression above.

We further assume that the color source densities have Gaussian statistics, enforcing the color neutrality condition, see e.g. [23]. Then, the only nontrivial average is given by

$$\langle\hat{\rho}^a(\boldsymbol{x},z)\hat{\rho}^b(\bar{\boldsymbol{x}},\bar{z})\rangle = \frac{1}{2C_{\bar{R}}}\delta^{ab}\delta^{(2)}(\boldsymbol{x}-\bar{\boldsymbol{x}})\delta(z-\bar{z})\rho(\boldsymbol{x},z), \tag{22}$$

or, equivalently,

$$\langle\hat{\rho}^a(\boldsymbol{q},z)\hat{\rho}^b(\bar{\boldsymbol{q}},\bar{z})\rangle = \frac{1}{2C_{\bar{R}}}\delta^{ab}\delta(z-\bar{z})\int_{\boldsymbol{x}}e^{-i(\boldsymbol{q}+\bar{\boldsymbol{q}})\cdot\boldsymbol{x}}\rho(\boldsymbol{x},z), \tag{23}$$

where $\rho(\boldsymbol{x},z)$ denotes the number density of the scattering centers in the medium, the sources are assumed to be in the same representation R, and $C_{\bar{R}}$ is the quadratic Casimir in the representation opposite to R. In coordinate space, $\hat{\rho}^a(\boldsymbol{x},z)$ is real, and its Fourier transform satisfies $\hat{\rho}^{a\dagger}(\boldsymbol{q},z) = \hat{\rho}^a(-\boldsymbol{q},z)$. Thus,

$$\begin{aligned}\langle\tilde{v}^a(\boldsymbol{x},z)\tilde{v}^{\dagger b}(\bar{\boldsymbol{x}},\bar{z})\rangle \simeq \frac{\delta^{ab}}{2C_{\bar{R}}}g^4\delta(z-\bar{z})\int_{q,Q}e^{iq\cdot(x-\bar{x})}\rho(z)(2\pi)^2\delta^{(2)}(\boldsymbol{Q})\\ \times\left[1+\hat{\boldsymbol{g}}\cdot\left(\frac{\boldsymbol{x}+\bar{\boldsymbol{x}}}{2}+\frac{\partial}{\partial\boldsymbol{Q}}\right)\right]v\left(\boldsymbol{q}+\frac{1}{2}\boldsymbol{Q},0,z\right)v^\dagger\left(\boldsymbol{q}-\frac{1}{2}\boldsymbol{Q},0,z\right)\Big|_{q_0=q_z=Q_0=Q_z=0},\end{aligned} \tag{24}$$

where the leading gradient corrections are accounted by $\hat{\boldsymbol{g}}$, see e.g. [38]. Taking the GW model as an illustrative example, this average reads

$$\langle \tilde{v}^a(\boldsymbol{x},z)\tilde{v}^{\dagger b}(\bar{\boldsymbol{x}},\bar{z})\rangle \simeq \frac{\delta^{ab}}{2C_{\bar{R}}} g^4 \delta(z-\bar{z})\left(1+\frac{\boldsymbol{x}+\bar{\boldsymbol{x}}}{2}\cdot\hat{\boldsymbol{g}}\right) \times \int_{\boldsymbol{q}} \frac{\rho(z)e^{i\boldsymbol{q}\cdot(\boldsymbol{x}-\bar{\boldsymbol{x}})}}{(\boldsymbol{q}^2+\mu^2(z))^2}. \tag{25}$$

Even in the presence of transverse gradients, the average (25) is still local in z. Consequently, an average of a product of single-particle propagators with no common support reduces to a product of averages. That allows us to write (21) as

$$\begin{aligned} 2(2\pi)^3\omega E\frac{d\mathcal{N}}{d\omega dEd^2\boldsymbol{k}} &= \lim_{z_f\to\infty}\frac{\alpha_s}{N_c\omega^2}\mathrm{Re}\int_0^\infty d\bar{z}\int_0^{\bar{z}} dz\int_{\boldsymbol{x}_{\mathrm{in}},\boldsymbol{y}} |J(\boldsymbol{x}_{\mathrm{in}})|^2 \\ &\times\left[(\boldsymbol{\nabla}_{\boldsymbol{x}}\cdot\boldsymbol{\nabla}_{\bar{\boldsymbol{x}}})\left\langle\mathcal{G}^{bc}(\boldsymbol{k},z_f;\boldsymbol{y},\bar{z})\mathcal{G}^{\dagger\bar{a}b}(\boldsymbol{k},z_f;\bar{\boldsymbol{x}},\bar{z})\right\rangle\right. \\ &\times\left.\left\langle\mathcal{G}^{ca}(\boldsymbol{y},\bar{z};\boldsymbol{x},z)\mathcal{W}_A^{\dagger a\bar{a}}(\boldsymbol{x}_{\mathrm{in}};\bar{z},z)\right\rangle\right]\Big|_{\boldsymbol{x}=\bar{\boldsymbol{x}}=\boldsymbol{x}_{\mathrm{in}}}, \end{aligned} \tag{26}$$

where we have used a mixed coordinate representation.

Because of the color triviality of the medium averages, one can simplify the color structure in (26), writing the full process in terms of an emission kernel, $\mathcal{K}$, with support in the interval $(z,\bar{z})$, and a broadening kernel, S_2, which describes the evolution of the radiated gluon after being produced. These kernels are defined to be

$$\begin{aligned} S_2(\boldsymbol{k},\boldsymbol{k},z_f;\boldsymbol{y},\bar{\boldsymbol{x}},\bar{z}) &= \frac{1}{N_c^2-1}\langle\mathcal{G}^{bc}(\boldsymbol{k},z_f;\boldsymbol{y},\bar{z})\mathcal{G}^{\dagger cb}(\boldsymbol{k},z_f;\bar{\boldsymbol{x}},\bar{z})\rangle, \\ \mathcal{K}(\boldsymbol{y},\boldsymbol{x}_{\mathrm{in}},\bar{z};\boldsymbol{x},\boldsymbol{x}_{\mathrm{in}},z) &= \frac{1}{N_c^2-1}\langle\mathcal{G}^{ba}(\boldsymbol{y},\bar{z};\boldsymbol{x},z)\mathcal{W}_A^{\dagger ab}(\boldsymbol{x}_{\mathrm{in}};\bar{z},z)\rangle, \end{aligned} \tag{27}$$

such that the full distribution can be compactly written as

$$2(2\pi)^3\omega E\frac{d\mathcal{N}}{d\omega dEd^2\boldsymbol{k}} = \frac{2\alpha_sC_F}{\omega^2}\mathrm{Re}\int_0^\infty d\bar{z}\int_0^{\bar{z}} dz\int_{\boldsymbol{x}_{\mathrm{in}},\boldsymbol{y}} |J(\boldsymbol{x}_{\mathrm{in}})|^2[\boldsymbol{\nabla}_{\boldsymbol{x}}\cdot\boldsymbol{\nabla}_{\bar{\boldsymbol{x}}}S_2(\boldsymbol{k},\boldsymbol{k},\infty;\boldsymbol{y},\bar{\boldsymbol{x}},\bar{z})\mathcal{K}(\boldsymbol{y},\boldsymbol{x}_{\mathrm{in}},\bar{z};\boldsymbol{x},\boldsymbol{x}_{\mathrm{in}},z)]|_{\boldsymbol{x}=\bar{\boldsymbol{x}}=\boldsymbol{x}_{\mathrm{in}}}. \tag{28}$$

Thus, the final soft gluon distribution factorizes into the two correlators even in the presence of transverse gradients, while the effects of the matter anisotropy enter each one of them independently.

Now, we can utilize the explicit form of the two-point correlator (25), taking into account the gradient corrections. Here, we will focus on the case of longitudinally uniform matter, keeping the algebra more compact, while the results can be straightforwardly generalized. The corresponding broadening two-point function has already been derived in [38] up to the first order in transverse gradients, and its in-medium part reads

$$\begin{aligned} &S_2(\boldsymbol{k},\boldsymbol{k},L;\boldsymbol{y},\bar{\boldsymbol{x}},\bar{z}) \\ &\simeq e^{-i\boldsymbol{k}\cdot\boldsymbol{u}}e^{-\mathcal{V}(\boldsymbol{u})(L-\bar{z})}\left[1+\frac{i(L-\bar{z})^3}{3\omega}\boldsymbol{\nabla}\mathcal{V}(\boldsymbol{u})\cdot\hat{\boldsymbol{g}}\mathcal{V}(\boldsymbol{u})\right. \\ &\quad -i\frac{(L-\bar{z})^2}{2\omega}\hat{\boldsymbol{g}}\cdot\boldsymbol{\nabla}\mathcal{V}(\boldsymbol{u})-\boldsymbol{w}\cdot\hat{\boldsymbol{g}}\mathcal{V}(\boldsymbol{u})(L-\bar{z}) \\ &\quad \left.-\frac{(L-\bar{z})^2}{2\omega}\boldsymbol{k}\cdot\hat{\boldsymbol{g}}\mathcal{V}(\boldsymbol{u})\right], \end{aligned} \tag{29}$$

where $\boldsymbol{u}=\boldsymbol{y}-\bar{\boldsymbol{x}}$, $\boldsymbol{w}=\frac{\boldsymbol{y}+\bar{\boldsymbol{x}}}{2}$, and L is the matter extension. The effective in-medium scattering potential $\mathcal{V}$ is often referred to as a dipole potential, and is given by

$$\mathcal{V}(\boldsymbol{q}) = -\mathcal{C}\rho\left(|v(\boldsymbol{q})|^2-\delta^{(2)}(\boldsymbol{q})\int_{\boldsymbol{k}}|v(\boldsymbol{k})|^2\right), \tag{30}$$

where $v(\boldsymbol{q})=v(\boldsymbol{q},0,z)$, and in the case of the GW model $v(\boldsymbol{q})=-\frac{g^2}{\boldsymbol{q}^2+\mu^2(z)}$ with $\mu(z)$ being constant. Here, we have also introduced an overall color coefficient $\mathcal{C}=\frac{N_c}{2C_{\bar{R}}}$. In turn, outside the medium ($z_f>\bar{z}>L$), the broadening two-point function is trivial, and can be obtained from (29) in the limit $\mathcal{V}\to 0$, reducing to $S_2(\boldsymbol{k},\boldsymbol{k},\infty;\boldsymbol{y},\bar{\boldsymbol{x}},L)=e^{-i\boldsymbol{k}\cdot\boldsymbol{u}}$.

The emission kernel is similar to the broadening two-point function in its structure, but is harder to evaluate for the general potential $\mathcal{V}$. Following [38], one can write the medium average of two Wilson lines up to the leading order in gradient corrections as

$$\begin{aligned} &\left\langle\mathcal{P}\exp\left\{i\int_z^{\bar{z}}d\tau T^a\tilde{v}^a(\mathbf{r},\tau)\right\}\mathcal{P}\exp\left\{-i\int_z^{\bar{z}}d\tau T^b\tilde{v}^b(\boldsymbol{x}_{\mathrm{in}},\tau)\right\}\right\rangle \\ &\simeq\exp\left\{-\int_z^{\bar{z}}d\tau\left(1+\frac{\mathbf{r}+\boldsymbol{x}_{\mathrm{in}}}{2}\cdot\hat{\boldsymbol{g}}\right)\mathcal{V}(\mathbf{r}-\boldsymbol{x}_{\mathrm{in}})\right\}, \end{aligned} \tag{31}$$

and the kernel can be expressed as the corresponding path integral, cf. with the homogeneous case [29,46–48]. Thus, it takes the form

$$\mathcal{K}(\boldsymbol{y},\boldsymbol{x}_{\rm in},\bar{z};\boldsymbol{x},\boldsymbol{x}_{\rm in},z)=\int_{\boldsymbol{x}}^{\boldsymbol{y}}\mathcal{D}\boldsymbol{r}e^{\frac{i\omega}{2}\int d\tau\dot{\boldsymbol{r}}^2-\int_z^{\bar{z}}d\tau(1+\frac{\boldsymbol{r}(\tau)+\boldsymbol{x}_{\rm in}}{2}\cdot\hat{\boldsymbol{g}})\mathcal{V}(\boldsymbol{r}(\tau)-\boldsymbol{x}_{\rm in})},\tag{32}$$

where the leading gradient corrections are also included. Here we notice that, when both of the longitudinal arguments in the kernel are outside the medium, it also becomes vacuum-like,

$$\mathcal{K}(\boldsymbol{y},\boldsymbol{x}_{\rm in},\bar{z};\boldsymbol{x},\boldsymbol{x}_{\rm in},z)|_{z>L}=\int_{\boldsymbol{k}}e^{i\boldsymbol{k}\cdot(\boldsymbol{y}-\boldsymbol{x})}e^{-i\frac{\boldsymbol{k}^2}{2\omega}(\bar{z}-z)},\tag{33}$$

while for $\bar{z}>L>z$ it can be expressed as a convolution,

$$\mathcal{K}(\boldsymbol{y},\boldsymbol{x}_{\rm in},\bar{z};\boldsymbol{x},\boldsymbol{x}_{\rm in},z)|_{\bar{z}>L>z}=\int_{\boldsymbol{k}}e^{i\boldsymbol{k}\cdot\boldsymbol{y}}e^{-i\frac{\boldsymbol{k}^2}{2\omega}(\bar{z}-L)}\times\mathcal{K}(\boldsymbol{k},\boldsymbol{x}_{\rm in},L;\boldsymbol{x},\boldsymbol{x}_{\rm in},z).\tag{34}$$

Thus, it is convenient to split the full distribution into three portions, coming from the three integration regions: $\bar{z}<L$, $z<L<\bar{z}$, and $L<z$. We will refer to these regions as "in-in," "in-out," and "out-out," respectively, see e.g. [46]. One readily finds that the in-medium contribution is given by

$$\begin{aligned}2(2\pi)^3\omega E\frac{dN^{\rm in-in}}{d\omega dEd^2\boldsymbol{k}}=&\frac{2\alpha_sC_F}{\omega^2}{\rm Re}\int_0^L d\bar{z}\int_0^{\bar{z}}dz\int_{\boldsymbol{x}_{\rm in}\boldsymbol{y}}e^{-i\boldsymbol{k}\cdot\boldsymbol{y}}|J(\boldsymbol{x}_{\rm in})|^2\mathcal{P}_{L-\bar{z}}(\boldsymbol{y})\\&\times\left\{\left[1+i\frac{(L-\bar{z})^2}{2\omega}\hat{\boldsymbol{g}}\mathcal{V}(\boldsymbol{y})\cdot\boldsymbol{\nabla}_{\boldsymbol{y}}-\frac{\boldsymbol{y}+2\boldsymbol{x}_{\rm in}}{2}\cdot\hat{\boldsymbol{g}}\mathcal{V}(\boldsymbol{y})(L-\bar{z})\right]\boldsymbol{\nabla}_{\boldsymbol{y}}-\hat{\boldsymbol{g}}\mathcal{V}(\boldsymbol{y})(L-\bar{z})\right\}\\&\cdot\boldsymbol{\nabla}_{\boldsymbol{x}}\mathcal{K}(\boldsymbol{y}+\boldsymbol{x}_{\rm in},\boldsymbol{x}_{\rm in},\bar{z};\boldsymbol{x},\boldsymbol{x}_{\rm in},z)\Big|_{\boldsymbol{x}=\bar{\boldsymbol{x}}=\boldsymbol{x}_{\rm in}},\end{aligned}\tag{35}$$

where we have substituted (29), and integrated by parts. We have also introduced a broadening probability

$$\mathcal{P}_{L-\bar{z}}(\boldsymbol{y})=e^{-\mathcal{V}(\boldsymbol{y})(L-\bar{z})}\left[1-\frac{i(L-\bar{z})^3}{6\omega}\boldsymbol{\nabla}\mathcal{V}(\boldsymbol{y})\cdot\hat{\boldsymbol{g}}\mathcal{V}(\boldsymbol{y})\right],\tag{36}$$

which controls the broadening process for a narrow initial distribution [38]. One may notice that the structure in the second line of (35) resembles the shift operator introduced in [38]. Indeed, the emission kernel $\mathcal{K}$ convoluted with the source of the parent parton J serves as a source for the consequent broadening of the emitted gluon. However, the broadening structure is more involved now, since the effective initial distribution is sensitive to the center of mass position of the color dipole $\boldsymbol{w}$ in (29), and new terms, absent in the results of [38], appear. In turn, the in-out contribution reads

$$\begin{aligned}2(2\pi)^3\omega E\frac{dN^{\rm in-out}}{d\omega dEd^2\boldsymbol{k}}=&\frac{2\alpha_sC_F}{\omega}{\rm Re}\int_0^L dz\int_{\boldsymbol{x}_{\rm in}}e^{i\boldsymbol{k}\cdot\boldsymbol{x}_{\rm in}}|J(\boldsymbol{x}_{\rm in})|^2\\&\times 2\frac{\boldsymbol{k}}{\boldsymbol{k}^2}\cdot\boldsymbol{\nabla}_{\boldsymbol{x}}\mathcal{K}(\boldsymbol{k},\boldsymbol{x}_{\rm in},L;\boldsymbol{x},\boldsymbol{x}_{\rm in},z)\Big|_{\boldsymbol{x}=\boldsymbol{x}_{\rm in}},\end{aligned}\tag{37}$$

where we have explicitly evaluated the $\bar{z}$ integral, noticing that the vacuum kernel is regulated to decay at the infinity. Finally, one may notice that the out-out contribution corresponds to the physical situation when the emission happens outside the matter, both in direct and conjugated amplitudes. Here, we will omit it, focusing solely on the medium induced part of the spectrum.

III. MEDIUM INDUCED SPECTRUM IN THE HARMONIC APPROXIMATION

In this section, we will focus on the medium induced gluon distribution at the leading order in gradients. However, even in the homogeneous limit, the resummed medium induced gluon distribution has highly nontrivial structure, and cannot be treated analytically. Here, we will rely on additional approximations, which considerably simplify the results and are commonly used in the homogeneous case, see e.g. [46–50].

First, we ignore the initial state effects, taking a broad source approximation and setting $|J(\boldsymbol{x}_{\rm in})|^2=f(E)\delta^{(2)}(\boldsymbol{x}_{\rm in})$. This allows us to simplify $\mathcal{K}$, and relate the particle distribution dN with the medium induced gluon spectrum dI in the regular way. Thus, we write

$$(2\pi)^2\omega E\frac{dN}{d\omega dEd^2\boldsymbol{k}}=(2\pi)^2\omega\frac{dI}{d\omega d^2\boldsymbol{k}}E\frac{dN_0}{dE},\tag{38}$$

where $E\frac{dN_0}{dE}=\frac{1}{2(2\pi)}f(E)$. The only dependence of the full final state distribution on the initial condition comes from the quark spectrum and can be trivially factorized. This effective form for the particle distribution can be argued to follow from the QCD factorization for soft radiation.

We further notice that the path integral in (32) cannot be performed analytically in the general case, see e.g. [46–50] for discussions, and even for the specified GW potential we are using here as an example. However, to illustrate the leading gradient effects more explicitly, we find it instructive to consider a tractable model. To do so, let us assume that the effective scattering potential is quadratic, $\mathcal{V}(\boldsymbol{y})=\frac{\hat{q}}{4}\boldsymbol{y}^2$, focusing on the so-called harmonic approximation. This effective potential can be understood as a separate medium model, but often it is considered as an approximation to other models, such as the GW one, see e.g. [50] for a recent discussion. The proportionality coefficient $\hat{q}$ is commonly referred to as the jet quenching parameter. It is closely related with the broadening process, and, in the general case, it is defined as $\hat{q} = \frac{\partial}{\partial L}\langle \boldsymbol{p}^2\rangle$. For instance, for the GW model, one finds that $\hat{q} = \frac{\mu^2\chi}{L}\log\frac{\Lambda^2}{\mu^2}$ with $\chi \equiv \frac{\mathcal{C}g^4\rho}{4\pi\mu^2}L$ being the medium opacity. The Coulomb logarithm is divergent and regulated by a momentum scale Λ, which can be understood as a free parameter of the medium model. Taking $\hat{q}$, as in the GW model, one may consider the harmonic approximation potential for $\mathcal{V}(\boldsymbol{y})$ as the leading contribution at small $\mu|\boldsymbol{y}|$ with a regulated logarithm. Here, we will not discuss this relation or its phenomenological relevance further, utilizing the harmonic potential and explicit form of $\hat{q}$ in the GW model only as illustrations of our general results (35) and (37).

Now, we can further simplify the emission spectrum, expanding the broadening two-point function and emission kernel as $\mathcal{K} \simeq \mathcal{K}^{(0)} + \delta\mathcal{K}$ and $\mathcal{P} \simeq \mathcal{P}^{(0)} + \delta\mathcal{P}$, where the perturbations are linear in gradients. In the absence of gradients, the path integral in (32) becomes Gaussian in the harmonic approximation. Thus, it can be readily evaluated [46–48,50], resulting in

$$\mathcal{K}^{(0)}(\boldsymbol{y},\bar{z};\boldsymbol{x},z) \equiv \mathcal{K}^{(0)}(\boldsymbol{y},0,\bar{z};\boldsymbol{x},0,z) \simeq \frac{A_{\bar{z}z}}{\pi i}\exp\{iA_{\bar{z}z}B_{\bar{z}z}(\boldsymbol{y}^2+\boldsymbol{x}^2) - 2iA_{\bar{z}z}\boldsymbol{y}\cdot\boldsymbol{x}\}, \tag{39}$$

where we have introduced $A_{\bar{z}z} = \frac{\omega\Omega}{2\sin(\Omega(\bar{z}-z))}$ and $B_{\bar{z}z} = \cos(\Omega(\bar{z}-z))$ with $\Omega = \frac{1-i}{2}\sqrt{\frac{\hat{q}}{\omega}}$, and set $\boldsymbol{x}_{\mathrm{in}} = 0$. Treating the leading gradient correction to the potential in (32) perturbatively, we further find that

$$\begin{aligned}\delta\mathcal{K}(\boldsymbol{y},\bar{z};\boldsymbol{x},z) &\equiv \mathcal{K}(\boldsymbol{y},\bar{z};\boldsymbol{x},z) - \mathcal{K}^{(0)}(\boldsymbol{y},\bar{z};\boldsymbol{x},z)\\ &= -\frac{1}{2}\boldsymbol{g}\cdot\int_{\boldsymbol{w}}\int_z^{\bar{z}} ds\,\boldsymbol{w}\,\mathcal{K}^{(0)}(\boldsymbol{y},\bar{z};\boldsymbol{w},s)\mathcal{V}(\boldsymbol{w},s)\\ &\quad\times\mathcal{K}^{(0)}(\boldsymbol{w},s;\boldsymbol{x},z),\end{aligned} \tag{40}$$

where $\hat{\boldsymbol{g}}$, acting solely on $\hat{q}$, has been replaced with $\boldsymbol{g} = \frac{1}{\hat{q}}\hat{\boldsymbol{g}}\,\hat{q}$. Similarly, in the harmonic approximation, the broadening probability is also Gaussian, and reads

$$\mathcal{P}_z^{(0)}(\boldsymbol{p}) \equiv \int_{\boldsymbol{x}} e^{-i\boldsymbol{p}\cdot\boldsymbol{x}}e^{-\mathcal{V}(\boldsymbol{x})z} = \frac{4\pi}{\hat{q}z}e^{-\frac{\boldsymbol{p}^2}{\hat{q}z}}, \tag{41}$$

while the leading gradient correction is given by

$$\begin{aligned}\delta\mathcal{P}_z(\boldsymbol{p}) &\equiv \int_{\boldsymbol{x}} e^{-i\boldsymbol{p}\cdot\boldsymbol{x}}e^{-\mathcal{V}(\boldsymbol{x})z}\left[-\frac{iz^3}{6\omega}\nabla\mathcal{V}(\boldsymbol{x})\cdot\boldsymbol{g}\mathcal{V}(\boldsymbol{x})\right]\\ &= \frac{4\pi}{\hat{q}z}e^{-\frac{\boldsymbol{p}^2}{\hat{q}z}}\frac{z}{6\omega}\left(\frac{\boldsymbol{p}^2-2\hat{q}z}{\hat{q}z}\right)\boldsymbol{g}\cdot\boldsymbol{p}.\end{aligned} \tag{42}$$

Expanding the medium induced soft gluon spectrum to the leading order in $\boldsymbol{g}$ we can write it with these notations as

$$\omega\frac{dI}{d\omega d^2\boldsymbol{k}} = \omega\frac{dI_0}{d\omega d^2\boldsymbol{k}} + \omega\frac{dI_{\mathcal{P}}}{d\omega d^2\boldsymbol{k}} + \omega\frac{dI_{\mathcal{K}}}{d\omega d^2\boldsymbol{k}} + \omega\frac{dI_{\hat{\mathsf{S}}}}{d\omega d^2\boldsymbol{k}}, \tag{43}$$

where the gradient corrections are grouped by their origin for convenience. While the notations for $dI_{\mathcal{P}}$ and $dI_{\mathcal{K}}$ are clear, they correspond to the gradient terms coming from $\delta\mathcal{P}$ and $\delta\mathcal{K}$, the last contribution in (43) has a subscript $\hat{\mathsf{S}}$. This object corresponds to the terms in the second line of (35), and it can be thought of as a generalization of the shift operator, adjusting the argument of the initial distribution by a gradient contribution in the case of simple momentum broadening in [38]. Here, the effective initial distribution of the emitted gluon is given by a convolution of $\mathcal{K}$ with J, while some additional terms appear due to the dependence of the answer on the center of mass position of the color dipole. Finally, we notice that, since the presence of the gradients is naturally attached to the presence of the medium, only $dI_{\mathcal{K}}$ may be nontrivial in the in-out region.

IV. THE GRADIENT CORRECTIONS

Now, we are in the position to evaluate the novel contributions. As a warm-up exercise, we start by considering the standard spectrum dI_0, appearing in the case of homogeneous medium. Some of the intermediate calculations, which are not shown explicitly here, can be found in great detail in the literature, see e.g. [50].

As has already been mentioned, the two different integration regions result in two contributions to the gluon spectrum. From (35) one readily finds that in the absence of the gradients the in-in part is given by

$$\begin{aligned}(2\pi)^2\omega\frac{dI_0^{\mathrm{in-in}}}{d\omega d^2\boldsymbol{k}} &= \frac{2\alpha_s C_F}{\omega^2}\mathrm{Re}\int_0^L d\bar{z}\int_0^{\bar{z}} dz\int_{\boldsymbol{y}} e^{-i\boldsymbol{k}\cdot\boldsymbol{y}}\mathcal{P}_{L-\bar{z}}^{(0)}(\boldsymbol{y})\boldsymbol{\nabla}_{\boldsymbol{y}}\\ &\quad\cdot\boldsymbol{\nabla}_{\boldsymbol{x}}\mathcal{K}^{(0)}(\boldsymbol{y},\bar{z};\boldsymbol{x},z)\Big|_{\boldsymbol{x}=0}\\ &= \frac{4\alpha_s C_F}{\omega}\mathrm{Re}\int_0^L d\bar{z}\frac{e^{\frac{\boldsymbol{k}^2\mathcal{T}_{\bar{z}}}{i-Q_{\bar{z}}^2\mathcal{T}_{\bar{z}}}}}{Q_{\bar{z}}^2\mathcal{T}_{\bar{z}}-i},\end{aligned} \tag{44}$$

where we have introduced shorthand notations $Q_{\bar{z}}^2 = \hat{q}(L-\bar{z})$ and $\mathcal{T}_z = \frac{\tan(\Omega z)}{2\omega\Omega}$. This is the simplest analytical form, which can be obtained without switching to the numerical tools, which we will do later.

In turn, the in-out part follows from (37), and in the absence of the gradients we readily find the standard answer

$$\begin{aligned}(2\pi)^2\omega\frac{dI_0^{\mathrm{in-out}}}{d\omega d^2\boldsymbol{k}} &= \frac{2\alpha_s C_F}{\omega}\mathrm{Re}\int_0^L dz\int_{\boldsymbol{y}} e^{-i\boldsymbol{k}\cdot\boldsymbol{y}}2\frac{\boldsymbol{k}}{\boldsymbol{k}^2}\cdot\boldsymbol{\nabla}_{\boldsymbol{x}}\mathcal{K}^{(0)}(\boldsymbol{y},L;\boldsymbol{x},z)\Big|_{\boldsymbol{x}=0}\\ &= -\frac{8\alpha_s C_F}{\boldsymbol{k}^2}\mathrm{Re}(1-e^{-i\boldsymbol{k}^2\mathcal{T}_L}). \end{aligned} \tag{45}$$

The $dI_{\mathcal{P}}$ term accounts for the gradient effects on the late time evolution of the gluon. As a consequence, it only has support in the in-in region. Explicitly, it can be written as

$$\begin{aligned}(2\pi)^2\omega\frac{dI_{\mathcal{P}}^{\mathrm{in-in}}}{d\omega d^2\boldsymbol{k}} &= \frac{2\alpha_s C_F}{\omega^2}\mathrm{Re}\int_0^L d\bar{z}\int_0^{\bar{z}} dz\int_{\boldsymbol{y}} e^{-i\boldsymbol{k}\cdot\boldsymbol{y}}\delta\mathcal{P}_{L-\bar{z}}(\boldsymbol{y})\boldsymbol{\nabla}_{\boldsymbol{y}}\cdot\boldsymbol{\nabla}_{\boldsymbol{x}}\mathcal{K}^{(0)}(\boldsymbol{y},\bar{z};\boldsymbol{x},z)\Big|_{\boldsymbol{x}=0}\\ &= \frac{8\alpha_s C_F\pi}{3\hat{q}\omega^2}\mathrm{Re}\int_0^L d\bar{z}\int_{\boldsymbol{q}} ie^{-\frac{\boldsymbol{q}^2}{Q_{\bar{z}}^2}}\left(\frac{\boldsymbol{q}^2-2Q_{\bar{z}}^2}{Q_{\bar{z}}^2}\right)\boldsymbol{g}\cdot\boldsymbol{q}e^{-i(\boldsymbol{k}-\boldsymbol{q})^2\mathcal{T}_{\bar{z}}}, \end{aligned} \tag{46}$$

where the remaining integral over $\boldsymbol{q}$ is Gaussian, and we find

$$(2\pi)^2\omega\frac{dI_{\mathcal{P}}^{\mathrm{in-in}}}{d\omega d^2\boldsymbol{k}} = \frac{2\alpha_s C_F}{3\hat{q}\omega^2}(\boldsymbol{g}\cdot\boldsymbol{k})\mathrm{Re}\int_0^L d\bar{z}e^{\frac{\boldsymbol{k}^2\mathcal{T}_{\bar{z}}}{i-Q_{\bar{z}}^2\mathcal{T}_{\bar{z}}}}Q_{\bar{z}}^6\mathcal{T}_{\bar{z}}^2\frac{2i+(\boldsymbol{k}^2-2Q_{\bar{z}}^2)\mathcal{T}_{\bar{z}}}{(i-Q_{\bar{z}}^2\mathcal{T}_{\bar{z}})^4}. \tag{47}$$

The $I_{\mathcal{K}}$ part of the spectrum is the only gradient correction, having support in both the in-in and in-out regions, and it results in two contributions. The in-in term is given by

$$(2\pi)^2\omega\frac{dI_{\mathcal{K}}^{\mathrm{in-in}}}{d\omega d^2\boldsymbol{k}} = \frac{2\alpha_s C_F}{\omega^2}\mathrm{Re}\int_0^L d\bar{z}\int_0^{\bar{z}} dz\int_{\mathbf{y}} e^{-i\boldsymbol{k}\cdot\boldsymbol{y}}\mathcal{P}_{L-\bar{z}}^{(0)}(\boldsymbol{y})\boldsymbol{\nabla}_{\boldsymbol{y}}\cdot\boldsymbol{\nabla}_{\boldsymbol{x}}\delta\mathcal{K}(\boldsymbol{y},\bar{z};\boldsymbol{x},z)\Big|_{\boldsymbol{x}=0}, \tag{48}$$

and, after some algebra, it can be written as

$$\begin{aligned}(2\pi)^2\omega\frac{dI_{\mathcal{K}}^{\mathrm{in-in}}}{d\omega d^2\boldsymbol{k}} &= -\frac{\alpha_s C_F\hat{q}}{4\pi\omega}\mathrm{Re}\int_0^L d\bar{z}\int_0^{\bar{z}} dz\int_{\boldsymbol{q},\boldsymbol{w}}\frac{e^{-i\mathcal{T}_{\bar{z}-z}\boldsymbol{q}^2}}{B_{\bar{z}z}}\mathcal{P}_{L-\bar{z}}^{(0)}(\boldsymbol{k}-\boldsymbol{q})\\ &\quad\times e^{\frac{i\boldsymbol{w}^2}{4\mathcal{T}_z}}(\boldsymbol{g}\cdot\boldsymbol{w})(\boldsymbol{q}\cdot\boldsymbol{w})\exp\left\{-i\left(\frac{\boldsymbol{q}\cdot\boldsymbol{w}}{B_{\bar{z}z}}-\frac{A_{\bar{z}z}(B_{\bar{z}z}^2-1)}{B_{\bar{z}z}}\boldsymbol{w}^2\right)\right\}, \end{aligned} \tag{49}$$

where we have changed the order of integration, and renamed the intermediate position s by z, while the initial z integration has been performed. The transverse integrals can be evaluated analytically, resulting in

$$\begin{aligned}(2\pi)^2\omega\frac{dI_{\mathcal{K}}^{\mathrm{in-in}}}{d\omega d^2\boldsymbol{k}} &= \frac{32\alpha_s C_F\hat{q}}{\omega}(\boldsymbol{g}\cdot\boldsymbol{k})\mathrm{Re}\int_0^L d\bar{z}\int_0^{\bar{z}} dze^{\frac{\boldsymbol{k}^2\mathcal{T}_{\bar{z}}}{i-Q_{\bar{z}}^2\mathcal{T}_{\bar{z}}}}\mathcal{T}_z^2\\ &\quad\times\frac{3Q_{\bar{z}}^4\mathcal{T}_z^2-B_{\bar{z}z}^2C_{\bar{z}z}^2(i-Q_{\bar{z}}^2\mathcal{T}_{\bar{z}-z})^2-2iB_{\bar{z}z}C_{\bar{z}z}\mathcal{T}_z(\boldsymbol{k}^2+Q_{\bar{z}}^2+iQ_{\bar{z}}^4\mathcal{T}_{\bar{z}-z})}{16C_{\bar{z}z}^4(i-Q_{\bar{z}}^2\mathcal{T}_{\bar{z}})^4B_{\bar{z}z}}, \end{aligned} \tag{50}$$

where $C_{ts}=\frac{\cos(\Omega t)}{\cos(\Omega s)}$. Finally, one may notice that in this form the z integration is sufficiently simple, resulting in

$$\begin{aligned}(2\pi)^2\omega\frac{dI_{\mathcal{K}}^{\mathrm{in-in}}}{d\omega d^2\boldsymbol{k}} &= \frac{8\alpha_s C_F}{3\hat{q}\omega^2}(\boldsymbol{g}\cdot\boldsymbol{k})\mathrm{Re}\int_0^L d\bar{z}\frac{e^{\frac{\boldsymbol{k}^2\mathcal{T}_{\bar{z}}}{i-Q_{\bar{z}}^2\mathcal{T}_{\bar{z}}}}}{(i-Q_{\bar{z}}^2\mathcal{T}_{\bar{z}})^4}\frac{\sin^2(\frac{\Omega\bar{z}}{2})}{\cos^2(\Omega\bar{z})}\\ &\quad\times\left\{-\omega\Omega\sin(\Omega\bar{z})+i\left[\boldsymbol{k}^2+iQ_{\bar{z}}^4\mathcal{T}_{\bar{z}}+\frac{2(\boldsymbol{k}^2+Q_{\bar{z}}^2)+3iQ_{\bar{z}}^4\mathcal{T}_{\bar{z}}}{\cos(\Omega\bar{z})}\right]\sin^2\left(\frac{\Omega\bar{z}}{2}\right)\right\}. \end{aligned} \tag{51}$$

In turn, the in-out term can be written in the form similar to (37), reading

$$(2\pi)^2\omega\frac{dI_{\mathcal{K}}^{\text{in-out}}}{d\omega d^2\boldsymbol{k}}=\frac{2\alpha_sC_F}{\omega}\text{Re}\int_0^L dz\int_{\boldsymbol{y}}e^{-i\boldsymbol{k}\cdot\boldsymbol{y}}2\frac{\boldsymbol{k}}{\boldsymbol{k}^2}\cdot\boldsymbol{\nabla}_{\boldsymbol{x}}\delta\mathcal{K}(\boldsymbol{y},L;\boldsymbol{x},z)\Big|_{\boldsymbol{x}=0},\tag{52}$$

and, after the transverse integrals are performed, it reduces to

$$(2\pi)^2\omega\frac{dI_{\mathcal{K}}^{\text{in-out}}}{d\omega d^2\boldsymbol{k}}=-\frac{4\alpha_s\hat{q}C_F}{\boldsymbol{k}^2}(\boldsymbol{g}\cdot\boldsymbol{k})\text{Re}\int_0^L dz\frac{\mathcal{T}_z^2}{C_{Lz}^3}e^{-i\boldsymbol{k}^2\mathcal{T}_L}(iB_{Lz}C_{Lz}+2\boldsymbol{k}^2\mathcal{T}_z).\tag{53}$$

Finally, we notice that the last z integral can be treated explicitly, leading to

$$(2\pi)^2\omega\frac{dI_{\mathcal{K}}^{\text{in-out}}}{d\omega d^2\boldsymbol{k}}=-\frac{4}{3\omega^2}\alpha_sC_F\hat{q}\frac{\boldsymbol{g}\cdot\boldsymbol{k}}{\boldsymbol{k}^2}\text{Re}\frac{e^{-i\boldsymbol{k}^2\mathcal{T}_L}}{\Omega^3}\left[i\frac{\sin^2(\frac{\Omega L}{2})\sin(\Omega L)}{\cos^2(\Omega L)}+\frac{\boldsymbol{k}^2}{\omega\Omega}(2+\cos(\Omega L))\frac{\sin^4(\frac{\Omega L}{2})}{\cos^3(\Omega L)}\right].\tag{54}$$

Now, we can turn to the $dI_{\hat{\mathsf{S}}}$ contribution. This term has support only inside the medium, and reads

$$(2\pi)^2\omega\frac{dI_{\hat{\mathsf{S}}}^{\text{in-in}}}{d\omega d^2\boldsymbol{k}}=\frac{2\alpha_sC_F}{\omega^2}\text{Re}\int_0^L d\bar{z}\int_0^{\bar{z}}dz\int_{\boldsymbol{y}}e^{-i\boldsymbol{k}\cdot\boldsymbol{y}}\mathcal{P}_{L-\bar{z}}^{(0)}(\boldsymbol{y})\left\{\left[i\frac{(L-\bar{z})^2}{2\omega}\hat{\boldsymbol{g}}\mathcal{V}(\boldsymbol{y})\cdot\boldsymbol{\nabla}_{\boldsymbol{y}}-\frac{\boldsymbol{y}}{2}\cdot\hat{\boldsymbol{g}}\mathcal{V}(\boldsymbol{y})(L-\bar{z})\right]\boldsymbol{\nabla}_{\boldsymbol{y}}-\hat{\boldsymbol{g}}\mathcal{V}(\boldsymbol{y})(L-\bar{z})\right\}$$
$$\cdot\boldsymbol{\nabla}_{\boldsymbol{x}}\mathcal{K}^{(0)}(\boldsymbol{y},\bar{z};\boldsymbol{x},z)\Big|_{\boldsymbol{x}=0}.\tag{55}$$

Evaluating the z integral, we bring it to a particularly simple form:

$$(2\pi)^2\omega\frac{dI_{\hat{\mathsf{S}}}^{\text{in-in}}}{d\omega d^2\boldsymbol{k}}=\frac{\alpha_sC_F\hat{q}}{2\pi\omega}\text{Re}\int_0^L d\bar{z}\int_{\boldsymbol{y}}e^{-i\boldsymbol{k}\cdot\boldsymbol{y}}e^{\frac{i}{4\mathcal{T}_{\bar{z}}}\boldsymbol{y}^2}\mathcal{P}_{L-\bar{z}}^{(0)}(\boldsymbol{y})(L-\bar{z})\left[i-\frac{\boldsymbol{y}^2}{4\mathcal{T}_{\bar{z}}}\left(1+\frac{L-\bar{z}}{2\omega\mathcal{T}_{\bar{z}}}\right)\right](\boldsymbol{g}\cdot\boldsymbol{y}).\tag{56}$$

The remaining Fourier transformation can be performed analytically, and one finds

$$(2\pi)^2\omega\frac{dI_{\hat{\mathsf{S}}}^{\text{in-in}}}{d\omega d^2\boldsymbol{k}}=-\frac{4\alpha_sC_F}{\omega}(\boldsymbol{g}\cdot\boldsymbol{k})\text{Re}\int_0^L d\bar{z}Q_{\bar{z}}^2\mathcal{T}_{\bar{z}}^2e^{\frac{\boldsymbol{k}^2\mathcal{T}_{\bar{z}}}{i-Q_{\bar{z}}^2\mathcal{T}_{\bar{z}}}}\frac{\left[i\left(1+\frac{L-\bar{z}}{2\omega\mathcal{T}_{\bar{z}}}\right)(\boldsymbol{k}^2\mathcal{T}_{\bar{z}}-2Q_{\bar{z}}^2\mathcal{T}_{\bar{z}}+2i)-(i-Q_{\bar{z}}^2\mathcal{T}_{\bar{z}})^2\right]}{(i-Q_{\bar{z}}^2\mathcal{T}_{\bar{z}})^4}.\tag{57}$$

Here, one should also notice that all the final expressions [(47), (51), (54), and (57)] are proportional to $(\boldsymbol{g}\cdot\boldsymbol{k})$, leading to the term $(\boldsymbol{g}\cdot\boldsymbol{k})dI_1$ in (1). Thus, on average, the emitted gluons have their momenta aligned with the direction of $\boldsymbol{g}$.

Turning to the further analysis of the analytic results above, we notice that the gradient corrections to the gluon spectrum have some similarity with (44) and (45). Indeed, the same exponential factors and similar polynomials of $Q_{\bar{z}}^2$ and $\mathcal{T}_{\bar{z}}$ appear in the results of this section, leaving the possibility that the gradient corrections can be obtained with an operator acting on the leading contributions. Another immediate observation is that the leading corrections depend on the same dimensionful scales, while the new scale introduced by the gradients is factorized. We leave these opportunities to deeper understand the qualitative properties of the results for future work, and focus on the overall behavior of the full spectrum in the next section.

V. THE SPECTRUM AND ITS PROPERTIES

In this section, we will focus on the properties of the medium induced soft gluon spectrum and its gradient corrections in the harmonic approximation. Despite all the simplifications, the last $\bar{z}$ integration in the in-in contributions, (44) and (45), is pretty involved even in the homogeneous limit, and usually treated numerically, see e.g. [46–53]. Here, we choose a set of phenomenologically relevant parameters [38], although the considered limit of the medium induced gluon spectrum is oversimplified and used for illustrative purposes. First, we define the medium to have $L = 5$ fm and $T = 0.3$ GeV, and assume that $\boldsymbol{\nabla}T \lesssim T^2$ for hydrodynamically evolving matter. If we treat the harmonic oscillator approximation as our model, then the only other parameter is $\hat{q}$, and its characteristic value can be chosen to be about $\hat{q} \simeq 1\ \text{GeV}^2\,\text{fm}^{-1}$, see e.g. [47,48,50]. On the other hand, to illustrate the logarithmic dependence in $\hat{q}$, which affects the

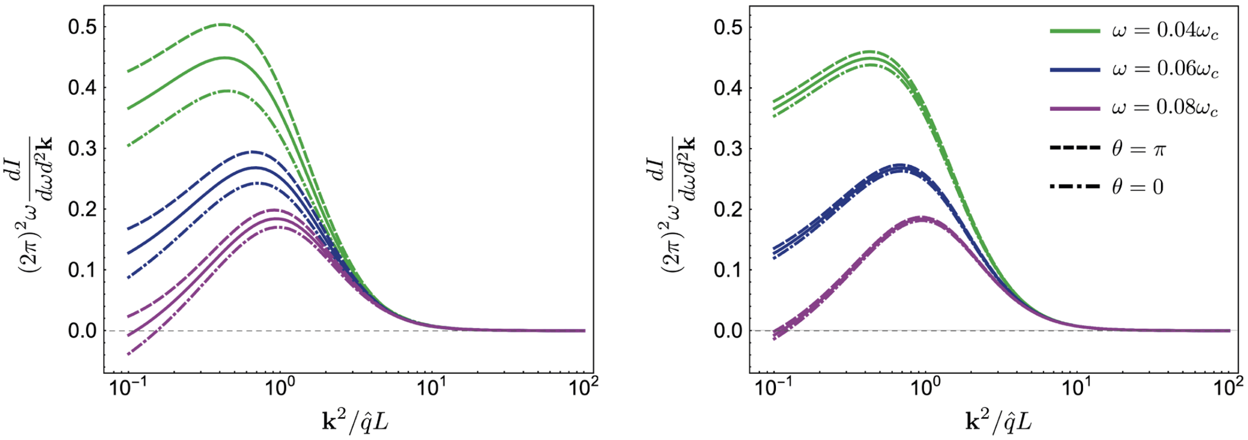

FIG. 2. The medium induced soft gluon spectrum is given for three gluon energies, $\omega = 0.04\omega_c$, $\omega = 0.06\omega_c$, and $\omega = 0.08\omega_c$. The solid lines denote the spectrum in the homogeneous limit. The dashed and dash-dotted lines correspond to the full spectrum with gradients along ($\theta = 0$) and opposite to ($\theta = \pi$) the direction of $\boldsymbol{k}$, respectively. The gradients are quantified with $\gamma_T = 0.05$ (left) and $\gamma_T = 0.01$ (right).

definition of the gradient vector $\boldsymbol{g}$, one may attempt at treating the harmonic effective potential as a crude approximation of the GW model. For this purpose, we set $\chi = 2.75$, $\mu = 0.6$ GeV, and choose $\Lambda^2 = E\mu$ with characteristic jet energy of 100 GeV, cf. with [18,38]. Then, one readily finds that $\hat{q} = \frac{\chi\mu^2}{L}\log\frac{E}{\mu} \simeq 1\ \text{GeV}^2\ \text{fm}^{-1}$, and the two values coincide. Finally, turning to the gradient vector, we notice that the form of $\boldsymbol{g}$ is controlled by the powers of temperature, entering into the scaling $\hat{q} \sim T^3\log\frac{\Lambda^2}{\mu^2}$ [38]. For instance, for the naive scaling of the jet quenching parameter $\boldsymbol{g} = 3\frac{\boldsymbol{\nabla}T}{T}$, while if one takes into account the logarithmic dependence as in the GW model with the given form of the cutoff it reads $\boldsymbol{g} = \frac{\boldsymbol{\nabla}T}{T}(3 - \log^{-1}\frac{E}{\mu})$. However, the characteristic value of Λ corresponding to our choice of $\hat{q}$ is such that the logarithmic factor in the GW model is sufficiently large, resulting in $\boldsymbol{g} \simeq 2.8\frac{\boldsymbol{\nabla}T}{T}$, and, for simplicity, we will use $\boldsymbol{g} = 3\frac{\boldsymbol{\nabla}T}{T}$ for all our estimates.

The medium induced soft gluon spectrum has an angular dependence controlled by $\boldsymbol{g}\cdot\boldsymbol{k}$, and we will focus on the two limiting cases, when the angle between the two vectors, θ, is either 0 or π. We will measure the gluon frequencies with respect to the critical medium frequency $\omega_c \equiv \hat{q}L^2 \simeq 125$ GeV, which in the case of no gradients can be identified with the typical frequency for gluons with formation length of the order of L. We will also introduce a dimensionless gradient parameter $\gamma_T = |\boldsymbol{\nabla}T/T^2|$, which controls the strength of the hydrodynamic gradients and distribution anisotropy.

In Fig. 2, we show the full spectrum up to first order in gradient corrections for $\omega = 0.04\omega_c$, $\omega = 0.06\omega_c$, and $\omega = 0.08\omega_c$, further differentiating for $\gamma_T = 0.05$ (left) and $\gamma_T = 0.01$ (right). For $\theta = 0$, the gradient effects suppress the gluon radiation at small values of $\boldsymbol{k}$, while when $\theta = \pi$, it is enhanced. One can notice that the gradient effects in Fig. 2 become stronger for softer gluons, and may be substantial even for sufficiently small γ_T. This behavior is in line with the properties of the gradient effects in broadening [38], where the anisotropic contributions are suppressed by the energy of the leading parton. Since the energy of soft emitted gluons is smaller than the energy of the leading parton, the gradient effects become more important. However, one should notice that very soft gluons lose their energy on shorter timescales, and the single gluon spectrum cannot describe the evolution of the system reliably in this case.

In quantifying the effect of the resulting anisotropy in the medium induced radiation, one may also consider integral characteristics of the spectrum, such as its moments, see e.g. [21–23,38]. Indeed, the gradient corrections to the spectrum are proportional to $\boldsymbol{g}\cdot\boldsymbol{k}$, being otherwise functions of $\boldsymbol{k}^2$, and, thus, its directional odd moments are nonzero, quantifying the average transverse momentum transmitted with the gluons. To illustrate this point, we focus on the differential average transverse momentum, defined as

$$\left\langle \frac{d\boldsymbol{k}}{d\omega} \right\rangle \equiv \int_\Gamma d^2\boldsymbol{k}\,\boldsymbol{k}\frac{dI}{d\omega d^2\boldsymbol{k}} = \frac{1}{2}\boldsymbol{g}\int_\Gamma d^2\boldsymbol{k}\,\boldsymbol{k}^2\frac{dI_1}{d\omega d^2\boldsymbol{k}}, \qquad (58)$$

where Γ is a particular phase space region, which should be specified to interpret the physical meaning of $\langle\frac{d\boldsymbol{k}}{d\omega}\rangle$. Here, we set the lower limit of $|\boldsymbol{k}|$ integration to zero, pushing the applicability of the harmonic approximation to the limit. However, one may readily check that the numerical results are only weakly affected if we would require $|\boldsymbol{k}| > \mu$. We further focus on the three particular upper cutoffs: $k_{\max} = 10\sqrt{\hat{q}L}$, $k_{\max} = \frac{2}{3}\omega$, and $k_{\max} = \frac{1}{3}\omega$, plotting the numerical results for $3T\frac{\boldsymbol{g}}{g^2}\cdot\langle\frac{d\boldsymbol{k}}{d\omega}\rangle$ in Fig. 3. Notice that $3T\frac{\boldsymbol{g}}{g^2}\cdot$

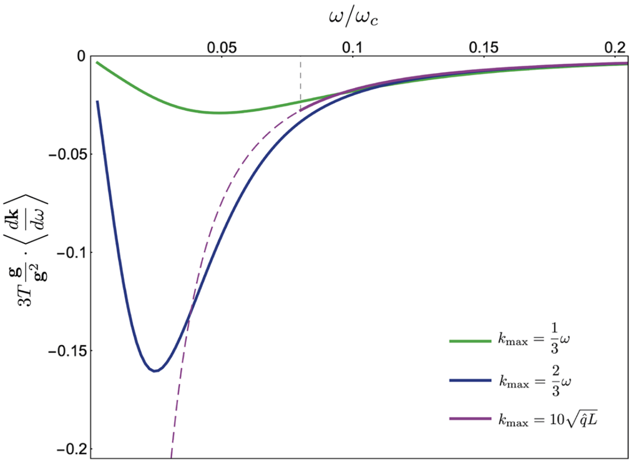

FIG. 3. The differential average transverse momentum is given by its dimensionless projection $3T\frac{\boldsymbol{g}}{\boldsymbol{g}^2}\cdot\langle\frac{d\boldsymbol{k}}{d\omega}\rangle$ for three choices of the upper cutoff $k_{\max}$ in (58). The curve corresponding to the ω-independent choice of $k_{\max}$ is shown with a solid line for sufficiently large energies $\omega>\sqrt{20\hat{q}L}$, and continued with a lighter dashed line beyond that point. The particular limiting value (indicated with a vertical gray dashed line) corresponds to the point along the spectrum plot, where it is visually close to zero, $\boldsymbol{k}^2=20\hat{q}L$. The remaining parameters are taken to be the same as in Fig. 2.

$\langle\frac{d\boldsymbol{k}}{d\omega}\rangle$ is independent of the value of $|\boldsymbol{\nabla}T|$, and normalized to give $|\langle\frac{d\boldsymbol{k}}{d\omega}\rangle|$, when its absolute value is multiplied by γ_T.

The first choice of $k_{\max}$ is independent of ω, and accounts for all the emitted gluons with $|\boldsymbol{k}|<10\sqrt{\hat{q}L}$. The soft gluon spectrum quickly goes to zero for large momenta, see Fig. 2, and a sufficiently large upper cutoff, such as $k_{\max}=10\sqrt{\hat{q}L}$ can be freely replaced with infinity. However, for smaller gluon energies, the gluons contributing to $\langle\frac{d\boldsymbol{k}}{d\omega}\rangle$ are not necessarily on shell (and not eikonal), and (58) cannot be used as a measure of the averaged emitted transverse momentum. The two other choices account only for the on-shell emitted gluons, although slightly pushing the results obtained under the eikonal approximation to the limit. These cutoffs applied in (58) account only for the gluons emitted within smaller conical segments around the leading parton momentum, simulating jet cones. Moving from harder to softer gluons, we notice that the averaged transverse momentum first grows in absolute value, since the leading gradient effects are suppressed by the gluon energy. Thus, as expected, the softer gluons are more sensitive to the matter anisotropies. However, later the spectrum is slightly depleted, while the maximal transverse momentum of contributing gluons is smaller, and the averaged emitted transverse momentum decreases. This results in the peaks on the curves with ω-dependent cutoffs in Fig. 3.

Thus, combining insights from this work and the previous studies for single parton broadening [18,38], one may summarize the picture of jet evolution in inhomogeneous matter in the following way. The partons inside a jet propagating through the matter broaden and radiate in an anisotropic way. The harder partons in the core of the jet are less affected by these directional effects caused by variations in the medium parameters, while the softer radiation can be affected substantially and possesses an imprint of the medium structure. The distribution of the emitted gluons is highly nontrivial, and, for instance, the differential averaged transverse momentum may be parallel or antiparallel to the temperature gradient, depending on the particular integration limits in (58). However, for wide enough conical segments $\langle\frac{d\boldsymbol{k}}{d\omega}\rangle$ is negative as is illustrated in Fig. 3.

VI. CONCLUSION AND OUTLOOK

In this paper, we have derived the double differential medium induced soft gluon spectrum in a dense static transversely inhomogeneous medium with finite longitudinal extension. The spectrum is obtained within a gradient expansion up to the leading first order. As in the case of the jet momentum broadening [38], the gradient effects only enter the final distributions upon averaging over the stochastic background field configurations. In addition to the general form of the spectrum in (35) and (37), we have considered its behavior for quadratic $\mathcal{V}(\boldsymbol{y})$, the so-called harmonic approximation, evaluating the path integrals explicitly. In this regime, the full spectrum can be written in a form suitable for numerical simulations, and its structure results in no additional computational complications, comparing to the homogeneous case. This indicates that the full soft gluon spectrum can be implemented in the jet quenching phenomenology and simulations for more realistic model potentials, see e.g. [50–52] for related discussions in the homogeneous limit.

In the harmonic approximation limit, we numerically evaluate the soft gluon spectrum and its leading odd moment $\langle\frac{d\boldsymbol{k}}{d\omega}\rangle$, and present our results in Figs. 2 and 3. The medium gradients distort the softer part of the jet substructure, while the harder radiation is less sensitive to the underlying medium structure. The spectrum is depleted for the transverse gradient vector $\boldsymbol{g}$ parallel with $\boldsymbol{k}$, and enhanced for the opposite situation, for most of the phase space. However, there are parametric regions, where the ordering is modified, and the spectrum is enhanced for $\boldsymbol{k}$ parallel with $\boldsymbol{g}$. Thus, we find that the medium induced soft gluons are preferably emitted along the temperature gradient but the particular direction depends on the region of the gluon phase space. We further study how the average transverse momentum of the medium induced gluons is distributed with energy and what fraction stays within a conical segment aligned with the initial leading parton momentum, see Fig. 3.

The present theoretical results should be further supplemented with a well-thought set of jet observables sensitive to the medium structure. However, searching for such observables is a nontrivial task, since they are sensitive to the medium anisotropy and are expected to be contaminated by the soft part of the particle spectrum. To overcome this issue, one may focus on substructure observables with less sensitivity to the correlated soft particles. Presently, the jet substructure techniques applied in the jet quenching phenomenology are still under development, but it is already possible to gauge the sensitivity of particular observables using simplified models for the jet in-medium evolution. Another potential option is to compute some global jet observable (e.g. jet shape) as a function of rapidity. Since in a real event the gradient effects substantially change with rapidity, the difference between such measurements could provide a better access to the medium structure. We leave the study of these questions for future work.

One should notice that this work makes only the first steps along the discussion of jet-medium interactions in evolving matter, and our results could be extended in multiple ways. For instance, it would be natural to consider higher order gradient corrections within the framework of the present paper. As have been shown in [25,39], in the case of momentum broadening, such terms may arise at the leading eikonal accuracy, while the directional gradient corrections to the final distribution are suppressed at larger energies. Thus, we expect that such higher order terms may significantly alter the medium induced soft gluon spectrum. Therefore, it would be interesting to derive the medium induced spectrum up to the second order in gradients, although such a calculation will be challenging.

In exploring the particle spectrum, it is necessary to account for more realistic spacetime profiles of the medium. For example, there is an ongoing effort to implement the flow effects in the pQCD description of jet-matter interactions [18,21,23]. However, in the case of the medium induced branching, such studies have so far only been applied to the dilute limit. Including higher opacity corrections and gradient effects in a single jet quenching framework is critical to describe jets in realistically evolving matter, and this is an essential step to further develop the tomographic toolkit in HIC. Such a framework can be implemented along with realistic hydrodynamic and/or kinetic theory simulations of the nuclear matter in HIC, providing further insight into the details of jet-matter interactions; for recent efforts in this direction see [21,54,55].

ACKNOWLEDGMENTS

The authors would like to thank C. Andres, N. Armesto, F. Dominguez, Y.-J. Lee, M. Sievert, K. Tywoniuk, and B. Wu for fruitful discussions and comments on the presented results. This work is supported by European Research Council Project No. ERC-2018-ADG-835105 YoctoLHC; by Maria de Maetzu excellence program under Project No. CEX2020-001035-M; by Spanish Research State Agency under Project No. PID2020–119632 GB-I00; and by Xunta de Galicia (Centro singular de investigación de Galicia accreditation 2019–2022), by European Union ERDF. The work of A. S. is also supported by the Marie Sklodowska-Curie Individual Fellowship under JetT project (Project Reference No. 101032858). J. B. is supported by the U.S. Department of Energy, Office of Science, Office of Nuclear Physics, under Contract No. DE-SC0012704. A contribución de X. M. L. contribution to this work is supported under scholarship No. PRE2021-097748, funded by MCIN/AEI/10.13039/501100011033 and FSE+.

[1] W. Busza, K. Rajagopal, and W. van der Schee, Heavy ion collisions: The big picture, and the big questions, Annu. Rev. Nucl. Part. Sci. **68**, 339 (2018).
[2] L. Apolinário, Y.-J. Lee, and M. Winn, Heavy quarks and jets as probes of the QGP, Prog. Part. Nucl. Phys. **127**, 103990 (2022).
[3] C. Adler *et al.* (STAR Collaboration), Centrality Dependence of High p_T Hadron Suppression in Au + Au Collisions at $\sqrt{s_{NN}} = 130$-GeV, Phys. Rev. Lett. **89**, 202301 (2002).
[4] K. Aamodt *et al.* (ALICE Collaboration), Suppression of charged particle production at large transverse momentum in central Pb-Pb collisions at $\sqrt{s_{NN}} = 2.76$ TeV, Phys. Lett. B **696**, 30 (2011).
[5] K. Adcox *et al.* (PHENIX Collaboration), Suppression of Hadrons with Large Transverse Momentum in Central Au + Au Collisions at $\sqrt{s_{NN}} = 130$-GeV, Phys. Rev. Lett. **88**, 022301 (2002).
[6] J. D. Bjorken, Energy Loss of Energetic Partons in Quark-Gluon Plasma: Possible Extinction of High p(t) Jets in Hadron-Hadron Collisions, https://inspirehep.net/literature/181746.
[7] Y. Mehtar-Tani, J. G. Milhano, and K. Tywoniuk, Jet physics in heavy-ion collisions, Int. J. Mod. Phys. A **28**, 1340013 (2013).
[8] G.-Y. Qin and X.-N. Wang, Jet quenching in high-energy heavy-ion collisions, Int. J. Mod. Phys. E **24**, 1530014 (2015).

[9] J.-P. Blaizot and Y. Mehtar-Tani, Jet structure in heavy ion collisions, Int. J. Mod. Phys. E **24**, 1530012 (2015).

[10] I. Vitev and M. Gyulassy, High p_T Tomography of $d + \mathrm{Au}$ and $\mathrm{Au} + \mathrm{Au}$ at SPS, RHIC, and LHC, Phys. Rev. Lett. **89**, 252301 (2002).

[11] E. Wang and X.-N. Wang, Jet Tomography of Dense and Nuclear Matter, Phys. Rev. Lett. **89**, 162301 (2002).

[12] J. Xu, A. Buzzatti, and M. Gyulassy, Azimuthal jet flavor tomography with CUJET2.0 of nuclear collisions at RHIC and LHC, J. High Energy Phys. 08 (2014) 063.

[13] M. Djordjevic, B. Blagojevic, and L. Zivkovic, Mass tomography at different momentum ranges in quark-gluon plasma, Phys. Rev. C **94**, 044908 (2016).

[14] L. Apolinário, J. G. Milhano, G. P. Salam, and C. A. Salgado, Probing the Time Structure of the Quark-Gluon Plasma with Top Quarks, Phys. Rev. Lett. **120**, 232301 (2018).

[15] M. Arratia, Z.-B. Kang, A. Prokudin, and F. Ringer, Jet-based measurements of Sivers and Collins asymmetries at the future electron-ion collider, Phys. Rev. D **102**, 074015 (2020).

[16] Y. He, L.-G. Pang, and X.-N. Wang, Gradient Tomography of Jet Quenching in Heavy-Ion Collisions, Phys. Rev. Lett. **125**, 122301 (2020).

[17] L. Apolinário, A. Cordeiro, and K. Zapp, Time reclustering for jet quenching studies, Eur. Phys. J. C **81**, 561 (2021).

[18] A. V. Sadofyev, M. D. Sievert, and I. Vitev, *Ab initio* coupling of jets to collective flow in the opacity expansion approach, Phys. Rev. D **104**, 094044 (2021).

[19] Y.-L. Du, D. Pablos, and K. Tywoniuk, Jet Tomography in Heavy Ion Collisions with Deep Learning, Phys. Rev. Lett. **128**, 012301 (2022).

[20] S. Hauksson, S. Jeon, and C. Gale, The momentum broadening of energetic partons in an anisotropic plasma, Phys. Rev. C **105**, 014914 (2022).

[21] L. Antiporda, J. Bahder, H. Rahman, and M. D. Sievert, Jet drift and collective flow in heavy-ion collisions, Phys. Rev. D **105**, 054025 (2022).

[22] A. V. Sadofyev, M. D. Sievert, and I. Vitev, Jets in evolving matter within the opacity expansion approach, SciPost Phys. Proc. **8**, 046 (2022).

[23] C. Andres, F. Dominguez, A. V. Sadofyev, and C. A. Salgado, Jet broadening in flowing matter—Resummation, Phys. Rev. D **106**, 074023 (2022).

[24] Y. Fu, J. Casalderrey-Solana, and X.-N. Wang, Asymmetric transverse momentum broadening in an inhomogeneous medium, Phys. Rev. D **107**, 054038 (2023).

[25] J. Barata, X. Du, M. Li, W. Qian, and C. A. Salgado, Medium induced jet broadening in a quantum computer, Phys. Rev. D **106**, 074013 (2022).

[26] S. Hauksson and E. Iancu, Jet polarisation in an anisotropic medium, arXiv:2303.03914.

[27] K. Boguslavski, A. Kurkela, T. Lappi, F. Lindenbauer, and J. Peuron, Jet momentum broadening during initial stages in heavy-ion collisions, arXiv:2303.12595.

[28] M. Gyulassy and X.-n. Wang, Multiple collisions and induced gluon bremsstrahlung in QCD, Nucl. Phys. **B420**, 583 (1994).

[29] B. G. Zakharov, Fully quantum treatment of the Landau-Pomeranchuk-Migdal effect in QED and QCD, JETP Lett. **63**, 952 (1996).

[30] R. Baier, Y. L. Dokshitzer, A. H. Mueller, S. Peigne, and D. Schiff, Radiative energy loss of high-energy quarks and gluons in a finite volume quark-gluon plasma, Nucl. Phys. **B483**, 291 (1997).

[31] U. A. Wiedemann, Transverse dynamics of hard partons in nuclear media and the QCD dipole, Nucl. Phys. **B582**, 409 (2000).

[32] U. A. Wiedemann, Gluon radiation off hard quarks in a nuclear environment: Opacity expansion, Nucl. Phys. **B588**, 303 (2000).

[33] M. Gyulassy, P. Levai, and I. Vitev, Reaction operator approach to non-Abelian energy loss, Nucl. Phys. **B594**, 371 (2001).

[34] M. Gyulassy, P. Levai, and I. Vitev, Reaction operator approach to multiple elastic scatterings, Phys. Rev. D **66**, 014005 (2002).

[35] P. B. Arnold, G. D. Moore, and L. G. Yaffe, Photon and gluon emission in relativistic plasmas, J. High Energy Phys. 06 (2002) 030.

[36] M. E. Carrington, A. Czajka, and S. Mrowczynski, Jet quenching in glasma, Phys. Lett. B **834**, 137464 (2022).

[37] A. Ipp, D. I. Müller, and D. Schuh, Anisotropic momentum broadening in the $2 + 1$D Glasma: analytic weak field approximation and lattice simulations, Phys. Rev. D **102**, 074001 (2020).

[38] J. Barata, A. V. Sadofyev, and C. A. Salgado, Jet broadening in dense inhomogeneous matter, Phys. Rev. D **105**, 114010 (2022).

[39] J. Barata, A. V. Sadofyev, and X.-N. Wang, Quantum partonic transport in QCD matter, Phys. Rev. D **107**, L051503 (2023).

[40] M. Lekaveckas and K. Rajagopal, Effects of fluid velocity gradients on heavy quark energy loss, J. High Energy Phys. 02 (2014) 068.

[41] K. Rajagopal and A. V. Sadofyev, Chiral drag force, J. High Energy Phys. 10 (2015) 018.

[42] A. V. Sadofyev and Y. Yin, The charmonium dissociation in an “anomalous wind,” J. High Energy Phys. 01 (2016) 052.

[43] S. Li, K. A. Mamo, and H.-U. Yee, Jet quenching parameter of the quark-gluon plasma in a strong magnetic field: Perturbative QCD and AdS/CFT correspondence, Phys. Rev. D **94**, 085016 (2016).

[44] J. Reiten and A. V. Sadofyev, Drag force to all orders in gradients, J. High Energy Phys. 07 (2020) 146.

[45] I. Y. Aref’eva, A. A. Golubtsova, and E. Gourgoulhon, Holographic drag force in 5d Kerr-AdS black hole, J. High Energy Phys. 04 (2021) 169.

[46] J. Casalderrey-Solana and C. A. Salgado, Introductory lectures on jet quenching in heavy ion collisions, Acta Phys. Pol. B **38**, 3731 (2007).

[47] Y. Mehtar-Tani, C. A. Salgado, and K. Tywoniuk, The radiation pattern of a QCD antenna in a dense medium, J. High Energy Phys. 10 (2012) 197.

[48] J.-P. Blaizot, F. Dominguez, E. Iancu, and Y. Mehtar-Tani, Medium-induced gluon branching, J. High Energy Phys. 01 (2013) 143.

[49] C. Andres, L. Apolinário, and F. Dominguez, Medium-induced gluon radiation with full resummation of multiple scatterings for realistic parton-medium interactions, J. High Energy Phys. 07 (2020) 114.

[50] J. Barata, Y. Mehtar-Tani, A. Soto-Ontoso, and K. Tywoniuk, Medium-induced radiative kernel with the improved opacity expansion, J. High Energy Phys. 09 (2021) 153.

[51] X. Feal and R. Vazquez, Intensity of gluon bremsstrahlung in a finite plasma, Phys. Rev. D **98**, 074029 (2018).

[52] X. Feal, C. A. Salgado, and R. A. Vazquez, Jet quenching test of the QCD matter created at RHIC and the LHC needs opacity-resummed medium induced radiation, Phys. Lett. B **816**, 136251 (2021).

[53] S. Caron-Huot and C. Gale, Finite-size effects on the radiative energy loss of a fast parton in hot and dense strongly interacting matter, Phys. Rev. C **82**, 064902 (2010).

[54] L. Barreto, F. M. Canedo, M. G. Munhoz, J. Noronha, and J. Noronha-Hostler, Jet cone radius dependence of R_{AA} and v_2 at PbPb 5.02 TeV from JEWEL $+$ T$_{\mathrm{R}}$ENTo $+$ v$-$USPhydro, arXiv:2208.02061.

[55] D. Zigic, I. Salom, J. Auvinen, P. Huovinen, and M. Djordjevic, DREENA—A framework as a QGP tomography tool, Front. Phys. **10**, 957019 (2022).

Article III

Jet quenching in the glasma phase: medium-induced radiation

Authors

João Barata[1], Sigtryggur Hauksson[2],

Xoán Mayo López[3], Andrey V. Sadofyev[4]

(1) Physics Department, Brookhaven National Laboratory, Upton, New York 11973, USA
(2) Institut de Physique Theorique, CEA/Saclay, Universite Paris-Saclay, 91191, Gif sur Yvette, France
(3) Instituto Galego de Física de Altas Enerxías, Universidade de Santiago de Compostela, Santiago de Compostela 15782, Galicia, Spain
(4) LIP, Avenida Professor Gama Pinto, 2, P-1649-003 Lisboa, Portugal

PhD Student Contribution

Independently derived the presented calculations and collaborated equally on the discussions and writing

Journal and Article Information

Journal name: Physical Review D
Publisher: American Physical Society
ISSN: 2470-0029
Year of publication: 2024
DOI: 10.1103/PhysRevD.110.094055
Impact factor in 2023: 4.6
CiteScore in 2023: 9.3
Quartile and decile in 2023: Q1 and D1

PHYSICAL REVIEW D **110,** 094055 (2024)

Jet quenching in the glasma phase: Medium-induced radiation

João Barata,[1,*] Sigtryggur Hauksson,[2,†] Xoán Mayo López,[3,‡] and Andrey V. Sadofyev[4,§]
[1]*Physics Department, Brookhaven National Laboratory, Upton, New York 11973, USA*
[2]*Institut de Physique Théorique, CEA/Saclay, Université Paris-Saclay, 91191, Gif sur Yvette, France*
[3]*Instituto Galego de Física de Altas Enerxías, Universidade de Santiago de Compostela,*
Santiago de Compostela 15782, Galicia, Spain
[4]*Laboratório de Instrumentação e Física Experimental de Partículas (LIP),*
Avenida Professor Gama Pinto 2, P-1649-003 Lisboa, Portugal

(Received 25 June 2024; accepted 19 October 2024; published 27 November 2024)

Inspired by the recent considerations of parton momentum broadening in the glasma phase, we study the medium-induced soft gluon radiation of jet partons at early times in heavy-ion collisions. The glasma state is assumed to be comprised of independent color domains with homogenous longitudinal fields that vary event by event, and we further complete this model with an event-averaging procedure accounting for the finite correlation length. Using this description, we evaluate the rate of medium-induced radiation from an energetic parton at midrapidity in the glasma phase. We mainly focus on SU(2) color fields for simplicity, also referring to the U(1) case and comparing with the Baier, Dokshitzer, Mueller, Peigné, Schiff, and Zakharov rate to gain further insight. Our results show that there is an intricate interplay of the synchrotron-like radiation in a single color domain with the destructive interference between different color domains, after the medium averaging is performed. Thus, we find that the emission rate is sensitive to the matter structure, decreasing for a glasma state populated by smaller color domains—i.e., for a glasma with a larger characteristic saturation scale. Our approach can be applied to more realistic backgrounds, and it sets the stage for the modeling of jet evolution in the early stages of heavy-ion collisions.

DOI: 10.1103/PhysRevD.110.094055

I. INTRODUCTION

Jets are essential probes of the nuclear medium formed in relativistic heavy-ion collisions and governed by quantum chromodynamics (QCD); for recent reviews, see [1,2]. As a jet traverses the medium, it loses energy and has its substructure modified, carrying information about the matter properties along its path. Thus, jet observables can provide access to the details of the medium evolution, and jets may serve as a tomographic tool; see, e.g., [3–13] and references therein.

To accurately model jet modification in heavy-ion collisions, one needs a detailed understanding of the evolution of the QCD medium. This work focuses on the earliest stage just after the collision of the heavy ions, which has been argued to be characterized by strong (classical) color fields, initially aligned along the beam axis. This state of matter is usually referred to as the glasma. The glasma is formed when the color fields in each nucleus, sourced by partons in the color-glass condensate framework, start interacting just after the initial collision [14–18]. In this regime, the matter has an intrinsic energy scale Q_s, known as the saturation scale, which controls the energy density of the glasma. The saturation scale furthermore sets the correlation length of the color fields to be $1/Q_s$. As a result, in the early stages of heavy-ion collisions, the QCD matter can be modeled as a collection of independent color domains with transverse size $1/Q_s$ within the glasma picture.

Due to the high occupation density of the gluons, the glasma obeys classical equations of motion which are commonly solved on a discrete lattice; see, e.g., [19–22]. The glasma framework has been successfully used to describe final-state correlations of soft hadrons in heavy-ion collisions [23–25]. More recently, it has been extended to full $(3+1)$D calculations, which do not assume boost invariance and have the potential to correctly predict correlations of final-state hadrons in rapidity [25–30].

The glasma stage of heavy-ion collisions is short-lived, lasting less than $1\ \mathrm{fm}/c$. As the medium expands, the occupation density of gluons rapidly goes down, and the

---

[*] Contact author: jlourenco@bnl.gov
[†] Contact author: sigtryggur.hauksson@ipht.fr
[‡] Contact author: xoan.mayo.lopez@usc.es
[§] Contact author: sadofyev@lip.pt

medium can no longer be described classically. At this stage, the matter is still far from equilibrium, and its thermalization process can be described by the QCD kinetic theory; see, e.g., [31–33]. Once the system approaches the thermalization, the bulk of the evolution of the medium sets in: the quark-gluon plasma (QGP) described by the relativistic hydrodynamics has been formed. Until very recently,[1] nearly all considerations of jets in medium have only included the QGP stage, and not the glasma and kinetic theory stages that precede it. The evolution of jets in the later stages of the medium evolution, when quarks and gluons have been confined to hadrons, has also been given little theoretical attention; see, e.g., [35].

Even though the glasma phase is short-lived, the energy density of the medium is very high, meaning that the glasma has the potential to substantially modify jet substructure. One way to estimate the relative importance of the glasma stage is to measure its jet-quenching parameter $\hat{q}$, the rate of the transverse momentum broadening of jet partons traversing it. This quantity has been measured in simulations of the glasma [36–38], as well as calculated analytically at very early times [39–41]. Despite considerable theoretical uncertainty, these studies clearly indicate that $\hat{q}$ in the glasma phase is very high. For instance, the results of [38] suggest that $\hat{q} \geq 5\ \mathrm{GeV}^2/\mathrm{fm}$ during the first $0.3\ \mathrm{fm}/c$ of the evolution, while the value extracted for the QGP phase at $T = 200$ MeV is $\hat{q} \simeq 0.12\ \mathrm{GeV}^2/\mathrm{fm}$; see [42]. In turn, the recent efforts to evaluate $\hat{q}$ during intermediate stages described by the kinetic theory also suggest rather large values of the jet-quenching parameter [43–46], thus connecting the earlier- and later-time evolution. Interestingly, the momentum broadening in both the glasma and kinetic theory stages is anisotropic, potentially leading to more observable phenomena, such as the polarization of partons [47–49] and photons [50].

However, it should be emphasized that more detailed studies are needed to quantify the importance of the early stages of the matter produced in heavy-ion collisions for in-medium evolution of jets. In particular, the high value of $\hat{q}$ could be compensated by the short lifetime of the glasma phase, while its imprints may be washed out by the hydrodynamic evolution in the later stages. Nevertheless, it has been argued [40] that at the level of simple estimates, the contributions of the glasma and hydrodynamic stages to the total momentum broadening are similar.

Transverse momentum broadening of jet partons leads to medium-induced radiation, since on-shell jet partons can radiate gluons due to the interactions with the matter. The high rate of momentum broadening in the glasma suggests that such radiation should occur during the glasma stage too. However, only a few works have considered the medium-induced radiation at such early times, including [51,52] which assumed a medium with a constant classical field and [34] that focused on a particular time-varying field without event-by-event averaging and spatial correlations. On the contrary, the medium-induced radiation has been studied in great detail in the QGP phase, and shown to modify the substructure of the jets compared with the vacuum case, leading to jet energy loss as soft gluons transport the jet energy down to the medium scale; see, e.g., [53,54] and discussion therein. Moreover, there is an ongoing effort to improve the jet-quenching theory in the QGP phase—e.g., by including the details of the medium evolution in the description [10–12,55–62] and by constructing tomographic observables sensitive to these effects [12,63]. Thus, further improvements of the jet-quenching theory in the neighboring phases are much needed, since only the overall effect of the matter on the jet observables is accessible experimentally.

Calculating the full spectrum of medium-induced emission in the glasma is a highly nontrivial task. An important feature of this stage of the matter evolution is the confinement of the gluon fields in domains of size $1/Q_s$ in the transverse plane. Thus, the fields cannot be assumed to have only local correlations in time—i.e., the classical fields generated during this stage should not satisfy $\langle A(t_1)A(t_2)\rangle \sim \delta(t_1 - t_2)$, where t_1 and t_2 are some positions along the jet path. Notice that this assumption drastically simplifies the jet-quenching calculations in the QGP phase, where local correlations are typically assumed. A complete calculation of gluon radiation in the glasma thus demands a detailed event-by-event profile for the gluon fields and requires doing a quantum evolution of partons in that profile; see, e.g., [64–66]. Another way to see the importance of the correlation length $1/Q_s$ is to note that when the formation time for an emission is shorter than the correlation length in the glasma, the emission happens in a nearly constant field, in contrast with the stochastic field picture underlying the jet-quenching theory in the QGP phase.

In this work, we simplify the problem of medium-induced gluon emission at early times by using a model that captures the essential features of the glasma. Our model assumes the medium to be composed of color domains with sizes $\ell \sim 1/Q_s$, where each color domain has a constant chromoelectric field that varies event by event and is aligned along the beam axis. The fields in two color domains are independent of each other. This introduces a correlation length ℓ, which relaxes the assumption of instantaneous/local correlations used in nearly all jet-quenching calculations. Using this model, we obtain the rate of the momentum broadening and soft medium-induced radiation, both before and after averaging over events. For simplicity, we mainly consider a medium with SU(2) gauge fields, also relying on the U(1) case for illustrations, but our methods are generalizable to the physical SU(3) case. This approach could be directly

---

[1] For a very early consideration of the jet quenching in glasma, see also [34].

applied to calculations with more realistic profiles: by dividing the full glasma profile in a single event into slices with nearly constant fields, and averaging over different events, our model can approximate the full glasma.

This paper is structured as follows: We start by discussing the single-parton momentum broadening in Sec. II, followed by a computation of the medium-induced soft gluon rate in Sec. III. We first consider the case where the field fluctuations inside each color tube follow a Gaussian distribution, and we verify our main conclusions within the same model completed with an alternative averaging procedure presented in Sec. IV. In Sec. V, we summarize our results and discuss possible future directions.

II. MOMENTUM BROADENING

Focusing on jet quenching at early times of heavy-ion collisions, we use a simple physical picture for the glasma, taking into account the nonlocal correlations of color fields with correlation length $\ell \sim 1/Q_s$ controlled by the saturation scale. We refer to the regions where color fields are highly correlated as color domains, or alternatively as flux tubes, and view the medium as composed of multiple such flux tubes of a fixed size. In our model, the chromoelectric field is constant within the given flux tube and aligned with the beam axis, as expected at very early times in heavy-ion collisions.

We define the coordinate system with respect to the jet axis, so that $\boldsymbol{x}$ is transverse to the momentum of the leading parton, and we assume that the jet is at midrapidity, so the beam axis is in the transverse direction, and the jet propagates along the z axis. We write the field of our model as

$$A^{a\mu}_{\mathrm{coh}}(\boldsymbol{x},z)=\delta^{0}_{\mu}\boldsymbol{x}\cdot\mathbf{E}^a(z)=\begin{cases}\delta^{\mu 0}\boldsymbol{x}\cdot\mathbf{E}^a_1, & 0\le z<\ell\\ \delta^{\mu 0}\boldsymbol{x}\cdot\mathbf{E}^a_2, & \ell\le z<2\ell\\ \delta^{\mu 0}\boldsymbol{x}\cdot\mathbf{E}^a_3, & 2\ell\le z<3\ell\\ \vdots & \end{cases}, \tag{1}$$

where the first tube is assumed to start at $z=0$. This field is compatible with the Lorenz gauge with an additional axial condition $A_z=0$, which allows working with the physical polarizations of the gluon field. In what follows, without loss of generality, we will choose the beam direction as the x axis, thus keeping only the x component of the electric field.[2]

As is usual in jet-quenching considerations, all the results should be necessarily averaged over multiple events. We treat the electric fields in each flux tube as independent variables with a Gaussian distribution[3] of width E_0. Thus, for any function $f(E^a_{1x},E^a_{2x},E^a_{3x},\ldots)$, the average over multiple events is

$$\langle f(E^a_{1x},E^a_{2x},E^a_{3x},\ldots)\rangle=\int_{E_1}e^{-E^2_{1x}/E^2_0}\int_{E_2}e^{-E^2_{2x}/E^2_0}\cdots \times f(E^a_{1x},E^a_{2x},E^a_{3x},\ldots), \tag{2}$$

where $E^2_{nx}=\sum_a(E^a_{nx})^2$ in the case of SU(N_c) fields, while E_{nx} is just the x component of the field in the given tube in the case of a U(1) background. Here, n refers to the particular tube, N_c is the number of colors, and we have introduced a shorthand notation: $\int_E=\int\frac{d^{N_c^2-1}E^a_x}{(\sqrt{\pi}E_0)^{N_c^2-1}}$ or $\int_E=\int_{-\infty}^{\infty}\frac{dE_x}{(\sqrt{\pi}E_0)}$ for the SU(N_c) and U(1) cases, respectively. Thus, our model only depends on two parameters, l and E_0, after event averaging.

It is instructive to start with evaluating the transverse momentum broadening in our model. While the form of the medium-induced field differs from that in most of the considerations within Baier, Dokshitzer, Mueller, Peigné, Schiff, and Zakharov (BDMPS-Z) formalism (see [68] for a pedagogical review), the amplitudes for transverse momentum broadening or gluon radiation can still be resummed. For instance, the jet-quenching parameter for a parton of energy ω in our model may be written as

$$\hat{q}=-\frac{1}{2(2\pi)^3\mathcal{N}}\frac{\partial}{\partial L}\int_{\boldsymbol{x}}\boldsymbol{\nabla}^2_{\boldsymbol{x}-\bar{\boldsymbol{x}}}(J^{\dagger}(\bar{\boldsymbol{x}})\mathcal{W}^{\dagger}(\bar{\boldsymbol{x}})\mathcal{W}(\boldsymbol{x})J(\boldsymbol{x}))_{\bar{\boldsymbol{x}}=\boldsymbol{x}}, \tag{3}$$

where $\mathcal{N}=\frac{1}{2(2\pi)^3}\int_{\boldsymbol{p}}|J(\boldsymbol{p})|^2$ is a normalization factor, and we keep track of how the sources $J(\boldsymbol{x})=J^i(\omega,\boldsymbol{x})$ are distributed in the color space, as controlled by the superscript i. Notice that we have not yet averaged over multiple events, and this definition of $\hat{q}$ corresponds to the broadening in an ensemble of partons penetrating the same field configuration.[4]

For the color field in our model, the Wilson lines are given by $\mathcal{W}(\boldsymbol{x})\equiv\mathcal{W}(\boldsymbol{x};L,0)=\mathcal{P}\exp\{i\int_0^L d\tau t^a\mathbf{E}^a\cdot\boldsymbol{x}\}$, with t^a being the generators of the particular representation of SU(N_c), and assuming that the parton initial position z_{in} coincides with the edge of the first tube—i.e., $z_{\mathrm{in}}=0$. For convenience, we will assume that the energetic partons are in the fundamental representation. The Wilson lines are governed by a simple evolution equation

---

[2] Notice, however, that the change of the field between two domains is assumed to be sufficiently slow, compared to the size of the domains, that the z component of the field can be neglected.

[3] Notice that a similar averaging procedure was used in [67] to describe the contribution of turbulent color fields to transverse momentum broadening.

[4] One may readily derive Eq. (3) by following, e.g., [68], keeping the form of the source function undefined, and avoiding imposing any specific averaging procedure.

$$\frac{\partial}{\partial L}\mathcal{W}(\boldsymbol{x}) = it^a\mathbf{E}^a(L)\cdot\boldsymbol{x}\mathcal{W}(\boldsymbol{x}), \tag{4}$$

which also controls their two-point functions:

$$\frac{\partial}{\partial L}\mathcal{W}(\boldsymbol{x})\mathcal{W}^\dagger(\bar{\boldsymbol{x}}) = i\mathbf{E}^a(L)\cdot\big[\boldsymbol{x}t^a\mathcal{W}(\boldsymbol{x})\mathcal{W}^\dagger(\bar{\boldsymbol{x}}) - \bar{\boldsymbol{x}}\mathcal{W}(\boldsymbol{x})\mathcal{W}^\dagger(\bar{\boldsymbol{x}})t^a\big]. \tag{5}$$

Projecting the latter equation on the subspaces of the color structures, we find

$$\begin{aligned}\frac{\partial}{\partial L}h^0 &= i\mathbf{E}^a(L)\cdot(\boldsymbol{x}-\bar{\boldsymbol{x}})h^a,\\ \frac{\partial}{\partial L}h^a &= i\mathbf{E}^b(L)\cdot\left[\frac{1}{2}(\boldsymbol{x}-\bar{\boldsymbol{x}})\left(\frac{\delta^{ab}}{N_c}h^0 + d^{abc}h^c\right)\right.\\ &\qquad\left. + \frac{i}{2}(\boldsymbol{x}+\bar{\boldsymbol{x}})f^{abc}h^c\right],\end{aligned} \tag{6}$$

where $h^0 = \mathrm{Tr}\mathcal{W}(\boldsymbol{x})\mathcal{W}^\dagger(\bar{\boldsymbol{x}})$ and $h^a = \mathrm{Tr}t^a\mathcal{W}(\boldsymbol{x})\mathcal{W}^\dagger(\bar{\boldsymbol{x}})$.

Since we are interested in $\hat{q}$ here, we have to compute only the particular path-length derivatives and transverse position gradients of the h's, and the problem can be further simplified. Indeed,

$$\begin{aligned}&\frac{\partial}{\partial L}\boldsymbol{\nabla}_y h^0|_{y=0} = 0,\\ &\frac{\partial}{\partial L}\boldsymbol{\nabla}_y^2 h^0|_{y=0} = 2i\mathbf{E}^a\cdot\boldsymbol{\nabla}_y h^a|_{y=0},\\ &\frac{\partial}{\partial L}\boldsymbol{\nabla}_y h^a|_{y=0} = i\left(\frac{\mathbf{E}^a}{2} + i(\mathbf{E}^b\cdot\boldsymbol{Y})f^{abc}\boldsymbol{\nabla}_y h^c\right)\bigg|_{y=0},\\ &\frac{\partial}{\partial L}\boldsymbol{\nabla}_y^2 h^a|_{y=0} = i(d^{abc}\mathbf{E}^b\cdot\boldsymbol{\nabla}_y h^c + i(\mathbf{E}^b\cdot\boldsymbol{Y})f^{abc}\boldsymbol{\nabla}_y^2 h^c)|_{y=0},\end{aligned} \tag{7}$$

where $\boldsymbol{Y} = \frac{\boldsymbol{x}+\bar{\boldsymbol{x}}}{2}$ and $\boldsymbol{y} = \boldsymbol{x}-\bar{\boldsymbol{x}}$ are the relative coordinates. Here, we have also used $h^a|_{y=0} = 0$ and $h^0|_{y=0} = N_c$, since the Wilson lines cancel for $\boldsymbol{y} = 0$. Furthermore, using $\boldsymbol{\nabla}_y^{n>0}h|_{L=0} = 0$, since $\mathcal{W}(\boldsymbol{x})|_{L=0} = I$, one readily finds that

$$\boldsymbol{\nabla}_y h^a|_{y=0} = \frac{i}{2}\int_0^L d\bar{\tau}\tilde{\mathcal{W}}^{ab}(\boldsymbol{Y};L,\bar{\tau})\mathbf{E}^b(\bar{\tau}), \tag{8}$$

where $\tilde{\mathcal{W}}^{ab}(\boldsymbol{x};L,0) = \mathcal{P}\exp\big(iT^c\int_0^L d\tau\mathbf{E}^c(\tau)\cdot\boldsymbol{x}\big)$ is the Wilson line in the adjoint representation, and $(T^c)_{ab} = -if^{abc}$ is the corresponding generator. The solutions for the second-order transverse gradients of the color projections can be explicitly obtained, and they read

$$\begin{aligned}\boldsymbol{\nabla}_y^2 h^0|_{y=0} &= -\int_0^L d\bar{\tau}\int_0^{\bar{\tau}} d\tau\tilde{\mathcal{W}}^{ab}(\boldsymbol{Y};\bar{\tau},\tau)\mathbf{E}^a(\bar{\tau})\cdot\mathbf{E}^b(\tau),\\ \boldsymbol{\nabla}_y^2 h^a|_{y=0} &= -\frac{1}{2}d^{ebc}\int_0^L d\bar{\tau}\int_0^{\bar{\tau}} d\tau\tilde{\mathcal{W}}^{ae}(\boldsymbol{Y};L,\bar{\tau})\\ &\qquad\times\tilde{\mathcal{W}}^{cd}(\boldsymbol{Y};\bar{\tau},\tau)\mathbf{E}^b(\bar{\tau})\cdot\mathbf{E}^d(\tau).\end{aligned} \tag{9}$$

The first relation of Eq. (9) measures total momentum broadening. The force exerted by the color field on the particle is integrated in time, both in the amplitude and in the conjugate amplitude. The Wilson line inserted between the two fields ensures gauge invariance and is in the adjoint representation, like the gauge fields themselves. In the second relation, we keep track of the final color of the particle. Thus, an additional Wilson line between the second field insertion and the measurement at time L is needed.

One should notice here that $\hat{q}$ may in principle contain a contribution due to the octet component of the initial distribution. It may also have a nontrivial dependence on the spatial distribution of the initial ensemble of partons. However, to illustrate the physical picture, let us consider a simpler model for the initial distribution (see, e.g., [69]), such that

$$\frac{1}{2(2\pi)^3\mathcal{N}}\sum_{\text{sources}} J(\omega,\boldsymbol{p})J^\dagger(\omega,\bar{\boldsymbol{p}}) = \frac{1}{2\pi w^2}(\mathbb{1}+n^a t^a)e^{-\frac{\boldsymbol{p}^2+\bar{\boldsymbol{p}}^2}{4w^2}}, \tag{10}$$

where we sum over possible initial sources, n^a parameterizes the octet component,[5] and w is the width of the initial distribution modeled by a Gaussian. Then, the jet-quenching parameter can be written as

$$\hat{q} = -\frac{w^2}{2\pi^3}\frac{\partial}{\partial L}\int_{\boldsymbol{Y}}\boldsymbol{\nabla}_y^2(h^0+n^a h^a)_{y=0}e^{-2w^2\boldsymbol{Y}^2}. \tag{11}$$

In what follows, we will assume that the initial ensemble of jet partons has no net color for simplicity, setting $n^a = 0$. Then, we can focus solely on the singlet part of the jet-quenching process, and find

$$\hat{q}(z) = \frac{w^2}{2\pi^3}\int_{\boldsymbol{Y}}\int_0^z d\tau\tilde{\mathcal{W}}^{ab}(\boldsymbol{Y};z,\tau)E_x^a(z)E_x^b(\tau)e^{-2w^2\boldsymbol{Y}^2}, \tag{12}$$

where z is the current position of the parton, and it is made explicit that only the x component[6] of the chromoelectric field is nonzero in the considered model. This form of $\hat{q}$, along with Eq. (9), is in close relation with the earlier

---

[5] In the QGP phase, the octet contribution to any jet observable is expected to vanish; see, e.g., [69–72]. However, in the presence of a coherent field, the octet contribution can survive, at least before averaging.

[6] In what follows, the x subscript is dropped to alleviate the notation.

results for the transverse momentum broadening in a background field; cf. [73,74].

The expression for $\hat{q}$ should be further averaged over multiple events, and we rely on the model in Eq. (1). While the piecewise form of the field is sufficiently simple, the averaging is still involved, and it is instructive to start with the simpler case of SU(2). Due to the path ordering, the Wilson line $\tilde{\mathcal{W}}(\boldsymbol{Y}; z, \bar{\tau})$ can be written as a product of Wilson lines for each flux tube:

$$\begin{aligned}\tilde{\mathcal{W}}(\boldsymbol{Y}; z, \bar{\tau}) &= \tilde{\mathcal{W}}(\boldsymbol{Y}; z, z_n)\tilde{\mathcal{W}}(\boldsymbol{Y}; z_n, z_{n-1}) \\ &\quad \times \tilde{\mathcal{W}}(\boldsymbol{Y}; z_{n-1}, z_{n-2}) \cdots \tilde{\mathcal{W}}(\boldsymbol{Y}; z_{k+1}, \bar{\tau}), \qquad (13)\end{aligned}$$

where $z_i = il$ and $z_{i-1} = (i-1)l$ are the boundaries of the ith flux slab, and we have suppressed the color indices. In the first and the last Wilson lines, only a part of the flux tube is traversed, with $z_{n+1} > z \geq z_n$ and $z_{k+1} > \bar{\tau} \geq z_k$. The single-tube Wilson lines are easily evaluated in SU(2), giving

$$\begin{aligned}\tilde{\mathcal{W}}^{ab}_{\mathrm{SU}(2)}(\boldsymbol{Y}; z_i, z_{i-1}) &= \exp\left[\epsilon^{abc} E^c_i Y \ell\right] \\ &= \delta^{ab} \cos\left(E_i Y \ell\right) + 2\frac{E^a_i E^b_i}{E^2_i} \\ &\quad \times \sin^2\left(\frac{1}{2} E_i Y \ell\right) \\ &\quad + \epsilon^{abc}\frac{E^c_i}{E_i}\sin\left(E_i Y \ell\right), \qquad (14)\end{aligned}$$

where ϵ^{abc} is the structure constant of SU(2). Thus, unless both chromoelectric fields in Eq. (12) belong to the same flux tube, the average is zero, either since the contributions are canceled by the antisymmetric structure constants, or due to the absence of a preferred color-space direction in the averaging procedure. Consequently, we find that

$$\begin{aligned}\langle \hat{q}(z) \rangle_{\mathrm{SU}(2)} &= \frac{w^2}{2\pi^3}\int_{\boldsymbol{Y}}\int_E \int_{z_n}^{z} d\bar{\tau} E^2 e^{-2w^2 \boldsymbol{Y}^2} e^{-\frac{E^2}{E_0^2}} \\ &= \frac{3E_0^2}{8\pi^2}(z - z_n), \qquad (15)\end{aligned}$$

where z_n is the last edge between two tubes penetrated by the parton when it is at z.

Turning to the physical case of SU(3), we immediately see that the same cancellation of the intermediate flux tubes is well expected. Indeed, the adjoint Wilson line $\tilde{W}(\boldsymbol{Y}; z, z_n)$ corresponding to the final tube can be expanded into a series, and all the terms except the zeroth-order term are transverse to $E^c(L)$. In turn, the zeroth-order term will average to zero due to the absence of any preferred direction in the color space, unless the other field is within the same tube. The resulting jet-quenching parameter can be readily written as

$$\begin{aligned}\langle \hat{q}(z) \rangle_{\mathrm{SU}(3)} &= \frac{w^2}{2\pi^3}\int_{\boldsymbol{Y}}\int_E \int_{z_n}^{z} d\bar{\tau} E^2 e^{-2w^2 \boldsymbol{Y}^2} e^{-\frac{E^2}{E_0^2}} \\ &= \frac{E_0^2}{\pi^2}(z - z_n). \qquad (16)\end{aligned}$$

Thus, we see that in our model, the jet-quenching parameter is linearly increasing while the parton propagates along the given tube, and then it falls to zero at the edge of the next tube, restarting the linear growth afterward. However, in any realistic setup, the initial position within the first flux tube, z_{in}, cannot be fixed, and one has to average over it. This is equivalent to averaging over the position within the last flux tube, $z - z_n$, and we readily find that

$$\langle \hat{q} \rangle_{\mathrm{SU}(2), z_{\mathrm{in}}} = \frac{3E_0^2}{16\pi^2}\ell, \qquad \langle \hat{q} \rangle_{\mathrm{SU}(3), z_{\mathrm{in}}} = \frac{E_0^2}{2\pi^2}\ell, \qquad (17)$$

where the subscript z_{in} indicates that the object has been additionally averaged over the initial position.

For illustrative purposes, it is instructive to estimate the characteristic value of the jet-quenching parameter in our model. To do so, we follow [38], setting $Q_s \sim 2$ GeV and $g \simeq 2$, and assuming a simple scaling of the other parameters of the model—e.g., $|E_0| \sim Q_s^2$, $\ell \sim 1/Q_s$. Then, we readily find that $\langle \hat{q} \rangle_{\mathrm{SU}(3), z_{\mathrm{in}}} \sim \frac{Q_s^3}{2\pi^2} \simeq 2\ \mathrm{GeV}^2/\mathrm{fm}$, and the resulting value is comparable with the results of the simulation in [38] at early times. Notice, however, that our rather simplified matter model disregards such features of the glasma phase as the longitudinal chromomagnetic fields, the transverse field components, and the variation of the correlation length ℓ (both in space and time), and it also assumes the tubes to be compactly packed. Consequently, the obtained values should be considered only as an order-of-magnitude estimate. We mention in passing that the longitudinal chromomagnetic and chromoelectric fields result in comparable contributions to the energy density, and one may expect that a more realistic field configuration would lead to at least doubled $\langle \hat{q} \rangle$.

III. MEDIUM-INDUCED RADIATION

We now turn to medium-induced radiation in our color-domain model of the glasma. The underlying formalism is the same as in BDMPS-Z calculations, but since correlations of color fields are not localized in the glasma, the calculation is more involved qualitatively. In particular, the averaging of the final distribution is not fully factorized into the broadening and emission kernels as in BDMPS-Z, making it more challenging to evaluate. Therefore, we choose to focus on the radiation rate in the soft-gluon limit, which is insensitive to the broadening of the emitted gluon. This quantity can still be reduced to an emission kernel, and it contains the relevant phenomenological information regarding the in-medium gluon production.

The rate of the medium-induced radiation for an ensemble of partons propagating through the given field configuration is defined as (see, e.g., [75]),

$$\frac{d\Gamma}{d\mathrm{x}} = \frac{2\alpha_s C_F}{\mathrm{x}\omega^2}\mathrm{Re}\int_0^t ds \boldsymbol{\nabla}_{\boldsymbol{x}} \cdot \boldsymbol{\nabla}_{\boldsymbol{y}} (\mathcal{K}(\boldsymbol{x},t;\boldsymbol{y},s) - \mathcal{K}_0(\boldsymbol{x},t;\boldsymbol{y},s))_{\boldsymbol{x}=\boldsymbol{y}=0}, \tag{18}$$

where ω is the energy of the emitted gluon, x is its energy fraction with respect to the emitter, $\mathcal{K}$ is the in-medium emission kernel, and $\mathcal{K}_0$ is the emission kernel in vacuum. We have also assumed that the initial distribution is broad in momentum space $|J(\boldsymbol{x})|^2 \sim \delta^{(2)}(\boldsymbol{x}-\boldsymbol{x}_0)$, and that it can be factorized. Notice that a change of the center of the initial distribution $\boldsymbol{x}_0$ corresponds to a shift of the color field in Eq. (1) by $\boldsymbol{x}_0 \cdot \mathbf{E}_i^a$ in each flux tube, which amounts to a gauge transformation. Gauge invariance, therefore, allows us to set $\boldsymbol{x}_0 = 0$ without loss of generality. Thus, the in-medium emission kernel is given by

$$\mathcal{K}(\boldsymbol{x},t;\boldsymbol{y},s) = \frac{1}{N_c^2-1} G^{ab}(\boldsymbol{x},t;\boldsymbol{y},s)\tilde{\mathcal{W}}^{\dagger ba}(0;t,s), \tag{19}$$

where G^{ab} is the single-particle (BDMPS-Z) propagator of the emitted gluon. More explicitly, the kernel can be expressed as a path integral, where the Wilson line accounts for the precession in the background color field:

$$\mathcal{K}(\boldsymbol{x},t;\boldsymbol{y},s) = \frac{1}{N_c^2-1}\int_{\mathbf{r}(s)=\mathbf{y}}^{\mathbf{r}(t)=\mathbf{x}} \mathcal{D}\mathbf{r} \exp\left[i\frac{\omega}{2}\int_s^t d\tau \dot{\boldsymbol{r}}^2\right] \times \mathrm{Tr}\mathcal{P}\exp\left[iT^c\int_s^t d\tau \mathbf{E}^c(\tau)\cdot\boldsymbol{r}(\tau)\right]. \tag{20}$$

A. Induced radiation in QED

The averaging procedure of our model is more involved, making it instructive to start with a toy consideration. For that purpose, let us focus on the U(1) case, which can be treated analytically. Then, the color structure becomes trivial:

$$\mathcal{K}_{\mathrm{U}(1)}(\boldsymbol{x},t;\boldsymbol{y},s) = \int \mathcal{D}\boldsymbol{r}\exp\left[i\int_s^t dt\left(\frac{\omega}{2}\dot{\boldsymbol{r}}^2 + \mathbf{E}(\tau)\cdot\boldsymbol{r}(\tau)\right)\right], \tag{21}$$

and the path integral can be straightforwardly evaluated (see, e.g., [34]):

$$\mathcal{K}_{\mathrm{U}(1)}(\boldsymbol{x},t;\boldsymbol{y},s) = \frac{\omega}{2\pi i(t-s)}\exp\left\{i\frac{\omega}{2}\frac{(\boldsymbol{x}-\boldsymbol{y})^2}{t-s} + \frac{i}{(t-s)}\left(\boldsymbol{x}\cdot\int_s^t d\tau(\tau-s)\mathbf{E}(\tau) + \boldsymbol{y}\cdot\int_s^t d\tau(t-\tau)\mathbf{E}(\tau)\right) - \frac{i}{\omega(t-s)}\int_s^t d\tau\int_s^\tau d\bar{\tau}(t-\tau)(\bar{\tau}-s)\mathbf{E}(\bar{\tau})\cdot\mathbf{E}(\tau)\right\}. \tag{22}$$

This form of the kernel is valid for general background field $\mathbf{E}(\tau)$, and we further focus on the piecewise case of our matter model.

The special case where emissions take place inside a single flux tube is particularly illustrative. For a single tube, the field $\mathbf{E}$ is constant, and the kernel is translationally invariant in the longitudinal direction, simplifying to

$$\mathcal{K}_{\mathrm{U}(1)}(\boldsymbol{x},t;\boldsymbol{y},0) = \frac{\omega}{2\pi i t}\exp\left\{i\left(\frac{\omega}{2t}(\boldsymbol{x}-\boldsymbol{y})^2 + \frac{\mathbf{E}t}{2}\cdot(\boldsymbol{x}+\boldsymbol{y}) - \frac{E^2}{24\omega}t^3\right)\right\}. \tag{23}$$

Thus, one may readily write the medium-induced radiation rate for a constant background field [51,52,76,77] as

$$\frac{d\Gamma_{\mathrm{U}(1)}}{d\mathrm{x}} = \frac{2\alpha_s C_F}{\mathrm{x}\pi}\mathrm{Re}\int_0^t ds\frac{1}{s^2}\left(1-\left(1-i\frac{E^2 s^3}{8\omega}\right)e^{-i\frac{E^2 s^3}{24\omega}}\right). \tag{24}$$

This regime, corresponding to the field being constant during the emission process, is realized when the correlation length $l \sim 1/Q_s$ is longer than the formation time.

Before averaging over the field configuration using Eq. (2), let us consider the rate in the given event for the case of a single flux tube. At earlier times, the rate in Eq. (24) grows as a power of the traveled distance: $\frac{d\Gamma_{\mathrm{U}(1)}}{d\mathrm{x}} \simeq \frac{7\alpha_s C_F}{24\mathrm{x}\pi}\frac{E^4}{\omega^2}\frac{t^5}{5!}$. At later times, it saturates, $\frac{d\Gamma_{\mathrm{U}(1)}}{d\mathrm{x}}|_{t\to\infty} = 3^{1/6}\Gamma(\frac{2}{3})\frac{\alpha_s C_F}{\mathrm{x}\pi}E^{2/3}\omega^{-1/3}$, after a characteristic time $t_{\mathrm{ch}} = (24\omega/E^2)^{1/3}$, which can be understood as the in-medium formation time. Indeed, the same parametric form follows from the scaling $t_{\mathrm{ch}} \sim \sqrt{\omega/\hat{q}(t_{\mathrm{ch}})}$, appearing in the BDMPS-Z considerations [68], if the form of the jet-quenching parameter in Eq. (16) is used for a single long tube—i.e., $\hat{q}(t_{\mathrm{ch}}) \sim E^2 t_{\mathrm{ch}}$. Thus, the in-medium formation time set by t_{ch} for the single-tube case is (parametrically) shorter than the correlation length $1/Q_s$ only for very soft gluons, such that $\omega < Q_s/24$ when $E \sim Q_s^2$.

One may further notice that the rate in Eq. (24) takes a particularly simple form if we scale it with the characteristic time, and its parametric dependence is captured by a single function, $t_{\mathrm{ch}}\frac{d\Gamma_{\mathrm{U}(1)}}{d\mathrm{x}} = f(t/t_{\mathrm{ch}})$. Alternatively, the parametric dependence of the rate can be reexpressed as a function of gluon energy $t\frac{d\Gamma_{\mathrm{U}(1)}}{d\mathrm{x}} = \tilde{f}(\omega/\omega_{\mathrm{ch}})$, with $\omega_{\mathrm{ch}} = E^2 t^3/24$.

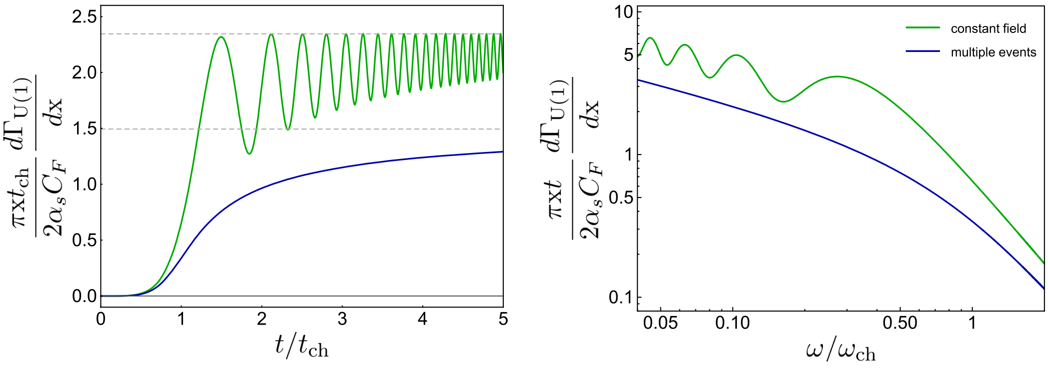

FIG. 1. The rate of the medium-induced radiation for the background U(1) field is plotted for the constant-field case (green) and Gaussian averaging over multiple events (blue), assuming a single long flux tube. Dashed lines indicate the corresponding asymptotic values. The characteristic time t_{ch} and the characteristic frequency ω_{ch} are defined with respect to E (green) and E_0 (blue).

The two functions are directly related, since $\omega/\omega_{\mathrm{ch}} = (t/t_{\mathrm{ch}})^{-3}$, and we show their behavior in Fig. 1. Notice that energetic gluons $\omega > \omega_{\mathrm{ch}}$ have barely had time to form by the measurement moment $t < t_{\mathrm{ch}}$, and the spectrum rapidly decays with $\omega/\omega_{\mathrm{ch}}$.

We now turn to the event-averaged results, still in the case of a single long tube. Averaging the emission kernel, Eq. (23), over multiple events, we get

$$\left\langle \boldsymbol{\nabla}_{\boldsymbol{x}} \cdot \boldsymbol{\nabla}_{\boldsymbol{y}} (\mathcal{K}_{\mathrm{U(1)}}(\boldsymbol{x}, t; \boldsymbol{y}, 0) - \mathcal{K}_0(\boldsymbol{x}, t; \boldsymbol{y}, 0))_{\boldsymbol{x}=\boldsymbol{y}=0} \right\rangle = \frac{\omega^2}{\pi t^2}\left[\frac{1}{\sqrt{i\frac{E_0^2 t^3}{24\omega} + 1}}\left(-1 + \frac{3}{2\left(1 - i\frac{24\omega}{E_0^2 t^3}\right)}\right) + 1\right], \tag{25}$$

where the Gaussian integration in Eq. (2) has been performed explicitly. Then, the averaged rate of the medium-induced radiation is given by

$$\left\langle \frac{d\Gamma_{\mathrm{U(1)}}}{d\mathrm{x}} \right\rangle = \frac{2\alpha_s C_F}{\pi \mathrm{x}} \mathrm{Re} \int_0^t \frac{ds}{s^2} \left[\frac{1}{\sqrt{i\frac{E_0^2 s^3}{24\omega} + 1}} \times \left(-1 + \frac{3}{2\left(1 - i\frac{24\omega}{E_0^2 s^3}\right)}\right) + 1\right]. \tag{26}$$

Taking the same limits as before, one can see that at earlier times, the averaged rate scales as $\langle\frac{d\Gamma_{\mathrm{U(1)}}}{d\mathrm{x}}\rangle \simeq \frac{7\alpha_s C_F}{32\mathrm{x}\pi}\frac{E_0^4}{\omega^2}\frac{t^5}{5!}$, while at later times it tends to $\langle\frac{d\Gamma_{\mathrm{U(1)}}}{d\mathrm{x}}\rangle|_{t\to\infty} = 3^{1/6}\Gamma(\frac{2}{3})\Gamma(\frac{5}{6})\frac{\alpha_s C_F}{\mathrm{x}\pi^{3/2}} E_0^{2/3}\omega^{-1/3}$. All these characteristic features of the single-flux-tube case are summarized in Fig. 1.

The structure of the rate is more involved for the more realistic case when the leading parton traverses multiple tubes. Redefining the characteristic time $t_{\mathrm{ch}} = (24\omega/E_0^2)^{1/3}$ with respect to E_0 of the averaging procedure in Eq. (2), one sees that the full multi-tube rate can be written simply as $t_{\mathrm{ch}}\frac{d\Gamma_{\mathrm{U(1)}}}{dx} = t_{\mathrm{ch}}\frac{d\Gamma_{\mathrm{U(1)}}}{dx}(t/t_{\mathrm{ch}}, \ell/t, \mathbf{E}_i/E_0)$. Averaging over the fields in each flux tube, the rate further simplifies, and its parametric dependence is captured by a single function $t_{\mathrm{ch}}\langle\frac{d\Gamma_{\mathrm{U(1)}}}{dx}\rangle = F(t/t_{\mathrm{ch}}, \ell/t)$, which depends solely on the ratios t/t_{ch} and ℓ/t. Finding analytic results for F quickly becomes unwieldy when ℓ/t is small—i.e., when the radiation occurs over multiple flux tubes—requiring multiple Gaussian integrals in the averaging procedure. However, with the explicit form of Eq. (22) in hand, one can readily evaluate any finite number of Gaussian integrations over the field in Eq. (2) numerically.

To illustrate the features of the spectrum, we present numerical results for $\langle\frac{d\Gamma_{\mathrm{U(1)}}}{dx}\rangle$ and $\langle\frac{d\Gamma_{\mathrm{U(1)}}}{dx}\rangle_{z_{\mathrm{in}}}$ in Fig. 2. We find that, while the leading parton is traversing the first tube, the rate follows the single-tube case. Upon crossing the border between two tubes, the rate experiences some destructive interference, falling after that point. However, propagating further within each given tube, the rate builds up, resembling its behavior in the first tube. This series of oscillations of the rate continues, staying under the single-tube curve. The peaks of the rate occur at the edges of the tubes, as depicted in the left panel of Fig. 2. If the starting position z_{in} within the first tube is varied, the rate curve gets modified, yet the overall pattern remains the same with the minima and peaks shifted. Averaging over the initial position of the leading parton in the first flux tube, we see that the series of minima and peaks is smeared, and the rate takes a shape similar to the constant-field case. The greater the number of tubes traversed by the leading parton by the given t/t_{ch}, the lower the averaged rate at that given point, and the curves for different ℓ/t_{ch} values appear to be ordered, as depicted in the middle panel of Fig. 2. Finally, we find it instructive to plot the rate $t\langle\frac{d\Gamma_{\mathrm{U(1)}}}{dx}\rangle_{z_{\mathrm{in}}}$ as a function of frequency $\omega/\omega_{\mathrm{ch}}$, as shown in the right panel of Fig. 2, and the curves are ordered in the same way. Notice that the averaged rate as a function of $\omega/\omega_{\mathrm{ch}}$ is independent of the particular position of measurement t when scaled with it.

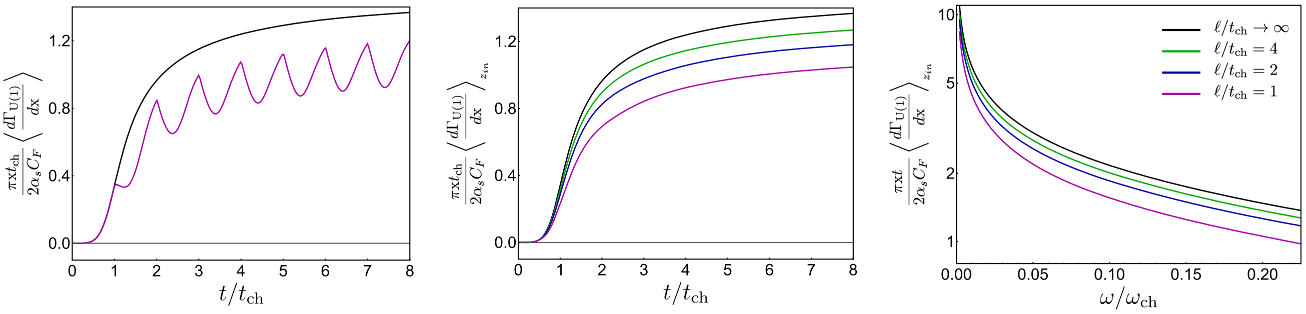

FIG. 2. An illustration of the U(1) averaged rate. The left panel gives $\frac{\pi x}{2\alpha_s C_f}t_{\rm ch}\langle\frac{d\Gamma_{\rm U(1)}}{dx}\rangle$, with the leading parton starting from the edge of the first tube $z_{\rm in}=0$. The middle and right panels depict $\frac{\pi x}{2\alpha_s C_f}t_{\rm ch}\langle\frac{d\Gamma_{\rm U(1)}}{dx}\rangle_{z_{\rm in}}$ and $\frac{\pi x}{2\alpha_s C_f}t\langle\frac{d\Gamma_{\rm U(1)}}{dx}\rangle_{z_{\rm in}}$, averaged over the starting position within the first tube. The colors correspond to the rate evaluated for different tube sizes, including the long-tube limit (black), which appears in all three panels and is given by Eq. (26).

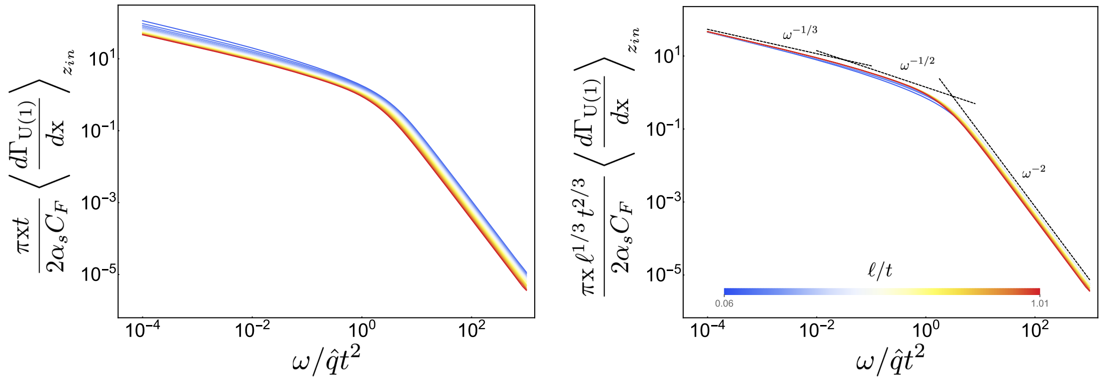

FIG. 3. An illustration of the U(1) rate at constant $\hat{q}t^2$. The left panel depicts $\frac{\pi x t}{2\alpha_s C_f}\langle\frac{d\Gamma_{\rm U(1)}}{dx}\rangle_{z_{\rm in}}$ as a function of $\omega/\hat{q}t^2$, and the right panel depicts its rescaled value, $\frac{\pi x\ell^{1/3}t^{2/3}}{2\alpha_s C_f}\langle\frac{d\Gamma_{\rm U(1)}}{dx}\rangle_{z_{\rm in}}$. The color of the solid lines corresponds to different values of ℓ/t, as indicated in the legend, while the black dashed lines denote the asymptotics, emphasizing the local scaling of the rate with powers of ω.

The ordering of the rate curves can also be understood at the level of the broadening pattern. Indeed, in the case of shorter flux tubes, accumulating transverse momentum is harder, as the fields in different tubes can oppose each other. This results in a longer in-medium formation time[7] for the emission process, leading to a lower rate. This effect is stronger for shorter tubes, reducing the rate. It is furthermore particularly important at larger measurement times $t/t_{\rm ch}$, when the system has had sufficient time to propagate through multiple flux tubes, and at higher energies, where the formation time is longer, and thus more flux tubes are traversed during the radiation process.

Finally, one may find it instructive to consider the parametric dependence of the rate in the regime where $\hat{q}$ is kept constant. Indeed, the BDMPS-Z formalism is often considered in the so-called harmonic approximation (see, e.g., [68]), which is fully controlled by $\hat{q}$, and one may wonder if it is the case in our model. Furthermore, the late-time behavior of the rate at fixed jet-quenching parameter $\langle\hat{q}\rangle_{\rm U(1)}=\frac{1}{8\pi^2}E_0^2\ell$ and varying correlation length provides an opportunity to study the dependence of the in-medium formation time on ℓ. In the regime of interest, the parametric dependence of the rate can be summarized as $t\langle\frac{d\Gamma_{\rm U(1)}}{dx}\rangle_{z_{\rm in}}\sim(t/\ell)^{1/3}(\hat{q}t^2/\omega)^{1/3}F(\omega/(\hat{q}t^2),\ell/t)$, and we illustrate this in the left panel of Fig. 3. Strikingly, we find that the dependence of the rate on ℓ/t is dominated by the prefactor $(t/\ell)^{1/3}$, as can be seen from the right panel of Fig. 3, suggesting that the in-medium formation time scales as $t_m/t\sim(\ell/t)^{1/3}$ at constant $\omega/(\hat{q}t^2)$. Notice that the weaker dependence of the function F on the correlation length is merely an observation, and further understanding of that behavior is required.

Turning to the energy dependence of the rate in Fig. 3, we readily notice that there are three distinct scaling regimes. At low energies, the formation time is small,

---

[7] Notice that $t_{\rm ch}$ is independent of the number of flux tubes, while the physical in-medium formation time does depend on ℓ. In the case of a constant field, corresponding to large ℓ, the two times coincide, but for shorter flux tubes, the in-medium formation time is longer than the characteristic time.

the partons only traverse a few flux tubes while radiating, and the prefactor $(\hat{q}t^2/\omega)^{1/3}$ dominates. This regime has the same energy scaling as in the case of a single flux tube, and the formation time parametrically follows the characteristic time $t_m/t \sim (\ell/t)^{1/3}(\omega/(\hat{q}t^2))^{1/3} \sim t_{\rm ch}/t$. In the transition region of Fig. 3, at larger energies, the scaling of the rate can be well approximated with $(\hat{q}/\omega)^{1/2}$, resembling the well-known behavior of the BDMPS-Z rate under the harmonic approximation, and the formation time scales as $t_m/t \sim (\ell/t)^{1/3}(\omega/(\hat{q}t^2))^{1/2}$. This is well expected, since for sufficiently high gluon energies, the formation time is larger than ℓ, and the partons traverse multiple flux tubes, receiving stochastic transverse momentum kicks with nearly local correlations. This picture closely follows the assumption used in the BDMPS-Z formalism, recovering it in this parametric region. At even higher energies, the formation time for the emission is larger than the measurement time t, the partons barely have time to radiate, and consequently, the rate steeply falls, scaling as $1/\omega^2$. This scaling, also appearing in the BDMPS-Z considerations, can be attributed to the limitations of the harmonic approximation, which cannot capture the Coulomb-type interactions, resulting in a less steep decline; see, e.g., [78,79]. However, our model includes no such hard transverse momentum exchanges in its current form, and in general, their presence and importance in the glasma phase should be further investigated. We leave this question of such potential corrections to the medium model at larger energies for future work.

B. Induced radiation for SU(2)

Although the general case of SU(N_c) is considerably more involved, some intuition regarding the nontrivial color dynamics can be gained by considering a SU(2) background, thanks to the relatively simple form of its general group element. This is particularly relevant, as many glasma simulations are based on SU(2) field theory; for a review, see, e.g., [80].

In our model, characterized by a piecewise field, the path-ordered exponential can be expressed as an ordered product of simple matrix exponentials; see Eq. (13). Each of these can then be expanded within the same matrix basis using Eq. (14). Averaging the rate over the orientation of the fields in the color space, one may notice that each such matrix exponential can be treated independently. Indeed,

$$\begin{aligned}&\langle \tilde{\mathcal{W}}^{ab}_{\mathrm{SU}(2)}(\boldsymbol{r}; z_i, z_{i-1})\rangle\\ &\quad = \left\langle \frac{1}{3}\delta^{ab}\left\{2\cos\left(E_i\int_{z_{i-1}}^{z_i} r_x(\tau)d\tau\right)+1\right\}\right\rangle, \qquad (27)\end{aligned}$$

while for the first and last flux tubes, the limits should be adjusted accordingly. Consequently, all the color structures in the kernel become trivial, and we can express the SU(2) kernel as a convolution of U(1) kernels before averaging the full expression over E_i.

To illustrate that, let us first focus on the case of a single flux tube. Then, we can express the full SU(2) kernel as

$$\begin{aligned}\langle \mathcal{K}_{\mathrm{SU}(2)}(\boldsymbol{x},t;\boldsymbol{y},0)\rangle = \frac{1}{3}\langle &\mathcal{K}_+(\boldsymbol{x},t;\boldsymbol{y},0)+\mathcal{K}_-(\boldsymbol{x},t;\boldsymbol{y},0)\\ &+\mathcal{K}_0(\boldsymbol{x},t;\boldsymbol{y},0)\rangle_{\mathrm{SU}(2)}, \qquad (28)\end{aligned}$$

where $\mathcal{K}_+$, $\mathcal{K}_-$, and $\mathcal{K}_0$ are the U(1) kernels for a single flux tube with electric fields E, $-E$, and $E=0$, respectively, with $E>0$, since the absolute value has been taken in the color space. However, one should notice that the averaging in Eq. (28) is for the SU(2) field strength E, and the residual radial integral $\int_0^\infty \frac{4\pi E^2 dE}{\pi^{3/2}E_0^3}$ incorporates a Jacobian from the full color averaging. Therefore, we keep the corresponding subscript on the averaging to indicate that point.

Noticing that the expression in Eq. (28) is even under $E\to -E$, one may further write

$$\begin{aligned}&\langle \mathcal{K}_+(\boldsymbol{x},t;\boldsymbol{y},0)+\mathcal{K}_-(\boldsymbol{x},t;\boldsymbol{y},0)\rangle_{SU(2)}\\ &\quad=\frac{4}{E_0^2}\langle E^2\mathcal{K}_+(\boldsymbol{x},t;\boldsymbol{y},0)\rangle_{\mathrm{U}(1)}, \qquad (29)\end{aligned}$$

where the E-integration on the rhs runs from $-\infty$ to ∞. In what follows, we will omit the U(1) subscript in the average of $\mathcal{K}_\pm$. Then, the averaged SU(2) radiation rate for the case of a single flux tube can be explicitly written as

$$\begin{aligned}\left\langle\frac{d\Gamma_{\mathrm{SU}(2)}}{dx}\right\rangle &= \frac{4\alpha_s C_F}{3x\omega^2}\mathrm{Re}\int_0^t ds \boldsymbol{\nabla}_{\boldsymbol{x}}\cdot\boldsymbol{\nabla}_{\boldsymbol{y}}\\ &\quad\times\left(\frac{2}{E_0^2}\langle E^2\mathcal{K}_+(\boldsymbol{x},t;\boldsymbol{y},s)\rangle-\mathcal{K}_0(\boldsymbol{x},t;\boldsymbol{y},s)\right)_{\boldsymbol{x}=\boldsymbol{y}=0}\\ &=\frac{4\alpha_s C_F}{3\pi x}\mathrm{Re}\int_0^t\frac{ds}{s^2}\left(\frac{1}{\left(i\frac{E_0^2 s^3}{24\omega}+1\right)^{\frac{3}{2}}}\right.\\ &\quad\left.\times\left(-1+\frac{9}{2\left(1-i\frac{24\omega}{E_0^2 s^3}\right)}\right)+1\right). \qquad (30)\end{aligned}$$

Similarly to the U(1) case, in the early-time limit, $\frac{d\Gamma_{\mathrm{SU}(2)}}{dx}\sim t^5$, while at later times it scales with the inverse of the characteristic time, $\langle\frac{d\Gamma_{\mathrm{SU}(2)}}{dx}\rangle|_{t\to\infty}\sim 1/t_{\rm ch}$.

With this simplification of the color structure of the averaged kernel, the case of multiple flux tubes can be treated in the same way as in the U(1) case. For instance, for $t<2\ell$, we can readily write

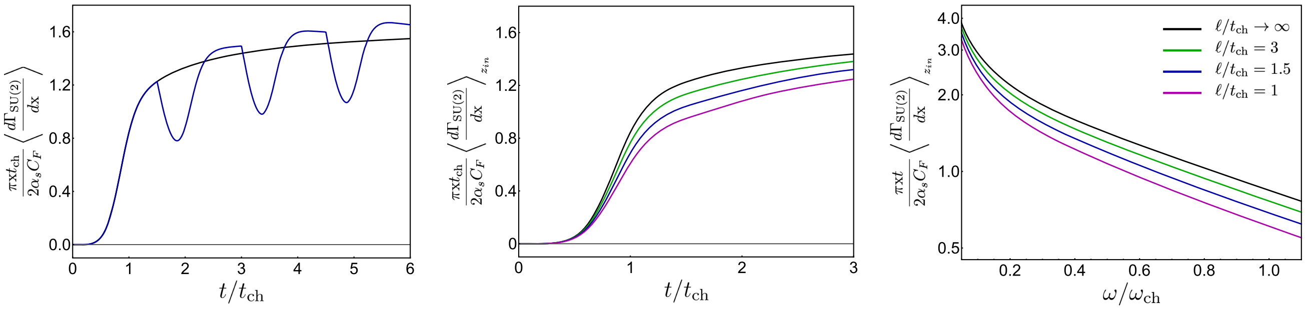

FIG. 4. An illustration of the SU(2) averaged rate. The left panel gives $\frac{\pi x}{2\alpha_s C_f} t_{\rm ch} \langle\frac{d\Gamma_{\rm SU(2)}}{dx}\rangle$, with the leading parton starting from the edge of the first tube, $z_{\rm in}=0$. The middle and right panels depict $\frac{\pi x}{2\alpha_s C_f} t_{\rm ch} \langle\frac{d\Gamma_{\rm SU(2)}}{dx}\rangle_{z_{\rm in}}$ and $\frac{\pi x}{2\alpha_s C_f} t \langle\frac{d\Gamma_{\rm SU(2)}}{dx}\rangle_{z_{\rm in}}$, averaged over the starting position within the first tube. The colors correspond to the rate evaluated for different tube sizes, including the long-tube limit (black), which appears in all three panels and is given by Eq. (30).

$$\begin{aligned}\left\langle\frac{d\Gamma_{\rm SU(2)}}{dx}\right\rangle = \frac{2\alpha_s C_F}{{\rm x}\omega^2}{\rm Re}\int_0^t ds \boldsymbol{\nabla}_{\boldsymbol{x}}\cdot\boldsymbol{\nabla}_{\boldsymbol{y}}((\theta(\ell-t)\\ +\theta(s-\ell))\langle\mathcal{K}^{(1)}_{\rm SU(2)}(\boldsymbol{x},t;\boldsymbol{y},s)\rangle\\ +\theta(t-\ell)\theta(\ell-s)\int_{\boldsymbol{w}}\langle\mathcal{K}^{(1)}_{\rm SU(2)}(\boldsymbol{x},t;\boldsymbol{w},\ell)\rangle\\ \times\langle\mathcal{K}^{(1)}_{\rm SU(2)}(\boldsymbol{w},\ell;\boldsymbol{y},s)\rangle-\mathcal{K}_0(\boldsymbol{x},t;\boldsymbol{y},s))_{\boldsymbol{x}=\boldsymbol{y}=0},\end{aligned} \tag{31}$$

where all the averagings run over SU(2) fields, and the superscript indicates that the particular kernels are taken for the single-tube (or, equivalently, constant-field) case as given by Eq. (28). One may also notice that the parameter dependence of the SU(2) rate can be treated in the same way as in the U(1) case, rescaling it with $t_{\rm ch}$ or t, and focusing on its dependence on $t/t_{\rm ch}$ or $\omega/\omega_{\rm ch}$, with the characteristic scales being the same.

Thus, obtaining the SU(2) kernel for a few tubes in a closed analytical form is sufficiently straightforward. However, the Gaussian integrals of the averaging procedure still need to be treated numerically. Additionally, the need for the integrations over the intermediate transverse positions at the edges of the tubes complicates the numerics, and we focus on a smaller number of tubes.

Following the logic of the previous subsection, we present the numerical results for $\langle\frac{d\Gamma_{\rm SU(2)}}{dx}\rangle$ and $\langle\frac{d\Gamma_{\rm SU(2)}}{dx}\rangle_{z_{\rm in}}$ in Fig. 4. As previously, the rate follows the constant-field case within the first tube, experiencing some destructive interference at the edges and growing within the tubes. However, in contrast with the case of U(1), the SU(2) rate may grow somewhat faster and mean that the curve is being approached from above (i.e., higher values)—see the left panel of Fig. 4. This behavior is featured by longer tubes, while for the shorter tubes, the rate tends to stay under the constant-field curve (at least within the range of times accessible in our numerics). Varying the starting position $z_{\rm in}$ within the first tube at a fixed tube size and averaging the rate, we find that the suppression still dominates—see the middle and right panels of Fig. 4, which show the dependence of the rate on $t/t_{\rm ch}$ and $\omega/\omega_{\rm ch}$, correspondingly. Thus, we find the physical picture to be sufficiently similar to the U(1) case: as the size of the flux tubes $l/t_{\rm ch}$ decreases, there is more destructive interference, the in-medium formation time is longer, and the rate goes down.

For illustrative purposes, one may further estimate the characteristic jet energy loss in the glasma phase by considering the single-flux-tube case for SU(2). Following the considerations for $\langle\hat{q}\rangle$, we choose the characteristic field value to be $|E_0|=\sqrt{2.5Q_s^2}$, naively matching with[8] $\langle\hat{q}\rangle_{{\rm SU(3)},z_{\rm in}}\simeq 5\ {\rm GeV}^2/{\rm fm}$. The radiative energy loss acquired by a jet of energy E traveling a distance L inside the glasma can then be obtained straightforwardly by integrating the radiation rate:

$$\Delta E = E\int_0^L dt\int_0^1 dx\, x\left\langle\frac{d\Gamma_{\rm SU(2)}}{dx}\right\rangle_{z_{\rm in}}. \tag{32}$$

Starting with an $E=50$ GeV parton, we find that $\Delta E=0.26$, 1.97, 5.57 GeV for distances of $L=0.2$, 0.4, 0.6 fm, correspondingly. Thus, we find that, despite the energy loss during the first moments of the glasma phase being rather small, in agreement with earlier estimates [52], its quick growth with the path may make it larger. Therefore, the milder decay of $\langle\hat{q}\rangle$ during the kinetic theory phase [44] and the larger values of the gluonic fields at the first moments [38] can indeed lead to a substantial quenching within the preequilibrium phases. Notice, however, that the interference effects due to the presence of multiple flux tubes should result in some suppression of the energy loss.

---

[8] Notice that we rely on the SU(2) rate but use $\langle\hat{q}\rangle_{{\rm SU(3)},z_{\rm in}}$ to match the numerical prefactor in the characteristic color field.

IV. AN ALTERNATIVE MATTER MODEL

In this work, we rely on a simple model for the initial stages of heavy-ion collisions, which has several limitations. One such limitation is that the averaging in Eq. (2) is centered at $E_i = 0$, while the strong glasma fields are expected to be predominantly nonzero in each event. To gain further insight into the physical picture, we explore an alternative averaging procedure in this section, addressing this specific aspect of the glasma field dynamics.

To do so, we enforce the chromoelectric field of any given tube's fluctuation in its direction along the beam axis and in its color, but keeping its absolute value fixed. Thus, the alternative averaging procedure can be summarized for the SU(N_c) case with

$$\langle f(E^a_{1x}, E^a_{2x}, E^a_{3x}, \ldots)\rangle = \int_{E_1} \frac{E_0}{2}\Gamma\left(\frac{N_c^2-1}{2}\right)\delta(E_{1x}-E_0)\int_{E_2} \frac{E_0}{2}\Gamma\left(\frac{N_c^2-1}{2}\right)\delta(E_{2x}-E_0)\cdots f\left(E^a_{1x}, E^a_{2x}, E^a_{3x}, \ldots\right), \tag{33}$$

where the integration runs over SU(N_c) phase space, and we have restored the x subscript. In turn, in the U(1) case, this procedure simplifies to

$$\langle f(E_{1x}, E_{2x}, E_{3x}, \ldots)\rangle = \left[\prod_n \int_{E_n} \frac{dE_{nx}}{2}\left(\delta(E_{nx}-E_0)+\delta(E_{nx}+E_0)\right)\right] f(E_{1x}, E_{2x}, E_{3x}, \ldots), \tag{34}$$

where E_{nx} is just the x component of the field in the nth tube.

Focusing first on the jet-quenching parameter, we average Eq. (12) using the new procedure, and readily find that

$$\langle \hat{q}(z)\rangle_{\mathrm{SU}(2)} = \langle \hat{q}(z)\rangle_{\mathrm{SU}(3)} = \frac{E_0^2}{4\pi^2}(z-z_n), \tag{35}$$

since the angular averaging over the color space of the field in the last flux tube still gives zero, unless the two fields in Eq. (12) are from the same flux tube. Similarly, when averaging the jet-quenching parameter over the starting position z_{in} in the first tube, we find

$$\langle \hat{q}(z)\rangle_{\mathrm{SU}(2),z_{\mathrm{in}}} = \langle \hat{q}(z)\rangle_{\mathrm{SU}(3),z_{\mathrm{in}}} = \frac{E_0^2}{8\pi^2}\ell. \tag{36}$$

Turning to the U(1) medium-induced radiation, we start with the single-flux-tube emission rate. After averaging, the rate reads

$$\left\langle \frac{d\Gamma_{\mathrm{U}(1)}}{dx}\right\rangle = \frac{2\alpha_s C_F}{x\pi}\mathrm{Re}\int_0^t ds\frac{1}{s^2}\left(1-\left(1-i\frac{E_0^2 s^3}{8\omega}\right)e^{-i\frac{E_0^2 s^3}{24\omega}}\right). \tag{37}$$

Thus, one may see that $\langle\frac{\Gamma_{\mathrm{U}(1)}}{dx}\rangle$ coincides with the constant-field rate [Eq. (24)] before averaging over multiple events, up to an identification $E = E_0$. The multiple oscillations of the rate do not average out now, and as we will see further, they reappear for finite tube sizes.

As before, the rate exhibits a more complex structure when the leading parton propagates through more than a single tube. Relying on the same overall parametric

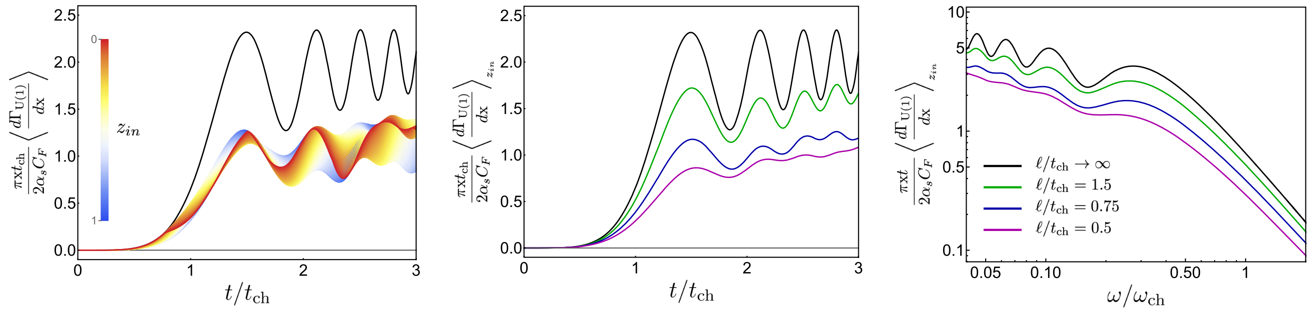

FIG. 5. An illustration of the U(1) rate averaged under the alternative procedure; see Eq. (34). The left panel displays a family of curves for $\frac{\pi x}{2\alpha_s C_f} t_{\mathrm{ch}}\langle\frac{d\Gamma_{\mathrm{U}(1)}}{dx}\rangle$ at $\ell/t_{\mathrm{ch}} = 0.75$, with the leading parton starting its path from different positions z_{in} within the first tube. These rate curves are distinguished by the color, as indicated in the legend of the left panel. The middle and right panels depict $\frac{\pi x}{2\alpha_s C_f} t_{\mathrm{ch}}\langle\frac{d\Gamma_{\mathrm{U}(1)}}{dx}\rangle_{z_{\mathrm{in}}}$ and $\frac{\pi x}{2\alpha_s C_f} t\langle\frac{d\Gamma_{\mathrm{U}(1)}}{dx}\rangle_{z_{\mathrm{in}}}$, averaged over the starting position within the first tube. The colors listed in the legend of the right panel correspond to the rate evaluated for different tube sizes, including the long-tube limit (black), which appears in all three panels and is given by Eq. (37).

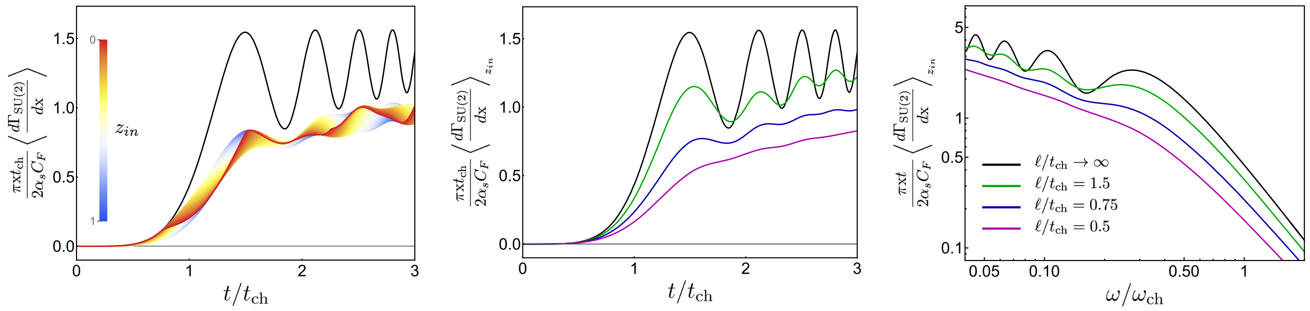

FIG. 6. An illustration of the SU(2) rate averaged under the alternative procedure; see Eq. (33). The left panel displays a family of curves for $\frac{\pi x}{2\alpha_s C_f} t_{\rm ch}\langle\frac{d\Gamma_{\rm SU(2)}}{dx}\rangle$ at $\ell/t_{\rm ch}=0.75$, with the leading parton starting its path from different positions $z_{\rm in}$ within the first tube. These rate curves are distinguished by the color, as indicated in the legend of the left panel. The middle and right panels depict $\frac{\pi x}{2\alpha_s C_f} t_{\rm ch}\langle\frac{d\Gamma_{\rm SU(2)}}{dx}\rangle_{z_{\rm in}}$ and $\frac{\pi x}{2\alpha_s C_f} L\langle\frac{d\Gamma_{\rm SU(2)}}{dx}\rangle_{z_{\rm in}}$, averaged over the starting positions within the first tube. The colors listed in the legend of the right panel correspond to the rate evaluated for different tube sizes, including the long-tube limit (black), which appears in all three panels and is given by Eq. (38).

dependence of the averaged rate for both averaging procedures, we evaluate the multiple-tube case numerically and present our results for $\langle\frac{d\Gamma_{\rm U(1)}}{dx}\rangle$ and $\langle\frac{d\Gamma_{\rm U(1)}}{dx}\rangle_{z_{\rm in}}$ in Fig. 5. In the left panel, we illustrate the long-flux-tube limit of the U(1) rate averaged under Eq. (34), identical to the constant-field rate Eq. (24) in this case. Here, we also depict a family of rates at $\ell/t_{\rm ch}=0.75$, plotted for different initial positions $z_{\rm in}$ of the leading parton within the first tube. The corresponding curves are distinguished by a color scheme and form a colored band. The shape of this band indicates that even after averaging over the initial positions, some oscillatory patterns of the constant-field rate persist. In turn, in the middle and right panels of Fig. 5, we present $t_{\rm ch}\langle\frac{d\Gamma_{\rm U(1)}}{dx}\rangle_{z_{\rm in}}$ and $t\langle\frac{d\Gamma_{\rm U(1)}}{dx}\rangle_{z_{\rm in}}$, additionally averaged over the starting position $z_{\rm in}$ in the first tube as functions of $t/t_{\rm ch}$ and $\omega/\omega_{\rm ch}$, respectively. We see that the rates averaged under the second procedure of Eq. (34) are again ordered with $\ell/t_{\rm ch}$, falling for shorter tube sizes.

Averaging the SU(2) rate with Eq. (33), we can still rely on the Wilson line decomposition in Eq. (13). Moreover, the angular averaging in the color space ensures the validity of Eq. (27). Thus, the averaged single-flux-tube emission rate in the SU(2) case reads

$$\begin{aligned}\left\langle\frac{d\Gamma_{\rm SU(2)}}{dx}\right\rangle_{\rm SU(2)} &= \frac{2\alpha_s C_F}{3x\omega^2}{\rm Re}\int_0^t ds\langle\boldsymbol{\nabla}_{\boldsymbol{x}}\cdot\boldsymbol{\nabla}_{\boldsymbol{y}}(\mathcal{K}_+(\boldsymbol{x},t;\boldsymbol{y},s)\\ &\quad+\mathcal{K}_-(\boldsymbol{x},t;\boldsymbol{y},s)-2\mathcal{K}_0(\boldsymbol{x},t;\boldsymbol{y},s))_{\boldsymbol{x}=\boldsymbol{y}=0}\rangle\\ &=\frac{4\alpha_s C_F}{3x\pi}{\rm Re}\int_0^t ds\frac{1}{s^2}\\ &\quad\times\left(1-\left(1-i\frac{E_0^2s^3}{8\omega}\right)e^{-i\frac{E_0^2s^3}{24\omega}}\right),\end{aligned}\tag{38}$$

differing from the U(1) case only by a numerical factor.

Similarly to the U(1) case, we focus on the numerical estimates of the SU(2) rate at finite tube length, presenting the results in Fig. 6. The left panel again exhibits the long-tube limit of the SU(2) rate averaged under Eq. (33), along with a family of the SU(2) rates at $\ell/t_{\rm ch}=0.75$ with different starting positions $z_{\rm in}$ of the leading parton within the first tube (distinguished by a color scheme). In turn, the middle and right panels depict $t_{\rm ch}\langle\frac{d\Gamma_{\rm SU(2)}}{dx}\rangle_{z_{\rm in}}$ and $t\langle\frac{d\Gamma_{\rm SU(2)}}{dx}\rangle_{z_{\rm in}}$, averaged over the initial position within the first tube, and one may see the same ordering of the rates with ℓ.

Thus, we conclude that, while certain nuances of the rate may vary depending on the specific matter model and gauge group, features such as the anticipated asymptotic behavior and qualitative dependence of the rate on $\ell/t_{\rm ch}$ stay untouched, indicating sufficient robustness of the physical picture obtained in this work.

V. CONCLUSIONS

In this work, we have developed a formalism to describe jet quenching during the early times of heavy-ion collisions, when the medium is dominated by strong color fields. Throughout our considerations, we have relied on a simplified matter model that captures the main features of this glasma phase. In particular, we have assumed that the matter is made up of color domains with chromoelectric fields confined in flux tubes aligned with the beam axis. The field is homogeneous and constant within any given tube, and independently varies in different domains on an event-by-event basis. Thus, we relax several assumptions that are ubiquitous in most of the jet-quenching considerations. First, we go beyond the approximation of local field correlations widely used in the jet-quenching calculations in the quark-gluon plasma context[9] and assume a finite correlation length. This is also in contrast with the constant (slowly varying) field limit employed in considerations of the synchrotron-like radiation of energetic partons. Second, we consider the event-by-event fluctuations of the glasma background and its interplay with the jet physics, providing a starting point for jet tomography of the early stages of heavy-ion collisions.

Using our model, we start by calculating the transverse momentum broadening of jet partons for both SU(2) and SU(3) backgrounds, investigating how the results depend on the size of the color domains ℓ. The jet-quenching parameter for a jet parton traversing the given flux tube increases with time. Conversely, for a jet parton traversing many small flux tubes, the stochastic kicks it receives average out, leading to a constant rate of broadening.[10]

We further focus on the medium-induced radiation in the glasma background, restricting our consideration to the emission rate in the soft gluon limit. Most of our results are obtained for a SU(2) background, where the model can be treated semianalytically, and compared with the toy consideration for the U(1) case. However, it should be emphasized that the presented formalism can be straightforwardly extended to the physical SU(3) case. We have also explored two different averaging procedures—a Gaussian averaging centered at zero field and a delta functional averaging with fluctuating direction—to probe the sensitivity of our results to the features of the medium model.

The behavior of the rate can be understood by comparing the relevant timescales of the problem. When a single flux tube is longer than the formation time for gluon emission, the resulting rate reproduces the well-known form for synchrotron radiation in a constant field. Considering the characteristic energy scales for the saturation and jet-quenching processes in heavy-ion collisions, one may expect this regime to be relevant only for very soft emissions. At higher energies, the partons traverse multiple flux tubes during the emission process. This leads to an intricate interplay between different flux tubes, due to both momentum kicks in different directions and color decoherence between flux tubes. The net result is a reduction in the rate when the flux tubes are smaller, which is especially pronounced for higher gluon energies or at later times. This result holds for both U(1) and SU(2) rates, and for both averaging procedures, as illustrated in Figs. 2, 4, 5, and 6.

Finally, we study the details of the in-medium formation time behavior for jet quenching in our medium model. To do this, we consider the rate as a function of energy and tube size at fixed $\hat{q}$ and t. The similarity of the SU(2) and U(1) rates (under two averaging procedures) suggests that such features are sufficiently universal, and we focus on the U(1) case with Gaussian averaging for simplicity (see Fig. 3), leaving more general investigation for the future. The U(1) rate exhibits three distinct scaling regimes: (i) At lower energies, the partons traverse only a few tubes, and the rate scales as $\omega^{-1/3}$, resembling the behavior in the case of a single long tube. (ii) For the transition region of intermediate energies, the partons traverse multiple tubes during the emission process, but the formation time is smaller than t. The rate scales as $\omega^{-1/2}$, recovering the behavior of the BDMPS-Z rate under the harmonic approximation. This is well expected, since in this limit the finite correlation length ℓ is small, and averages are near local. (iii) For larger energies, the formation time is larger than t, and the rate scales as ω^{-2}, further recovering the large-energy behavior of the BDMPS-Z rate under the harmonic approximation. The latter region goes beyond the applicability of the harmonic approximation in the BDMPS-Z case, and it is taken over by the small number of hard interactions of the opacity expansion regime; see, e.g., [81] for a review. It would be interesting to further study whether similar larger transverse momentum exchanges may take place in the glasma phase and investigate their relevance in the case of SU(N_c). We leave such a study for future work.

We also find that simple numerical estimates for the characteristic value of $\langle\hat{q}\rangle$ obtained within our model are consistent with the results of the recent simulations [36–38]. The characteristic energy loss stays sufficiently small for the very early times but quickly grows with the distance traveled by the parton. Thus, one may argue that the slower decay of $\langle\hat{q}\rangle$ during the preequilibrium stages, recently observed in simulations [44], can lead to a substantial energy loss, depending on the details of the time evolution of the matter.

The presented results can be extended in several ways to achieve a more realistic description of jets during the early stages of heavy-ion collisions. A natural and promising future step would be to combine our approach with realistic numerical simulations of the glasma. This would allow us to compute the medium-induced soft gluon rate, similarly to the previous studies on single-particle momentum broadening [36–38]. In particular, such an exercise would help determine if the early-time evolution of jets is indeed described by a multiple scattering picture, in the style of the BDMPS-Z formalism. Beyond this application, in order to compute realistic jet observables, our model needs to be complemented with the virtuality cascade of the jet evolution and account for the subsequent stages of matter evolution.

---

[9] The recent developments of the jet-quenching theory in anisotropic media may provide another example of going beyond the limit of local correlations in the transverse directions; see, e.g., [59].

[10] The interference suppression at the edges of the tubes also appears for the spectrum, although some oscillatory behavior can be inherited from the constant-field rate and may survive averaging over the initial position.

ACKNOWLEDGMENTS

We thank D. Avramescu, K. Boguslavski, F. Gelis, E. Iancu, T. Lappi, F. Lindenbauer, C. Salgado, and B. Schenke for helpful discussions related to this work. J. B. is supported by the United States Department of Energy under Grant Contract No. DESC001270. S. H. is grateful to the EIC Theory Institute and to Brookhaven National Laboratory for the hospitality and support during the early stages of this work. X. M. L. is supported under scholarship No. PRE2021-097748, funded by MCIN/AEI and FSE + . X. M. L. is also supported by Xunta de Galicia (Centro singular de investigación de Galicia accreditation 2019–2022), by European Union ERDF; and by Grant No. CEX2023-001318-M funded by MICIU/AEI and by ERDF/EU. A. V. S. is supported by Fundação para a Ciência e a Tecnologia (FCT) under Contract No. 2022.06565.CEECIND. A. V. S. and X. M. L. also acknowledge the support from European Research Council Project No. ERC-2018-ADG-835105 YoctoLHC. This work has been also supported by STRONG-2020, "The strong interaction at the frontier of knowledge: Fundamental research and applications," which received funding from the European Union's Horizon 2020 research and innovation program under Grant Agreement No. 824093.

[1] L. Cunqueiro and A. M. Sickles, Studying the QGP with jets at the LHC and RHIC, Prog. Part. Nucl. Phys. **124**, 103940 (2022).

[2] L. Apolinário, Y.-J. Lee, and M. Winn, Heavy quarks and jets as probes of the QGP, Prog. Part. Nucl. Phys. **127**, 103990 (2022).

[3] I. Vitev and M. Gyulassy, High p_T tomography of $d + \mathrm{Au}$ and Au + Au at SPS, RHIC, and LHC, Phys. Rev. Lett. **89**, 252301 (2002).

[4] E. Wang and X.-N. Wang, Jet tomography of dense and nuclear matter, Phys. Rev. Lett. **89**, 162301 (2002).

[5] K. M. Burke *et al.* (JET Collaboration), Extracting the jet transport coefficient from jet quenching in high-energy heavy-ion collisions, Phys. Rev. C **90**, 014909 (2014).

[6] B. Betz and M. Gyulassy, Constraints on the path-length dependence of jet quenching in nuclear collisions at RHIC and LHC, J. High Energy Phys. 08 (2014) 090; 10 (2014) 043(E).

[7] J. Xu, A. Buzzatti, and M. Gyulassy, Azimuthal jet flavor tomography with CUJET2.0 of nuclear collisions at RHIC and LHC, J. High Energy Phys. 08 (2014) 063.

[8] M. Djordjevic, B. Blagojevic, and L. Zivkovic, Mass tomography at different momentum ranges in quark-gluon plasma, Phys. Rev. C **94**, 044908 (2016).

[9] L. Apolinário, J. G. Milhano, G. P. Salam, and C. A. Salgado, Probing the time structure of the quark-gluon plasma with top quarks, Phys. Rev. Lett. **120**, 232301 (2018).

[10] Y. He, L.-G. Pang, and X.-N. Wang, Gradient tomography of jet quenching in heavy-ion collisions, Phys. Rev. Lett. **125**, 122301 (2020).

[11] A. V. Sadofyev, M. D. Sievert, and I. Vitev, *Ab initio* coupling of jets to collective flow in the opacity expansion approach, Phys. Rev. D **104**, 094044 (2021).

[12] L. Antiporda, J. Bahder, H. Rahman, and M. D. Sievert, Jet drift and collective flow in heavy-ion collisions, Phys. Rev. D **105**, 054025 (2022).

[13] Y.-L. Du, D. Pablos, and K. Tywoniuk, Jet tomography in heavy-ion collisions with deep learning, Phys. Rev. Lett. **128**, 012301 (2022).

[14] E. Iancu and R. Venugopalan, The color glass condensate and high-energy scattering in QCD, in *Quark-Gluon Plasma 4*, edited by R. C. Hwa and X.-N. Wang (World Scientific, Singapore, 2004), pp. 249–3363, 10.1142/9789812795533_0005.

[15] T. Lappi and L. McLerran, Some features of the glasma, Nucl. Phys. **A772**, 200 (2006).

[16] F. Gelis, E. Iancu, J. Jalilian-Marian, and R. Venugopalan, The color glass condensate, Annu. Rev. Nucl. Part. Sci. **60**, 463 (2010).

[17] F. Gelis, Color glass condensate and glasma, Int. J. Mod. Phys. A **28**, 1330001 (2013).

[18] F. Gelis, Initial state and thermalization in the color glass condensate framework, Int. J. Mod. Phys. E **24**, 1530008 (2015).

[19] T. Lappi, Production of gluons in the classical field model for heavy ion collisions, Phys. Rev. C **67**, 054903 (2003).

[20] K. Fukushima and F. Gelis, The evolving glasma, Nucl. Phys. **A874**, 108 (2012).

[21] J. Berges, K. Boguslavski, S. Schlichting, and R. Venugopalan, Universal attractor in a highly occupied non-Abelian plasma, Phys. Rev. D **89**, 114007 (2014).

[22] A. Ipp and D. Müller, Implicit schemes for real-time lattice gauge theory, Eur. Phys. J. C **78**, 884 (2018).

[23] B. Schenke, P. Tribedy, and R. Venugopalan, Fluctuating glasma initial conditions and flow in heavy ion collisions, Phys. Rev. Lett. **108**, 252301 (2012).

[24] B. Schenke, P. Tribedy, and R. Venugopalan, Initial-state geometry and fluctuations in Au + Au, Cu + Au, and U + U collisions at energies available at the BNL relativistic heavy ion collider, Phys. Rev. C **89**, 064908 (2014).

[25] S. McDonald, S. Jeon, and C. Gale, 3 + 1D initialization and evolution of the glasma, Phys. Rev. C **108**, 064910 (2023).

[26] B. Schenke and S. Schlichting, 3D glasma initial state for relativistic heavy ion collisions, Phys. Rev. C **94**, 044907 (2016).

[27] D. Gelfand, A. Ipp, and D. Müller, Simulating collisions of thick nuclei in the color glass condensate framework, Phys. Rev. D **94**, 014020 (2016).

[28] A. Ipp and D. I. Müller, Progress on $3+1$D glasma simulations, Eur. Phys. J. A **56**, 243 (2020).

[29] S. Schlichting and P. Singh, 3-D structure of the glasma initial state—Breaking boost-invariance by collisions of extended shock waves in classical Yang-Mills theory, Phys. Rev. D **103**, 014003 (2021).

[30] A. Ipp, D. I. Müller, S. Schlichting, and P. Singh, Spacetime structure of $(3+1)$D color fields in high energy nuclear collisions, Phys. Rev. D **104**, 114040 (2021).

[31] P. B. Arnold, G. D. Moore, and L. G. Yaffe, Effective kinetic theory for high temperature gauge theories, J. High Energy Phys. 01 (2003) 030.

[32] A. Kurkela and Y. Zhu, Isotropization and hydrodynamization in weakly coupled heavy-ion collisions, Phys. Rev. Lett. **115**, 182301 (2015).

[33] A. Kurkela, A. Mazeliauskas, J.-F. Paquet, S. Schlichting, and D. Teaney, Effective kinetic description of event-by-event pre-equilibrium dynamics in high-energy heavy-ion collisions, Phys. Rev. C **99**, 034910 (2019).

[34] P. Aurenche and B. G. Zakharov, Parton energy loss in glasma, Phys. Lett. B **718**, 937 (2013).

[35] P. Dorau, J.-B. Rose, D. Pablos, and H. Elfner, Jet quenching in the hadron gas: An exploratory study, Phys. Rev. C **101**, 035208 (2020).

[36] A. Ipp, D. I. Müller, and D. Schuh, Anisotropic momentum broadening in the $2+1$D glasma: Analytic weak field approximation and lattice simulations, Phys. Rev. D **102**, 074001 (2020).

[37] A. Ipp, D. I. Müller, and D. Schuh, Jet momentum broadening in the pre-equilibrium glasma, Phys. Lett. B **810**, 135810 (2020).

[38] D. Avramescu, V. Băran, V. Greco, A. Ipp, D. I. Müller, and M. Ruggieri, Simulating jets and heavy quarks in the glasma using the colored particle-in-cell method, Phys. Rev. D **107**, 114021 (2023).

[39] M. E. Carrington, A. Czajka, and S. Mrowczynski, Heavy quarks embedded in glasma, Nucl. Phys. **A1001**, 121914 (2020).

[40] M. E. Carrington, A. Czajka, and S. Mrowczynski, Jet quenching in glasma, Phys. Lett. B **834**, 137464 (2022).

[41] M. E. Carrington, A. Czajka, and S. Mrowczynski, Transport of hard probes through glasma, Phys. Rev. C **105**, 064910 (2022).

[42] S. Cao *et al.* (JETSCAPE Collaboration), Determining the jet transport coefficient $\hat{q}$ from inclusive hadron suppression measurements using Bayesian parameter estimation, Phys. Rev. C **104**, 024905 (2021).

[43] S. Hauksson, S. Jeon, and C. Gale, Momentum broadening of energetic partons in an anisotropic plasma, Phys. Rev. C **105**, 014914 (2022).

[44] K. Boguslavski, A. Kurkela, T. Lappi, F. Lindenbauer, and J. Peuron, Jet momentum broadening during initial stages in heavy-ion collisions, Phys. Lett. B **850**, 138525 (2024).

[45] K. Boguslavski, A. Kurkela, T. Lappi, F. Lindenbauer, and J. Peuron, Jet quenching parameter in QCD kinetic theory, Phys. Rev. D **110**, 034019 (2024).

[46] K. Boguslavski, A. Kurkela, T. Lappi, F. Lindenbauer, and J. Peuron, Limiting attractors in heavy-ion collisions, Phys. Lett. B **852**, 138623 (2024).

[47] A. Kumar, B. Müller, and D.-L. Yang, Spin polarization and correlation of quarks from the glasma, Phys. Rev. D **107**, 076025 (2023).

[48] S. Hauksson and E. Iancu, Jet polarisation in an anisotropic medium, J. High Energy Phys. 08 (2023) 027.

[49] J. Barata, C. A. Salgado, and J. M. Silva, Gluon to $q\bar{q}$ antenna in anisotropic QCD matter: Spin-polarized and azimuthal jet observables, arXiv:2407.04774.

[50] S. Hauksson and C. Gale, Polarized photons from the early stages of relativistic heavy-ion collisions, Phys. Rev. C **109**, 034902 (2024).

[51] E. V. Shuryak and I. Zahed, Jet quenching in high-energy heavy ion collisions by QCD synchrotron-like radiation, Phys. Rev. D **67**, 054025 (2003).

[52] B. G. Zakharov, Parton energy loss due to synchrotron-like gluon emission, JETP Lett. **88**, 475 (2008).

[53] Y. Mehtar-Tani, S. Schlichting, and I. Soudi, Jet thermalization in QCD kinetic theory, J. High Energy Phys. 05 (2023) 091.

[54] J.-P. Blaizot, E. Iancu, and Y. Mehtar-Tani, Medium-induced QCD cascade: Democratic branching and wave turbulence, Phys. Rev. Lett. **111**, 052001 (2013).

[55] A. V. Sadofyev, M. D. Sievert, and I. Vitev, Jets in evolving matter within the opacity expansion approach, SciPost Phys. Proc. **8**, 046 (2022).

[56] J. Barata, A. V. Sadofyev, and C. A. Salgado, Jet broadening in dense inhomogeneous matter, Phys. Rev. D **105**, 114010 (2022).

[57] C. Andres, F. Dominguez, A. V. Sadofyev, and C. A. Salgado, Jet broadening in flowing matter—Resummation, Phys. Rev. D **106**, 074023 (2022).

[58] Y. Fu, J. Casalderrey-Solana, and X.-N. Wang, Asymmetric transverse momentum broadening in an inhomogeneous medium, Phys. Rev. D **107**, 054038 (2023).

[59] J. Barata, A. V. Sadofyev, and X.-N. Wang, Quantum partonic transport in QCD matter, Phys. Rev. D **107**, L051503 (2023).

[60] J. Barata, X. Mayo López, A. V. Sadofyev, and C. A. Salgado, Medium induced gluon spectrum in dense inhomogeneous matter, Phys. Rev. D **108**, 034018 (2023).

[61] M. V. Kuzmin, X. Mayo López, J. Reiten, and A. V. Sadofyev, Jet quenching in anisotropic flowing matter, Phys. Rev. D **109**, 014036 (2024).

[62] M. V. Kuzmin and X. Mayo López, Gluon radiation inside a flowing medium, arXiv:2406.14628.

[63] J. Barata, J. G. Milhano, and A. V. Sadofyev, Picturing QCD jets in anisotropic matter: From jet shapes to energy energy correlators, Eur. Phys. J. C **84**, 174 (2024).

[64] M. Li, T. Lappi, and X. Zhao, Scattering and gluon emission in a color field: A light-front Hamiltonian approach, Phys. Rev. D **104**, 056014 (2021).

[65] M. Li, T. Lappi, X. Zhao, and C. A. Salgado, Momentum broadening of an in-medium jet evolution using a light-front Hamiltonian approach, Phys. Rev. D **108**, 036016 (2023).

[66] J. Barata, X. Du, M. Li, W. Qian, and C. A. Salgado, Quantum simulation of in-medium QCD jets: Momentum broadening, gluon production, and entropy growth, Phys. Rev. D **108**, 056023 (2023).

[67] B. G. Zakharov, Effect of color randomization on p_T broadening of fast partons in turbulent quark-gluon plasma, arXiv:2311.18607.

[68] J. Casalderrey-Solana and C. A. Salgado, Introductory lectures on jet quenching in heavy ion collisions, Acta Phys. Pol. B **38**, 3731 (2007), https://www.actaphys.uj.edu.pl/R/38/12/3731.

[69] J. Barata, J.-P. Blaizot, and Y. Mehtar-Tani, Quantum to classical parton dynamics in QCD media, Phys. Rev. D **108**, 014039 (2023).

[70] J.-P. Blaizot and M. A. Escobedo, Quantum and classical dynamics of heavy quarks in a quark-gluon plasma, J. High Energy Phys. 06 (2018) 034.

[71] J.-P. Blaizot and E. Iancu, Lifetimes of quasiparticles and collective excitations in hot QED plasmas, Phys. Rev. D **55**, 973 (1997).

[72] E. Braaten and R. D. Pisarski, Calculation of the gluon damping rate in hot QCD, Phys. Rev. D **42**, 2156 (1990).

[73] J. Casalderrey-Solana and D. Teaney, Transverse momentum broadening of a fast quark in a $N = 4$ Yang Mills plasma, J. High Energy Phys. 04 (2007) 039.

[74] A. Majumder, B. Muller, and S. Mrowczynski, Momentum broadening of a fast parton in a perturbative quark-gluon plasma, Phys. Rev. D **80**, 125020 (2009).

[75] B. G. Zakharov, Radiative energy loss of high-energy quarks in finite size nuclear matter and quark-gluon plasma, JETP Lett. **65**, 615 (1997).

[76] V. Baier and V. Katkov, Deviation from standard QEC at large distances: Influence of transverse dimension of colliding beams on bremstrahlung, J. Exp. Theor. Phys. **26**, 854 (1968), https://cds.cern.ch/record/898066/files/cer-002568497.pdf.

[77] B. G. Zakharov, Effect of magnetic field on the photon radiation from quark-gluon plasma in heavy ion collisions, Eur. Phys. J. C **76**, 609 (2016).

[78] J. Barata and Y. Mehtar-Tani, Improved opacity expansion at NNLO for medium induced gluon radiation, J. High Energy Phys. 10 (2020) 176.

[79] J. H. Isaksen, A. Takacs, and K. Tywoniuk, A unified picture of medium-induced radiation, J. High Energy Phys. 02 (2023) 156.

[80] J. Berges, M. P. Heller, A. Mazeliauskas, and R. Venugopalan, QCD thermalization: *Ab initio* approaches and interdisciplinary connections, Rev. Mod. Phys. **93**, 035003 (2021).

[81] M. D. Sievert and I. Vitev, Quark branching in QCD matter to any order in opacity beyond the soft gluon emission limit, Phys. Rev. D **98**, 094010 (2018).

Resumo estendido

O obxectivo principal desta tese é investigar as propiedades do estado da materia formado nos momentos iniciais das colisións de ións pesados empregando jets. Para iso, desenvolvemos un conxunto de novas ferramentas analíticas que amplían o formalismo actual do jet quenching para incorporar o efecto da evolución e estrutura da materia durante as diferentes etapas das HIC. A presente tese estruturase da seguinte forma: primeiro revisamos o marco conceptual do traballo, logo introducimos brevemente o formalismo empregado, e rematamos resumindo os resultados obtidos e as conclusións acadadas.

Marco conceptual

QCD e as súas propiedades

O auxe dos descubrimentos de partículas subatómicas durante a década de 1950 facilitado por novas técnicas experimentais, revelou unha gran cantidade de partículas máis pesadas que os pións, denominadas hadróns. Esta abundancia suxería que os hadróns non eran partículas fundamentais, senón compostas. O *eightfold way*, proposto na década de 1960, proporcionou un esquema organizativo para os hadróns, suxerindo a existencia de quarks, que serían os seus constituíntes fundamentais. Porén, o modelo de quarks non abondaba para explicar as propiedades de todas as partículas descubertas, polo que se propuxo introducir unha simetría do grupo $SU(3)$ asociada a unha nova carga conservada: a cor. Pouco despois, os experimentos de *deep inelastic scatterings* levados a cabo en SLAC en 1968 proporcionaron a primeira evidencia directa dos quarks. Estes descubrimentos culminaron no desenvolvemento da Cromodinámica Cuántica (QCD) na década de 1970, unha teoría cuántica de campos que describe a forza forte mediada por gluóns, coa carga de cor como a súa fonte.

En termos de teoría cuántica de campos, a QCD é unha teoría de Yang-Mills do grupo $SU(3)$ composta por partículas vectoriais sen masa de espín-1, bosóns de gauge chamados gluóns; e partículas masivas de espín-1/2, fermións denominados quarks. Na actualidade, coñécense seis quarks diferentes –u,d,c,s,t,b– que se soen agrupar en tres xeracións, de dous quarks cada unha, con masas crecentes. Cada xeración inclúe un quark con cargas eléctricas $+2/3\,\mathrm{e}$ ou outro cunha carga de $-1/3\,\mathrm{e}$. A carga asociada á simetría correspondente, equivalente á carga eléctrica para a electrodinámica cuántica, coñécese como cor. Cando se realizan cálculos empregando a QCD, é habitual considerar unha teoría xeral de Yang-Mills $SU(N_c)$, onde N_c representa o número de cores. Deste xeito, aínda que a QCD correspondería a $N_c = 3$, manter o numero de cores xenérico permítenos identificar estruturas de cor e simplificar os cálculos, particularmente no límite de N_c grande ($N_c \to \infty$), no cal certos diagramas en cada orde perturbativa poden ser desprezados.

Unha das propiedades máis extraordinarias da QCD é que a intensidade da interacción forte, cuantificada pola constante de acomplamente α_s, diminúe ao aumentar a escala de enerxía do proceso estudado Q. Este comportamento está gobernado pola ecuación do grupo de renormalización, que se obtén ao renormalizar as diverxencias ultravioletas da teoría. A altas enerxías ($Q \gg \Lambda_{\mathrm{QCD}}$), o acoplamento efectivo vólvese pequeno, $\alpha_s \to 0$, co que quarks e gluóns pasan a comportarse como os graos de liberdade relevantes da teoría, permitindo así a aplicación de técnicas perturbativas. Este fenómeno coñécese como liberdade asintótica. Pola contra, a baixas enerxías, ($Q \sim \Lambda_{\mathrm{QCD}}$), o acoplamento fortalécese, o que leva a que quarks e gluóns permanezan ligados dentro dos hadróns. De feito, hai unha gran cantidade de evidencia experimental apoiando o feito de que as partículas con carga de cor non poden ser observadas directamente, senón que sempre se combinan para formar estados neutros de cor, os hadróns. Este fenómeno coñécese como confinamento de cor. Tanto a escala Λ_{QCD} que delimita estes dous réximes, o polo de Landau de QCD, como a variación do acoplamento coa enerxía do proceso a estudar foron medidos de xeito experimental con gran precisión.

Outra propiedade fundamental da teoría da interacción forte é a factorización. Esta propiedade permite separar os *hard scatterings*, calculables perturbativamente a altas enerxías, dos aspectos non perturbativos da estrutura dos hadróns aos estudar colisións hadrónicas. Grazas a factorización, a sección transversal da colisión pode expresarse como a convolución de funcións de distribución de partóns, que describen a probabilidade de atopar un partón cunha fracción de momento dada dentro dun hadrón, funcións de fragmentación, que describen como os partóns se convirten en hadróns, e a sección transversal partónica do proceso, que pode ser calculada á orde requirido en teoría de perturbacións. Aínda que só foi probada rigorosamente para un conxunto limitado de procesos, os esquemas de factorización motivados por argumentos fenomenolóxicos acadaron éxitos notables na descrición de diferentes observables en múltiples procesos físcos.

Jets en experimentos de colisións de partículas

Nas colisións de partículas a alta enerxía, prodúcense partóns moi enerxético a través de *hard scatterings*. Estes experimentan unha cascada de partóns, emitindo gluóns que se dividen en outros gluóns e en pares de quarks e antiquarks. A medida que o sistema se expande ata lonxitudes do orde $\sim 1/\Lambda_{\mathrm{QCD}}$, os quarks e gluóns sofren hadronización, formando hadróns que poden ser detectados no estado final. O estudo destes chorros colimados de hadróns, coñecidos como **jets**, revela propiedades esenciais da cascada de partóns inicial e é crucial na física de partículas moderna. Por exemplo, un dos seus grandes logros históricos é o descubrimento da existencia do gluón. Porén, os jets non son obxectos fundamentais en QFT, senón que deben ser definidos fenomenoloxicamente por algoritmos de reconstrución de jets. Estes algoritmos, cuxa función é agrupar as partículas nos correspondentes jets, deben ser aplicables a varios tipos de obxectos, incluíndo partóns, hadróns, e torres de medición de calorímetro; e ser seguros nos limites infravermello e colineal, o que permite facer predicións empregando QCD perturbativa.

Nas últimas décadas, a combinación de técnicas experimentais e teóricas para analizar a estrutura interna dos jets, coñecida como a súa subestructura, converteuse nunha peza fundamental da física de partículas moderna. Examinar a estrutura interna dos jets ofrece unha fiestra única á QCD e á cascada de radiación sufrida polo partón inicial. As técnicas de subestrutura acadaron un éxito notable nos últimos anos, por exemplo, ao permitir identificar e estudar obxectos relativistas como quarks top e bosóns de Higgs, o que mellora moito a sensibilidade das procuras de física máis alá do Modelo Estándar.

A QCD en condicións extremas

O diagrama de fases da QCD como función da temperatura e da densidade bariónica predí varios estados exóticos da materia hadrónica, proporcionando información sobre aspectos fundamentais da forza forte, das condicións nos primeiros intres do universo, e da composición das estrelas de neutróns, entre outros fenómenos. A pesar da extensa investigación existente, o diagrama de fases da QCD segue estando inexplorado na súa meirande parte, tanto teórica como experimentalmente. Un dos seus estados exóticos máis interesantes é o QGP, un fluído case perfecto onde quarks e gluóns están deconfinados dos hadróns.

O QGP, xunto con outros estados complexos da materia hadrónica, pode ser producido en colisións ultra-relativistas de ións pesados no RHIC e no LHC, o que permite sistematizar o seu estudo. A evolución da materia creada nas HICs transcorre a través de diferentes fases que, de xeito simplificado, son: 1) unha etapa de pre-equilibrio coñecida como glasma, onde a materia está caracterizada por unha alta ocupación de gluóns que se pode describir en termos de campos non abelianos moi intensos; 2) unha etapa térmica descrita pola hidrodinámica viscosa, na que o QGP se forma e expande; e 3) unha etapa de conxelación, na que as partículas do medio hadronizan e pasan a formar estados ligados neutros en cor.

Observar directamente os constituíntes do glasma ou QGP é imposible debido á súa curta vida. Polo tanto, as súas propiedades deben ser inferidas empregando diferentes tipos de sonda, que se poden agrupar segundo: 1) Correlacións de partículas de baixo-p_T, que revelan fluxo colectivo e fluxo anisotrópico, e poden ser parametrizados polos coeficientes da expansión en serie de Fourier da distribución de momentos; 2) Sondas electromagnéticas (fotóns e dileptóns), emitidas ao longo de toda a evolución do QGP, escapan do medio de xeito sinxelo xa que teñen un camiño libre medio moito superior ao dos hadróns por seren neutras de cor; 3) Quarks pesados, como o *charm* ou o *bottom*, cuxos estados ligados (quarkonia) son modificados polo QGP, ofrecendo información sobre as súas propiedades, como a temperatura e densidade, a través da taxa de supresión e recombinación; e 4) Jet quenching, onde os partóns *hard* perden enerxía ao atravesar o QGP, modificando os jets e suprimindo o seu espectro.

Sondas de alta enerxia en HICs

Os jets e os quarks pesados, partículas con interacción forte xeradas a escalas de moi alta enerxía ou masa nos primeiros intres das HICs, son ferramentas esenciais para comprender a natureza da materia nuclear complexa xerada nestas colisións. A súa interacción co medio durante a súa evolución revela información crucial sobre as diferentes fases da mesma. Unha das modificacións máis relevantes dos jets en HICs é a perda de enerxía, unha sinatura clave da formación do medio de cor, que pode ser cuantificada en termos do factor de modificación nuclear (R_{AA}) definido en (1.14). Os experimentos amosan que $R_{AA} < 1$, o que indica a supresión do espectro de jets nas HICs en comparación coas colisións protón-protón, cunha maior supresión nas colisións máis centrais, nas que se espera máis volume do medio xerado.

Máis aló da perda de enerxía, os jets sofren outras modificacións, incluíndo cambios no cascada de partóns e nos patróns de fragmentación, que poden ser detectados empregando observables de subestrutura de jets. O conxunto de modificacións máis xerais que sofren os jets ao atravesar medios de cor recibe o nome de **jet quenching** na literatura. O principal obxectivo dos estudos de jet quenching é empregar estas modificacións para obter información das propiedades da materia de QCD creada e da súa evolución, feito coñecido como tomografía de jets. Para lograr este obxectivo é esencial unha comprensión teórica robusta das interaccións entre jets e medio. Esta tese desenvolve un novo marco teórico que incorpora efectos ata agora desprezados, como a estrutura e a evolución dinámica do medio, ao formalismo de jet quenching existente.

Ademais, a presenza de correlacións de partículas de baixo-p_T en sistemas de colisión pequenos, como as colisións protón-núcleo, sen a correspondente supresión de jets observada nas HICs presenta un enigma. O marco teórico desta tese ofrece un enfoque prometedor para comprender o jet quenching nos sistemas pequenos, nos que se esperan maior desviación do equilibrio e gradentes máis intensos facendo que os efectos da anisotropía e evolución do medio sexan máis relevantes, e potencialmente resolver esta discrepancia.

Fundamentos do formalismo teórico

Procedamos a revisar os fundamentos do formalismo teórico desenvolto nesta tese. No seguinte, entenderemos un partón ‘moi enerxético’ como aquel cunha enerxía moito superior ao seu momento transverso, a calquera escala característica do medio, como a temperatura na fase termalizada, e ao polo de Landau da teoría $\Lambda_{\rm QCD}$. Deste xeito adoitase asumir que a interacción entre partóns e materia é perturbativa, e polo tanto poderemos empregar técnicas da QCD perturbativa para realizar os cálculos pertinentes. En particular, os dous procesos perturbativos dominantes que calcularemos son o ensanchamento do momento transversal e a radiación inducida polo medio. Este último é o mecanismo de perda de enerxía dominante para os partóns moi enerxéticos, a diferenza do réxime de máis baixas enerxías no que prevalece a perda de enerxía por colisións elásticas co medio. Nesta tese desenvolvemos un novo formalismo para sondas de alta enerxía centrándonos nestes dous procesos clave, tanto na fase de glasma como no QGP. En ámbalas fases se modelan as interaccións sonda-materia como partóns enerxéticos interactuando cun campo de fondo de cor, que fará as veces do medio.

O número efectivo de interaccións entre os partóns e o campo de fondo vén determinada polas características da materia. No límite de materia densa, os partóns sofren múltiples interaccións co campo de fondo, que poden ser resumadas en propagadores efectivos (2+1D) para os partóns que incorporan os efectos do medio. Este enfoque e coñecido como o formalismo de Baier, Dokshitzer, Mueller, Peigné, Schiff - Zakharov (BDMPS-Z). No límite de materia diluída, espérase que o número efectivo de interaccións co campo de fondo sexa próximo á unidade, permitindo unha expansión en opacidade e simplificando os cálculos. Este enfoque e coñecido como o formalismo de Gyulasy, Levai, Vitev - Wiedemann (GLV-W). É importante destacar que estes dous enfoques son equivalentes, coa resumación da expansión en opacidade devolvendo o obtido co formalismo BDMPS-Z.

Campo de fondo

O estudo de como se comportan os partóns enerxéticos ao atravesar materia nuclear densa está moi inspirado nos traballos seminais de Landau, Pomeranchuk e Migdal (LPM) en QED. A mediados do século XX, LPM demostrou que unha partícula cargada de alta enerxía que sofre múltiples interaccións cun medio denso experimentará efectos de interferencia entre interaccións adxacentes, o que resulta nunha supresión xeral da radiación de *bremsstrahlung*, coñecida como o efecto LPM. Nos anos 90, impulsado particularmente polo próximo experimento RHIC, dedicouse un esforzo considerable a estender estes estudos a fondos non abelianos, investigando a influencia dos medios de cor densos na propagación de partículas que interactúan fortemente. Estes traballos utilizan un enfoque semiclásico, no que a materia é tratada como un campo de fondo clásico producido por un conxunto estocástico de partículas cargadas con correlacións determinadas polas propiedades da materia. Este segue sendo o formalismo máis empregado para tratar os procesos de jet quenching ata a data.

De acordo con este enfoque histórico, no estudo da interacción de partóns de alta enerxía co medio de QCD, o efecto da materia pode ser modelado por un campo xerado por un conxunto de partóns cargados baixo o grupo $SU(N_c)$, que pode expresarse en xeral segundo a ecuación (2.2). Este campo de fondo está determinado principalmente por dúas cantidades que caracterizan as propiedades da materia: a densidade de fontes de cor, ρ^a, e o potencial de interacción de cada fonte, $v(q)$, onde q é o 4-momento transferido. O potencial v contén información sobre a interacción partón-materia e, polo tanto, espérase que varíe nas distintas fases da evolución da materia creada nas HICs. Ademais, dado que o campo é xerado por un conxunto estocástico de fontes no medio, é crucial caracterizar as súas propiedades estatísticas, codificadas nos seus correladores. A estatística máis apropiada para modelar a materia depende da fase da evolución, e estes correladores, que adoitan expresarse en termos de correladores da densidade de fontes de cor, adoptarán formas distintas para reflectir as propiedades do medio en cada unha das fases estudadas.

Ensanchamento do momento transverso

Comezamos polo estudo do proceso perturbativo dominante máis sinxelo na modificación de jets nun medio de cor, o ensanchamento do momento transverso, examinándoo na fase do QGP, investigando o impacto das anisotropías e do fluxo da materia, e na fase do glasma, analizándoo baixo os campos fortes característicos dos intres iniciais das HICs. Para obter a distribución final do momento transverso en calquera etapa da evolución da materia, debe calcularse a amplitude dun partón que se propaga a través do campo de fondo. En contraste coa imaxe clásica, en QFT unha partícula que interactúa cun campo de fondo experimenta unha superposición de todos os posibles números de interaccións, non un número fixo delas. Polo tanto, a amplitude completa do proceso pode escribirse como a seguinte serie $M = \sum_{N=0}^{\infty} M_N = M_0 + M_1 + M_2 + \dots$, onde M_N é a amplitude con N interaccións e M_0 corresponde ao baleiro. Como xa se introduciu, existen dous enfoques para calcular o elemento de matriz, é dicir, a amplitude ao cadrado promediada sobre os números cuánticos e as configuracións do medio. Por unha banda, o formalismo BDMPS-Z resuma a serie antes de elevar ao cadrado e promediar, construíndo propagadores efectivos para as liñas partónicas; e por outra banda o GLV-W, elevando ao cadrado e promediando cada termo da serie por separado, permitindo un cálculo de cada orde da expansión en opacidade por separado.

Para ilustrar como cada un destes formalismos se estende para incorporar as novidades do modelo do medio, revisamos tres cálculos de ensanchamento do momento transverso. Primeiro, revisitamos o cálculo en QGP con fluxo e anisotropías no límite de materia diluída, usando o formalismo GLV a primeira orde en opacidade ($N_\chi = 1$), como se presenta en [1]. Neste estudo, centrámonos nas correccións derivadas da interacción fluxo-gradentes de anisotropía, que resultan nun reescalamento da distribución do momento transverso, dos momentos da distribucións e do parámetro de jet quenching. Logo, consideramos o ensanchamento nun QGP estático e anisotrópico dentro do límite de materia densa, usando o formalismo BDMPS-Z, como se derivou orixinalmente en [111]. Presentamos as correccións de primeira orde por gradentes de anisotropía á distribución de momentos transversos e os primeiros momentos da distribución. Finalmente, revisitamos a derivación do ensanchamento no glasma, usando o formalismo BDMPS-Z como en [3], obtendo o parámetro de jet quenching derivado da interacción do partón cos campos fortes dos momentos inicias da HIC. Nótese que [1] e [3] forman parte desta tese, véxase o Capítulo 4.

Radiación inducida polo medio

O estudo das emisións de gluóns inducidas polo medio é crucial para comprender os jets dentro da materia QCD. En particular, a perda de enerxía dos jets, unha sinatura clave da formación do QGP, está impulsada principalmente por este mecanismo. Ademais, o espectro de emisión de gluóns dentro do medio proporciona información esencial sobre as modificacións da materia nas cascadas de partóns. As emisións inducidas alteran a subestrutura do jet en comparación cos jets no baleiro, ofrecendo unha ferramenta teórica para comprender o efecto da presenza do medio e extraer información sobre as propiedades deste en análises posteriores. De xeito análogo ao discutido para o ensanchamento do momento transverso, a amplitude do proceso de radiación pódese escribir como unha serie $\mathcal{R} = \sum_{N=0}^{\infty} \mathcal{R}_N = \mathcal{R}_0 + \mathcal{R}_1 + \mathcal{R}_2 + \dots$, na que $\mathcal{R}_N$ é a amplitude con N interaccións e $\mathcal{R}_0$ corresponde ao baleiro. Todos os cálculos de radiación inducida elaborados nesta tese obtéñense, como moito, ata a primeira orde subdominante na expansión eikonal. Polo tanto, os efectos de espín con supresión de enerxía adicional poden ignorarse, e o quark é considerado unha partícula escalar. Ademais, o campo de fondo empregado en todos os casos, derivado no gauge de Lorenz, cumpre $A_z = 0$, co que podemos empregar o gauge axial, simplificando os cálculos ao ter que considerar só as dúas polarizacións físicas do gluón.

A amplitude xeral da emisión dun gluón con N interaccións co campo de fondo pódese escribir en xeral segundo (2.74). Ao igual que no caso do ensanchamento do momento transverso, hai dous métodos posibles para obter o elemento de matriz promediado a partires da amplitude xeral. Seguindo o enfoque BDMPS-Z, resúmanse o número de interaccións co medio ao nivel da amplitude, obtendo un propagador efectivo para cada unha das patas partónicas do proceso. Logo, a amplitude é elevada ao cadrado e realízanse os promedios sobre os números cuánticos e as configuracións do medio. Este é o enfoque empregado en [2] e [3], ámbolos dous parte desta tese, véxase o Capítulo 4. No primeiro, derívase o espectro de radiación inducida de gluóns nun medio estático con correccións de gradentes producidos pola anisotropía a primeiro orde. No segundo, obtense a taxa de radiación inducida polo medio nos instantes iniciais das HICs, estudando cómo as características dos campos fortes presentes no glasma afectan a radiación de gluóns. Por outra banda, seguindo o enfoque GLV, a amplitude completa $\mathcal{R}$ é elevada ao cadrado antes de resumar a serie, e os promedios sobre as configuracións do medio realízanse en cada termo por separado. Este enfoque é utilizado en [1], tamén parte desta tese, no que se calcula o espectro de radiación inducida por un medio anisotrópico e con fluxo. En particular, obtéñense as correccións de gradentes a primeira orde no límite de materia estática, así como o efecto da interacción do fluxo e os gradente no orde dominante da expansión eikonal.

Conclusións

Esta tese introduciu un novo marco teórico para comprender o jet quenching, abordando o papel da evolución da materia e as súas anisotropías. Despois de revisar os conceptos fundamentais e situala en contexto, revisitamos a derivación do formalismo, examinando os fundamentos da teoría do jet quenching, e discutimos os resultados clave, que foron publicados en [1, 2, 3]. Estes tres artigos contribúen ao desenvolvemento desta nova ferramenta analítica abordando tres obxectivos específicos. O artigo [1] presenta o cálculo das correccións principais ao ensanchamento do jet e o espectro de gluóns radiados inducidos polo medio, considerando a interacción entre o fluxo e os gradentes hidrodinámicos dentro dun medio QCD diluído. En [2], calculamos o espectro de gluóns xerados pola emisión dun quark enerxético nun medio QCD denso e anisotrópico. Finalmente, o artigo [3] calcula o ensanchamento, a radiación inducida polo medio e a taxa de perda de enerxía dos jets que atravesan o glasma formado nas etapas iniciais das HICs.

O traballo presentado nesta tese só dá os primeiros pasos na discusión da interacción jet-medio en materia anisotrópica en evolución, e os resultados poderían e deberían estenderse de múltiples maneiras, por exemplo, obtendo os principais efectos de gradente e fluxo no limite de materia densa resumando múltiples interaccións co medio, estendendo os cálculos máis alá da primeira orde na expansión de gradentes ou mellorando os modelos de materia para facelos cada vez máis realistas. Ademais, o traballo presentado deberia incluirse en consideracións fenomenolóxicas de observables particulares. Por exemplo, a posible modificación substancial en $\hat{q}$ e a taxa de perda de enerxia debido á interacción de fluxo e gradentes poden afectar considerablemente as simulacións existentes de jets que interactúan con fondos en evolución. Ademais, os efectos direccionais obtidos na fase do QGP distorsionan fortemente os compoñentes menos enerxéticos do jet, deixando a radiación de máis enerxia relativamente menos afectada, facendo da subestrutura do jet unha ferramenta tomográfica altamente sensible. Polo tanto, estudar as modificacións nos observables da subestrutura do jet, como o limite colineal dos energy-energy corrrelators ou o v_n dentro dos jets, debido á evolución e as anisotropias da materia é esencial para desentrañar as propiedades das interaccións jet-materia. Outra dirección prometedora seria combinar o noso formalismo para o jet quenching nas primeiras etapas das HICs con simulacións numéricas realistas do glasma, o que permitiria calcular a taxa de emisión de gluóns inducidos polo medio.

Bibliography

[1] M. Kuzmin, X. Mayo López, J. Reiten & A. V. Sadofyev, *"Jet quenching in anisotropic flowing matter"*, Phys. Rev. D **109**, 014036 (2024), `arXiv:2309.00683`.

[2] J. Barata, X. Mayo López, A. V. Sadofyev & C. A. Salgado, *"Medium induced gluon spectrum in dense inhomogeneous matter"*, Phys. Rev. D **108**, 034018 (2023), `arXiv:2304.03712`.

[3] J. Barata, S. Hauksson, X. Mayo López & A. V. Sadofyev, *"Jet quenching in the glasma phase: Medium-induced radiation"*, Phys. Rev. D **110**, 094055 (2024), `arXiv:2406.07615`.

[4] M. Gell-Mann, *"The Eightfold Way: A Theory of strong interaction symmetry"*.

[5] Y. Ne'eman, *"Derivation of strong interactions from a gauge invariance"*, Nucl. Phys. **26**, 222 (1961).

[6] M. Gell-Mann, *"A Schematic Model of Baryons and Mesons"*, Phys. Lett. **8**, 214 (1964).

[7] G. Zweig, *"An SU(3) model for strong interaction symmetry and its breaking. Version 2"*, in *"DEVELOPMENTS IN THE QUARK THEORY OF HADRONS. VOL. 1. 1964 - 1978"*, ed: D. B. Lichtenberg & S. P. Rosen, p. 22–101.

[8] O. W. Greenberg, *"Spin and Unitary Spin Independence in a Paraquark Model of Baryons and Mesons"*, Phys. Rev. Lett. **13**, 598 (1964).

[9] M. Y. Han & Y. Nambu, *"Three Triplet Model with Double SU(3) Symmetry"*, Phys. Rev. **139**, B1006 (1965).

[10] E. D. Bloom et al., *"High-Energy Inelastic e p Scattering at 6-Degrees and 10-Degrees"*, Phys. Rev. Lett. **23**, 930 (1969).

[11] M. Breidenbach, J. I. Friedman, H. W. Kendall, E. D. Bloom, D. H. Coward, H. C. DeStaebler, J. Drees, L. W. Mo & R. E. Taylor, *"Observed behavior of highly inelastic electron-proton scattering"*, Phys. Rev. Lett. **23**, 935 (1969).

[12] F. Wilczek, *"What QCD tells us about nature - and why we should listen"*, Nucl. Phys. A **663**, 3 (2000), `hep-ph/9907340`.

[13] F. Gross et al., *"50 Years of Quantum Chromodynamics"*, Eur. Phys. J. C **83**, 1125 (2023), `arXiv:2212.11107`.

[14] R. Utiyama, *"Invariant theoretical interpretation of interaction"*, Phys. Rev. **101**, 1597 (1956).

[15] F. Halzen & A. D. Martin, *"QUARKS AND LEPTONS AN INTRODUCTORY COURSE IN MODERN PARTICLE PHYSICS"*.

[16] R. K. Ellis, W. J. Stirling & B. R. Webber, *"QCD and collider physics"*, Cambridge University Press (2011).

[17] M. D. Schwartz, *"Quantum Field Theory and the Standard Model"*, Cambridge University Press (2014).

[18] M. E. Peskin & D. V. Schroeder, *"An Introduction to quantum field theory"*, Addison-Wesley (1995), Reading, USA.

[19] D. J. Gross & F. Wilczek, *"Asymptotically Free Gauge Theories - I"*, Phys. Rev. D **8**, 3633 (1973).

[20] H. D. Politzer, *"Reliable Perturbative Results for Strong Interactions?"*, Phys. Rev. Lett. **30**, 1346 (1973).

[21] J. Greensite, *"The Confinement problem in lattice gauge theory"*, Prog. Part. Nucl. Phys. **51**, 1 (2003), `hep-lat/0301023`.

[22] R. W. Haymaker, *"Confinement studies in lattice QCD"*, Phys. Rept. **315**, 153 (1999), `hep-lat/9809094`.

[23] P. D. Group, *"Review of Particle Physics"*, PTEP **2020**, 083C01 (2020).

[24] J. C. Collins, D. E. Soper & G. F. Sterman, *"Factorization of Hard Processes in QCD"*, Adv. Ser. Direct. High Energy Phys. **5**, 1 (1989), `hep-ph/0409313`.

[25] R. K. Ellis, H. Georgi, M. Machacek, H. D. Politzer & G. G. Ross, *"Perturbation Theory and the Parton Model in QCD"*, Nucl. Phys. B **152**, 285 (1979).

[26] TASSO Collaboration, R. Brandelik et al., *"Evidence for Planar Events in e+ e- Annihilation at High-Energies"*, Phys. Lett. B **86**, 243 (1979).

[27] JADE Collaboration, W. Bartel et al., *"Observation of Planar Three Jet Events in e+ e- Annihilation and Evidence for Gluon Bremsstrahlung"*, Phys. Lett. B **91**, 142 (1980).

[28] PLUTO Collaboration, C. Berger et al., *"Evidence for Gluon Bremsstrahlung in e+ e- Annihilations at High-Energies"*, Phys. Lett. B **86**, 418 (1979).

[29] D. P. Barber et al., *"Discovery of Three Jet Events and a Test of Quantum Chromodynamics at PETRA Energies"*, Phys. Rev. Lett. **43**, 830 (1979).

[30] R. Kogler et al., *"Jet Substructure at the Large Hadron Collider: Experimental Review"*, Rev. Mod. Phys. **91**, 045003 (2019), `arXiv:1803.06991`.

[31] G. P. Salam, *"Towards Jetography"*, Eur. Phys. J. C **67**, 637 (2010), `arXiv:0906.1833`.

[32] S. Catani, Y. L. Dokshitzer, M. H. Seymour & B. R. Webber, *"Longitudinally invariant K_t clustering algorithms for hadron hadron collisions"*, Nucl. Phys. B **406**, 187 (1993).

[33] Y. L. Dokshitzer, G. D. Leder, S. Moretti & B. R. Webber, *"Better jet clustering algorithms"*, JHEP **9708**, 001 (1997), `hep-ph/9707323`.

[34] M. Cacciari, G. P. Salam & G. Soyez, *"The anti-k_t jet clustering algorithm"*, JHEP **0804**, 063 (2008), `arXiv:0802.1189`.

[35] A. J. Larkoski, I. Moult & B. Nachman, *"Jet Substructure at the Large Hadron Collider: A Review of Recent Advances in Theory and Machine Learning"*, Phys. Rept. **841**, 1 (2020), `arXiv:1709.04464`.

[36] J. C. Collins & M. J. Perry, *"Superdense Matter: Neutrons Or Asymptotically Free Quarks?"*, Phys. Rev. Lett. **34**, 1353 (1975).

[37] N. Cabibbo & G. Parisi, *"Exponential Hadronic Spectrum and Quark Liberation"*, Phys. Lett. B **59**, 67 (1975).

[38] W. Busza, K. Rajagopal & W. van der Schee, *"Heavy Ion Collisions: The Big Picture, and the Big Questions"*, Ann. Rev. Nucl. Part. Sci. **68**, 339 (2018), `arXiv:1802.04801`.

[39] R. S. Bhalerao, *"Relativistic heavy-ion collisions"*, in *"1st Asia-Europe-Pacific School of High-Energy Physics"*, p. 219–239.

[40] ALICE Collaboration, S. Acharya et al., *"The ALICE experiment: a journey through QCD"*, Eur. Phys. J. C **84**, 813 (2024), `arXiv:2211.04384`.

[41] STAR Collaboration, J. Adams et al., *"Experimental and theoretical challenges in the search for the quark gluon plasma: The STAR Collaboration's critical assessment of the evidence from RHIC collisions"*, Nucl. Phys. A **757**, 102 (2005), `nucl-ex/0501009`.

[42] PHENIX Collaboration, K. Adcox et al., *"Formation of dense partonic matter in relativistic nucleus-nucleus collisions at RHIC: Experimental evaluation by the PHENIX collaboration"*, Nucl. Phys. A **757**, 184 (2005), `nucl-ex/0410003`.

[43] PHOBOS Collaboration, B. B. Back et al., *"The PHOBOS perspective on discoveries at RHIC"*, Nucl. Phys. A **757**, 28 (2005), `nucl-ex/0410022`.

[44] BRAHMS Collaboration, I. Arsene et al., *"Quark gluon plasma and color glass condensate at RHIC? The Perspective from the BRAHMS experiment"*, Nucl. Phys. A **757**, 1 (2005), `nucl-ex/0410020`.

[45] ALICE Collaboration, K. Aamodt et al., *"Elliptic flow of charged particles in Pb-Pb collisions at 2.76 TeV"*, Phys. Rev. Lett. **105**, 252302 (2010), `arXiv:1011.3914`.

[46] U. Heinz & R. Snellings, *"Collective flow and viscosity in relativistic heavy-ion collisions"*, Ann. Rev. Nucl. Part. Sci. **63**, 123 (2013), `arXiv:1301.2826`.

[47] STAR Collaboration, , *"Temperature Measurement of Quark-Gluon Plasma at Different Stages"*, `arXiv:2402.01998`.

[48] ALICE Collaboration, S. Acharya et al., *"Dielectron production in central Pb—Pb collisions at $\sqrt{s_{\mathrm{NN}}}$ = 5.02 TeV"*, `arXiv:2308.16704`.

[49] F. Geurts & R.-A. Tripolt, *"Electromagnetic probes: Theory and experiment"*, Prog. Part. Nucl. Phys. **128**, 104004 (2023), `arXiv:2210.01622`.

[50] T. Matsui & H. Satz, *"J/ψ Suppression by Quark-Gluon Plasma Formation"*, Phys. Lett. B **178**, 416 (1986).

[51] F. Karsch, D. Kharzeev & H. Satz, *"Sequential charmonium dissociation"*, Phys. Lett. B **637**, 75 (2006), `hep-ph/0512239`.

[52] L. Apolinário, Y.-J. Lee & M. Winn, *"Heavy quarks and jets as probes of the QGP"*, Prog. Part. Nucl. Phys. **127**, 103990 (2022), `arXiv:2203.16352`.

[53] CMS Collaboration, V. Khachatryan et al., *"Measurement of inclusive jet cross sections in pp and PbPb collisions at $\sqrt{s_{NN}}$ = 2.76 TeV"*, Phys. Rev. C **96**, 015202 (2017), `arXiv:1609.05383`.

[54] ATLAS Collaboration, M. Aaboud et al., *"Measurement of the nuclear modification factor for inclusive jets in Pb+Pb collisions at $\sqrt{s_{\mathrm{NN}}} = 5.02$ TeV with the ATLAS detector"*, Phys. Lett. B **790**, 108 (2019), `arXiv:1805.05635`.

[55] J. D. Bjorken, *"Energy Loss of Energetic Partons in Quark - Gluon Plasma: Possible Extinction of High p(t) Jets in Hadron - Hadron Collisions"*.

[56] CMS Collaboration, V. Khachatryan et al., *"Charged-particle nuclear modification factors in PbPb and pPb collisions at $\sqrt{s_{\mathrm{N\,N}}} = 5.02$ TeV"*, JHEP **1704**, 039 (2017), `arXiv:1611.01664`.

[57] ATLAS Collaboration, G. Aad et al., *"Transverse momentum and process dependent azimuthal anisotropies in $\sqrt{s_{\mathrm{NN}}} = 8.16$ TeV p+Pb collisions with the ATLAS detector"*, Eur. Phys. J. C **80**, 73 (2020), `arXiv:1910.13978`.

[58] M. V. Kuzmin & X. Mayo López, *"Gluon radiation inside a flowing medium"*, `arXiv:2406.14628`.

[59] S. Abreu, X. Mayo López, G. Milhano & A. Soto-Ontoso, *"A generalized picture of colour decoherence in dense QCD media"*, `arXiv:2410.24135`.

[60] J. Barata, Z.-B. Kang, X. Mayo López & J. Penttala, *"Energy-Energy Correlator for jet production in pp and pA collisions"*, `arXiv:2411.11782`.

[61] J. Casalderrey-Solana & C. A. Salgado, *"Introductory lectures on jet quenching in heavy ion collisions"*, Acta Phys. Polon. B **38**, 3731 (2007), `arXiv:0712.3443`.

[62] M. Lekaveckas & K. Rajagopal, *"Effects of Fluid Velocity Gradients on Heavy Quark Energy Loss"*, JHEP **1402**, 068 (2014), `arXiv:1311.5577`.

[63] K. Rajagopal & A. V. Sadofyev, *"Chiral drag force"*, JHEP **1510**, 018 (2015), `arXiv:1505.07379`.

[64] A. V. Sadofyev & Y. Yin, *"The charmonium dissociation in an "anomalous wind""*, JHEP **1601**, 052 (2016), `arXiv:1510.06760`.

[65] J. Reiten & A. V. Sadofyev, *"Drag force to all orders in gradients"*, JHEP **2007**, 146 (2020), `arXiv:1912.08816`.

[66] I. Y. Aref'eva, A. A. Golubtsova & E. Gourgoulhon, *"Holographic drag force in 5d Kerr-AdS black hole"*, JHEP **2104**, 169 (2021), `arXiv:2004.12984`.

[67] H. Liu, K. Rajagopal & U. A. Wiedemann, *"Wilson loops in heavy ion collisions and their calculation in AdS/CFT"*, JHEP **0703**, 066 (2007), `hep-ph/0612168`.

[68] G. Nijs, B. Scheihing-Hitschfeld & X. Yao, *"Generalized gluon distribution for quarkonium dynamics in strongly coupled N=4 Yang-Mills theory"*, Phys. Rev. D **109**, 094043 (2024), `arXiv:2310.09325`.

[69] J. Casalderrey-Solana, D. C. Gulhan, J. G. Milhano, D. Pablos & K. Rajagopal, *"Predictions for Boson-Jet Observables and Fragmentation Function Ratios from a Hybrid Strong/Weak Coupling Model for Jet Quenching"*, JHEP **1603**, 053 (2016), `arXiv:1508.00815`.

[70] A. Kurkela & U. A. Wiedemann, *"Picturing perturbative parton cascades in QCD matter"*, Phys. Lett. B **740**, 172 (2015), `arXiv:1407.0293`.

[71] J.-P. Blaizot, F. Dominguez, E. Iancu & Y. Mehtar-Tani, *"Probabilistic picture for medium-induced jet evolution"*, JHEP **1406**, 075 (2014), `arXiv:1311.5823`.

[72] R. Baier, A. H. Mueller, D. Schiff & D. T. Son, *"'Bottom up' thermalization in heavy ion collisions"*, Phys. Lett. B **502**, 51 (2001), `hep-ph/0009237`.

[73] S. Jeon & G. D. Moore, *"Energy loss of leading partons in a thermal QCD medium"*, Phys. Rev. C **71**, 034901 (2005), `hep-ph/0309332`.

[74] J.-P. Blaizot, E. Iancu & Y. Mehtar-Tani, *"Medium-induced QCD cascade: democratic branching and wave turbulence"*, Phys. Rev. Lett. **111**, 052001 (2013), `arXiv:1301.6102`.

[75] E. Braaten & M. H. Thoma, *"Energy loss of a heavy quark in the quark - gluon plasma"*, Phys. Rev. D **44**, R2625 (1991).

[76] R. Baier, D. Schiff & B. G. Zakharov, *"Energy loss in perturbative QCD"*, Ann. Rev. Nucl. Part. Sci. **50**, 37 (2000), `hep-ph/0002198`.

[77] R. Baier, Y. L. Dokshitzer, A. H. Mueller, S. Peigne & D. Schiff, *"Radiative energy loss and p(T) broadening of high-energy partons in nuclei"*, Nucl. Phys. B **484**, 265 (1997), `hep-ph/9608322`.

[78] R. Baier, Y. L. Dokshitzer, A. H. Mueller, S. Peigne & D. Schiff, *"Radiative energy loss of high-energy quarks and gluons in a finite volume quark - gluon plasma"*, Nucl. Phys. B **483**, 291 (1997), `hep-ph/9607355`.

[79] B. G. Zakharov, *"Fully quantum treatment of the Landau-Pomeranchuk-Migdal effect in QED and QCD"*, JETP Lett. **63**, 952 (1996), `hep-ph/9607440`.

[80] B. G. Zakharov, *"Radiative energy loss of high-energy quarks in finite size nuclear matter and quark - gluon plasma"*, JETP Lett. **65**, 615 (1997), `hep-ph/9704255`.

[81] R. Baier, Y. L. Dokshitzer, S. Peigne & D. Schiff, *"Induced gluon radiation in a QCD medium"*, Phys. Lett. B **345**, 277 (1995), `hep-ph/9411409`.

[82] R. Baier, Y. L. Dokshitzer, A. H. Mueller, S. Peigne & D. Schiff, *"The Landau-Pomeranchuk-Migdal effect in QED"*, Nucl. Phys. B **478**, 577 (1996), `hep-ph/9604327`.

[83] B. G. Zakharov, *"Light cone path integral approach to the Landau-Pomeranchuk-Migdal effect"*, Phys. Atom. Nucl. **61**, 838 (1998), `hep-ph/9807540`.

[84] N. Armesto, C. A. Salgado & U. A. Wiedemann, *"Medium induced gluon radiation off massive quarks fills the dead cone"*, Phys. Rev. D **69**, 114003 (2004), `hep-ph/0312106`.

[85] C. A. Salgado & U. A. Wiedemann, *"Calculating quenching weights"*, Phys. Rev. D **68**, 014008 (2003), `hep-ph/0302184`.

[86] M. Gyulassy, P. Levai & I. Vitev, *"Jet quenching in thin quark gluon plasmas. 1. Formalism"*, Nucl. Phys. B **571**, 197 (2000), `hep-ph/9907461`.

[87] M. Gyulassy, P. Levai & I. Vitev, *"NonAbelian energy loss at finite opacity"*, Phys. Rev. Lett. **85**, 5535 (2000), `nucl-th/0005032`.

[88] M. Gyulassy, P. Levai & I. Vitev, *"Reaction operator approach to nonAbelian energy loss"*, Nucl. Phys. **B594**, 371 (2001), `nucl-th/0006010`.

[89] U. A. Wiedemann, *"Transverse dynamics of hard partons in nuclear media and the QCD dipole"*, Nucl. Phys. B **582**, 409 (2000), `hep-ph/0003021`.

[90] U. A. Wiedemann, *"Gluon radiation off hard quarks in a nuclear environment: Opacity expansion"*, Nucl. Phys. B **588**, 303 (2000), `hep-ph/0005129`.

[91] U. A. Wiedemann, *"Jet quenching versus jet enhancement: A Quantitative study of the BDMPS-Z gluon radiation spectrum"*, Nucl. Phys. A **690**, 731 (2001), `hep-ph/0008241`.

[92] F. Gelis, T. Lappi & R. Venugopalan, *"High energy factorization in nucleus-nucleus collisions"*, Phys. Rev. D **78**, 054019 (2008), `arXiv:0804.2630`.

[93] R. Sassot, M. Stratmann & P. Zurita, *"Fragmentations Functions in Nuclear Media"*, Phys. Rev. D **81**, 054001 (2010), `arXiv:0912.1311`.

[94] L. D. Landau & I. Pomeranchuk, *"Limits of applicability of the theory of bremsstrahlung electrons and pair production at high-energies"*, Dokl. Akad. Nauk Ser. Fiz. **92**, 535 (1953).

[95] A. B. Migdal, *"Bremsstrahlung and pair production in condensed media at high-energies"*, Phys. Rev. **103**, 1811 (1956).

[96] M. Gyulassy & X.-n. Wang, *"Multiple collisions and induced gluon Bremsstrahlung in QCD"*, Nucl. Phys. B **420**, 583 (1994), `nucl-th/9306003`.

[97] X.-N. Wang, M. Gyulassy & M. Plumer, *"The LPM effect in QCD and radiative energy loss in a quark gluon plasma"*, Phys. Rev. D **51**, 3436 (1995), `hep-ph/9408344`.

[98] S. Cao & X.-N. Wang, *"Jet quenching and medium response in high-energy heavy-ion collisions: a review"*, Rept. Prog. Phys. **84**, 024301 (2021), `arXiv:2002.04028`.

[99] M. Gyulassy, I. Vitev, X.-N. Wang & P. Huovinen, *"Transverse expansion and high p(T) azimuthal asymmetry at RHIC"*, Phys. Lett. B **526**, 301 (2002), `nucl-th/0109063`.

[100] M. Gyulassy, I. Vitev & X. N. Wang, *"High p(T) azimuthal asymmetry in noncentral A+A at RHIC"*, Phys. Rev. Lett. **86**, 2537 (2001), `nucl-th/0012092`.

[101] R. Baier, Y. L. Dokshitzer, A. H. Mueller & D. Schiff, *"Radiative energy loss of high-energy partons traversing an expanding QCD plasma"*, Phys. Rev. C **58**, 1706 (1998), `hep-ph/9803473`.

[102] R. Baier, A. H. Mueller & D. Schiff, *"How does transverse (hydrodynamic) flow affect jet-broadening and jet-quenching ?"*, Phys. Lett. B **649**, 147 (2007), `nucl-th/0612068`.

[103] T. Renk, J. Ruppert, C. Nonaka & S. A. Bass, *"Jet-quenching in a 3D hydrodynamic medium"*, Phys. Rev. C **75**, 031902 (2007), `nucl-th/0611027`.

[104] N. Armesto, C. A. Salgado & U. A. Wiedemann, *"Measuring the collective flow with jets"*, Phys. Rev. Lett. **93**, 242301 (2004), `hep-ph/0405301`.

[105] N. Armesto, C. A. Salgado & U. A. Wiedemann, *"Low-p(T) collective flow induces high-p(T) jet quenching"*, Phys. Rev. C **72**, 064910 (2005), `hep-ph/0411341`.

[106] Y. He, L.-G. Pang & X.-N. Wang, *"Gradient Tomography of Jet Quenching in Heavy-Ion Collisions"*, Phys. Rev. Lett. **125**, 122301 (2020), `arXiv:2001.08273`.

[107] A. V. Sadofyev, M. D. Sievert & I. Vitev, *"Ab initio coupling of jets to collective flow in the opacity expansion approach"*, Phys. Rev. D **104**, 094044 (2021), `arXiv:2104.09513`.

[108] A. Ipp, D. I. Müller & D. Schuh, *"Anisotropic momentum broadening in the 2+1D Glasma: analytic weak field approximation and lattice simulations"*, Phys. Rev. D **102**, 074001 (2020), `arXiv:2001.10001`.

[109] S. Hauksson, S. Jeon & C. Gale, *“Momentum broadening of energetic partons in an anisotropic plasma”*, Phys. Rev. C **105**, 014914 (2022), `arXiv:2109.04575`.

[110] M. E. Carrington, A. Czajka & S. Mrowczynski, *“Jet quenching in glasma”*, Phys. Lett. B **834**, 137464 (2022), `arXiv:2112.06812`.

[111] J. Barata, A. V. Sadofyev & C. A. Salgado, *“Jet broadening in dense inhomogeneous matter”*, Phys. Rev. D **105**, 114010 (2022), `arXiv:2202.08847`.

[112] Y. Fu, J. Casalderrey-Solana & X.-N. Wang, *“Asymmetric transverse momentum broadening in an inhomogeneous medium”*, Phys. Rev. D **107**, 054038 (2023), `arXiv:2204.05323`.

[113] J. Barata, A. V. Sadofyev & X.-N. Wang, *“Quantum partonic transport in QCD matter”*, Phys. Rev. D **107**, L051503 (2023), `arXiv:2210.06519`.

[114] S. Hauksson & E. Iancu, *“Jet polarisation in an anisotropic medium”*, JHEP **2308**, 027 (2023), `arXiv:2303.03914`.

[115] K. Boguslavski, A. Kurkela, T. Lappi, F. Lindenbauer & J. Peuron, *“Jet momentum broadening during initial stages in heavy-ion collisions”*, Phys. Lett. B **850**, 138525 (2024), `arXiv:2303.12595`.

[116] J. Barata, J. G. Milhano & A. V. Sadofyev, *“Picturing QCD jets in anisotropic matter: from jet shapes to energy energy correlators”*, Eur. Phys. J. C **84**, 174 (2024), `arXiv:2308.01294`.

[117] C. Andres, F. Dominguez, A. V. Sadofyev & C. A. Salgado, *“Jet broadening in flowing matter: Resummation”*, Phys. Rev. D **106**, 074023 (2022), `arXiv:2207.07141`.

[118] S. Caron-Huot & C. Gale, *“Finite-size effects on the radiative energy loss of a fast parton in hot and dense strongly interacting matter”*, Phys. Rev. C **82**, 064902 (2010), `arXiv:1006.2379`.

[119] E. Iancu & R. Venugopalan, *“The Color glass condensate and high-energy scattering in QCD”*, in *“Quark-gluon plasma 4”*, ed: R. C. Hwa & X.-N. Wang, p. 249–3363.

[120] T. Lappi & L. McLerran, *“Some features of the glasma”*, Nucl. Phys. A **772**, 200 (2006), `hep-ph/0602189`.

[121] F. Gelis, E. Iancu, J. Jalilian-Marian & R. Venugopalan, *“The Color Glass Condensate”*, Ann. Rev. Nucl. Part. Sci. **60**, 463 (2010), `arXiv:1002.0333`.

[122] F. Gelis, *“Color Glass Condensate and Glasma”*, Int. J. Mod. Phys. A **28**, 1330001 (2013), `arXiv:1211.3327`.

[123] F. Gelis, *“Initial state and thermalization in the Color Glass Condensate framework”*, Int. J. Mod. Phys. E **24**, 1530008 (2015), `arXiv:1508.07974`.

[124] M. D. Sievert & I. Vitev, *“Quark branching in QCD matter to any order in opacity beyond the soft gluon emission limit”*, Phys. Rev. **D98**, 094010 (2018), `arXiv:1807.03799`.

[125] Y. Mehtar-Tani, C. A. Salgado & K. Tywoniuk, *"The Radiation pattern of a QCD antenna in a dense medium"*, JHEP **1210**, 197 (2012), `arXiv:1205.5739`.

[126] J.-P. Blaizot, F. Dominguez, E. Iancu & Y. Mehtar-Tani, *"Medium-induced gluon branching"*, JHEP **1301**, 143 (2013), `arXiv:1209.4585`.

[127] J. Barata, Y. Mehtar-Tani, A. Soto-Ontoso & K. Tywoniuk, *"Medium-induced radiative kernel with the Improved Opacity Expansion"*, JHEP **2109**, 153 (2021), `arXiv:2106.07402`.

[128] P. Aurenche & B. G. Zakharov, *"Parton energy loss in glasma"*, Phys. Lett. B **718**, 937 (2013), `arXiv:1205.6462`.

[129] V. Baier & V. Katkov, JETP **26**, 854 (1968).

[130] B. G. Zakharov, *"Parton energy loss due to synchrotron-like gluon emission"*, JETP Lett. **88**, 475 (2008), `arXiv:0809.0599`.

[131] E. V. Shuryak & I. Zahed, *"Jet quenching in high-energy heavy ion collisions by QCD synchrotron - like radiation"*, Phys. Rev. D **67**, 054025 (2003), `hep-ph/0207163`.

[132] B. G. Zakharov, *"Effect of magnetic field on the photon radiation from quark-gluon plasma in heavy ion collisions"*, Eur. Phys. J. C **76**, 609 (2016), `arXiv:1609.04324`.

[133] Y. He, T. Luo, X.-N. Wang & Y. Zhu, *"Linear Boltzmann Transport for Jet Propagation in the Quark-Gluon Plasma: Elastic Processes and Medium Recoil"*, Phys. Rev. C **91**, 054908 (2015), `arXiv:1503.03313`, [Erratum: Phys.Rev.C 97, 019902 (2018)].

[134] J. H. Putschke et al., *"The JETSCAPE framework"*, `arXiv:1903.07706`.

[135] D. Zigic, I. Salom, J. Auvinen, P. Huovinen & M. Djordjevic, *"DREENA-A framework as a QGP tomography tool"*, Front. in Phys. **10**, 957019 (2022), `arXiv:2110.01544`.

[136] S. Stojku, J. Auvinen, L. Zivkovic, P. Huovinen & M. Djordjevic, *"Jet-perceived anisotropy revealed through high-p⊥ data"*, Phys. Lett. B **835**, 137501 (2022), `arXiv:2110.02029`.

[137] L. Barreto, F. M. Canedo, M. G. Munhoz, J. Noronha & J. Noronha-Hostler, *"Jet cone radius dependence of RAA and v2 at PbPb 5.02 TeV from JEWEL+TRENTo+v-USPhydro"*, Phys. Lett. B **860**, 139217 (2025), `arXiv:2208.02061`.

[138] D. Pablos, M. Singh, S. Jeon & C. Gale, *"Minijet quenching in a concurrent jet+hydro evolution and the nonequilibrium quark-gluon plasma"*, Phys. Rev. C **106**, 034901 (2022), `arXiv:2202.03414`.

[139] M. Singh, M. Kurian, S. Jeon & C. Gale, *"Open charm phenomenology with a multistage approach to relativistic heavy-ion collisions"*, Phys. Rev. C **108**, 054901 (2023), `arXiv:2306.09514`.

[140] J. Barata, C. A. Salgado & J. a. M. Silva, *"Gluon to $q\bar{q}$ antenna in anisotropic QCD matter: spin-polarized and azimuthal jet observables"*, JHEP **2412**, 023 (2024), `arXiv:2407.04774`.

[141] Y.-X. Xiao, Y. He, L.-G. Pang, H. Zhang & X.-N. Wang, *"Asymmetric jet shapes with two-dimensional jet tomography"*, Phys. Rev. C **109**, 054906 (2024), `arXiv:2402.00264`.

[142] A. Ipp, D. I. Müller & D. Schuh, *"Jet momentum broadening in the pre-equilibrium Glasma"*, Phys. Lett. B **810**, 135810 (2020), `arXiv:2009.14206`.

[143] D. Avramescu, V. Baran, V. Greco, A. Ipp, D. I. Müller & M. Ruggieri, *"Simulating jets and heavy quarks in the glasma using the colored particle-in-cell method"*, Phys. Rev. D **107**, 114021 (2023), `arXiv:2303.05599`.

USC
UNIVERSIDADE
DE SANTIAGO
DE COMPOSTELA

CAMPUS VIDA
CAMPUS DE EXCELENCIA INTERNACIONAL

Studying Quantum Chromodynamics under extreme conditions provides a window into fascinating phenomena: from the fundamental properties of the strong interaction, a fundamental force governing the subatomic world, to the conditions present in the primordial Universe. This is achieved through the study of relativistic heavy-ion collisions, where a novel phase of complex nuclear matter is created. This thesis presents a novel formalism for describing jet propagation within this complex matter, designed to use jets as differential probes of its spatio-temporal structure. This thesis details this novel formalism, deriving the two dominant perturbative processes of jet modifications, transverse momentum broadening and medium-induced gluon radiation, in the presence of an evolving medium with non-trivial structure.